RAIN ATTENUATION MODELLING FOR LINE-OF-SIGHT TERRESTRIAL LINKS

Kumaran Naicker

April 2006

Submitted in fulfilment of the academic requirements for the degree of MScEng in
the School of Electrical, Electronic and Computer Engineering,
University of KwaZulu-Natal, Durban, South Africa.

Abstract

In today's rapidly expanding communications industry, there is an ever-increasing demand for greater bandwidth, higher data rates and better spectral efficiency. As a result current and future communication systems will need to employ advanced spatial, temporal and frequency diversity techniques in order to meet these demands. Even with the utilisation of such techniques, the congestion of the lower frequency bands, will inevitably lead to the increased usage of the millimetre-wave frequencies in terrestrial communication systems. Before such systems can be deployed, radio system designers require realistic and readily useable channel and propagation models at their disposal to predict the behaviour of such communication links and ensure that reliable and efficient data transmission is achieved

The scattering and attenuation of electromagnetic waves by rain is a serious problem for microwave and millimetre-wave frequencies. The conversion of rain rate to specific attenuation is a crucial step in the analysis of the total path attenuation and hence radio-link availability. It is now common practice to relate the specific attenuation and the rain rate using the simple power law relationship. The power-law parameters are then used in the path attenuation model, where the spatial variations of rainfall are estimated by a path-integration of the rain rate. These power law parameters are strongly influenced by the drop-size-distribution (DSD). Thus an examination of the various DSDs and their influence on the specific attenuation and link availability is warranted.

Several models for the DSD have been suggested in literature, from the traditional exponential, to the gamma, lognormal and Weibull distributions. The type of DSD varies depending on the geographical location and rainfall type. An important requirement of the DSD is that it is consistent with rain rate (i.e. the DSD must satisfy the rain-rate integral equation). Thus before application in the specific attenuation calculations, normalisation needs to be performed to ensure the consistency, as done in this study.

Once the specific attenuation has been evaluated for necessary frequency and rain-rate range, path averaging is performed to predict the rain attenuation over the communication link. The final step in this dissertation is the estimation of the percentage of time of such occurrences. For this, cumulative time statistics of surface-point rain rates are needed. The resulting cumulative distribution model of the fade depth and duration due to rain is a valuable tool for system designers. With such models the system designer can then determine the appropriate fade margin for the communication system and resulting period of unavailability for the link

Preface

The research and simulations presented in this dissertation have been undertaken by the author and submitted in fulfilment of the academic requirements for the degree of MScEng in the School of Electrical, Electronic and Computer Engineering at the University of KwaZulu-Natal, Howard College Campus. All work has been undertaken under the supervision of Professor S. H. Mneney at the Centre of Radio Access Technologies, and with the financial assistance from Telkom S.A. Ltd. and Alcactel S.A.

Certain aspects of this dissertation have been presented at and published in the proceedings of SATNAC 2004 (Stellenbosch, SA) and AFRICON 2004 (Gaborone, Botswana) conferences. Part of the research has also been submitted for publication in the transactions of the SAIEE.

This dissertation is completely the work of the author and has not otherwise been submitted in any form, for any other degree or diploma, to any other tertiary institution. Any use of the published or unpublished work of others has been duly acknowledged within the text.

Acknowledgements

I am forever indebted to my family for their encouragement and support during my studies. My deepest gratitude must most of all go to my parents for affording me the opportunity to pursue an academic life and complementing this with never-ending love and comfort in every regard.

I would like to express my gratitude to my supervisor Prof. S. H. Mneney for his unyielding assistance and guidance throughout my studies at the University of KwaZulu-Natal. I greatly appreciate the time and help that you have provided me with. I would also like to thank the technical staff at UKZN for their assistance in the installation of line-of-sight link apparatus, the Department of Science for granting the permission for the installation at the Westville Campus and Mr van Heetkamp for providing a safe and secure location of the transmitter equipment. I must also acknowledge Telkom S.A. Ltd. and Alcatel S.A. for their financial assistance and for providing the equipment necessary for the completion of this study.

I must thank my friends, especially Navern, Nishkar and Jerry, for always providing me with valuable input, constant support and a memorable academic life. Special thanks must go to Karusha, my inspiration and pillar of support, for the countless hours spent assisting in the verification and capturing of data and the proof-reading of this dissertation. Her unwavering commitment and support was instrumental in the completion of this dissertation.

Last but certainly not least, I would like to thank God and my spiritual preceptors Sri Swami Sivananda and Sri Swami Sahajananda for their grace upon my entire life.

Contents

Chapter 4 Rain-Rate statistics 90

List of Acronyms

AU	Atlas and Ulbrich
CS	Continental - Shower
CT	Continental – Thunderstorm
CW	Continuous-wave
DDF	Depth-Duration-Frequency
DSD	Drop-size distribution
I.C.A.N	International Committee of Air Navigation
ITU	International Telecommunications Union
JD	Joss-Drizzle
JT	Joss-Thunderstorm
JW	Joss-Widespread
LOS	Line-of-sight
MAR	Mean annual rainfall
MP	Marshall Palmer
RBW	Resolution Bandwidth
SAWB	South Africa Weather Bureau

S.T.	Summer Tropical Standard Atmosphere
TS	Tropical -Shower
TT	Tropical – Thunderstorm
VBW	Video Bandwidth
WB	Weibull
UKZN	University of Kwazulu-Natal
XPI	Cross-Polarization Interference

List of Notation and Mathematical Symbols

ε	Complex dielectric constant of water
ε'	Real part of dielectric constant of water
ε''	Imaginary part of dielectric constant of water
ζ	Complex refractive index
ζ'	Real part of refractive index of water
ζ''	Imaginary part of refractive index of water
ρ_w	Density of water
λ	Wavelength in free-space
γ	Attenuation coefficient
a	Raindrop radius
f	Frequency
k_0	Wave number
v	Terminal velocity of raindrops
$A_{0.01}$	Attenuation exceeded for 0.01 % of the year
A_a	Atmospheric Absorption loss
A_s	Specific Attenuation

A_t	Total system loss
C_{abs}	Absorption Cross Section
C_b	Back-scattering Cross Section
C_{bi}	Bistatic Radar Cross Section
$C_d\left(\hat{\boldsymbol{K}}_1,\hat{\boldsymbol{K}}_2\right)$	Differential Cross Section
C_{ext}	Extinction Cross Section
C_g	Geometric Cross Section
C_{sca}	Scattering Cross Section
D	Raindrop Diameter
F_1	First Fresnel elipsoid
F_A	Total volume of rain-water arriving at a horizontal surface
F_W	Fraction of liquid-water content
F_V	Volume fraction of rain-water in air
G_a	Amplifier gain
G_t	Transmitter antenna gain
G_r	Receiver antenna gain
$H^{\tau-\min}$	τ -minute rain depth
N_A	Area-based drop-size distribution

N_T	Total number of raindrops
N_V	Volumetric-based drop-size distribution
P	Atmospheric pressure
P_0	Standard atmospheric pressure at sea level
P_r	Power at receiver power
P_t	Transmitter output power
Q_{sca}	Scattering Efficiency
Q_{ext}	Extinction Efficiency
Q_{abs}	Absorption Efficiency
R	Rain rate
$R_{0.01}$	Rain rate exceeded for 0.01 % of the year
R_p	Point rainfall rate
R_N	Rain-rate integral equation
$R^{1-\min}$	1-minute rain rate
$R^{5-\min}$	5-minute rain rate
$R^{\tau-\min}$	τ -minute rain rate
T	Atmospheric temperature
T_0	Standard atmospheric temperature at sea level

$\mathrm{erfc}(\sim)$	Complimentary Error Function
$\mathrm{Im}(\sim)$	Imaginary component
$\ln(\sim)$	Natural logarithm
$Norm$	Normalising function
$\mathrm{Re}(\sim)$	Real component
$f(\hat{\boldsymbol{K}}_1,\hat{\boldsymbol{K}}_2)$	Forward-scattering amplitude
$\boldsymbol{E}^i$	Electric field of incident wave
$\boldsymbol{E}^s$	Electric field of scatterer wave
$\boldsymbol{E}^t$	Electric field of transmitted wave
$\boldsymbol{H}^i$	Magnetic field of incident wave
$\boldsymbol{H}^s$	Magnetic field of scatterer wave
$\boldsymbol{H}^t$	Magnetc field of transmitted wave
$\hat{\boldsymbol{E}}_i$	Unit vector in the direction of polarization
$\hat{\boldsymbol{K}}_1$	Unit vector in the direction of propagation
$\hat{\boldsymbol{K}}_2$	Unit vector directed form origin to observation point

List of Tables

List of Figures

Chapter 1

Introduction

Propagation models are developed to describe the multitude of propagation phenomena occurring readily in nature. These models provide a wealth of knowledge to scientists, radio engineers and communication system designers and are instrumental for the understanding and design of radar and communication systems. Propagation models are developed from our theoretical understanding of the particular phenomena, experimental observations thereof and more often a combination of both. Thus the modelling process is fairly iterative. As our theoretical understanding improves and new experimental observations are obtained, propagation models continue to evolve and advance. Propagation models and experimental measurements thus complement one another and whenever possible, the two should be implemented in parallel.

In this study, a theoretical model for the attenuation due to rain is provided. The empirical evidence of several authors has been examined and used as a foundation and as constituent elements in the rain attenuation model. For comparison, a measurement campaign was also implemented from February 2004 – September 2005 to examine the attenuation effects of rain on an experimental terrestrial line-of-sight (LOS) link operating at 19.5 GHz.

Rain has for a long time been identified as a serious problem for radar and communication systems, employing microwave and millimetre-wave frequencies.

During World War 2, Ryde and Ryde (1944, cited Medhurst 1965) developed one of the earliest theoretical models for rain attenuation. Two decades later Medhurst (1965) revised this model and provided a comparison between experimental measurements and the model's predictions. In this critical review, Medhurst (1965) questioned the validity of the existing theory when it was found that the measurements tended to exceed the maximum-value predicted. However, Crane (1974) performed measurements of the attenuation for simulated rain with a controlled drop-size-distribution and the results showed strong agreement with the classical Mie scattering theory.

A year later, Crane (1975) re-examined the Medhurst (1965) data along with the new data available in the ensuing decade and showed that on average model predictions and measurements do correspond within the expected statistical deviations. The discrepancies were attributed to the inadequacy of the meteorological models and measurements at the time. The classical theory for the scattering of single, independent raindrops was thus applicable for the evaluation of rain attenuation. Any minute error arising from multiple scattering or other higher order effects would always be less than the uncertainty in the meteorological parameters, such as the raindrop size, shape and drop-size distribution (Watson 1976). Also for coherent transmission communication systems, the effects of multiple scattering do not significantly affect the attenuation experienced due to rain for microwave and millimetre-wave frequencies (Crane 1983).

To date many investigators (e.g. Crane 1980, 1985, 1996; Olsen 1978, 1982; Oguchi 1977, 1981 1983; de Wolf 1996, 2001 and Matzler 2002, 2003) have provided adjustments and modifications to the theory in an attempt to improve upon the modelling of the attenuation due to rain. Several authors have focussed their research primarily on improving the knowledge of the microphysical properties of rain and have performed measurements and developed models for the terminal velocity of raindrops (e.g. Gunn and Kinzer 1949; Best 1950 and Matzler 2002), the shape of realistic raindrops (e.g. Pruppacher and Pitter 1971; Beard and Chaung 1987, 1990 and Li et al. 1994) and the drop-size distribution (e.g. Laws and Parsons 1943; Marshall and Palmer 1948; Joss et al. 1968; Ulbrich 1983; Feingold and Levin 1986 and de Wolf 2001). Other authors (e.g. Oguchi 1973 and 1977, Olsen 1978, de Wolf 1996 and Li et al. 1995, 1998) have concentrated their efforts on the scattering of electromagnetic waves by raindrops and the computations thereof.

A third set of investigators (e.g. Lin 1975, 1978; Crane 1980; 1985; 1996; Ajayi and Ofoche 1983; Moupfouma 1987 and Moupfouma and Martin 1995) have devoted their research to the statistical analysis of rainfall and rain attenuation and derived models for the cumulative distributions of the fade depths and durations due to rain. The modelling of rain and its effects on the propagation of electromagnetic waves has thus been the subject of substantial research over the decades. The intensity of this research is growing rapidly as microwave and millimetre-wave frequencies are being employed increasingly in terrestrial communication systems. The need for propagation models to account for the attenuation due to rain and cumulative statistics thereof is thus paramount in our telecommunication-driven world.

1.1 Specific Attenuation for Rain

The specific attenuation for rain at any point in space depends upon the properties of the incident electromagnetic wave (e.g. the frequency, polarization and direction of propagation) and the microphysical properties characterizing the rain at that point (e.g. the size, shape and orientation of the raindrops and the drop-size distribution). A simple model, incorporating these parameters, would be highly desirable, especially if the specific attenuation can be related directly to the surface–point rain-rate. It would then be possible to synthesize attenuation predictions based on the available rainfall data.

Olsen et al. (1978) found the power law relation to be an excellent approximation for the relationship between the specific attenuation and the rain rate. The power law relationship has been subsequently used by several authors and has also been as a standard by the International Telecommunications Union (ITU).

The derivation of the specific attenuation lies in scattering theory of raindrops. Early work examined Mie theory for spherical raindrops (e.g. Medhurst 1965; Olsen et al. 1978; Matzler 2002, 2003). The evaluation of Mie scattering for nonspherical raindrops is very complicated and several numerical and analytical techniques are required. To reduce the complexity some authors (e.g. Oguchi 1973; Morrison and Cross 1974; de Wolf 2001) have approximated the deformation of raindrops as oblate spheroids. Over the past few years the scattering of more realistically shaped raindrops has received increasing attention (e.g. Li et al. 1994, 1995, 1998 and Der-Phone and Chen 2001). Most of the attention has been focussed on the Pruppacher and Pitter (1971) raindrops, which is currently the most well-accepted drop shape model.

The shape of realistic raindrops becomes increasingly distorted as the raindrop size increases. The base becomes more flattened and spreads laterally, while the top surface remains fairly rounded. Thus the vertical dimension becomes slightly smaller and the horizontal dimension larger. Consequently, the resulting attenuation will be slightly smaller for vertical polarizations and greater for horizontal polarizations. Matzler (2003) showed that the specific attenuation, although not exactly the same as that calculated using Mie theory for spherical raindrops, requires only a small correction (less than 8 %). Also the shape of the raindrop is more instrumental in evaluating the depolarization and cross-polarization effects as opposed to the attenuation.

Since Mie scattering calculations are computationally intense for non-spherical shapes, such as for spheroidal and realistically-shaped raindrops (e.g. Pruppacher and Pitter 1971), the classical approach of using spherical raindrops has been adopted in this study. Furthermore, the focus of this research has been devoted primarily to the influence of the drop-size distribution on the specific attenuation, path attenuation and the cumulative distributions of the fade depths and durations. Future work will entail the study of the effects of drop shape on the rain attenuation. The models developed and Matlab® code thereof, are thus fully integrable and written for this purpose. Preliminary studies on the drop shape have already been performed and are provided in the Appendix A.

The calculation of the specific attenuation is strongly influenced by the drop-size-distribution (DSD). DSDs vary depending on the climate and geographical location and can strongly dominate the evaluation of the specific attenuation and resulting path attenuation. Variations of up to 50 % in the calculated specific attenuation can result from changing the DSD in calculations. Consequently, this research aims to investigate the influence of the DSD on the specific attenuation by examining several theoretical and empirical DSDs discussed in literature. Raindrops have been assumed to be spherical in shape, hence Mie theory for dielectric spheres has been applied. This will substantially reduce computation time. Future work can involve the variation of both drop shape and the DSD.

In this study several DSD models have been examined. These include the Laws and Parsons (1942) DSD, the exponential distributions of Marshall and Palmer (1948) and Joss et al. (1968), the gamma distributions of de Wolf (2001) and Atlas and Ulbrich (1974, cited Jiang et al. 1997), the lognormal models in Ajayi and Adimula (1996) and the Weibull distribution discussed in Sekine et al. (1987). As pointed out by several authors, (e.g. Olsen et al. 1978; de Wolf 2001; Matzler 2002) DSDs are not necessarily consistent with the rain rate. Thus each DSD must be normalised before being applied in the evaluation of the specific attenuation and subsequent calculations. In this study, a second order polynomial is used as the normalisation function and ensures consistency.

1.2 Attenuation Statistics

With the aid of the specific attenuation model it is possible to determine the path attenuation at any rain rate for any given radio-link path and frequency of interest. Knowledge of the cumulative distributions of the fade depth and durations due to rain are now necessary. Depending on the link availability requirements, communication system designers may need the fade depth exceeded for 0.1, 0.01 or 0.001% of the year.

If such systems employ microwave and millimetre-wave frequencies, the dominant cause for attenuation over these durations is due to precipitation, namely rain, snow and sleet. For South Africa (excluding the Drakensberg and surrounding areas) the occurrence of snow and sleet can be neglected. Thus rain becomes the principal cause of unwanted attenuation and of major concern to system designers, especially when evaluating fade margins of high-availability systems.

To perform this task knowledge of the surface-point rain rate is a prerequisite. Rain exhibits considerable temporal and spatial variability and even an integration time of 5 minutes is often too large and inadequate to account for these fluctuations. Thus the rain-rate distributions of even shorter integration intervals are needed. Fortunately, truly instantaneous rain rates are not necessary because rapid fluctuations in the rain rate rarely translate into equivalent fluctuations in attenuation due to the spatial averaging over the propagation path. For application in rain attenuation statistics, 1-minute rain rates have been found to be the most desirable and assist in removing variations due to rain gauge limitations (e.g. small sampling area) and contamination due to atmospheric turbulences (Crane 1996). Subsequently, 1-minute rates have been adopted as the standard for the evaluation of rain attenuation by researchers and the International Telecommunications Union (ITU).

However, measurements of 1-minute rain rates are not readily available throughout the world. Even when available, records need to span several years (typically 10 years or more) before "stable" annual statistics can be obtained (Crane 1996). To overcome the unavailability of 1-minute rainfall data, several investigators (e.g. Rice and Holmberg 1973; Lin 1976, 1978; Dutton and Dougherty 1979, 1984; Tattelman and Scharr 1983; and Tattelman et al. 1994) have devised models to estimate the 1-minute rain-rate distributions from the available climatologically data.

Seeber (1985) examined the extreme-value model of Lin (1976) and it was found to be particularly suitable for application in the South African climate. The extreme-value model (Lin 1976; Seeber 1985) was thus considered in this study. 1-minute rain-rate distributions have subsequently been obtained using measurements of the rainfall extremes, together with the conversion ratio of Ajayi and Ofoche (1983).

Several global rain-rate models (e.g. Crane 1980; ITU-R P.837) have been suggested in literature. These climate-based rain-rate models provide a useful estimate of the rain-rate distribution, when there is a lack of meteorological data. These models are however coarse and based on the climatic designation. Thus whenever possible, one should take advantage of the available rainfall records to augment these global maps.

The latest ITU recommendation (ITU-R P.837-4) uses 15 years of data from the European centre of medium-range weather forecast to generate global maps of the rain rate exceeded for 0.01% of the year. The rain rate exceeded for other percentages of the year are also useful, thus a model for evaluating these percentages using 0.01% of the year rain rate is also provided. Some investigators (e.g. Moupfouma 1987 and Moupfouma and Martin 1995) have suggested alternative rain-rate models.

The statistics relating to the rain-induced attenuation experienced by radio systems is an invaluable resource to communication systems designers. If accurate and appropriate models are available, radio engineers can predict and possibly reduce the number of systems failures resulting from the excessive fading from rain. Lin (1973, 1976, 1977) performed comprehensive studies on the statistics of rain and suggested the lognormal relation be used. The lognormal distribution provides a good fit for 0.01% of the time and higher probabilities. At the low-percentages (i.e. < 0.01%) lognormal models may tend to over-estimate the attenuation and produce pessimistic results. Some authors (e.g. Watson 1976 and Moupfouma and Martin 1995) have questioned the use of lognormal distributions for this probability range and suggested the use of the gamma distribution and other hybrid models.

This estimate of the surface-point 1-minute rain rate is only the first step. Rain exhibits significant spatial and temporal variation. Hence the rain-rate profile along the propagation path is also required. Crane (1980) developed an attenuation model to convert the point rain-rate to a path-averaged rain rate. The only required inputs are the power-law parameters for the specific attenuation and the surface-point rain rate. This simple and versatile model has been adopted in this study.

1.3 Formulation of the problem

In the past, most fixed link systems operated at frequencies below about 15 GHz. At these frequencies, microwave systems were traditionally used in long haul regional networks and in areas where it was too difficult or too expensive to use other transmission systems (ERC 1994). Unfortunately, with the rapid congestion of these frequency bands, it has become increasingly difficult to introduce new links to meet the requirements of newly emerging applications and services. Furthermore, the demand for greater bandwidth, higher data rates and better spectral efficiency has become unrelenting. The exploitation of higher frequency bands (i.e. the millimetre-wave frequencies) is thus inevitable. Millimetre-wave frequencies have several advantages (ERC 1994), including

- Availability and re-usability

The millimetre-wave frequency bands can meet the demands for higher data rates and wider bandwidths. Furthermore they can be easily integrated into communication systems in environments where the lower bands are already congested. Problems of interference with the existing systems are thus alleviated. The stronger atmospheric absorption (especially around 60 GHz) allow for short distance re-use.

- Low cost, flexibility and ease of installation

The installation of cables and optical fibre is very expensive and cable-theft is a serious problem. It may also be difficult to obtain the necessary authorisation in urban environments. The use of wireless communications systems is thus a cost effective alternative. The use of higher frequencies in such wireless systems will reduce the size of the antenna and equipment, making the systems and corresponding infrastructure relatively cheap. Due to the compact size, radio systems can be easily deployed in both urban and rural environments. Existing radio systems can also be easily moved to new sites as the demands of the network change providing high flexibility to the network.

Unfortunately, the performance of wireless communication systems depends heavily on the propagation characteristics of the transmission medium. For millimetre-wave terrestrial links this is the troposphere (the lowest part of the atmosphere) and poses a major problem. Tropospheric effects include attenuation, depolarization and scintillation and cause signal degradations for substantial percentages of the year.

At millimetre-waves frequencies, the attenuation effects of the troposphere is most dominant of these effects and is caused mainly by rain, water vapour, oxygen, clouds and fog. Of these, rain attenuation is the most severe. Rain can cause large variations in the received signal power, with little predictability and many sudden changes. Although this kind of signal fading is also prevalent at lower frequencies, the resulting fade levels are much smaller. Thus a small fixed fade margin in the link budget can compensate the attenuation loss and maintain the required performance.

At the millimetre-wave and higher frequencies, the attenuation caused by rain is too severe and a ruthless limitation to system performance. In order to provide an equivalent performance as those in the lower frequency bands, a large fade margin would be required. This is clearly uneconomical since such a power margin is not required all the time. Furthermore, during clear-sky conditions, this can cause interference to other communication systems operating at the same frequency band.

Scintillation is also of concern in system design and refers to the rapid fluctuations in signal strength and phase caused by turbulences in the atmosphere. Turbulence-induced irregularities in the temperature, humidity and pressure of the atmosphere translate into small-scale variations in refractive index. Electromagnetic waves passing through such a medium will encounter various refraction and scattering effects, resulting in a multipath effect. However, for millimetre waves, scintillation effects and humidity fluctuations are minor when compared to the dominant effect of rain attenuation. Hence these effects are more of concern in low-availability systems.

For high-availability systems, the attenuation due to rain poses the serious problem in microwave and millimetre-wave communication systems. The theory and analysis of the rain attenuation can be divided into two main areas. The first area deals with the relationship between the rain rate and attenuation. This relationship is often expressed in the form of the specific attenuation, the amount of attenuation experienced for a given rate, uniformly distributed over path length of 1 km. Thereafter a path-integrated rain attenuation model is devised, based upon the specific attenuation, to incorporate the spatial structure of rain. The second area of interest satisfies the requirements of the communication system designer and revolves around the cumulative distribution s of the fade depth and durations due to the rain. For the radio-link path and frequency of interest, the system engineer requires the fade depth exceeded for 0.1, 0.01 and 0.001% of the year. Both of these areas are the subject of this dissertation.

1.4 Thesis Objectives

The scattering and attenuation of electromagnetic waves by rain is a serious problem for microwave and millimetre-wave frequencies. The conversion of rain rate to specific attenuation is a crucial step in the analysis of the total path attenuation and hence radio-link availability. It is now common practice to relate the specific attenuation and the rain rate using the simple power law relationship. The power-law parameters are then used in the path attenuation model, where the spatial variations of rainfall are estimated by a path-integration of the rain rate. These power law parameters are strongly influenced by the drop-size-distribution (DSD). Thus an examination of the various DSDs and their influence on the specific attenuation and link availability is warranted.

Many models for the DSD have been suggested in literature, from the traditional exponential, to the gamma, lognormal and Weibull distributions. The type of DSD varies depending on the geographical location and rainfall type. An important requirement of the DSD is that it is consistent with rain rate (i.e. the DSD must satisfy the rain-rate integral equation). Thus before application in the specific attenuation calculations, normalisation needs to be performed to ensure the consistency, as done in this study.

Once the specific attenuation has been evaluated for necessary frequency and rain-rate range, path averaging is performed to predict the rain attenuation over the communication link. The final step in this dissertation is the estimation of the percentage of time of such occurrences. For this cumulative time statistics of surface-point rain rates are needed. The resulting cumulative distribution model of the fade depth and duration due to rain is a valuable tool for system designers. With such models the system designer can then determine the appropriate fade margin for the communication system and resulting period of unavailability for the link.

1.5 Outline of the dissertation

The numerical calculation of the scattering and attenuation of electromagnetic waves by rain requires detailed knowledge of the microphysical properties of raindrops such as raindrop size, shape, fall velocity and drop-size distribution (DSD). This is the focus of Chapter 2 of this dissertation.

In Section 2.2, the fall velocity of raindrops is examined using the Gunn and Kinzer (1949) measurements of the terminal velocity at sea level and several analytical descriptions thereof are discussed. Thereafter models for arbitrary atmospheric conditions are examined, concluding with the Best (1950) model for variation with height in the S.T. (Summer Tropical) and I.C.A.N. standard atmospheres (International Committee of Air Navigation).

The size and shape of a raindrop is necessary for the calculation of the scattering and extinction cross section of a single raindrop. A brief preamble to raindrop scattering is given in Section 2.3. To extend the scattering and extinction model of a single raindrop to that experienced during a rain event, the drop-size distribution of raindrops is required. DSDs exhibit significant spatial and temporal variability. The average DSDs for several rainfall types are thus examined in Section 2.4. Firstly, the Laws and Parson (1943) measurements of the drop-size distribution is discussed. Thereafter several analytical descriptions for the DSD are investigated including the exponential, gamma, lognormal and Weibull functions.

This chapter is concluded with an investigation of the dielectric properties of water in Section 2.5. The Debye approximations and empirical models of Ray (1972) and Liebe (1991) are examined for frequencies up to 1 THz. The frequency and temperature dependent complex refractive index of water is instrumental in the calculation of the total and scattering cross-section of raindrops.

The attenuation and scattering of electromagnetic waves by raindrops is evaluated by applying the scattering theory for a single, lossy dielectric sphere. Typical raindrops have diameters ranging from 0.1 mm to 7 mm. Thus, for millimetre-wave frequency range the drop-size is comparable to wavelength hence Mie scattering theory is applicable. Evaluation begins with the computation of the extinction and scattering cross sections of a single raindrop as examined in Section 3.2.

The specific attenuation is heavily dependent upon the chosen DSD and statistics relating to the location of these drops within the volume. In this study it is assumed that the raindrops are distributed throughout the volume in accordance with the Poisson process. In most calculations the Laws and Parsons DSDs is typically assumed. In Section 3.4 several DSD models have been evaluated from the conventional exponential distributions to the gamma, lognormal and Weibull distributions. The more sophisticated DSDs overcome the shortfalls of the exponential distributions which tend to over-estimate the number of small and large raindrops.

In section 3.5 the difference between the extinction cross section is evaluated for spherical raindrops and for the more realistic Prupacher and Pitter (1971). Vertical polarizations will have a slightly smaller specific attenuation and horizontal polarizations a slightly larger specific attenuation than that calculated using Mie theory for spheres. Hence future work should entail the evaluation of the extinction cross sections for realistically-shaped raindrops and include the effect of drop shape in this model.

The final step that remains is the prediction of the rain attenuation statistics. To achieve this short-duration precipitation rates are required. This is the focus of Chapter 4. First, the global rain-rate climate models are discussed in Section 4.2. These models are based upon the climatic classification of the region, thus a description of the various climatic zones in South Africa is also useful and is provided in the Appendix. Both Crane's global rain-rate climate model and the ITU-R P.837 global rain-rate model are discussed and simulated.

Thereafter a discussion of extreme value theory and the procedure for obtaining 5-minute rain-rate distributions for any location in South Africa is given in Section 4.3. The procedure involves the use of the depth-duration-frequency curve for South Africa. More accurate 5-minute distributions can be provided by using actual rainfall data from annual maxima series when available. Consequently 5-minute distributions are obtained for 8 locations with approximately 40 years of measurements. Thereafter these distributions are converted to 1-minute rain-rate distributions using the conversion ratio of Ajayi and Ofoche (1983).

Other models such as those of Moupfouma (1987) and Moupfouma and Martin (1995) are also discussed and simulated for South Africa in Section 3.4 and Section 4.5, respectively. A comparison of all the models with 1-minute rain-rate measurements in Durban is given in Section 4.6.

This estimate of the surface-point 1-minute rain rate is only the first step. Rain exhibits significant spatial and temporal variation. Hence the rain-rate profile along the propagation path is also required. The Crane (1980) attenuation model and the ITU recommendation (ITU-R P530-9) are discussed in Section 4.7.

In Chapter 5, the path attenuation and exceedance probabilities are evaluated for the 6.73 km LOS link established between the two campuses of the University of KwaZulu-Natal (UKZN). The various LOS link details such as the equipment setup, link parameters, path profile and link budget were provided in Section 5.2. Sample link measurements are also given.

In Section 5.3 the specific attenuation was calculated using the exponential, gamma, lognormal and Weibull DSDs. Analysis of the effects of the DSD on the specific attenuation is then discussed.

The Crane (1980, 1996) attenuation model is then applied to convert the surface-point rain-rate to a path integrated rain-rate. The results are given in Section 5.4. The results in this chapter focus on 19.5 GHz, the operating frequency of the LOS link. At the frequencies around 19.5 GHz, the specific attenuation and hence the path attenuation is relatively invariant of the DSD. This is because at 19.5 GHz the attenuation is strongly influenced by the medium-sized raindrops. At others frequencies, the variations due to the DSD are quite considerable and can result in changes up to 50 % in the calculated path attenuation. To illustrate this effect, analysis was also performed at the frequencies f = 4, 12, 15, 40 and 80 GHz and the results are given in the Appendix D.

Finally, the various 1-minute rain-rate distributions discussed in Chapter 4 were applied to provide the exceedance probabilities for the path attenuation on the LOS link. The results using the proposed extreme-value model for the 1-minute cumulative distributions, along with the Seeber (1985) model, the ITU-R P.837 global rain-rate climate model, the Moupfouma (1987) model and the Moupfouma and Martin (1995) temperate and tropical/subtropical models are presented in Section 5.5. These cumulative rain-rate distributions together with the path attenuation can be used to analyse the time any particular path attenuation is exceeded.

Finally the results presented in this dissertation are summarised along with concluding remarks in Chapter 6. Future work in the field is also provided. Knowledge of the specific attenuation is invaluable to determine the path lengths, operating frequency and fade margins required for communication systems. Since the specific attenuation is heavily dependent on the DSD, the influence of the DSD on link availability must be examined and hence is the subject of this research.

During rain events, a large fade margin may often be required. It would be uneconomical to implement such margins since they are only needed for a fraction of the time. A cumulative distribution model of the fade depth and duration due to rain is thus a valuable tool for a system designer. With such models the system designer can then determine the appropriate fade margin and resulting outage period for the link.

Chapter 2

Microphysical Properties of Raindrops

2.1 Introduction

In today's rapidly expanding communications industry, there is an ever-increasing demand for greater bandwidth, higher data rates and better spectral efficiency. To meet these demands current and future communication systems are employing increasingly higher operating frequencies along with advanced spatial, temporal and frequency diversity techniques. The millimetre-wave frequency bands, which over a decade ago were used primarily for space-earth communications, are now common place in present terrestrial systems. Unfortunately, at these smaller wavelengths, system performance becomes significantly influenced by the presence of hydrometeors; such as rain, snow and hail along the propagation path.

In terrestrial communication systems, this propagation path is the troposphere, namely the lower part of the atmosphere and the region where most meteorological phenomena take place. Consequently, the possibility of the presence of hydrometeors along the communication link cannot be neglected. In many cases rainfall can cover a substantial portion of the propagation path culminating in several undesirable propagation phenomena including attenuation, depolarization and scatter interference. Some of the most severe cases of degradation, often resulting in unavailability of services, can be attributed to such incidences of rain. Consequently, the interactions between millimetre-waves and rain have become increasingly important to today's radio engineer.

The numerical calculation of the scattering and attenuation of electromagnetic waves by rain requires detailed knowledge of the microphysical properties of raindrops such as raindrop size, shape, fall velocity, canting angle and drop-size distribution (DSD). These properties of raindrops were initially examined only from a meteorological standpoint. However with the advent of more sophisticated communications systems such as those described above, necessity has forced their examination to fall under the scrutiny of radio engineers as well.

Several investigations by both meteorologists and radio engineers on the microphysical properties of raindrops have been examined during this study. The relevant empirical and analytical models will be discussed in detail in this chapter. The models and data provided in this chapter will be used as building blocks for evaluating the scattering and attenuation of millimetre-waves in the subsequent chapters.

2.1.1 Outline of the chapter

In this chapter the microphysical properties of raindrops are discussed. These include raindrop size and shape, fall velocity, canting angle and drop-size distribution (DSD). The fall velocity is often approximated by the terminal velocity and it is examined in Section 2.2. Firstly, the Gunn and Kinzer (1949) measurements of the terminal velocity at sea level and several analytical descriptions thereof are discussed. Thereafter models for arbitrary atmospheric conditions are examined, concluding with the Best (1950) model for variation with height in the S.T. and I.C.A.N. standard atmospheres.

The size and shape of a raindrop is required in scattering and extinction cross sections calculations. Hence Section 2.3 is dedicated to this subject. As the drop size increases, its shape becomes increasingly distorted. In this study raindrops have been assumed to be spherical in shape. Preliminary studies on the raindrop shape are provided in Appendix A, where axial ratios and three models for raindrop shape, namely for oblate spheroidal, Pruppacher and Pitter (1971) and Beard and Chuang (1987, 1990) raindrops are considered. Appendix B contains the research on another microphysical property, namely the canting angle of raindrops. Both raindrop shape and canting angle is used in the evaluation of the depolarization and cross-polarization due to rain and the model discussed in the appendix can be used in subsequent research.

To extend the scattering and extinction model of a single raindrop to that experienced during a rain event, the drop-size distribution of raindrops is required. DSDs exhibit significant spatial and temporal variability. Consequently in Section 2.4 the average DSDs for several rainfall types are examined. Firstly, the Laws and Parson (1943) drop-size distribution is discussed. Thereafter several analytical descriptions for the DSD are investigated including the exponential, gamma, lognormal and Weibull functions.

This chapter is concluded in Section 2.5, where the dielectric properties of water are investigated. The Debye approximations and empirical models of Ray (1972) and Liebe (1991) are examined for frequencies up to 1 THz.

2.2 Terminal Fall Velocity

The fall velocity of a raindrop is an important characteristic describing the behaviour of realistic raindrops in nature. The actual fall velocity is variable and may be modified by updrafts and downdrafts. Hence it is common place to use the idealised terminal fall velocity in several calculations such as the drop shape, drop-size distributions and subsequently rain attenuation. The terminal velocity of raindrops has been examined by many investigators. The results of these studies will be discussed in this section.

The fall velocity of a raindrop depends upon gravity and the drag due to the surrounding atmosphere. The drag experienced by a raindrop depends on the size of the raindrop as well as the density and viscosity of the atmosphere. Since the atmospheric pressure, temperature and humidity may vary with time and location it is common place in meteorology to consider a standard atmosphere, where these parameters are only functions of height. For example the atmospheric conditions at sea level are an atmospheric pressure of 1013 mbar, a temperature of 20 °C and a relative humidity of 50%. Best (1950) considered two standard atmospheres, namely, the I.C.A.N standard atmosphere and the standard summer tropical (S.T.) atmosphere, where the temperature, density and viscosity are functions of height above sea level.

Terminal fall velocity refers to the maximum vertical fall velocity that a raindrop can reach. This occurs when the gravitational force equals the drag force. A common assumption, and one which will be adopted in this study, is that there is zero vertical wind velocity. Thus the vertical fall velocity of the raindrop approximately equals the terminal fall velocity. This is a good approximation when considering raindrops falling far from obstacles such as buildings.

For small raindrops the terminal fall velocity increases considerably as the raindrop gets larger. Once reaching a diameter size of approximately 2.0 mm, the rate of increase in the terminal velocity begins to diminish. The terminal velocity eventually reaches its peak for raindrops with diameter size around 5.0 mm. Further increase in drop size results in only a marginal increase in the terminal fall velocity.

If raindrops were spherical in shape the terminal fall velocity would have continued to increase beyond this maximum but this is not the case. The raindrop shape becomes increasingly distorted as the drop size increases. For raindrops beyond a drop diameter of 7 mm this deformation becomes so critical that it eventually results in drop break-up. The shape of raindrops with size will be discussed in further detail in the next section.

For now it is sufficient to recognize that if the shape is deformed this affects the drag and thus limits the terminal velocity. Stringently, a horizontal component of wind would also influence the fall velocity by further deforming the shape of the raindrop and hence the drag as well. Such effects are beyond the scope of this study and will thus be neglected. In this study the presence of wind will be neglected.

2.2.1 Gunn and Kinzer Terminal Velocity at sea level

The terminal fall velocity in standard atmospheric conditions has been examined by several investigators, most notably Gunn and Kinzer (1949) and Best (1950). Their measurements and formulations are still used today. Further work by Foot and Du Toit (1969), Beard (1976) and Matzler (2002) have expanded these formulations to other atmospheric conditions as well.

Gunn and Kinzer (1949) performed extensive measurements of the terminal fall velocity for the standard atmospheric conditions at sea level. These measurements have been used as a standard in several subsequent studies. Medhurst (1965) tabulated the Gunn and Kinzer (1949) measurements at several useful drop diameters. These values are presented in Table 2-1.

Several analytical functions for the terminal velocity have been proposed in literature. The simple power law relationship of Sekhon and Srivastava (1971) is given by

$$v(D) = 14.20 \cdot (0.1D)^{0.5}. \tag{2.1}$$

Similarly, Atlas et al. (1977) suggested the following power law function to the measurements of Gunn and Kinzer (1949)

$$v(D) = 17.67 \cdot (0.1D)^{0.67} = 3.78D^{0.67}. \tag{2.2}$$

In both (2.1) and (2.2), v is the terminal velocity in m s^{-1} and a factor of 0.1 allows for D, the drop diameter in mm. The above formulas are valid for 0.5 mm $< D <$ 5 mm. Although these power laws fits are very easy to implement in calculations, their accuracy is relatively poor, especially at larger drop sizes.

Table 2-1 : Terminal velocity measurements of Gunn Kinzer (1949), from Medhurst (1965, Table II)

Drop Diameter , D (mm)	**Terminal Velocity, v (m s^{-1})**
0.5	2.06
1.0	4.03
1.5	5.40
2.0	6.49
2.5	7.41
3.0	8.06
3.5	8.53
4.0	8.83
4.5	9.00
5.0	9.09
5.5	9.13
6.0	9.14
6.5	9.14
7.0	9.14

A more accurate fit of the Gunn and Kinzer (1949) measurements is suggested by van Mook (2002) is given by

$$v(D) = 9.40 \cdot \left\{1 - \exp\left[-1.57 \times 10^{3} (0.001D)^{1.15}\right]\right\}. \tag{2.3}$$

Foot and Du Toit (1969) demonstrated that an N^{th} degree polynomial can provide an analytical fit of any degree of accuracy to the measurements of Gunn and Kinzer (1949) by simply increasing the order of N. The polynomial is of the form

$$v(D) = \sum_{j=0}^{N} a_j D^j , \tag{2.4}$$

where D is the drop diameter in mm. The polynomial form for the terminal velocity v, is not only convenient and simple but also very accurate. The method of least-squares was used in this study to evaluate the values for the coefficients a_j for 3 different polynomials with order N = 3, 5 and 9. The results are given in Table 2-2. In Figure 2-1 it is shown that a polynomial of order N = 3 suffices for approximating the Gunn and Kinzer (1949) measurements. If further accuracy is needed a higher order polynomial can be used.

Table 2-2 : Coefficient values for polynomials of order N = 3, 5 and 9

J	a_j		
	$N = 3$	$N = 5$	$N = 9$
0	-5.09804×10^{-3}	-2.35403×10^{-2}	-9.17687×10^{-4}
1	4.68387×10^{0}	4.74022×10^{-0}	2.93021×10^{-0}
2	-8.00130×10^{-1}	-8.21097×10^{-1}	5.06359×10^{-0}
3	4.54651×10^{-2}	4.21924×10^{-2}	-7.24830×10^{-0}
4		1.94576×10^{-3}	4.63845×10^{-0}
5		-1.74137×10^{-4}	-1.69708×10^{-0}
6			3.72294×10^{-1}
7			-4.83983×10^{-2}
8			3.43884×10^{-3}
9			-1.02928×10^{-4}

Atlas et al. (1973) also gave the excellent fit given by

$$v(D) = 9.65 - 10.30 \cdot \exp(-0.6D) . \tag{2.5}$$

These formulae are more accurate than the power law fits and valid for 0.1 mm < D < 7 mm. However, a problem with (2.5) is that negative values exist for D < 0.1 mm.

Matzler (2002) suggested a solution and provided a step-wise modification as given in (2.6).

$$v(D) = \begin{cases} 0 & D < 0.03 \text{ mm} \\ 4.233 \cdot (D - 0.03) & 0.03 \text{ mm} < D < 0.6 \text{ mm} \\ 9.65 - 10.30 \cdot \exp(-0.6D) & D > 0.6 \text{ mm.} \end{cases} \tag{2.6}$$

The formula is a split into 3 step-wise expressions. The third expression is the same as Atlas et al. (1973). The second expression is a linear fit to the Gunn and Kinzer (1949) measurements and provides a smooth transition with the third. The first expression avoids the negative values resulting from the second. Figure 2-1 shows the different analytical approximations for terminal velocity along with the Gunn and Kinzer (1949) measurements.

2.2.2 Terminal Velocity for arbitrary atmospheric conditions

The above representations are valid for standard atmospheric pressure. A simple adjustment to (2.6) allowing for a variation in atmospheric pressure is given by

$$v(D,P) = v(D) \cdot \left(\frac{P_0}{P} \right)^{0.291 + 0.0256D} , \tag{2.7}$$

where D is the drop diameter in mm, P is the atmospheric pressure in mbar and P_0 is the standard atmospheric pressure of 1013 mbar.

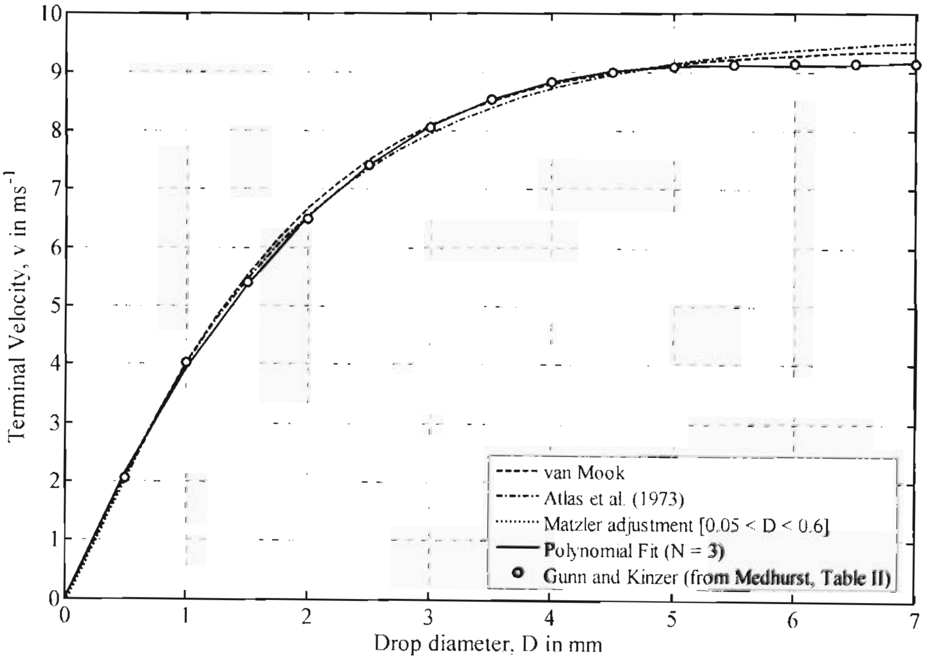

Figure 2-1 : Analytical approximations for the Gunn Kinzer (1949) terminal velocity measurements.

A more accurate form is given in Foote and Du Toit (1969) shown as

$$v(D,T,P) = v(D)\cdot 10^{Y}\cdot\left[1+0.0023\cdot\left(1.1-\frac{P}{P_0}\right)(T-T_0)\right], \tag{2.8}$$

where T_0 is 20 °C, P_0 is 1013 mbar and the parameter Y is given as follows

$$Y = 0.43\log\left(\frac{P_0}{P}\right) - 0.4\cdot\left[\log\left(\frac{P_0}{P}\right)\right]^{2.5}. \tag{2.9}$$

The terminal velocity of raindrops under several arbitrary atmospheric conditions is illustrated for comparison in Figure 2-2.

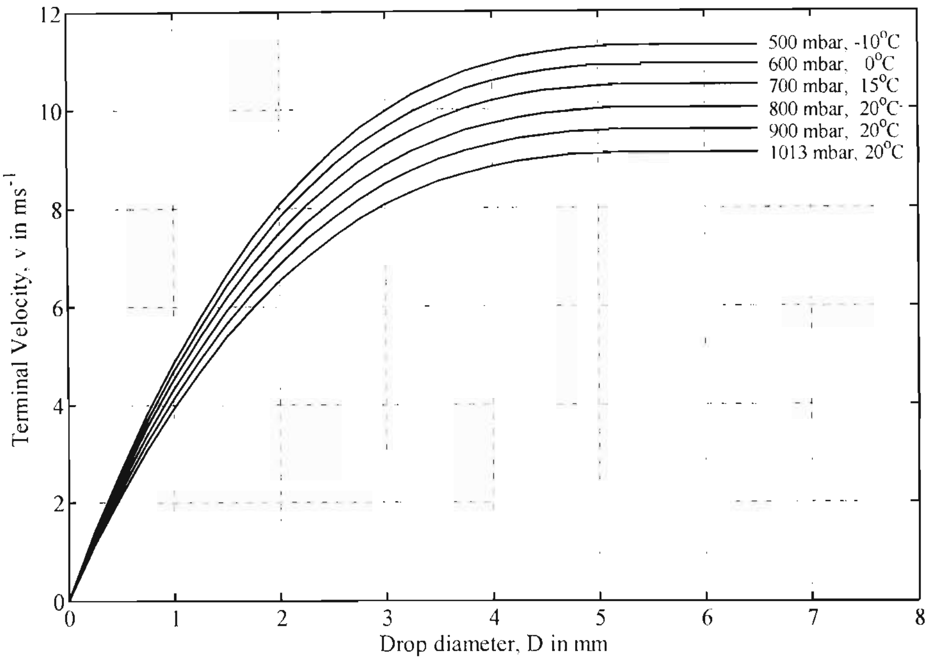

Figure 2-2 : Variation of terminal velocity with atmospheric conditions.

2.2.3 Best Terminal Velocity in the Standard Atmospheres

C.N. Davies (1942, cited Best 1950) performed extensive measurements of the terminal fall velocity at sea level conditions as well as at various reduced air densities. Using these measurements, Best (1950) provided a simple formula for the terminal velocity of raindrops in the I.C.A.N and S.T. standard atmosphere as a function of height.

$$v(D,z) = A\exp bz\left(1-\exp\left[-\left(D/a\right)^{n}\right]\right), \tag{2.10}$$

where v is the terminal velocity in m s^{-1}, z is the height above the surface in km and D is drop diameter in mm. A, a, b and n are atmospheric dependent parameters.

Best (1950) provided the parameter values for the I.C.A.N and S.T. standard atmosphere for two diameter ranges. These values are given in Table 2-3.

Table 2-3 : Parameter values for I.C.A.N and S.T. atmosphere, from Best (1950)

Drop Diameter D(mm)	**I.C.A.N atmosphere**				**Summer tropical atmosphere**			
	A	b	a	n	A	b	a	n
0.3 − 6.0	9.32	0.0405	1.77	1.147	9.58	0.0354	1.77	1.147
0.05 − 0.3	1.91	0.0290	0.316	1.754	1.88	0.0256	0.304	1.819

It is noted that the deviation in velocity is less than 4% for a heights below 1 km and below 1% for heights below 250 m. If the effect of height is neglected, the terminal velocity for 0.3 mm < D < 6.0 mm in the S.T. and I.C.A.N. atmosphere are given, respectively by

$$\begin{aligned} v_{ST}(D) &= 9.58\cdot\left(1-\exp\left[-\left(D/1.77\right)^{1.147}\right]\right), \text{ and} \\ v_{ICAN}(D) &= 9.32\cdot\left(1-\exp\left[-\left(D/1.77\right)^{1.147}\right]\right). \end{aligned} \tag{2.11}$$

Foot and Du Toit (1969) considered both the measurements of C.N. Davies (1942) and Gunn and Kinzer (1949) and suggested the following function

$$v(D) = 9.43\cdot\left(1-\exp\left[-\left(D/1.77\right)^{1.147}\right]\right). \tag{2.12}$$

The above-mentioned analytical formulas for height z < 1 km are shown in Figure 2-3 along with the original measurements by Gunn and Kinzer (1949) and Davies (1942). The terminal velocity is essential in estimating the raindrop shape, canting angle and the DSD. For terrestrial applications, the use of the Gunn Kinzer polynomial approximation is valid as shown in this section. If the effect of air pressure and height is necessary (e.g in high altitude locations or slant paths for satellite links), the models in Section 2.2.2 and Section 2.2.3 can be implemented.

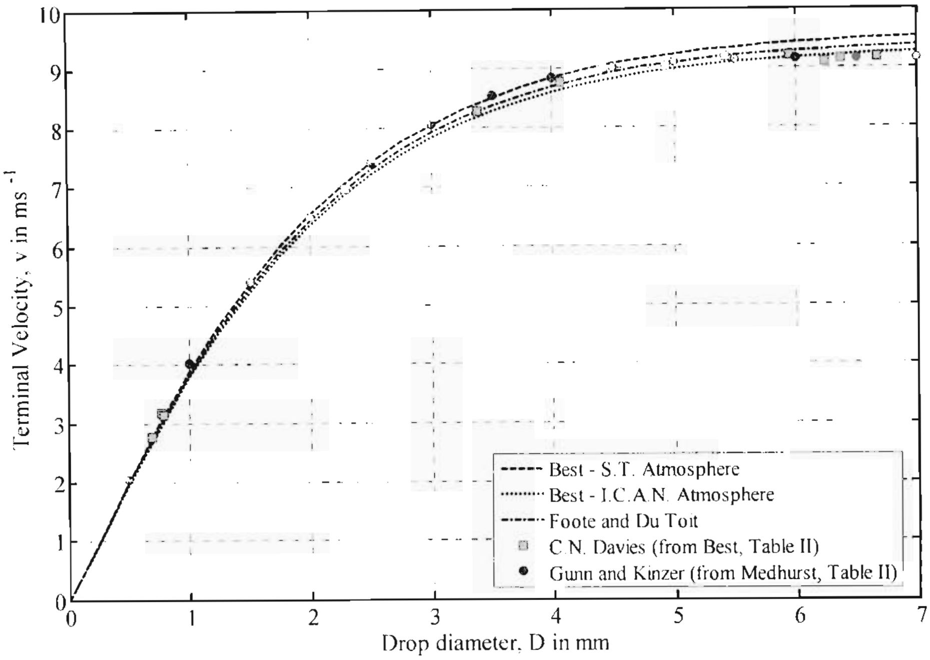

Figure 2-3 : Terminal velocity of raindrops in the I.C.A.N and S.T. standard atmospheres.

2.3 Raindrop Size and Shape

The size of raindrops can vary from the tiniest drops comparable to those found in clouds ($D \simeq 0.1$ mm) to relatively large drops, with diameter $D \simeq 7.0$ mm. Raindrops larger than about 7 mm are hydrodynamically unstable and thus break up very quickly as they fall towards the ground. Not all raindrops are spherical in shape and as the raindrop increases in size, the shape begins to distort.

Only very small raindrops, with diameter $D \leq 0.3$ mm are spherical in shape. For diameters, 0.3 mm $< D <$ 1.0 mm, raindrops are slightly deformed and are better approximated by oblate spheroids. Thereafter, the deformation increases progressively and in the diameter range 1.0 mm $< D <$ 4.0 mm, raindrops are better described as asymmetric oblate spheroids, with flat bases. For $D >$ 4.0 mm the base becomes even more flattened and spreads laterally.

Knowledge of drop shape and their variation with drop size is essential for the calculation of the scattering and extinction cross sections. Mie scattering calculations are computationally intense for non-spherical shapes, such as those discussed in Appendix A, thus to reduce computation time, the classical approach of using spherical raindrops was adopted in this study. All calculations henceforth will use the equivolumetric or effective diameter, and is simply referred to as the drop diameter D. This is the diameter of a sphere with the same volume as that of the deformed raindrop. In some cases it may be more convenient to use the equivolumetric or effective radius a_0, where $a_0 = 0.5D$

If Mie theory for spheres is used in attenuation calculations, the results will slightly over-estimate for vertical polarizations and under-estimate for horizontal polarizations. However, Matzler (2003) showed that the specific attenuation requires only a small correction (less than 8 %) and thus this approximation is warranted since it will significantly reduce computation complexity.

In the next section drop-size distributions (DSDs) will be examined. The scattering and attenuation of electromagnetic waves by rain is highly dependent upon the chosen DSD hence several theoretical and empirical DSDs will be discussed in detail.

2.4 Drop-Size Distributions

2.4.1 Historical Review

The study of the drop-size distributions (DSDs) has been the subject of theoretical and practical interest by meteorologists and radio engineers for over half a century. DSDs provide one of the most comprehensive descriptions of rain and together with its moments form the basis of the definition and computation of parameters in a wide array of applications, most appropriately in this study of rain attenuation for microwave and millimetre-waves. The scattering and attenuation due to rain is highly dependent upon the chosen DSD. DSDs exhibit significant spatial and temporal variability. Consequently the average DSDs for several climatic regions and rainfall types will be examined and discussed in this section. These DSD functions will be used as input parameters in the ensuing chapters.

Detailed documentation of DSD measurements date back as early as Weisner (1895, cited Campos 1999). The DSD measurements were undertaken over the tropics using an absorbent filter paper method. Sheets of filter paper dusted with a water soluble-dye were exposed to rain for a brief time interval. After impacting with the sheet each raindrop would cause a spot marked permanently by the dye. A known empirical relation was then used to convert the size of the spots to the actual raindrop size. The simplicity of this method led to its subsequent usage by many investigators most notably Marshall and Palmer (1948). However, this method has a crucial flaw, namely the spot diameter size is a function of not only the raindrop size but also the fall velocity. Furthermore, large raindrops would splatter upon impact with the sheet and this making it difficult to determine their exact size.

Another common method was the flour method of Laws and Parsons (1943). Their pioneering measurements for different rain types in Washington DC are still used as a standard today. In the flour method a pan containing a thin layer of fine flour is exposed to rain for a few seconds. After a while, each raindrop forms a dry, hard dough pellet. A known relationship between the size or mass of the dough pellets and raindrop size was then used. It was noted that for rain events, the DSD would vary appreciably even when the rain rate was the same. Hence averaged distributions for different rain rates ranging from 0.25 mm h^{-1} to 150 mm h^{-1} were computed. Over 60 years later, the Laws and Parsons DSD measurements are still considered typical of the average DSD for both widespread rain (lower rain rates) and convective rain (higher rain rates). Marshall and

Palmer (1948) showed that both their measurements in Ottawa and those of Laws and Parsons (1943) can be modelled using a negative exponential relation (Marshall and Palmer 1948). Both Marshall and Palmer (1948) and Laws and Parsons (1943) are the most commonly used DSDs for the evaluation of the scattering and attenuation of electromagnetic waves by rain and will be discussed in greater detail later in this chapter.

Other techniques include the camera method (e.g. Jones 1959, 1992; Cataneo and Stout 1968) and the oil method (Ugai et al. 1977). In the camera method, two perpendicularly aligned cameras take synchronous pictures of the raindrops. However, the marginal increase in accuracy did not warrant the considerable calculations which this method entails. Hence to date, camera methods have been used predominantly for drop shape measurements, most notably Pruppacher and Pitter (1971). In the oil method a pan of castor oil is exposed to rain and the size of the raindrops floating in the oil is then measured. The viscosity of the oil can be adjusted so even raindrops with radius as small as 0.025 mm can be measured.

The techniques mentioned so far are very laborious and time consuming. More sophisticated measurement techniques have been implemented with the development of automated recording devices. These devices have made use of electromechanical, optical and even electrostatic sensors. The most widely used of theses devices is the distrometer of Joss and Waldvogel (1967). It contains an electromechanical sensor to measure the momentum of each raindrop and subsequently the DSD. Using this instrument, Joss et al. (1968) found that DSD varied significantly for different rain types. The parameters for the average exponential distributions of 3 different rain types were obtained. They include the "drizzle" distribution (JD), for very light widespread rain, the "thunderstorm" distribution (JT), for extreme convective rain and the "widespread" distribution (JW), which is nearly identical to Marshall and Palmer (1948) distribution (MP). These DSDs will be discussed in further detail later in this section.

The simplicity of the single-parameter exponential distributions (MP, JD, JW and JT) has led to its application by many investigators. However it has been shown on several occasions that it fails to accurately model measurements taken over a short period of time (Joss and Gori 1978; Zawadzki and de Agostinho Antonio 1988). The number of raindrops with very small and large diameters tends to be overestimated. Even if two-parameter exponential distributions are adopted this problem is not alleviated. Another problem with the traditional exponential distribution is that they may not necessarily be consistent with the rain-rate integral equation, (e.g. Olsen et al. 1978; de Wolf 2001; Matzler 2002). Minor modifications and normalisations may be required as will be discussed later in this section.

To prevent such shortfalls and improve accuracy more complicated multi-parameter distributions were necessary. This was made possible with the introduction of sophisticated remote sensing techniques. By measuring more than one remotely sensed variable simultaneously, the parameters of multi-parameter distributions were evaluated promptly without the need for intricate empirical relations. This was shown by Atlas and Ulbrich (1974), by measuring the radar reflectivity and microwave attenuation, to evaluate a two parameter gamma model. An alternative method was adopted by Seliga and Bringi (1976) where a dual-polarization radar was used to concurrently measure both the vertical and horizontal polarized reflectivity factors.

To date many investigators have used advanced techniques such as those discussed above and have proposed DSD functions providing greater accuracy and flexibility. The most noteworthy are the modified gamma distribution (e.g. Ulbrich 1983; Willis, 1984; de Wolf, 2001) and the lognormal distribution (e.g. Feingold and Levin 1986; Ajayi and Olsen 1986; Adimula and Ajayi 1996). The gamma distribution is most practical since it has a single curvature parameter with which to model deviations from the exponential distribution. Furthermore it reduces to the traditional exponential distribution when this curvature parameter tends to zero. The lognormal distributions are equally advantageous since higher moments of such distributions are also lognormally distributed. The overview of the history and the evolution of DSD measurements and modelling is now completed. In the next subsection the basic definitions and formulas will be given. This will be followed by the mathematics and implementations of the prominent DSDs.

2.4.2 Drop-size distribution definitions and formalism

The drop-size distribution (DSD) is simply the number of raindrops of a given diameter range per unit volume of air. However most ground-based devices only measure the surface distribution, which is the number of raindrops of a given diameter range passing though an horizontal surface of unit area per unit time. Thus two definitions of DSD namely a volumetric-based $N_V(D,R)$ and a flux-based $N_A(D,R)$ arise.

The volumetric-based drop-size distribution $N_V(D,R)$ is defined as the mean number of raindrops of diameter D per unit volume of air and per increment in drop diameter dD. N_V is generally a function of rain rate R in mm h^{-1} and the equivolumetric drop diameter D in mm and hence has the units m^{-3} mm^{-1}.

The alternative form (Uijlenhoet 2001) is $N_A(D,R)$, which is the mean number of raindrops of diameter D arriving at a horizontal surface of unit area, per unit time and per increment in drop diameter dD. N_A has the units m^{-2} mm^{-1} s^{-1}. Measurements performed by most ground-based devices such as distrometers provide N_A and not N_V. It is important to differentiate between the two forms of DSDs and note that N_V is the desired form for the calculation of rain attenuation since it yields the drop-size distribution in 3-dimensional space. Henceforth, N_V and its moments will de discussed.

To convert between the two forms N_A and N_V the simple expression, ignoring the effects of wind, turbulence and raindrop interactions, as given in (2.13) may be applied.

$$N_A(D,R)=v(D)N_V(D,R), \tag{2.13}$$

where $v(D)$ is the terminal fall velocity of a raindrop of diameter D. The terminal velocity is dependent on the atmospheric conditions. For the standard atmosphere at sea level the measurements of Gunn and Kinzer (1949) are commonly used. For other altitudes, the dependence on air pressure can be accounted for by using $v(D,P)$ as given in (2.7) or alternatively by the more accurate form $v(D,T,P)$ given in (2.8).

The total number N_T of raindrops per unit volume is given by the zeroth order moment in D of N_V as follows

$$N_T=\int_0^\infty N_V(D,R)\,dD. \tag{2.14}$$

The third order moment in D of N_V gives the volume fraction F_V of rain-water in air. F_V is simply the total volume of rain-water per unit volume of air and is hence dimensionless if the drop diameter D is in m.

$$F_V=\frac{\pi}{6}\int_0^\infty D^3N_V(D,R)\,dD. \tag{2.15}$$

For the total volume of rain-water F_A arriving at a horizontal surface of unit area per unit time, the third order moment of N_A must be considered. Using (2.13) F_A can be written in terms of N_V as follows

$$F_A=\frac{\pi}{6}\int_0^\infty D^3N_V(D,R)v(D)\,dD, \tag{2.16}$$

where D is the drop diameter in m. F_A is thus the downward flux density of rain-water volume, more commonly referred to as the rain rate. F_A has units m s^{-1}. It is often more convenient to express the rain rate in mm h^{-1} and have the drop diameter D in mm. Thus (2.16) can be modified to yield the rain-rate integral equation given by

$$R_N(R) = 6\pi \times 10^{-4} \int_0^{\infty} D^3 N_V(D,R) v(D) dD, \tag{2.17}$$

where D is the drop diameter in mm and R_N has units mm h^{-1}. The rain-rate integral equation (2.17) may be used to verify the self-consistency of the various DSDs in literature. If $N_V(D,R)$ is self-consistent, $R_N = R$ and the rain-rate integral equation will be satisfied. However if $R_N \neq R$, $N_V(D,R)$ will have to be normalised by applying

$$Norm(R) = \frac{R}{R_N(R)}, \tag{2.18}$$

to transform $N_V(D,R)$ to the normalised self-consistent distribution $N_N(D,R)$ as follows

$$N_N(D,R) = Norm(R) \cdot N_V(D,R). \tag{2.19}$$

Another useful quantity is the liquid-water content W, which is the mass of liquid water per unit volume of air.

$$W = \rho_w \cdot \frac{\pi}{6} \int_0^{\infty} D^3 N_V(D,R) dD, \tag{2.20}$$

where ρ_w is the density of water in kg m^{-3} and D is the drop diameter in m.

The fraction of liquid water $F_W(\partial)$ in air contributed by drops with diameter $D < \partial$ is given by

$$F_W(\partial) = \frac{\int_0^{\partial} D^3 N_V(D,R)\,dD}{\int_0^{\infty} D^3 N_V(D,R)\,dD}. \tag{2.21}$$

The median volume diameter D_o can then defined as

$$F_W(D_o) = \frac{1}{2}. \tag{2.22}$$

Using the above definitions and formulae the prominent average DSDs for several climatic regions and rainfall types will now be examined. Minor modifications and normalisations may be required as will be discussed.

2.4.3 The Laws and Parsons DSD

As mentioned Laws and Parsons (1943) performed extensive measurements of the DSD variation for several rain types in Washington DC. Today the Laws and Parsons (1943) DSD measurements are still considered typical for continental temperate rainfall. The Laws and Parsons (1943) DSD is probably the most widely used DSD to date and has been adopted as a standard for the calculation of specific attenuation by the International Telecommunications Union (ITU).

Laws and Parsons (1943) observed that the individual DSDs exhibited noticeable variability. Consequently the averaged distributions at several rain rates ranging from 0.25 mm h^{-1} to 150 mm h^{-1} were computed. Laws and Parsons (1943) tabulated their results as volume fractions $M(D)dD$ and not directly as drop-size distributions N_V.

For each respective rain rate, $M(D)dD$ is the fraction of the total rain-water volume reaching the horizontal ground surface as contributed by raindrops within each differential range $(D-0.5dD, D+0.5dD)$. Integrating over all drop diameters yields $\int_0^\infty M(D)dD = 1$. The Laws and Parsons (1943) measurements have been tabulated in Medhurst (1965) for drop diameter intervals dD = 0.5 mm. The volume fractions $M(D)dD$ were represented as the percentage contributions at each respective rain rate as shown in Table 2-4.

Table 2-4 : Laws and Parsons (1943) measurements represented as percentages of the total rain-water volume, from Medhurst (1965, Table III)

Rain rate (mm h^{-1}) / **Drop Diameter Interval (mm)**	**Total rain-water volume as percentages, $M(D)dD \times 100$**								
	0.25	**1.25**	**2.5**	**5**	**12.5**	**25**	**50**	**100**	**150**
0−0.25	1.0	0.5	0.3	0.2	0.1	0	0	0	0
0.25−0.75	27.0	10.4	7.0	4.5	2.5	1.7	1.2	1.0	1.0
0.75−1.25	50.1	37.1	27.8	20.3	11.5	7.6	5.4	4.6	4.1
1.25−1.75	18.2	31.3	32.8	31.0	24.5	18.4	12.5	8.8	7.6
1.75−2.25	3.0	13.5	19.0	22.2	25.4	23.9	19.9	13.9	11.7
2.25−2.75	0.7	4.9	7.9	11.8	17.3	19.9	20.9	17.1	13.9
2.75−3.25	0	1.5	3.3	5.7	10.1	12.8	15.6	18.4	17.7
3.25−3.75	0	0.6	1.1	2.5	4.3	8.2	10.9	15.0	16.1
3.75−4.25	0	0.2	0.6	1.0	2.3	3.5	6.7	9.0	11.9
4.25−4.75	0	0	0.2	0.5	1.2	2.1	3.3	6.8	7.7
4.75−5.25	0	0	0	0.3	0.6	1.1	1.8	3.0	3.6
5.25−5.75	0	0	0	0	0.2	0.5	1.1	1.7	2.2
5.75−6.25	0	0	0	0	0	0.3	0.5	1.0	1.2
6.25−6.75	0	0	0	0	0	0	0.2	0.7	1.0
6.75−7.25	0	0	0	0	0	0	0	0	0.3

However, Table 2-4 provides the volume fraction $M(D)dD$ for only the selected rain rates. Using the original measurements of Laws and Parsons (1943), several authors (e.g. Markowitz 1976; de Wolf 2001) have suggested analytical functions, to extend to other rain rates as well. Of these, de Wolf (2001) suggested an excellent gamma function for $M(D)dD$ as given by

$$M(D)dD = (33.44)R^{-1.28}D^{5.93}\exp\left(-5.38R^{-0.186}D\right), \tag{2.23}$$

where D is the drop diameter in mm and R is the rain rate in mm h^{-1}.

For each respective rain rate, the continuous gamma function given by (2.23) and the original Laws and Parsons (1943) measurements have been plotted on the same axes in Figure 2-4. As shown the analytical function provides an excellent fit to the measurements.

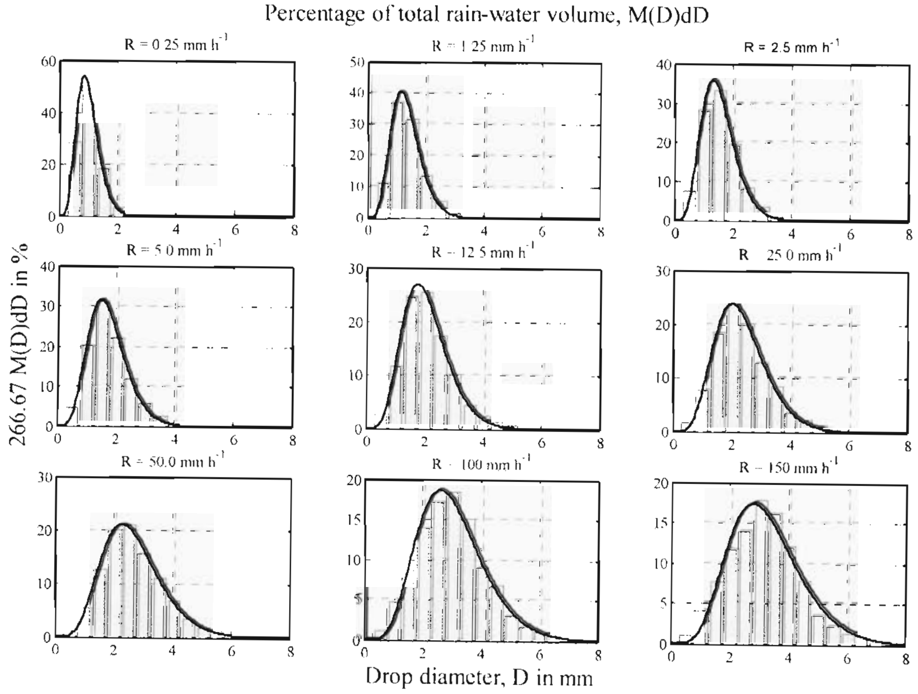

Figure 2-4 : de Wolf (2001) analytical fit for volume fraction *M(D)dD* and Laws and Parsons (1943) measurements.

As in Table 2-4, the Laws and Parsons (1943) measurements have been plotted as the percentage contributions in histograms with bins of size 0.5 mm. A factor of 266.67 was incorporated to convert the continuous spacing of (2.23) into the discrete bin size for comparison.

As shown in Figure 2-4 for very low rain rates and drizzle the volume contributions of small raindrops with diameter $D < 1.5$ mm dominate. As the rain rate increases the distribution becomes more expanded. The contribution of large raindrops with diameter $D > 3.5$ mm becomes more significant for heavy showers. To better illustrate the above points, the volume fractions $M(D)dD$ have been plotted as percentage contributions on the same axes in Figure 2-5(a). This diagram better illustrates the shift in the contribution from small raindrops to larger ones as the rain rate increases. One should bear in mind that instantaneous drop-size distributions may exhibit great variability even during the same rain event. Thus it is common practice to use the models of the average distributions, as will be discussed later in this section.

The volume fractions $M(D)dD$ still need to be converted to drop-size distributions $N_V(D)dD$. For each respective rain rate R, the volume fraction $M(D)dD$ and DSD $N_V(D,R)dD$ are related as follows

$$M(D)dD = \frac{\pi}{6F_A} D^3 N_V(D,R) v(D) dD . \tag{2.24}$$

Substituting (2.17) into (2.24) and making $N_V(D,R)dD$ subject of the formula gives

$$N_V(D,R)dD = \frac{10^4}{6\pi} \frac{R_N(R) M(D) dD}{D^3 v(D)} . \tag{2.25}$$

For several rain rates, the values of $M(D)dD$ as given in Table 2-1 have been converted to drop-size distributions $N_V(D,R)dD$ using (2.25). These results are plotted in Figure 2-5 (right). Many authors (e.g. Marshall and Palmer 1948; Markowitz 1976; de Wolf 2001) have suggested analytical fits to the Laws and Parsons (1943) distribution. However, before these analytical models are discussed, an overview of the different types of rain is provided.

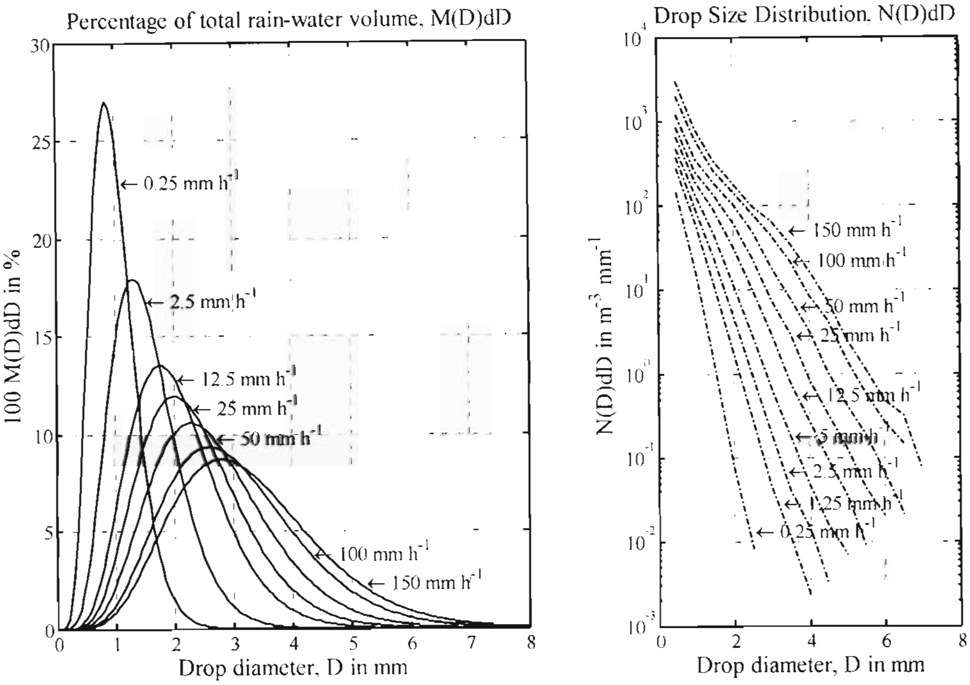

Figure 2-5 : Volume fraction *M(D)dD* as percentages (a) and drop-size distribution *N(D)dD* (b).

2.4.4 Types of Rainfall

Instantaneous DSDs exhibit considerable spatial and temporal variability thus the average DSDs are generally employed. Even so the parameters describing the average DSDs still vary noticeably depending on the type and nature of the associated rain event. Hence before proceeding further with the analytical descriptions of DSDs, the different types of rain need to be discussed. The macroscopic characteristics for each rain type will also be briefly overviewed.

In meteorology, rainfall is often classified into two groups, namely stratiform and convective. In communications, it is common to further classify these types of rain into drizzle, widespread, shower and thunderstorm.

Stratiform rain originates from low-lying horizontally stratified clouds such as status, nimbostratus and stratocumulus. Stratiform clouds produce both drizzle and widespread spread rain. Drizzle refers to very light widespread rain, with rain rates generally below 1–2 mm h^{-1}. It is characterized by a large concentration in raindrops with small diameters. Widespread rain generally refers to the higher rain rates up to 25 mm h^{-1} and is characterized by raindrops with small to medium diameters.

Stratiform rain cells cover large geographical areas typically exceeding 100 km and are associated with rain rates less than 25 mm h^{-1}. The rain rate is mostly uniform across the entire cell for long durations, often exceeding 1 hour. In communication systems, where stratiform rain dominates, these sizeable durations often warrant the usage of an appropriate link margin to negate the resulting attenuation.

Convective rain originates from cumulonimbus clouds, large towering clouds that extend the entire troposphere. This type of rain results when masses of relatively warm air rise to higher levels in the troposphere. Upon reaching these upper levels these air masses are cooled and return to the lower levels producing heavy showers and thunderstorm. Showers generally refer to rain rates below 50 mm h^{-1} and are characterized by raindrops with medium to large diameters. Thunderstorm refers to very heavy rainfall with rain rates up to 200 mm h^{-1}.

Convective rain cells generally extend for only a few kilometers and are embedded within larger stratiform rain cells and thunderstorms. Due to the localised nature of these cells, they generally pass over the communication link within a few minutes. Nevertheless, they cause severe attenuation and the required fade margin is often too large to be implemented and uneconomical since it is required for only short duration of time. The above-mentioned Laws and Parsons (1943) DSD measurements are considered typical for both widespread rain and convective rain. Other DSDs and their analytical forms will now be discussed.

2.4.5 Exponential Drop-Size Distributions

The first analytical description of the average DSD was presented in Marshall and Palmer (1948). Using the filter paper method, Marshall and Palmer (1948) measured the DSD for rain rates up to 23 mm h^{-1}. The measurements were taken for raindrops with diameter 1 mm < D < 3.5 mm and showed good agreement with Laws and Parsons (1943) over this range. Marshall and Palmer (1948) derived the following inverse exponential function to describe the observed average DSDs

$$N_V(D,R) = N_0 e^{-\Lambda D}, \text{ and } \quad \Lambda = \alpha R^{-\beta}, \tag{2.26}$$

where N_0 is a constant representing $N_V(0,R)$ in m^{-3} mm^{-1}, Λ is the slope of the $N_V(D,R)$ curve on a semi-logarithmic plot in mm^{-1}, D is the drop diameter in mm, R is the rain rate in units mm h^{-1} and α and β are constants.

From their measurements, Marshall and Palmer (1948) empirically found that

$$N_0 = 8\times10^3 \text{ m}^{-3}\text{mm}^{-1}, \text{ and } \quad \Lambda = 4.1R^{-0.21} \text{ mm}^{-1}. \tag{2.27}$$

Even though the relations in (2.27) are based on measurements for R < 23 mm h^{-1}, it has been found to be valid for the average DSD at higher rain rates as well. The Marshall and Palmer (1948) exponential DSD is simple and convenient in calculations. Consequently, it has been used by several investigators.

Subsequent studies (e.g. Srivastava 1971; Waldvogel 1974; Joss and Gori 1978) have shown that even though exponential distributions may provide an adequate description of the average DSD, their parameters may show great variability. Both N_0 and Λ vary not only for different rain events and rain types but also exhibit deviation during the same rain event.

Waldvogel (1974) provided an excellent description of the variation of N_0 and showed that it decreases with increasing convectivity. Thus thunderstorms showing low convectivity may still exhibit high concentrations of raindrops with small diameters.

Joss and Gori (1978) examined the shape of instant (accumulated during 1 minute or less) DSDs. It was found that the shape of instant distributions exhibited considerable deviation from the Marshall and Palmer (1948) exponential shape and tended towards monodispersity. For both widespread and thunderstorm rain, the best-fit exponential distribution over-estimated the number of small and large raindrops. This deviation became more pronounced at the lower rain rates. However, by averaging these instant DSDs over space or time the shape of the resultant average DSD moved away from monodispersity and towards an exponential shape.

The exponential shape is thus adequate for applications where the average over space or time is relevant. For this study, namely rain attenuation, the average distribution over the propagation path is required. Hence the usage of the above-mentioned exponential distributions can be warranted, especially for temperate-continental climates. Only the variation of N_0 need be considered.

Joss et al. (1968) used their distrometer to perform measurements for several rain types in Switzerland. It was found that DSD varied significantly depending on the rain type. Joss et al. (1968) evaluated the parameters for the average exponential distributions of 3 different rain types. They include the "drizzle" distribution (JD), for very light widespread rain, the "thunderstorm" distribution (JT), for extreme convective rain and the "widespread" distribution (JW), which is nearly identical to Marshall and Palmer (1948) distribution (MP). These parameters have been provided in Table 2-5.

As pointed out by several authors, (e.g. Olsen et al. 1978; de Wolf 2001; Matzler 2002) the above-mentioned exponential distributions are not necessarily consistent with the rain-rate integral equation (2.17). JT is inaccurate up to 40% and MP, JD and JW show inaccuracies up to 20%. Each of these DSDs was hence normalised using equations (2.18) and (2.19). As shown in Matzler (2002), normalised function $Norm(R)$ can be fitted by a second order polynomial of $X = \ln(R)$, i.e. the natural logarithm of R.

$$Norm(R) = aX^2 + bX + c \,. \tag{2.28}$$

Table 2-5 contains the values of the parameters for MP, JD, JT and JW. The normalised function $Norm(R)$ was calculated using the terminal velocity at sea level. Hence $Norm(R) = Norm(R, P_0)$. After normalisation, JW and MP are approximately equal. Hence only the normalised forms of MP, JD and JT will be used in ensuing calculations.

Table 2-5 : Parameters for the exponential distributions of Marshall and Palmer (1948) and Joss et al. (1968).

Distribution Function	N_0 **in** $m^{-3}mm^{-1}$	$\Lambda = aR^{-\beta}$ **in** mm^{-1}	$Norm(R)$; $X = \ln(R)$, R **in mm**
MP	8×10^3	$4.1R^{-0.21}$	$0.8425 - 0.00889X + 0.00687X^2$
JW	7×10^3	$4.1R^{0.21}$	$0.9628 - 0.01016X + 0.00786X^2$
JD	30×10^3	$5.7R^{-0.21}$	$1.1122 - 0.03343X + 0.00791X^2$
JT	0.14×10^3	$3.0R^{-0.21}$	$1.4163 - 0.19851X + 0.04496X^2$

If necessary variation with altitude can also be accounted for as given below

$$Norm(R,P) = Norm(R,P_0)\cdot\left(\frac{P_0}{P}\right)^{0.35}, \tag{2.29}$$

As the altitude increases, there is a decrease in atmospheric pressure and hence an increase in the terminal fall velocity as reflected in (2.29). The dependence of the terminal velocity on atmospheric pressure is given in (2.7). The exponent in (2.7) shows a weak dependence on the drop diameter D and hence in (2.29) it is replaced by the effective mean value of 0.35.

In Figure 2-6 the MP, JD and JT exponential DSDs for a rain rate R = 15 mm h^{-1} are shown.

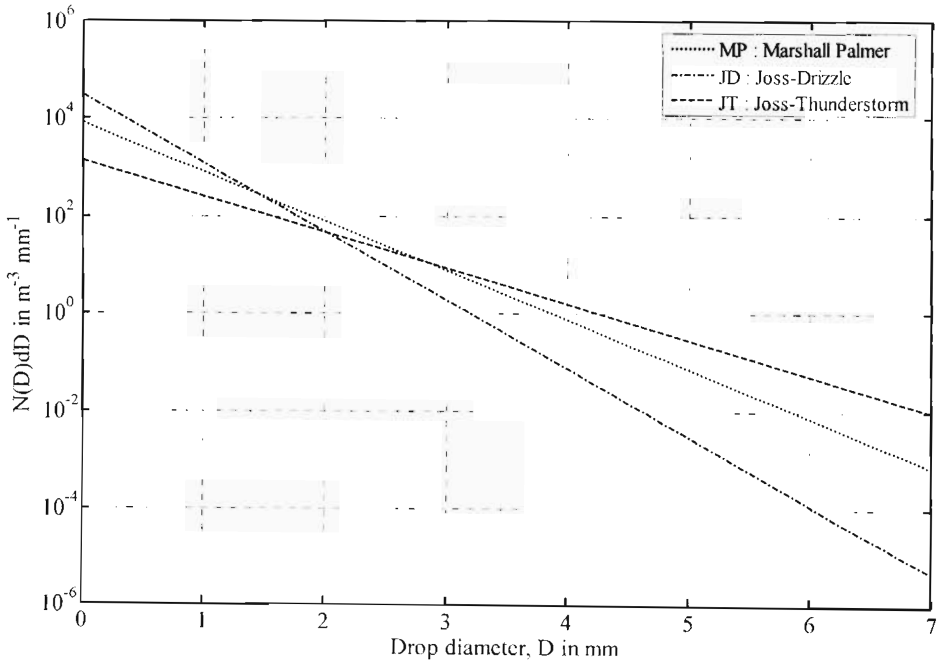

Figure 2-6 : The normalised exponential drop-size distributions MP, JD and JT for R = 15 mm h^{-1}.

As expected JD has a greater concentration of small raindrops and lesser large raindrops as compared to MP. Such a distribution may also be representative of heavy rain with little to no convective activity. For highly convective rain JT is a good representation since it has a greater concentration of large raindrops and few small ones. Next the gamma DSDs will be discussed. As will be shown, the above-mentioned exponential distributions are simplifications of the general gamma DSDs.

2.4.6 Gamma Drop-Size Distributions

Due to the reduction in computation, DSDs have been assumed traditionally to have an exponential shape as described above. As explained previously, the exponential distribution fails to accurately model measurements taken over a short period of time (Joss and Gori 1978; Zawadzki and de Agostinho Antonio 1988) and is most suitable when sufficient averaging over either space or time is relevant.

Also exponential distributions tend to overestimate the number of raindrops with very small and large diameters. This may be explained theoretically by the microphysical and kinematic processes influencing the DSD shape. Drop coalescence is influential for small drops and results in a decrease in small drops and increase in the larger drops sizes. Drop breakup has the opposite effect and is more important for large raindrops. The combined effect of drop coalescence and breakup is a decrease in the number of small and large raindrops and an increase in the medium-sized drops.

Evaporation is another factor that reduces the number of small raindrops that reach the surface. Updrafts have a similar effect as evaporation. Downdrafts have the opposite effect and increase the number of smaller raindrops at the lower levels. Considering all of the above process it can be seen that the shape of DSDs should tend towards monodispersity.

Multi-parameter distributions are thus required to accurately model the shape of such DSDs. These include the modified gamma distribution (e.g. Ulbrich 1983; Willis, 1984; de Wolf, 2001), the lognormal distribution (e.g. Feingold and Levin 1986; Ajayi and

Olsen 1986; Adimula and Ajayi 1996) and the Weibull distribution (e.g. Sekine et al. 1987).

The modified gamma distribution suggested by Ulbrich (1983) has the form

$$N_V\left(D,R\right)=N_0D^{\mu}e^{-\Lambda D},\text{ and }\quad \Lambda=\alpha R^{-\beta}, \tag{2.30}$$

where the exponent μ can be any real number, the coefficient N_0 has units m^{-3} mm$^{-1-\mu}$ and the remaining parameters are the same as that for the exponential distribution. The gamma distribution is thus particularly convenient since it is a generalization of the traditional exponential distribution and reduces to this form if μ = 0.

Ulbrich (1983) showed that not all three of the gamma distribution parameters are independent. N_0 and μ are theoretically and empirically related as follows

$$N_0=C_Ne^{3.2\mu} \tag{2.31}$$

where C_N is a constant. This is particularly advantageous since dual-measurement techniques can be employed to estimate these parameters with N_0 and μ expressed in terms of one another.

de Wolf (2001) suggested an excellent gamma distribution fit to the measurements of Laws and Parsons (1943). The parameters are given below

$$\begin{aligned}&N_0=1.98\times10^4\ \text{m}^{-3}\text{mm}^{-1-\mu},\\&\mu=2.93,\ \text{and}\\&\Lambda=5.38R^{-0.186}\ \text{mm}^{-1}.\end{aligned} \tag{2.32}$$

To improve accuracy, two normalisations were calculated using the terminal velocity at sea level, namely $Norm_L$ for $R\leq 25$ mm h^{-1} and $Norm_H$ for $R>25$ mm h^{-1}.

$$
\begin{aligned}
Norm_L &= 1.1274 - 0.0866X + 0.01287X^2 \\
Norm_H &= 1.0484 - 0.0416X + 0.006404X^2
\end{aligned}
\qquad (2.33)
$$

Figure 2-7 shows gamma DSD suggested in de Wolf (2001) and the exponential DSD in Marshall and Palmer (1948). It has been pointed out on several occasions (e.g. Ajayi and Olsen 1985; de Wolf 2001; Matzler 2002) that exponential distributions overestimate the number of small raindrops ($D < 1$ mm). As can be seen in Figure 2-7 the gamma distribution can better approximate this diameter range.

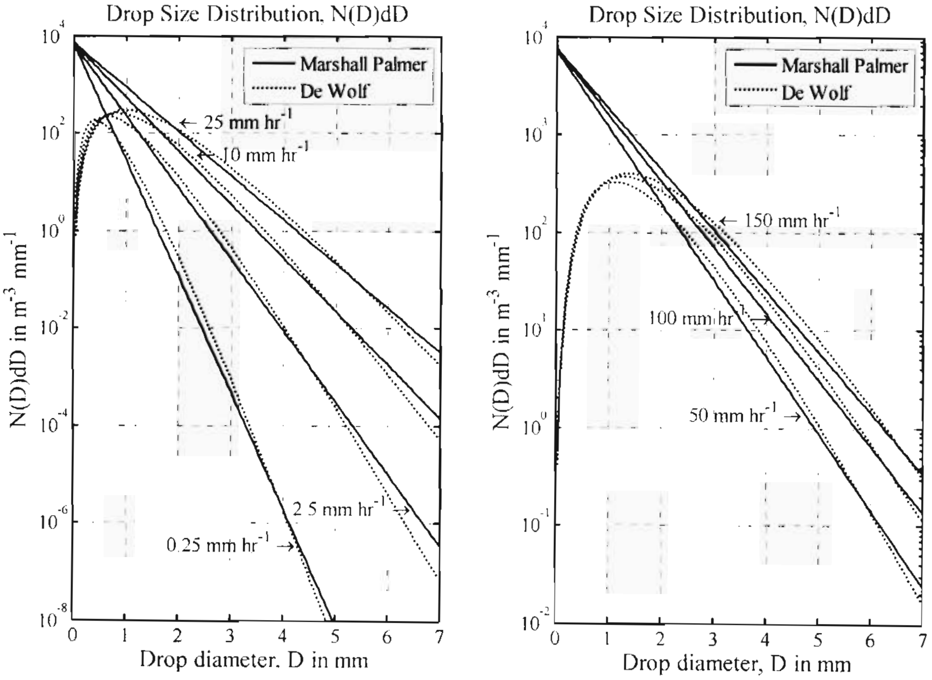

Figure 2-7 : Comparison of the de Wolf (2001) gamma DSD and the Marshall and Palmer (1948) exponential DSD.

Previously communication system and radar applications employed lower frequencies, where the effects of small raindrops were negligible. Hence the inaccuracy of the exponential distribution was insignificant. In millimetre-waves applications the effect of raindrops with $D < 1$ mm becomes significant and hence needs to be modelled appropriately.

The gamma distribution is particularly useful in tropical climate regions where the exponential distribution has been found on numerous occasions to be inadequate (e.g. Willis 1984; Adimula and Ajayi 1996). The highly convective precipitation in the tropics is also applicable to mid-latitude summer thunderstorms. Atlas and Ulbrich (1974, cited Jiang et al 1997) suggested the following gamma distribution

$$N_V(D,R) = 64500D^2 \exp\left(-7.09R^{-0.27}D\right), \tag{2.34}$$

where the drop diameter D is in mm.

Normalisation for (2.34) yields

$$Norm = 2.392 - 0.6364X + 0.05827X^2. \tag{2.35}$$

2.4.7 Lognormal Drop-Size Distributions

The lognormal distribution has also been found to be particularly useful in for the modelling of the DSD observed tropical climates (e.g. Ajayi and Olsen 1985; Adimula and Ajayi 1996). The lognormal DSD is defined as follows

$$N_V(D,R) = \frac{N_T}{\sigma_g\sqrt{2\pi}D}\exp\left[\frac{-\left(\ln D - \mu_g\right)^2}{2\sigma_g^{\ 2}}\right], \tag{2.36}$$

where N_T is the total number of raindrops per m^3 and μ_g is the mean of $\ln D$ and σ_g is the standard deviation. The lognormal distribution is advantageous since all three parameters have physical meaning. In additions, since the DSD is lognormally distributed then the higher order moments will also be lognormally distributed.

Fang and Chen (1982) summarised the numerical values of the lognormal parameters for both showers and thunderstorms. These values are given in Table 2-6.

Table 2-6 : Fang and Chen (1982) coefficients for shower and thunderstorm rain lognormal models

Rain Type		N_T	μ_g	σ_g
Showers	$R \leq 50\ \mathrm{mm\ h^{-1}}$	$40R^{-0.64}$	$\ln\left(1.14 + 0.18 \ln R\right)$	$0.29 + 0.001R$
Thunderstorms	$R \leq 50\ \mathrm{mm\ h^{-1}}$	$46R^{-0.55}$	$\ln\left(0.222 + 0.397 \ln R\right)$	$0.5 + 0.0035R$
	$R > 50\ \mathrm{mm\ h^{-1}}$	$8.8R$	$\ln\left(1.76 + 7.33 \times 10^{-4} \ln R\right)$	0.3148

Adimula and Olsen (1996) measured the DSDs for several locations in Nigeria. It was found that a lognormal distribution provided an excellent fit for shower and thunderstorm rain in both the continental and tropical regions. The numerical values are given in Table 2-7.

Table 2-7 : Adimula and Olsen (1996) coefficients for shower and thunderstorm lognormal models.

Rain Type		N_T	μ_g	${\sigma_g}^2$
Continental	**Showers**	$127R^{-0.477}$	$-0.476 + 0.221 \ln R$	$0.269 - 0.043 \ln R$
	Thunderstorms	$70R^{-0.564}$	$-0.378 + 0.224 \ln R$	$0.306 - 0.059 \ln R$
Tropical	**Showers**	$137R^{-0.370}$	$-0.414 + 0.234 \ln R$	$0.223 - 0.034 \ln R$
	Thunderstorms	$63R^{-0.491}$	$-0.178 + 0.195 \ln R$	$0.209 - 0.030 \ln R$

The lognormal distributions are generally more consistent with the rain-rate integral equation (2.17) as compared to the exponential distributions covered in Section 2.4.5. Normalisation was nevertheless performed and the results are given in Table 2-8.

Table 2-8 : Normalisation functions for the shower and thunderstorm lognormal distributions

Rain Type		$Norm(R)$; $X = \ln(R)$, R in mm
Fang and Chen (1982)		
Showers	$R \leq 50\,\text{mm h}^{-1}$	$1.167 - 0.2314X + 0.04632X^2$
Thunderstorms	$R \leq 50\,\text{mm h}^{-1}$	$5.508 - 2.798X + 0.4253X^2$
	$R > 50\,\text{mm h}^{-1}$	$0.9952 - 1.446\times10^{-3}X + 1.379\times10^{-6}X^2$
Adimula and Olsen (1996)		
Continental	**Showers**	$0.9936 - 4.721\times10^{-3}X + 6.587\times10^{-4}X^2$
	Thunderstorms	$1.019 - 7.353\times10^{-3}X + 1.100\times10^{-3}X^2$
Tropical	**Showers**	$0.9894 - 6.257\times10^{-3}X + 1.851\times10^{-3}X^2$
	Thunderstorms	$1.000 - 5.032\times10^{-3}X + 1.088\times10^{-3}X^2$

In Figure 2-8 the lognormal models for both continental and tropical climates as given in Table 2-7 and with normalisation functions given in Table 2-8 are shown for rain rate $R = 50$ mm h^{-1}. The MP and JT exponential DSDs are also shown for comparison.

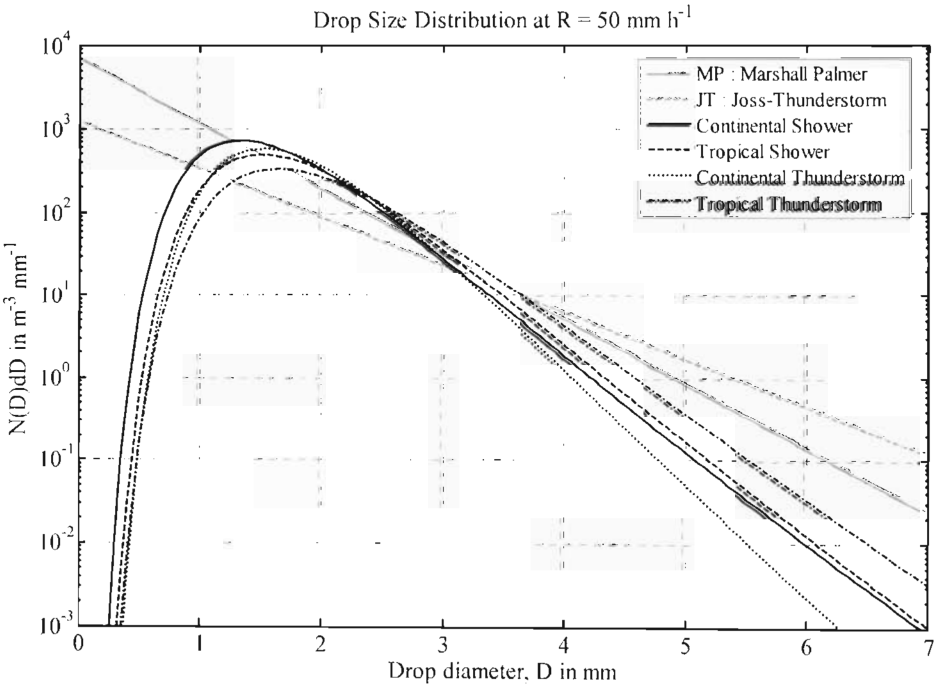

Figure 2-8 : Adimula and Olsen (1996) lognormal DSDs for continental and tropical climates.

Once again it can be seen that the exponential function is an inadequate representation for the DSD and over-estimates the number of small and large raindrops. It should also be noted that as the level of convectivity increases there is an increased number of large raindrops and decrease in smaller ones.

2.4.8 Weibull Drop-Size Distributions

Sekine et al. (1987) proposed yet another three parameter distribution, namely the Weibull distribution given by

$$N_V\left(D,R\right)=N_T\frac{\eta}{\sigma}\left(\frac{D}{\sigma}\right)^{\eta-1}\exp\left[-\left(\frac{D}{\sigma}\right)^{\eta}\right] \tag{2.37}$$

where N_T = 1000 m^3, the shape parameter $\eta=0.95R^{0.14}$, the scale parameter $\sigma=0.26R^{0.42}$ and R is the rain rate in mm h^{-1}. The above-mentioned distribution was proposed for drizzle widespread and shower rain. The normalisation function is given by

$$Norm=1.184-0.03466X-0.02591X^2. \tag{2.38}$$

Figure 2-9 shows the Weibull DSD along with the Atlas and Ulbrich (1974) gamma DSD at a rain rate R = 50 mm h^{-1}. The MP and JT exponential distributions given in Table 2-5 are also shown for comparison. Figure 2-7, Figure 2-8 and Figure 2-9 show that DSDs are typically characterised by a peak that shifts towards larger drop diameters as the rain rate increases. The exponential distributions are thus not adequate and over-estimate the number of small and large raindrops. Gamma, lognormal and Weibull distributions have been shown to consistently provide an accurate description of the DSD shape and are particularly useful for millimetre-wave applications.

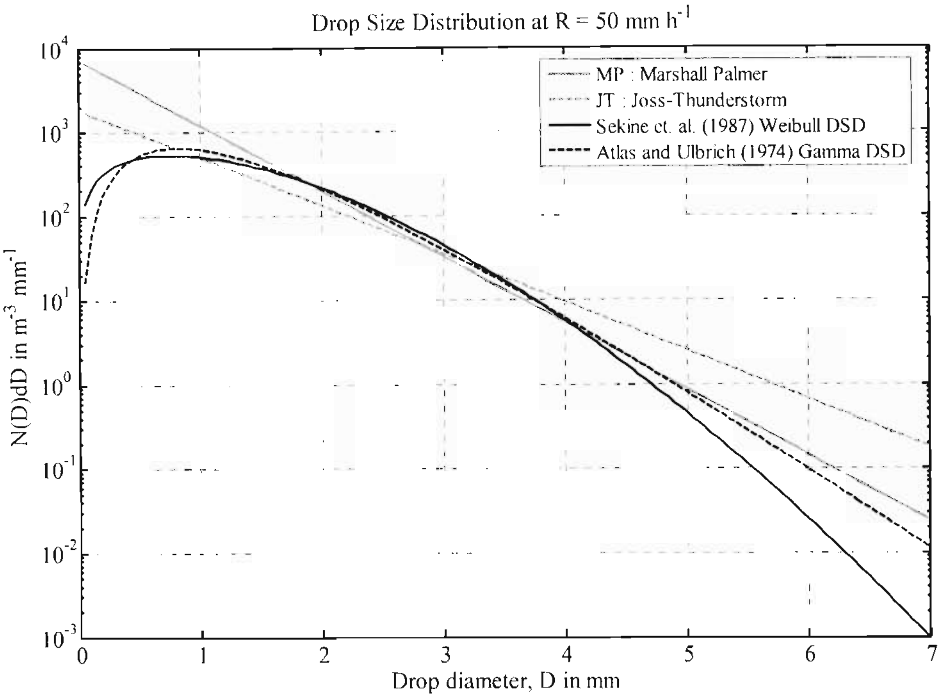

Figure 2-9 : Sekine et al. (1987) Weibull distribution and Atlas and Ulbrich (1974) gamma distribution.

2.5 Dielectric Properties of Raindrops

The dielectric property of rain is the final requirement necessary to calculate attenuation and scattering parameters. Rain comprises of drops of water of various sizes and shapes. The dielectric property of water is both frequency and temperature dependent and hence needs to be examined. This is the subject of this section. Raindrops occurring in the natural world may contain several impurities. The ionic conductivity of such impurities may alter the dielectric property of raindrops from that of pure water but such effects are negligible at microwave and millimetre-wave as discussed in Oguchi (1983). It was also mentioned in Ray (1972) that the effect of impurities becomes influential only at low frequencies.

Most of the earlier investigations (e.g. Olsen et al. 1978; Oguchi 1981, 1983) have used the empirical model for the complex refractive index of water by Ray (1972). A newer and more accurate model of Liebe (1991) will also be examined here.

The relative dielectric constant or complex permittivity ε_r and the complex refractive index ζ are defined as follows

$$\begin{aligned} &\varepsilon_r = \frac{\varepsilon}{\varepsilon_0} = \varepsilon' - i\varepsilon'', \text{ and} \\ &\zeta = \zeta' - i\zeta''. \end{aligned} \tag{2.39}$$

In (2.39) ε' is the dielectric constant, ε'' is the dielectric loss and ζ' and ζ'' are the real and imaginary components of the refractive index. The complex refractive is often denoted by m. However to avoid confusion in later chapters, where m is used to denote the order of the associated Legendre functions, ζ has been chosen instead

The above definitions are related as follows

$$\begin{aligned} &\zeta = \sqrt{\varepsilon_r}, \\ &\varepsilon' = (\zeta')^2 - (\zeta'')^2, \text{ and} \\ &\varepsilon'' = 2\zeta'\zeta''. \end{aligned} \tag{2.40}$$

2.5.1 Debye Relaxation and the Empirical Model by Ray

In Cole and Cole (1941, cited Ray 1972), the complex permittivity of water was represented using the Debye relaxation. The Debye approximation was shown to be valid for frequencies, $f < 200$ GHz.

The Debye relaxation equations are given in (2.41).

$$\begin{aligned} \varepsilon' &= \varepsilon_\infty + \frac{(\varepsilon_s - \varepsilon_\infty)}{\left(1+(\lambda_s/\lambda)^2\right)}, \text{ and} \\ \varepsilon'' &= \frac{(\varepsilon_s - \varepsilon_\infty)(\lambda_s/\lambda)}{\left(1+(\lambda_s/\lambda)^2\right)}, \end{aligned} \tag{2.41}$$

where λ is wavelength in cm, ε_∞ is the high frequency dielectric constant, ε_s is the static dielectric constant and λ_s is the relaxation wavelength.

Cole and Cole (1941, cited Ray 1972) modified the classical Debye relaxation equations shown above by including the frequency independent conductivity σ and the spread parameter α as follows

$$\begin{aligned} \varepsilon' &= \varepsilon_\infty + \frac{(\varepsilon_s - \varepsilon_\infty)\left[1+(\lambda_s/\lambda)^{1-\alpha}\sin(\alpha\pi/2)\right]}{\left(1+2\cdot(\lambda_s/\lambda)^{1-\alpha}\sin(\alpha\pi/2)+(\lambda_s/\lambda)^{2\cdot(1-\alpha)}\right)}, \text{ and} \\ \varepsilon'' &= \varepsilon_\infty + \frac{(\varepsilon_s - \varepsilon_\infty)(\lambda_s/\lambda)^{1-\alpha}\cos(\alpha\pi/2)}{\left(1+2\cdot(\lambda_s/\lambda)^{1-\alpha}\sin(\alpha\pi/2)+(\lambda_s/\lambda)^{2\cdot(1-\alpha)}\right)} + \frac{\sigma\lambda}{18.8496\times10^{10}}. \end{aligned} \tag{2.42}$$

When σ and α are zero (2.42) reduces to the classical Debye equations (2.41). The parameter $\sigma = 12.5664 \times 10^8$ for all temperatures of meteorological interest. The remaining temperature dependent parameters are given as follows

$$\begin{aligned} &\varepsilon_\infty = 5.27137 + 0.021647\cdot T - 0.00131198\cdot T^2, \\ &\varepsilon_s = 78.54\cdot\left[1.0 - 4.579\times10^{-2}T_* + 1.19\times10^{-5}T_*^2 - 2.80\times10^{-8}T_*^3\right], \\ &\alpha = 0.0609265 - 16.8129/T_{**}, \text{ and} \\ &\lambda_s = 0.00033836\cdot\exp\left[2513.98/T_{**}\right], \end{aligned} \tag{2.43}$$

where

$$\begin{aligned} T_* &= T - 25.0, \text{ and} \\ T_{**} &= T + 273, \end{aligned} \tag{2.44}$$

such that T may be given in °C.

Ray (1972) developed an empirical broadband model to extend to $f < 300$ THz. This empirical model was divided in several frequency ranges and required over 100 parameters. The absorption spectrum of liquid water has several absorption bands. Each of these bands were analytically modelled by Ray (1972) hence resulting in the large number of required parameters. The complex refraction index of water was calculated at 25 °C and illustrated in Figure 2-10. The dashed line in Figure 2-10 represents the Debye contribution given by (2.42). The solid line is from the analytical model of Ray (1972). Three dot-dashed lines are also shown to indicate f = 20, 200 and 1000 GHz. The spikes in the analytical model indicate the existence of several absorptions bands.

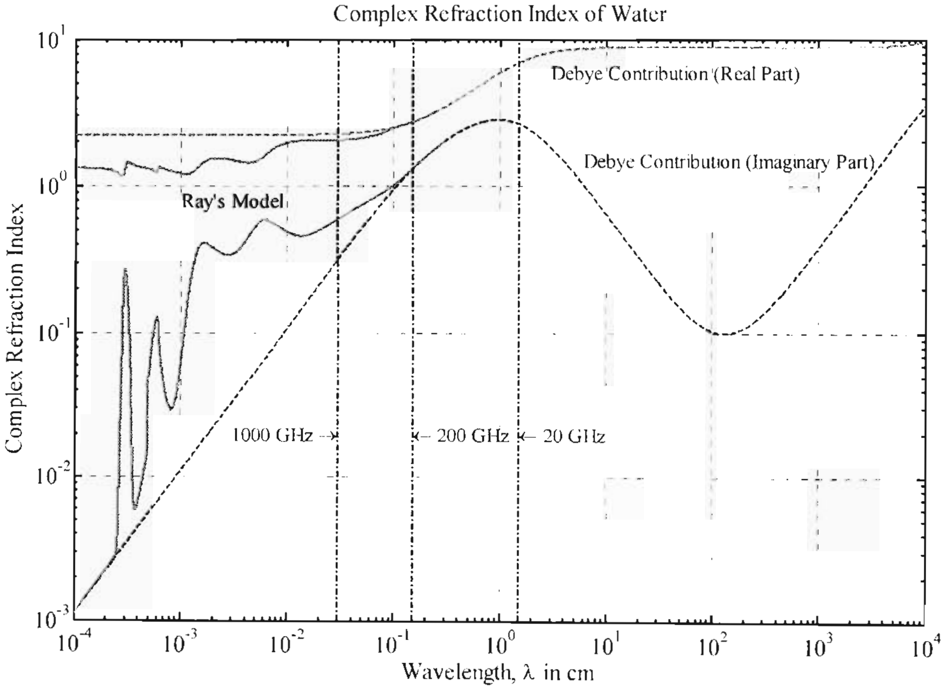

Figure 2-10 : The complex refraction index of water at $T = 25$ °C.

The dependence of the complex refractive index on temperature is examined in Figure 2-11. The complex refractive index for 3 selected temperatures, T = -10, 0 and 20 °C was calculated using (2.42) for 0.1 cm < λ < 100 cm.

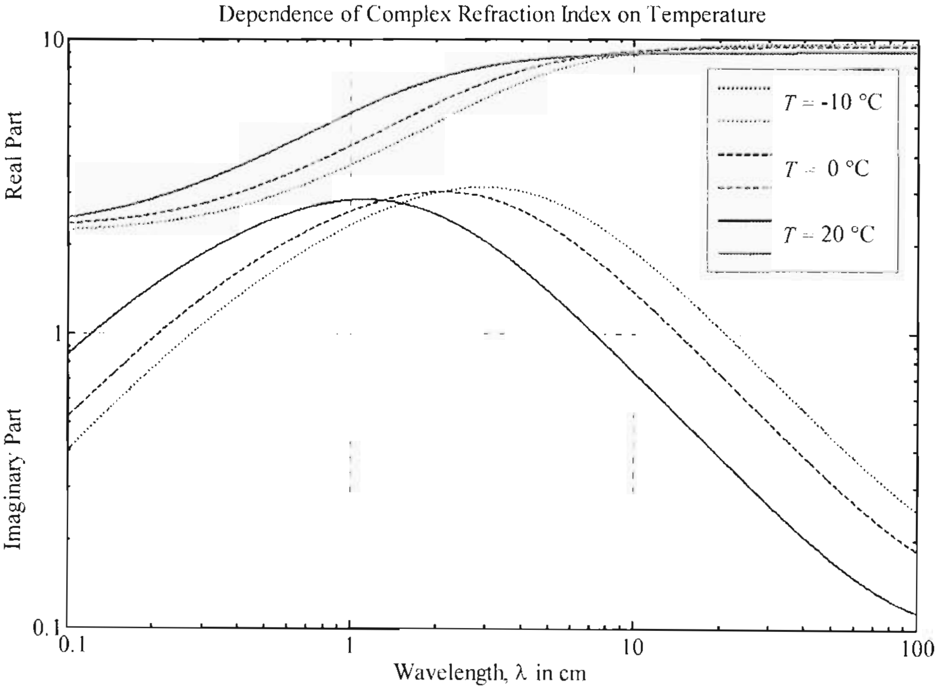

Figure 2-11 : Dependence of complex refraction index on temperature.

2.5.2 The Double-Debye Model by Leibe

In Liebe (1991) a model was presented for f < 1 THz. By taking into consideration the considerable experimental measurements since 1972, Liebe (1991) developed a more accurate and simpler model than Ray (1972). The static dielectric constant ε_0 is given by

$$\varepsilon_0 = 77.66 - 103.3 \cdot \theta, \tag{2.45}$$

where $\theta = 1 - 300/(273.15 - T)$ and T is given in °C.

Liebe (1991) also considered the classical Debye relaxation equations. A single Debye model was sufficient to fit all experimental data below 100 GHz. The formula for the single Debye model may be written as follows

$$\varepsilon_r = \frac{(\varepsilon_0 - \varepsilon_\infty)}{1 - i(f/\gamma_D)} + \varepsilon_\infty, \tag{2.46}$$

where ε_∞ is the high frequency dielectric constant, and γ_D is the relaxation frequency given by

$$\begin{aligned} &\varepsilon_\infty = 0.066 \cdot \varepsilon_0, \text{ and} \\ &\gamma_D = 20.27 + 146.5 \cdot \theta + 314 \cdot \theta^2. \end{aligned} \tag{2.47}$$

To extend for 100 GHz < f < 1000 GHz, a double Debye model was required as given in (2.48).

$$\varepsilon_r = \frac{(\varepsilon_0 - \varepsilon_1)}{1 - i(f/\gamma_1)} + \frac{(\varepsilon_1 - \varepsilon_2)}{1 - i(f/\gamma_2)} + \varepsilon_2, \tag{2.48}$$

where ε_0 and ε_1 are the first and second high frequency dielectric constants, γ_1 and γ_2 denote the primary and secondary relaxation frequency and f is frequency in GHz. After fitting the experimental data in this frequency range, the principle Debye parameters remained essential the same ($\varepsilon_1 \approx \varepsilon_\infty$, $\gamma_1 \approx \gamma_D$) as can be seen by their formula given by

$$\begin{aligned} &\varepsilon_1 = 0.0671 \cdot \varepsilon_0, \\ &\gamma_1 = 20.20 + 146.4 \cdot \theta + 316 \cdot \theta^2, \\ &\varepsilon_2 = 3.52 + 7.52 \cdot \theta, \text{ and} \\ &\gamma_2 = 39.8 \cdot \gamma_1. \end{aligned} \tag{2.49}$$

The real component ε' and imaginary component ε'' are given as follows.

$$\varepsilon' = \frac{(\varepsilon_0-\varepsilon_1)}{1+(f/\gamma_1)^2} + \frac{(\varepsilon_1-\varepsilon_2)}{1+(f/\gamma_2)^2} + \varepsilon_2, \text{ and}$$
$$\varepsilon'' = \frac{(\varepsilon_0-\varepsilon_1)(f/\gamma_1)}{1+(f/\gamma_1)^2} + \frac{(\varepsilon_1-\varepsilon_2)(f/\gamma_2)}{1+(f/\gamma_2)^2}. \tag{2.50}$$

The dependence of the complex permittivity on temperature is shown for 4 selected temperatures T = 0, 10, 20 and 30 °C in Figure 2-12.

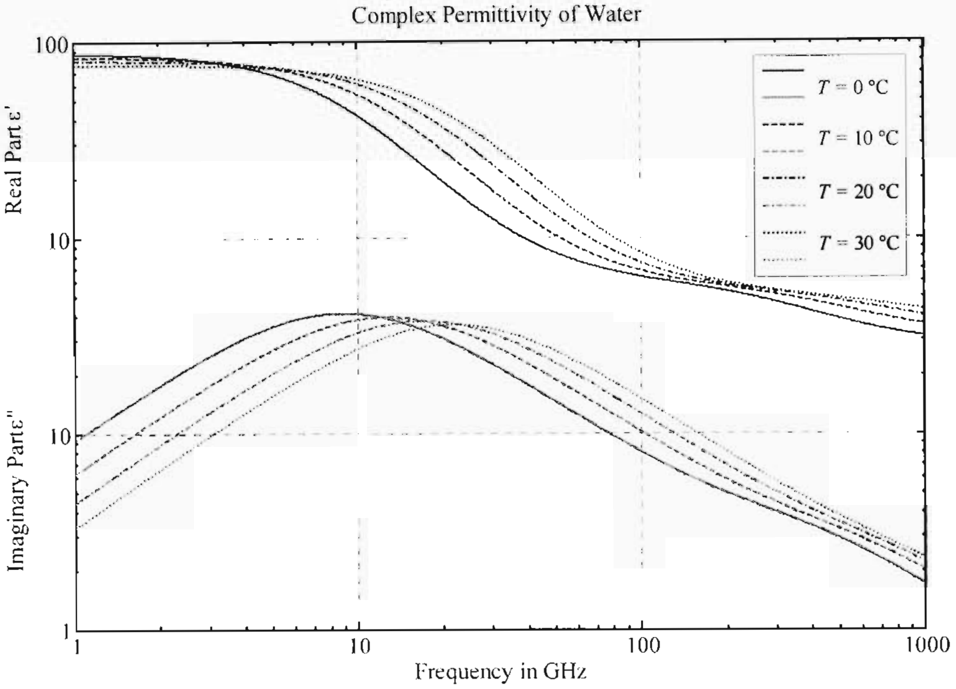

Figure 2-12 : Dependence of complex permittivity on temperature.

The above 7 parameter model is sufficient to evaluate the complex permittivity of water for all temperatures and frequencies of interest in this study. It is far simpler than the analytical model by Ray (1972). The complex permittivity and complex refractive index at T = 20 °C are given in Figure 2-13 and Figure 2-14, respectively.

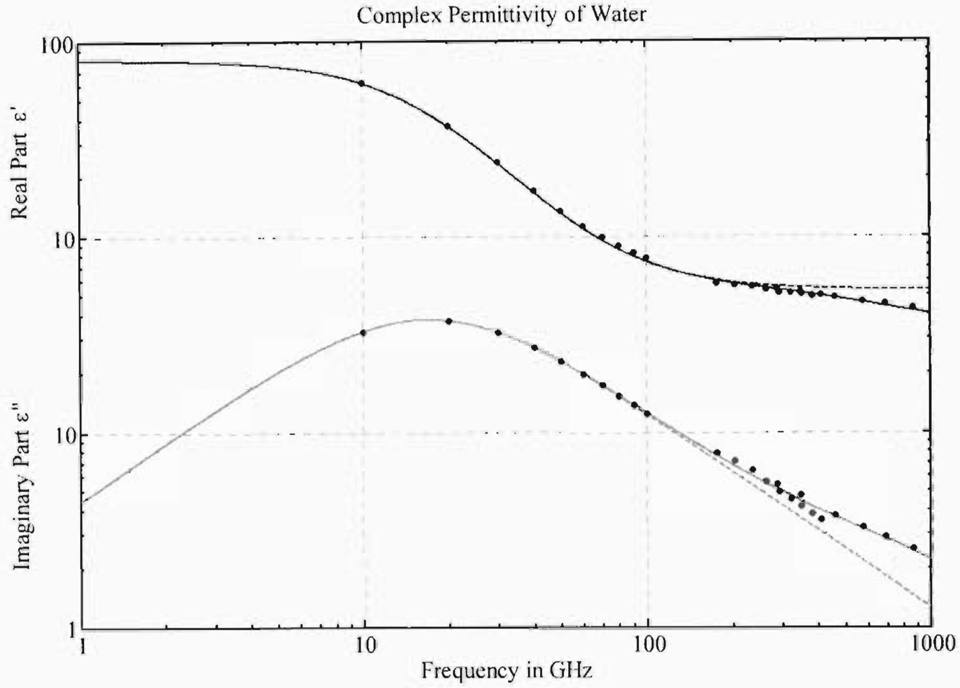

Figure 2-13 : Complex permittivity of water at $T = 20$ °C.

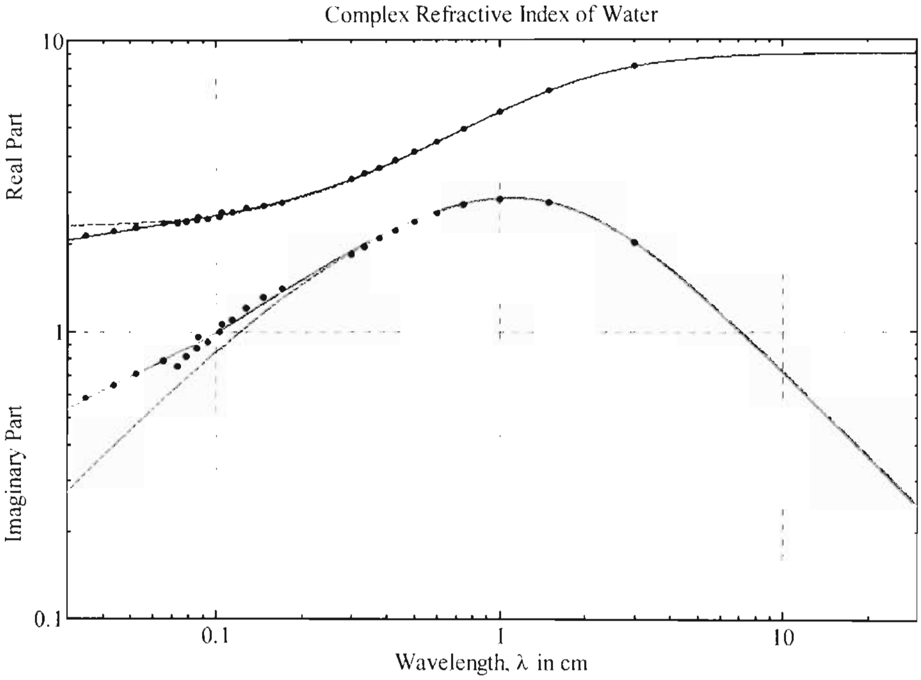

Figure 2-14 : Complex refractive index of water at $T = 20$ °C.

The single Debye and double Debye models are represented by the dashed and solid lines, respectively. Experimental data (Liebe 1991, Table I) is also indicated for comparison. As can be seen the double Debye model provides a simple and accurate fit for f < 1000 GHz.

2.6 Conclusion

In this chapter the microphysical properties of raindrops have been discussed. These include raindrop size and shape, fall velocity and drop-size distribution (DSD). The fall velocity is often approximated by the terminal velocity. Gunn and Kinzer (1949) measurements of the terminal velocity at sea level and several analytical descriptions thereof have been discussed along with models for arbitrary atmospheric conditions including with the Best (1950) model for variation with height in the S.T. and I.C.A.N. standard atmospheres.

The size and shape of a raindrop is required in the scattering and extinction cross sections calculations. In this study raindrops have been assumed to be spherical in shape. Preliminary studies on the raindrop shape are provided in Appendix A. Appendix B contains the research on another microphysical property, namely the canting angle of raindrops. Both raindrop shape and canting angle is used in the evaluation of the depolarization and cross-polarization due to rain and the model discussed in the appendix can be used in subsequent research.

From all the microphysical properties, the DSD is the most important parameter in the calculation of the specific attenuation. DSDs vary depending on the climate and geographical location and can strongly dominate calculations of the path attenuation link availability. Variations of up to 50 % in the calculated specific attenuation can result from changing the DSD in calculations. Consequently, this research aims to investigate the influence of the DSD on the specific attenuation by examining several theoretical and empirical DSDs discussed in literature. Raindrops have been assumed to be spherical in shape, hence Mie theory for dielectric spheres has been applied. This will substantially reduce computation time and future work can entail the variation of both drop shape and the DSD.

The DSD is used to extend the scattering and extinction model of a single raindrop to that experienced during a rain event. DSDs exhibit significant spatial and temporal variability. Consequently the average DSDs for several rainfall types are examined. Firstly, the Laws and Parson (1943) drop-size distribution is discussed. Thereafter several analytical descriptions for the DSD are investigated including the exponential, gamma, lognormal and Weibull functions.

Finally the dielectric properties of water were investigated. The Debye approximations and empirical models of Ray (1972) and Liebe (1991) were then examined for frequencies up to 1 THz.

Using the microphysical properties discussed here, the scattering and extinction cross-section of a single raindrop can be computed as will be discussed in Chapter 3.

Chapter 3

Mie Scattering

3.1 Introduction

In Chapter 2 the microphysical properties of rain, such as the raindrop size, shape, and drop-size distribution (DSD) were examined. These properties significantly influence the numerical computation for the scattering and attenuation of electromagnetic waves by rain. The ratio between the drop diameter D and the wavelength λ determines what regime of scattering theory need be applied. When $D << \lambda$, the Rayleigh approximation can be used. For $D \simeq \lambda$, Mie theory is applicable and optical approximations are relevant for $\lambda << D$. Rayleigh and optical approximations are comparatively simple, whereas Mie theory is a more rigorous solution. The diameter size of raindrops typical range from 0.1 mm to 7 mm thus for millimetre-wave frequencies the wavelength is comparable and Mie scattering becomes relevant.

Mie theory is well established for spherical raindrops and has been examined by several authors (e.g. Medhurst 1965; Olsen et al. 1978; Matzler 2002). However, the evaluation of Mie scattering for nonspherical raindrops is considerably complicated and several numerical and analytical techniques are required. Thus in this study, raindrops are assumed to be equivolumetric spheres. After all, the ultimate goal of this study is to evaluate the specific attenuation for various DSDs and this assumption will significantly reduce computation complexity.

3.1.1 Outline of the chapter

In this chapter the specific attenuation for rain is evaluated. In order to evaluate the specific attenuation, the scattering and extinction cross sections of raindrops must be calculated. For millimetre -wave frequencies, Mie theory is used to achieve this goal. In Section 3.2 the assumptions and definitions used in this chapter are established. For rain attenuation in coherent systems, single, independent scattering can be assumed. The validity and consequences of this assumption are discussed. The scattering geometry and definition for the different cross section and efficiencies are introduced.

The scattering of raindrops using both Rayleigh and Mie theory is discussed in Section 3.3. The solution for Mie scattering of spherical dielectric is much more complicated than the Rayleigh scattering equations. It involves the evaluation of associated Legendre polynomials, spherical Bessel functions (with complex arguments) and their derivatives. These functions are solved in Matlab®, using the recurrence relations equations in Abramowitz and Stegun (1964). The scattering and extinction cross sections are in the form of an infinite series of the Mie scattering coefficients. The convergence relation in Bohren and Huffman (1983) has been shown to be accurate and reliable (e.g. Matzler 2002, 2003) and is used in this dissertation.

The attenuation due to raindrops is calculated in Section 3.4. First the extinction cross section is evaluated for individual raindrops. The results are shown for several selected frequencies. Thereafter the specific attenuation is evaluated at these frequencies. The accuracy of the calculated specific attenuation is heavily dependent on the chosen DSD. In most calculations the Laws and Parsons DSDs is typically assumed. In Section 3.4 several DSD shapes have been evaluated from the conventional exponential distributions to the gamma, lognormal and Weibull distributions. The more sophisticated DSDs overcome the shortfalls of the exponential distributions which tend to over-estimate the number of small and large raindrops.

In section 3.5 the difference between the extinction cross section evaluated for spherical raindrops and for the more realistic Prupacher and Pitter (1971) is shown. Vertical polarizations will have a slightly smaller specific attenuation and horizontal polarizations a slightly larger specific attenuation than that calculated using Mie theory for spheres. Hence future work should entail the evaluation of the extinction cross sections for realistically-shaped raindrops and include the effect of drop shape in this model.

3.2 Assumptions and formalisms

When an arbitrary electromagnetic wave propagating in a medium encounters a particle with dielectric properties differing from the medium, the incident energy is scattered in various directions. Part of the incident energy is also absorbed by the particle itself. Thus both absorption and scattering remove energy from the incident electromagnetic wave. This attenuation is also called extinction and these terms are related as follows

$$\text{Extinction} = \text{scattering} + \text{absorbtion}\ . \tag{3.1}$$

Throughout this study, independent, single scattering is assumed. This is the standard assumption and proven to be a suitable approximation for the evaluation of rain attenuation in coherent communication systems (e.g. Watson 1976; Oguchi 1981, 1983; Crane 1983; Matzler 2002, 2003).

The assumptions are as follows

1. The scattered wave and the incident wave have the same frequency. Effects such as the Raman effect and quantum transitions can be ignored, thus scattering only changes the direction of propagation and not the wavelength.
2. Independent scattering is assumed. Particles are sufficiently far from each other such that each particle can form its own scattering pattern undisturbed by the presence of other particles in the medium.
3. Multiple scattering will be neglected. It is assumed that each particle is exposed only to the radiation of the incident electromagnetic wave and not the scattered radiation from other particles. Hence for a medium containing N identical particles the total absorption, scattering and extinction due to the medium is the N times that for a single particle.

The geometry and formula for the scattering of electromagnetic wave by spheres are available in a variety of texts (e.g. Stratton 1941; van de Hulst 1957; Ishimaru 1978; Bohren and Huffman 1983; Sadiku 2001). Unfortunately, the notations and definitions in these texts are not always uniform and depend upon the approach of the author. The definitions, geometry and formula adopted in this study are established in the forthcoming sections.

3.2.1 Scattering Amplitudes and Cross Sections

Consider a linearly polarised electromagnetic plane wave propagating in a medium with dielectric constant ε_0 and permeability μ_0. Let $\boldsymbol{E}^i$ denote the electric field given by

$$\boldsymbol{E}^i = E_0 e^{-ik_0 r \hat{\boldsymbol{K}}_1} \hat{\boldsymbol{E}}_i, \tag{3.2}$$

where E_0 is the amplitude of the electric field, $\hat{\boldsymbol{E}}_i$ is the unit vector in the direction of its polarization and $\hat{\boldsymbol{K}}_1$ is the unit vector in the direction of wave propagation (also called the forward direction). A $e^{i\omega t}$ time convention is assumed and is suppressed throughout this study. The wave number $k_0 = \omega\sqrt{\mu_0\varepsilon_0} = 2\pi/\lambda_0$ and λ_0 is the wavelength in the medium. For a unit-amplitude electric field E_0 equals 1 volt meter^{-1}. Figure 3-1 illustrates the geometry when such an electromagnetic wave falls incident upon an arbitrary particle with dielectric constant ε and permeability μ. The origin has been chosen within the particle. The scattered field at any observation point $\boldsymbol{r}$, with distance r from the origin, behaves as a spherical wave if $r >> D^2/\lambda$, where D is the dimension of the particle. This is called the far-field region.

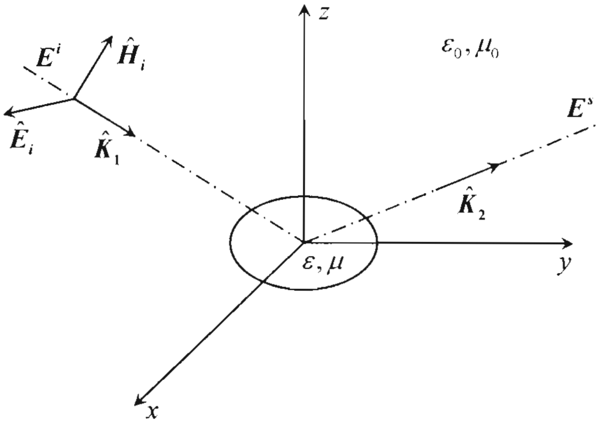

Figure 3-1 : Geometry of the incident and scattered fields for an arbitrary scatterer.

The electric field of the scattered wave in the far-field region, is denoted by $\boldsymbol{E}^s$ and may be given by

$$\boldsymbol{E}^s = E_0 \frac{e^{-ik_0 r}}{r^{-1}} f\left(\hat{\boldsymbol{K}}_2, \hat{\boldsymbol{K}}_1\right), \tag{3.3}$$

where $\hat{\boldsymbol{K}}_2$ is the unit vector directed from the origin to the observation point $\boldsymbol{r}$ and $f(\hat{\boldsymbol{K}}_2,\hat{\boldsymbol{K}}_1)$ is the vector-scattering amplitude. The scattering amplitude $f(\hat{\boldsymbol{K}}_2,\hat{\boldsymbol{K}}_1)$ provides a complete description of the amplitude, phase and polarization of the scattered wave in direction $\hat{\boldsymbol{K}}_2$ when a unit-amplitude plane wave propagating in the direction $\hat{\boldsymbol{K}}_1$ falls incident upon the particle. $f(\hat{\boldsymbol{K}}_2,\hat{\boldsymbol{K}}_1)$ depends on the polarization of the incident wave, the shape, size, orientation and dielectric properties of the particle and the direction $\hat{\boldsymbol{K}}_2$.

It is convenient to define the differential cross section C_d as follows

$$C_d(\hat{\boldsymbol{K}}_2,\hat{\boldsymbol{K}}_1)=\left|f(\hat{\boldsymbol{K}}_2,\hat{\boldsymbol{K}}_1)\right|^2. \tag{3.4}$$

If the scattered power flux density as observed in the direction $\hat{\boldsymbol{K}}_2$ was extended uniformly over 1 steradian of solid angle about $\hat{\boldsymbol{K}}_2$, then the differential cross section is the cross section of a particle that would provide the equivalent amount of scattering. C_d thus varies with $\hat{\boldsymbol{K}}_2$. Integrating C_d over the entire 4π steradians of solid angle yields the total scattered power around the particle. The cross section of a particle that will produce this amount of scattering is called the scattering cross section C_{sca} and is given by

$$C_{sca}=\int_{4\pi}C_d(\hat{\boldsymbol{K}}_2,\hat{\boldsymbol{K}}_1)\,d\Omega_s=\int_{4\pi}\left|f(\hat{\boldsymbol{K}}_2,\hat{\boldsymbol{K}}_1)\right|^2 d\Omega_s, \tag{3.5}$$

where $d\Omega_s=\sin\theta_s d\theta_s d\phi_s$ is the differential solid angle. Similarly, the absorption cross section C_{abs} can be defined as the cross section of particle that corresponds to the total power absorbed by the particle. According to (3.1) the extinction cross section also called the total cross section is then given by

$$C_{ext}=C_{sca}+C_{abs}. \tag{3.6}$$

The single-scattering albedo of the particle W_0 is the ratio of the scattering cross section to the total cross section and given by

$$W_0 = \frac{C_{sca}}{C_{ext}}. \tag{3.7}$$

Other useful cross sections include the bistatic radar cross section C_{bi} and the back-scattering cross section C_b. Each are related to C_d as follows

$$\begin{aligned} C_{bi}\left(\hat{\boldsymbol{K}}_2,\hat{\boldsymbol{K}}_1\right) &= 4\pi\cdot C_d\left(\hat{\boldsymbol{K}}_2,\hat{\boldsymbol{K}}_1\right), \text{ and} \\ C_b\left(\hat{\boldsymbol{K}}_2,\hat{\boldsymbol{K}}_1\right) &= 4\pi\cdot C_d\left(-\hat{\boldsymbol{K}}_1,\hat{\boldsymbol{K}}_1\right). \end{aligned} \tag{3.8}$$

3.2.2 General properties of cross sections

It is sometimes convenient to relate the various cross sections to the geometric cross section C_g of the particle. For a sphere with radius a, the geometric cross section $C_g = \pi a^2$. The ratio between each cross section and the geometric cross section is referred to as efficiency and they are defined as follows

$$\begin{aligned} Q_{ext} &= C_{ext}/C_g, \\ Q_{sca} &= C_{sca}/C_g, \\ Q_{abs} &= C_{abs}/C_g, \text{ and} \\ Q_{ext} &= Q_{sca} + Q_{abs}. \end{aligned} \tag{3.9}$$

For $D << \lambda$, Rayleigh scattering theory is relevant and $Q_{sca} \propto (D/\lambda)^4$ and $Q_{abs} \propto (D/\lambda)$. When the size of the particle $D >> \lambda$, optical scattering theory applies. The extinction efficiency Q_{ext} approaches 2 and the absorption efficiency Q_{abs} approaches a constant somewhat less than 1 (Ishimaru 1978). These properties are proven for hydrometeors in the next section.

Another important relation is given by the forward scattering theorem or extinction theorem which states that the extinction cross section C_{ext} is related to the imaginary part of the scattering amplitude in the forward direction $f\left(\hat{\boldsymbol{K}}_2, \hat{\boldsymbol{K}}_1\right)$ as follows

$$C_{ext} = \frac{4\pi}{k_0} \operatorname{Im}\left[f\left(\hat{\boldsymbol{K}}_2, \hat{\boldsymbol{K}}_1\right) \cdot \hat{\boldsymbol{E}}_i \right], \tag{3.10}$$

where Im denotes the imaginary component.

3.3 Hydrometeors

For this study the scattering particles are raindrops (typical diameter size ranges from 0.1 mm to 7.0 mm) and the ambient medium is the atmosphere. Thus ε_0 and μ_0 are the dielectric constant and magnetic permeability for free space. Each raindrop is considered to be a homogenous dielectric consisting of pure water with permeability $\mu = \mu_0$. The complex relative dielectric constant is that of pure water given by

$$\varepsilon_r = \frac{\varepsilon}{\varepsilon_0} = \varepsilon' - i\varepsilon''. \tag{3.11}$$

The complex relative permittivity ε_r is related to the complex refractive index ζ as follows

$$\zeta = \sqrt{\varepsilon_r} = \frac{k}{k_0}, \tag{3.12}$$

where k_0 is the wave number in free space and k is the wave number in water. The complex refractive index for water has been evaluated as described in Section 2.5 using Liebe (1991) for a temperature T=20°C.

The single-scattering albedo of spherical raindrops is shown in Figure 3-2 for frequencies f = 1, 2, 5, 10, 20, 50 and 100 GHz. The markers on each curve correspond, from left to right, to raindrops with radii a = 0.5, 1.0, 1.5, 2.0, 2.5 and 3.0 mm. Figure 3-2 shows that for frequencies below 5 GHz, the majority of the extinction is due to absorption. As the frequency increases beyond 5 GHz, scattering begins to dominate and for larger raindrops account for 60% to 70% of the total energy lost.

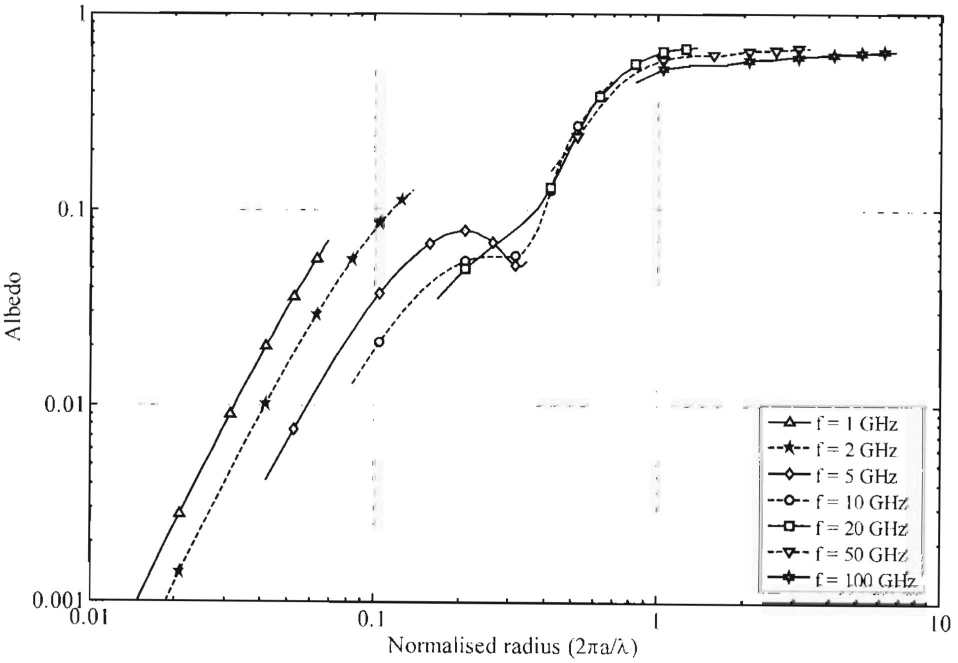

Figure 3-2 : The single-scattering albedo W_0 for spherical raindrops as a function of the normalised radius $2\pi a/\lambda$.

For the evaluation of rain attenuation, the total power loss from the forward-propagating incident wave must be evaluated. Thus the combined effect due to both scattering and absorption by the particle must be calculated, namely the total or extinction cross section. Figure 3-3 shows the normalised extinction efficiency for spherical raindrops with radii a = 0.5, 1.0, 1.5, 2.0, 2.5, 3.0 and 3.5 mm.

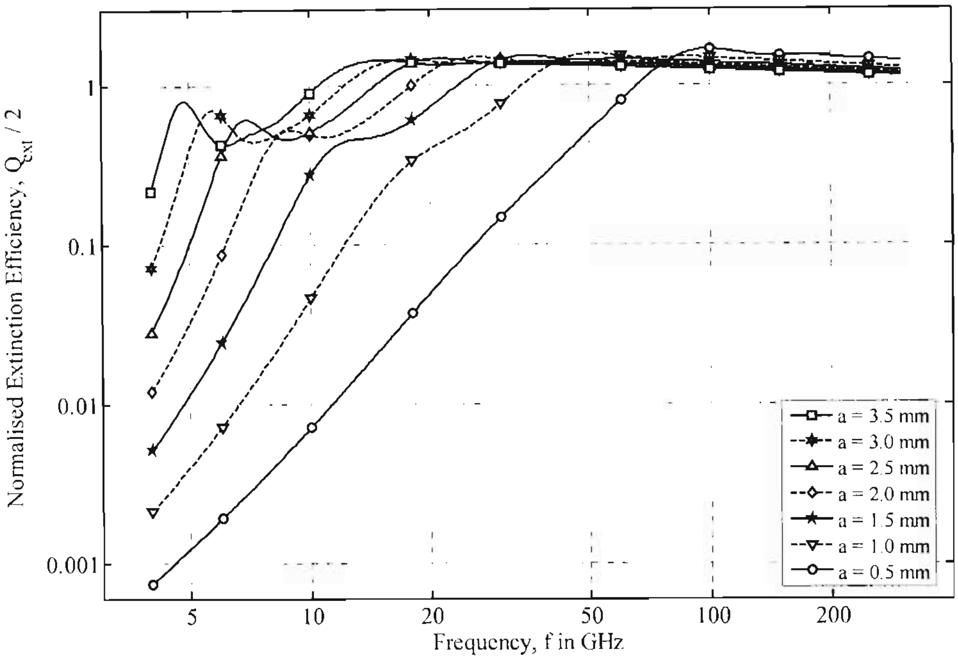

Figure 3-3 : The normalised extinction efficiency Q_{ext} as a function of frequency.

As shown in Figure 3-3 when the size of the raindrops is large compared to the wavelength, the normalised extinction efficiency approaches 1, which is the optical limit. For microwave and millimetre-wave frequencies the extinction varies considerably and Rayleigh theory or the more tedious Mie theory needs to be applied.

3.3.1 Rayleigh Scattering

Rayleigh scattering is applicable only when the size of the scattering particle is small compared to the wavelength. For raindrops, the equivolumetric radius rarely exceeds 3.5 mm and thus Rayleigh scattering is only applicable up to 3 GHz. The derivations for the scattering and extinction cross sections are available in a variety of texts.

The equations are given by

$$C_{ext} = -4\pi k_0 a^3 \operatorname{Im}\left(\frac{\varepsilon - 1}{\varepsilon + 2}\right), \text{ and}$$
$$C_{sca} = \frac{8\pi}{3} k_0^4 a^6 \left|\frac{\varepsilon - 1}{\varepsilon + 2}\right|^2. \tag{3.13}$$

3.3.2 Mie Scattering

Mie scattering of spherical dielectric is much more complicated than the above-mentioned Rayleigh scattering equations. It involves the evaluation of associated Legendre polynomials and spherical Bessel functions with complex arguments. The equations for the scattering and extinction cross sections are in the form of an infinite series as given below

$$C_{ext} = \frac{2\pi}{k_0^2} \operatorname{Re} \sum_{n=1}^{\infty} (2n+1)(a_n + b_n), \text{ and}$$
$$C_{sca} = \frac{2\pi}{k_0^2} \operatorname{Re} \sum_{n=1}^{\infty} (2n+1)\left(|a_n|^2 + |b_n|^2\right), \tag{3.14}$$

where, a_n and b_n are the Mie expansion coefficients of the scattered fields. The derivations are available in variety of texts, for continuity a few of the important equations are given below.

Consider a plane wave propagating along the positive $z-$axis, with electric field along the $x-$axis. The geometry is given in Figure 3-4. Let $\hat{\boldsymbol{a}}_x$, $\hat{\boldsymbol{a}}_y$, and $\hat{\boldsymbol{a}}_z$ denote the unit vectors along the $x-$, $y-$ and $z-$axes.

The incident wave is expressed in the Cartesian coordinate system as follows

$$\boldsymbol{E}^i = E_0 e^{-ik_0 z} \hat{\boldsymbol{a}}_x, \text{ and}$$
$$\boldsymbol{H}^i = \frac{E_0}{\eta} e^{-ik_0 z} \hat{\boldsymbol{a}}_y, \tag{3.15}$$

where, $\eta_0 = \sqrt{\mu_0/\varepsilon_0}$ is the wave impedance, $\hat{\boldsymbol{E}}_i = \hat{\boldsymbol{a}}_x$, $\hat{\boldsymbol{H}}_i = \hat{\boldsymbol{a}}_y$ and $\hat{\boldsymbol{K}}_1 = \hat{\boldsymbol{a}}_z$.

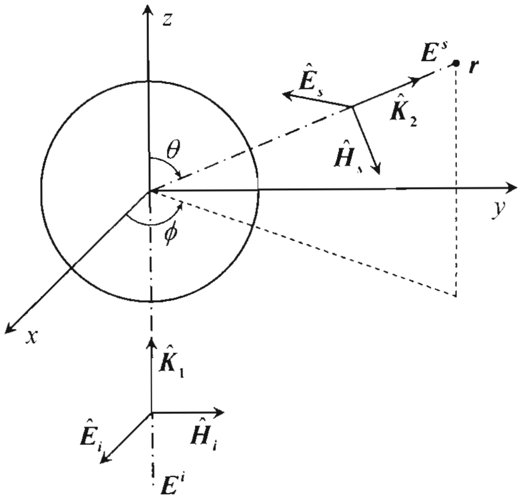

Figure 3-4 : Geometry of the incident and scattered fields for a spherical dielectric.

In the spherical coordinate system, the incident wave can then be expressed in terms of spherical wave functions $\boldsymbol{M}_n$ and $\boldsymbol{N}_n$ as follows

$$\begin{aligned} \boldsymbol{E}^i &= E_0 \sum_{n=1}^{\infty} (-i)^n \frac{(2n+1)}{n(n+1)} \left[\boldsymbol{M}_n^{(1)}(k_0) + i\boldsymbol{N}_n^{(1)}(k_0) \right], \\ \boldsymbol{H}^i &= -\frac{E_0}{\eta} \sum_{n=1}^{\infty} (-i)^n \frac{(2n+1)}{n(n+1)} \left[\boldsymbol{M}_n^{(1)}(k_0) - i\boldsymbol{N}_n^{(1)}(k_0) \right]. \end{aligned} \tag{3.16}$$

The formula for the spherical vector wave functions $\boldsymbol{M}_n$ and $\boldsymbol{N}_n$ comprise of spherical Bessel functions of order n with complex argument χ denoted by $z_n(\chi)$ and associated Legendre functions of degree n and order m denoted by $P_n^m(\cos\phi)$ and are given as indicated in (3.17).

The spherical Bessel function z_n may represents spherical Bessel functions of the first kind j_n, spherical Bessel functions of the second kind y_n, spherical Bessel functions of the third kind (also called spherical Hankel functions of the first kind) $h_n^{(1)}$ or spherical

Bessel functions of the fourth kind (also called spherical Hankel functions of the second kind) $h_n^{(2)}$.

$$\begin{aligned}\boldsymbol{M}_n(k_0) &= \frac{1}{\sin\theta} z_n(k_0 r) P_n^1(\cos\theta)\cos\phi\hat{\boldsymbol{a}}_\theta \\ &\quad - z_n(k_0 r)\frac{dP_n^1(\cos\theta)}{d\theta}\sin\phi\hat{\boldsymbol{a}}_\phi, \\ \boldsymbol{N}_n(k_0) &= \frac{n(n+1)}{k_0 r} z_n(k_0 r) P_n^1(\cos\phi)\cos\phi\hat{\boldsymbol{a}}_r \\ &\quad + \frac{1}{k_0 r}\frac{d}{dr}\left[z_n(k_0 r)\right]\frac{dP_n^1(\cos\theta)}{d\theta}\cos\phi\hat{\boldsymbol{a}}_\theta \\ &\quad + \frac{1}{k_0 r\sin\theta}\frac{d}{dr}\left[z_n(k_0 r)\right]P_n^1(\cos\phi)\sin\phi\hat{\boldsymbol{a}}_\phi.\end{aligned} \tag{3.17}$$

Each spherical Bessel function is related to the corresponding Bessel function J_n, Y_n, $H_n^{(1)}$ or $H_n^{(2)}$. as follows

$$z_n(\chi) = \sqrt{\frac{\pi}{2\chi}} Z_{n+0.5}(\chi), \tag{3.18}$$

where $z_n = j_n, y_n, h_n^{(1)}$, or $h_n^{(2)}$ and $Z_n = J_n, Y_n, H_n^{(1)}$ or $H_n^{(2)}$.

The superscript (1) on the spherical vector wave functions $\boldsymbol{M}_n$ and $\boldsymbol{N}_n$ in (3.16) indicate that the spherical Bessel function z_n as given in the definition (3.17) corresponds to spherical Bessel functions of the first kind j_n.

The scattered field is similarly defined as follows

$$\begin{aligned}\boldsymbol{E}^s &= E_0\sum_{n=1}^{\infty}(-i)^n\frac{(2n+1)}{n(n+1)}\left[a_n\boldsymbol{M}_n^{(4)}(k_0)+ib_n\boldsymbol{N}_n^{(4)}(k_0)\right], \\ \boldsymbol{H}^s &= -\frac{E_0}{\eta}\sum_{n=1}^{\infty}(-i)^n\frac{(2n+1)}{n(n+1)}\left[a_n\boldsymbol{M}_n^{(4)}(k_0)-ib_n\boldsymbol{N}_n^{(4)}(k_0)\right].\end{aligned} \tag{3.19}$$

The superscript (4) on the spherical vector wave functions $\boldsymbol{M}_n$ and $\boldsymbol{N}_n$ in (3.19) indicate that the spherical Bessel function z_n as given in the definition (3.17) corresponds to spherical Bessel functions of the fourth kind $h_n^{(2)}$. This choice is appropriate since the asymptotic behaviour of $h_n^{(2)}$ as given in (3.20) represents a outgoing spherical wave when combined with the time factor $e^{i\omega t}$.

$$h_n^{(2)}(k_0 r) \sim i^{n+1} \frac{e^{-ik_0 r}}{k_0 r}. \tag{3.20}$$

The transmitted field inside the sphere is given by

$$\begin{aligned} \boldsymbol{E'} &= E_0 \sum_{n=1}^{\infty} (-i)^n \frac{(2n+1)}{n(n+1)} \left[c_n \boldsymbol{M}_n^{(1)}(k_0) + i d_n \boldsymbol{N}_n^{(1)}(k_0) \right], \\ \boldsymbol{H'} &= -\frac{E_0}{\eta} \sum_{n=1}^{\infty} (-i)^n \frac{(2n+1)}{n(n+1)} \left[c_n \boldsymbol{M}_n^{(1)}(k_0) - i d_n \boldsymbol{N}_n^{(1)}(k_0) \right]. \end{aligned} \tag{3.21}$$

The unknown expansion coefficients a_n, b_n, c_n and d_n are determined using the boundary conditions, i.e. the continuity of the tangential components of the total electric and magnetic fields on the surface of the sphere at $r = a$.

This yields the following equations

$$\begin{aligned} a_n &= \frac{j_n(\zeta\rho)\left[\rho j_n(\rho)\right]' - j_n(\rho)\left[\zeta\rho j_n(\zeta\rho)\right]'}{j_n(\zeta\rho)\left[\rho h_n^{(2)}(\rho)\right]' - h_n^{(2)}(\rho)\left[\zeta\rho j_n(\zeta\rho)\right]'}, \\ b_n &= \frac{j_n(\rho)\left[\zeta\rho j_n(\zeta\rho)\right]' - \zeta^2 j_n(\zeta\rho)\left[\rho j_n(\rho)\right]'}{h_n^{(2)}(\rho)\left[\zeta\rho j_n(\zeta\rho)\right]' - \zeta^2 j_n(\rho)\left[\rho h_n^{(2)}(\rho)\right]'}, \end{aligned} \tag{3.22}$$

and

$$\begin{aligned} c_n &= \frac{j_n(\rho)\left[\rho h_n^{(2)}(\rho)\right]' - h_n^{(2)}(\rho)\left[\rho j_n(\rho)\right]'}{j_n(\zeta\rho)\left[\rho h_n^{(2)}(\rho)\right]' - h_n^{(2)}(\rho)\left[\zeta\rho j_n(\zeta\rho)\right]'}, \\ d_n &= \frac{\zeta h_n^{(2)}(\rho)\left[\rho j_n(\rho)\right]' - \zeta j_n(\rho)\left[\rho h_n^{(2)}(\rho)\right]'}{h_n^{(2)}(\rho)\left[\zeta\rho j_n(\zeta\rho)\right]' - \zeta^2 j_n(\rho)\left[\rho h_n^{(2)}(\rho)\right]'}. \end{aligned} \tag{3.23}$$

In (3.22) $\zeta = k/k_0$ denotes the complex refractive index of water and $\rho = k_0 a$ is the size parameter. The prime sign at the brackets indicate differentiation of the Bessel function with respect to the argument as follows

$$\left[\chi z_n(\chi)\right]' = \frac{d}{d\chi}\left[\chi z_n(\chi)\right]. \tag{3.24}$$

Using the Mie expansion coefficients defined in (3.22) and by substituting $h_n^{(2)}(kr)$ with its asymptotic form given in (3.20), the spherical components of scattered field in (3.19) may be simplified as follows

$$\begin{aligned} \boldsymbol{E}_\theta^s = \eta \boldsymbol{H}_\phi^s &= -iE_0 \cos\phi \frac{e^{-ik_0 r}}{k_0 r} \sum_{n=1}^{\infty} \frac{(2n+1)}{n(n+1)} \left[b_n \frac{P_n^1(\cos\theta)}{\sin\theta} + a_n \frac{dP_n^1(\cos\theta)}{d\theta} \right], \\ -\boldsymbol{E}_\phi^s = \eta \boldsymbol{H}_\theta^s &= -iE_0 \sin\phi \frac{e^{-ik_0 r}}{k_0 r} \sum_{n=1}^{\infty} \frac{(2n+1)}{n(n+1)} \left[a_n \frac{P_n^1(\cos\theta)}{\sin\theta} + b_n \frac{dP_n^1(\cos\theta)}{d\theta} \right]. \end{aligned} \tag{3.25}$$

The radial components of the scattered field $\boldsymbol{E}_r^s$ and $\boldsymbol{H}_r^s$ tend to zero.

It is often convenient to represent (3.25) in terms of the scattering amplitudes $\boldsymbol{S}_1(\theta)$ and $\boldsymbol{S}_2(\theta)$ as follows

$$\begin{aligned} \boldsymbol{E}_\theta^s = \eta \boldsymbol{H}_\phi^s &= -iE_0 \cos\phi \frac{e^{-ik_0 r}}{k_0 r} \boldsymbol{S}_2(\theta), \\ -\boldsymbol{E}_\phi^s = \eta \boldsymbol{H}_\theta^s &= -iE_0 \sin\phi \frac{e^{-ik_0 r}}{k_0 r} \boldsymbol{S}_1(\theta), \end{aligned} \tag{3.26}$$

where,

$$\begin{aligned}\boldsymbol{S}_1(\theta)&=\sum_{n=1}^{\infty}\frac{(2n+1)}{n(n+1)}\left[a_n\pi(\cos\theta)+b_n\tau(\cos\theta)\right],\\ \boldsymbol{S}_2(\theta)&=\sum_{n=1}^{\infty}\frac{(2n+1)}{n(n+1)}\left[b_n\pi(\cos\theta)+a_n\tau(\cos\theta)\right].\end{aligned}\tag{3.27}$$

The angular functions $\pi(\cos\theta)$ and $\tau(\cos\theta)$ are defined as follows

$$\begin{aligned}\pi(\cos\theta)&=\frac{P_n^1(\cos\theta)}{\sin\theta},\\ \tau(\cos\theta)&=\frac{dP_n^1(\cos\theta)}{d\theta}.\end{aligned}\tag{3.28}$$

By combining the field components in (3.26), the scattered field becomes

$$\boldsymbol{E}^s=iE_0\frac{e^{-ik_0r}}{k_0r}\left[\hat{\boldsymbol{\theta}}\boldsymbol{S}_2(\theta)\cos\phi-\hat{\boldsymbol{\phi}}\boldsymbol{S}_1(\theta)\sin\phi\right].\tag{3.29}$$

For the forward scattering direction $(\theta=0)$ the scattering amplitudes reduces to

$$\boldsymbol{S}_1(\theta=0)\;=\;\boldsymbol{S}_2(\theta=0)\;=\;\boldsymbol{S}(0)\;=\;\frac{1}{2}\sum_{n=1}^{\infty}(2n+1)(a_n+b_n).\tag{3.30}$$

Using (3.3), (3.29) and (3.30), the scattered field in the forward direction then becomes

$$\boldsymbol{E}^s=E_0\frac{e^{-ik_0r}}{r}\frac{i}{k_0}\hat{\boldsymbol{a}}_x\sum_{n=1}^{\infty}\frac{(2n+1)}{2}(a_n+b_n)=E_0\frac{e^{-ik_0r}}{r}\boldsymbol{f}\left(\hat{\boldsymbol{K}}_2,\hat{\boldsymbol{K}}_2\right).\tag{3.31}$$

Applying the forward scattering theorem in (3.10) yields

$$C_{ext} = \left(\frac{4\pi}{k_0}\right)\mathrm{Im}\left[f\left(\hat{\boldsymbol{K}}_2, \hat{\boldsymbol{K}}_2\right)\cdot\hat{a}_x\right]$$
$$= \frac{2\pi}{k_0^2}\mathrm{Re}\sum_{n=1}^{\infty}(2n+1)(a_n + b_n). \tag{3.32}$$

Figure 3-1 shows the normalised extinction efficiency for raindrops with radii a = 0.25, 0.75, 1.25, 1.75, 2.25, 2.75, 3.25, 3.75 and 4.25 mm (shown form left to right). The normalised efficiencies are calculated using both Mie and Rayleigh theory. The optical limit is also shown for comparison.

As can be seen Rayleigh scattering does not apply beyond about 3 GHz and its application will result in inaccurate results of attenuation. Mie theory does provide a complete solution and has thus been applied in this study for rain attenuation at millimetre-waves.

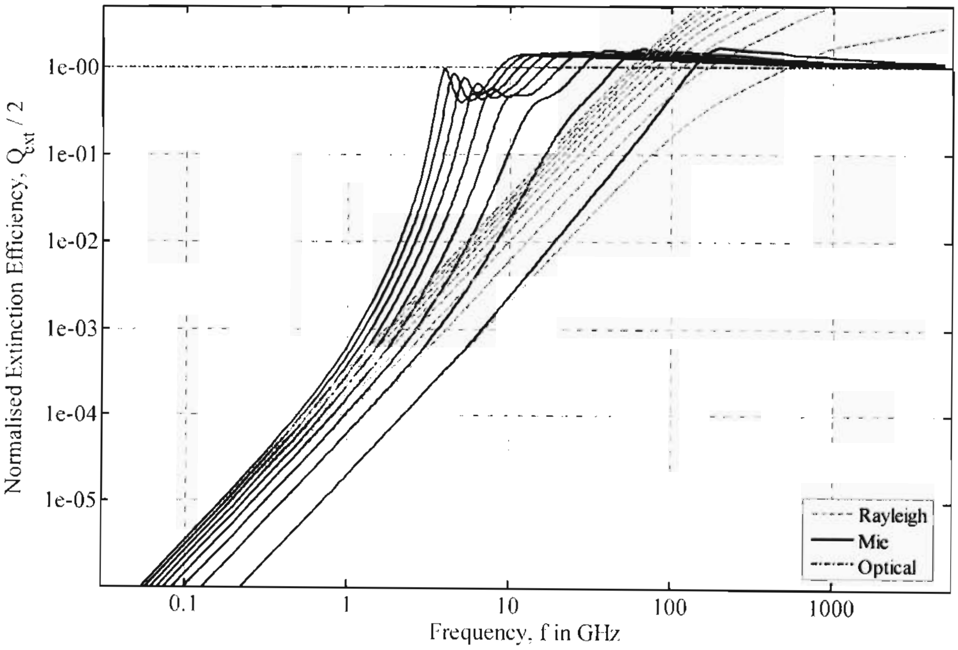

Figure 3-5 : The normalised extinction efficiency Q_{ext} for raindrops with radii a = 0.25, 0.75, 1.25, 1.75, 2.25, 2.75, 3.25, 3.75 and 4.25 mm (shown form left to right).

3.4 Attenuation due to raindrops

Given the assumptions specified in Section 3.2, the amplitude of an electromagnetic wave travelling through a volume, containing N identical raindrops with radius a, at any distance decrease by the amount $e^{-\gamma l}$. The attenuation coefficient $\gamma = NC_{ext}(a)$ and $C_{ext}(a)$ is the extinction cross section for a single raindrop with radius a.

The attenuation of the wave is then given in dB as follows

$$A_{dB} = 10\log_{10}\frac{1}{e^{-\gamma l}} = 4.343\gamma l, \qquad (3.33)$$

and the specific attenuation in dB km^{-1} becomes $A = 4.343 \times 10^{3}\gamma$.

The specific attenuation due to rain is thus the contribution of raindrops of all sizes and is given by

$$A_s = 0.4343\int_0^{\infty} C_{ext}(a)N(a)da, \qquad (3.34)$$

where $C_{ext}(a)$ is the extinction cross section in cm^2 and $N(a)$ is the DSD in m^{-3} mm^{1} for a raindrop of radius a in mm.

Thus the total attenuation is dependent on the extinction cross section C_{ext} and the DSD. C_{ext} acts as the weighting function and determines what range of raindrop sizes will influence the overall attenuation. In Figure 3-6 the extinction cross section of spherical raindrops is shown as a function of raindrop size for frequencies f = 4, 12, 15, 19.5, 40 and 80 GHz.

For frequencies f = 4, 12 and 15 GHz, C_{ext} shows a steady increase for the entire drop size range. As the frequency increases beyond about 20 GHz C_{ext} begins to flatten out for larger radii sizes (a > 2.5 mm) and the dominance of the smaller and medium-size raindrops (a < 2.5 mm) becomes more prominent.

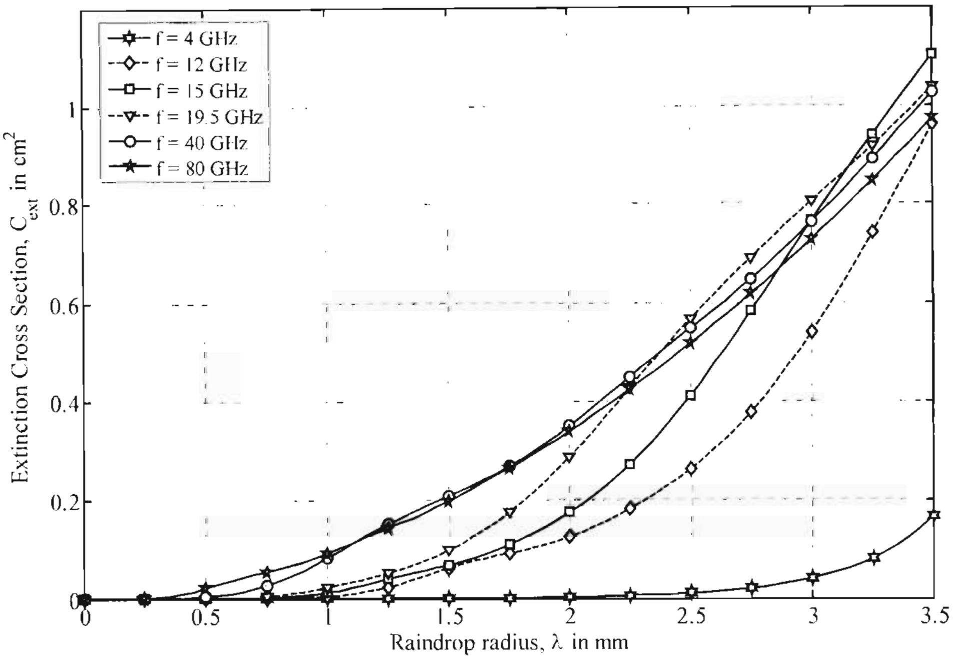

Figure 3-6 : The extinction cross section of spherical raindrops for frequencies f = 4, 12, 15, 19.5, 40 and 80 GHz.

For frequencies, 19.5, 40 and 80 GHz C_{ext} is very close for radii a > 2.5 mm. However for a < 2.5 mm, the difference at these frequencies is immediately noticeable. As the frequency increases, C_{ext} over this range becomes increasingly important and no longer negligible and an accurate DSD for the drop-size range is instrumental in obtaining accurate specific attenuation predictions.

At the lower frequencies f < 4 GHz, C_{ext} is approximately zero for radii a < 2.5 mm. At these lower frequencies, the overestimation of the number of small raindrops in the exponential distributions had little effect. For these frequencies, the specific attenuation is dominated by the number of large raindrops (radii a > 2.5 mm).

Using the extinction cross sections in Figure 3-6, the specific attenuation was evaluated for spherical raindrops using the following theoretical and empirical drop size distributions

- LP – Laws and Parsons (1943),

three exponential DSDs, namely

- MP – Marshall Palmer (1948),
- JD – Joss-Drizzle (Joss et al. 1968), and
- JT – Joss-Thunderstorm(Joss et al. 1968),

two gamma DSD, namely

- de Wolf – de Wolf (2001), and
- AU – (Atlas and Ulbrich 1974, cited Jiang et al. 1997),

four lognormal DSDs (Adimula and Olsen 1996), namely

- CS (continental shower),
- TS (tropical shower),
- CT (continental thunderstorm), and
- TT (tropical thunderstorm),

and the Weibull DSD,

- WB – Sekine et al. (1987).

The effect of the drop size distribution on the computed specific attenuation A_s is shown in Figure 3-7 and Figure 3-8 for frequencies f = 12, 19.5 and 40 GHz.

Figure 3-7 (a) - (c) show the specific attenuation using the MP, JT and JD exponential DSDs. The influence of the MP, LP and de Wolf DSDs on the specific attenuation are shown in Figure 3-7 (d) – (f).

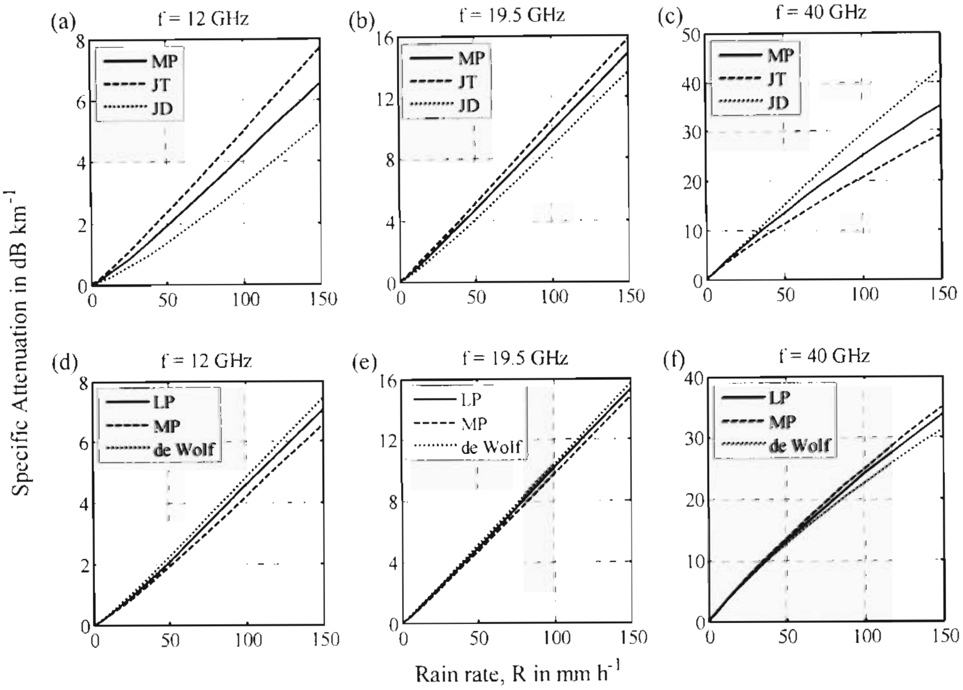

Figure 3-7 : Specific attenuation for frequencies f = 12, 19.5 and 40 GHz, using the MP, JT and JD exponential DSDs, LP DSD and de Wolf gamma DSD.

For 12 GHz, the effect of the larger raindrops dominate, thus as shown Figure 3-7 (a), A_s is greatest for the JT DSD, followed by MP DSD and then JD DSD. This is the case for frequencies below about 12 GHz any inaccuracy in the number of large raindrops in the DSD will significantly influence the calculated specific attenuation. The number of small raindrops (a < 1.0 mm) does not play as significant a role. This is shown in Figure 3-7 (d), where at the lower rain rates (R < 50 mm h^{-1}) there is no major impact. For rain rates R > 50 mm h^{-1}, the de Wolf DSD, and LP DSD to a certain extent, have more medium-sized raindrops (1.0 mm < a < 2.5 mm) and thus the specific attenuation is slightly larger. But the variation is not as pronounced as in Figure 3-7 (a).

At 19.5 GHz, shown in Figure 3-7 (b), the difference between the 3 exponential DSDs is not as pronounced. This is generally the case for frequencies between about 20 GHz and 30 GHz. At this frequency range the specific attenuation is less affected by the DSD.

For 40 GHz, as shown in Figure 3-7 (c), the effect of the smaller raindrops dominate, thus A_s is greatest for the JD DSD. Similarly, the MP DSD has the largest specific attenuation Figure 3-7 (f). This is over-estimation of the smaller raindrops is very important for frequencies greater than 30 GHz.

The MP exponential DSD tends to over-estimate at higher frequencies and under-estimate at lower frequencies. The LP DSD and de Wolf gamma distribution remove this effect and is thus generally more preferable in specific attenuation calculations. The JT and JD DSDs are useful for the analysis of the effect of having an increased number of large raindrops or small raindrops.

Figure 3-8 (a) – (c) show the specific attenuation for the MP and JT exponential DSDs and four lognormal DSDs, namely CS (continental shower), TS (tropical shower), CT (continental thunderstorm) and TT (tropical thunderstorm) lognormal distributions. Figure 3-8 (d) – (f) show the specific attenuation for the AU gamma distribution and the WB Weibull distribution.

The lognormal DSD is particularly useful for tropical and subtropical regions. In such climates there is an increased number of medium and large raindrops while in continental regions, there are typically more small drops and fewer larger drops. Thus two sets of lognormal DSDs are examined, for continental and tropical climates.

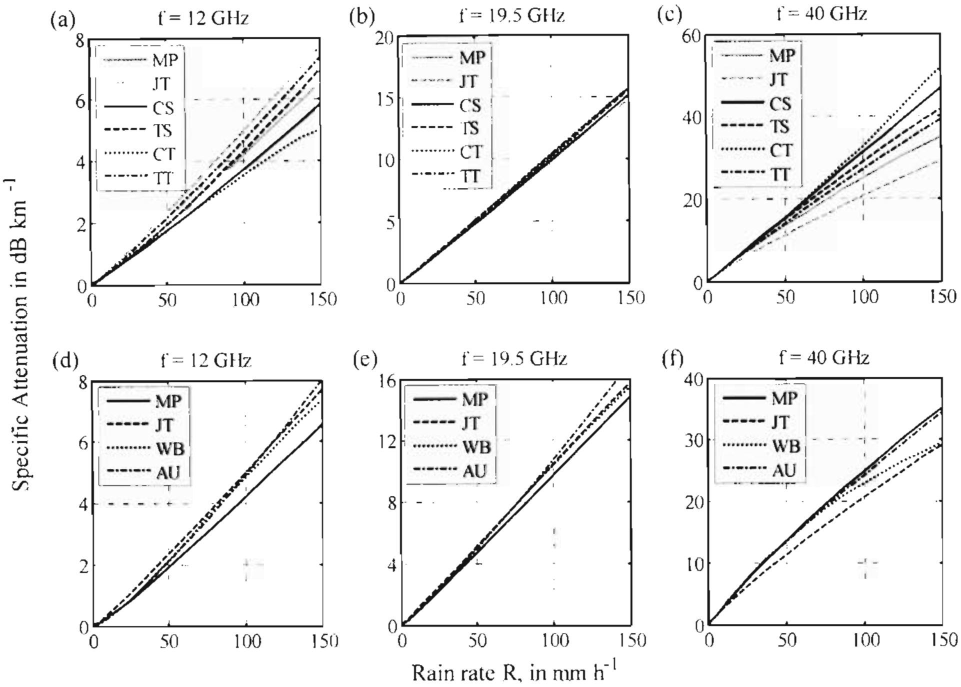

Figure 3-8 : Specific attenuation for frequencies *f* = 12, 19.5 and 40 GHz, using the MP and JT exponential DSDs, CS, TS, CT and TT lognormal distributions, AU gamma distribution and the WB Weibull distribution.

The CS, CT, TS and TT lognormal distributions have overcome the typical problems of exponential DSDs (i.e. they do not over-estimate the number of small and large raindrops and under-estimate in the medium size ranges). The tropical models TS and TT, naturally, have more large raindrops (a > 1.5 mm) and the continental models CS and CT have a greater concentration of the smaller raindrops (a < 1.5 mm).

Thus for 12 GHz and the lower frequencies, A_s is greatest for TT, followed by TS, and then CS and CT, as shown in Figure 3-8 (a). The opposite is true for 40 GHZ and this is shown in Figure 3-8 (c).

For 19.5 GHz, the effect of the decrease in the number of large raindrops is cancelled by the increase in the number of smaller raindrops. Thus the specific attenuation is relatively inert to variations in the DSD. In Figure 3-8 (b), it is shown that the difference in the specific attenuation for the four DSDs is less than 5%.

Gamma and Weibull DSDs are highly favourable for the high-latitude regions and in temperate and continental climates. The results for the de Wolf gamma DSD was shown in Figure 3-7. Another useful gamma DSD was introduced in Atlas and Ulbrich 1974, cited Jiang et al. 1997. Both the AU and WB DSDs exhibit behaviour in between the MP and JT DSDs and thus the results for A_s lie between that of the two exponential DSDs. The AU DSD does have slightly more larger raindrops than the JT DSD and at larger rain rates $R > 75$ mm h^{-1}, the specific attenuations thus slightly larger.

The calculation of the specific attenuation is thus strongly influenced by the drop-size-distribution (DSD). DSDs vary depending on the climate and geographical location and thus the DSD for several climatic regions has been discussed in this section. Variations of up to 50 % in the calculated specific attenuation can result from changing the DSD in calculations, as shown for 12 GHz and 40 GHz. At 19.5 GHz the specific attenuation is more tolerable to variations in the DSD.

3.5 Effect of polarization

In this section of the dissertation, Mie scattering calculations were performed using spherical raindrops. The focus of this research has been devoted primarily to the influence of the drop-size distribution on the specific attenuation, path attenuation and the cumulative distributions of the fade depths and durations.

However, the shape of realistic raindrops becomes increasingly distorted as the drop-size increases. This results in the vertical dimension becomes slightly smaller and the horizontal dimension larger. Consequently, the resulting attenuation will be slightly smaller for vertical polarizations and greater for horizontal polarizations. Matzler (2003) showed that the specific attenuation, although not exactly the same as that calculated using Mie theory for spherical raindrops, requires only a small correction (less than 8

%). Also the shape of the raindrop is more instrumental in evaluating the depolarization and cross-polarization effects as oppose to the attenuation.

Oguchi (1977) performed an analysis of the scattering of Pruppacher and Pitter (1971) raindrops. This drop shape is discussed in Appendix A.4. Oguchi (1973) evaluated the forward scattering amplitudes for both vertical and horizontal polarizations at frequencies f = 11, 13, 19.3 and 34.8 GHz. Using these results, the extinction cross sections can be obtained. A comparison of the results for extinction cross section for the vertical and horizontal polarizations is given in Figure 3-9. In this study, this study spherical raindrops have been assumed, thus the scattering cross section for spherical raindrops is also shown for comparison.

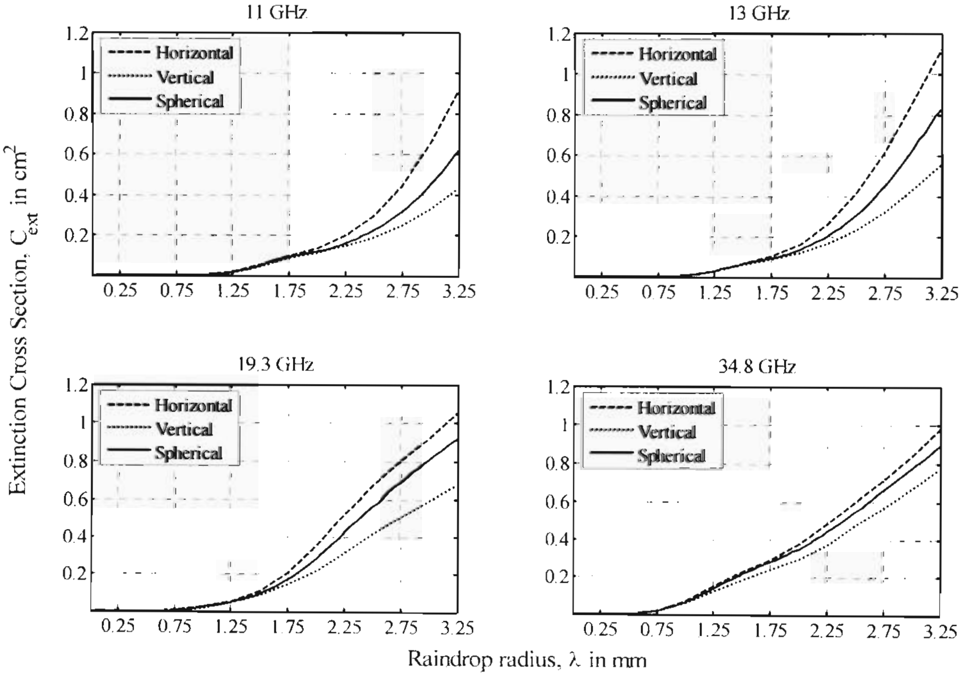

Figure 3-9 : The extinction cross section for horizontal and vertical polarizations using Pruppacher and Pitter raindrops (forward scattering amplitudes obtained from Oguchi 1977) and spherical raindrops (Mie Theory).

As shown in Figure 3-9, the difference between the extinction cross sections obtained using Mie theory for spheres and those for realistic raindrop are negligible for medium-sized and small raindrops (i.e. $a < 2.25$ mm). For the larger raindrops, the difference is quite noticeable. In specific attenuation calculations, the number of larger raindrops (i.e. $a > 2.25$ mm) is usually small compared to the other drop-sizes, especially in the gamma, lognormal and Weibull DSDs. Thus variations in the calculated specific attenuation arising from drops shape are not as pronounced as those observed for changes in the DSD. Matzler (2003) showed that the specific attenuation requires only a small correction (less than 8 %), with vertical polarizations having a slightly smaller attenuation and horizontal polarizations a slightly larger attenuation. The deviation is more marked for vertical polarization and horizontal polarizations have almost the same specific attenuation as that for spherical raindrops. This can be seen from the results for 19.3 and 34.8 GHz in Figure 3-9. Also for the higher frequencies, the difference in the scattering cross section for vertical and horizontal polarizations becomes smaller as indicated for 34.8 GHz in Figure 3-9. Nevertheless to improve results, the shape of raindrops should be included, especially for vertical polarizations. Hence future work should entail the evaluation of the extinction cross sections for realistically-shaped raindrops and include the effect of drop shape in this model.

3.6 Conclusion

In this chapter the specific attenuation for rain at several selected frequencies and rain rates was evaluated. The specific attenuation is dependent upon the microphysical properties of rain, such as drop shape, DSD and drop orientation, and the properties of the incident electromagnetic wave, such as frequency and polarization.

The attenuation and scattering of electromagnetic waves by raindrops is evaluated by applying the scattering theory for a single, lossy dielectric sphere. The basic definitions and formula and scattering geometry is given in Section 3.2.

For millimetre-wave frequency range the drop-size is comparable to wavelength hence Mie scattering theory is applicable and discussed in Section 3.3. Evaluation begins with the computation of the extinction and scattering cross sections of a single raindrop. Thereafter the chosen DSD and statistics relating to the location of these drops within the volume can be used to extend the extinction and scattering cross sections to that for the entire volume. In this study it is assumed that the raindrops are distributed throughout the volume in accordance with the Poisson process and the specific attenuation was hence computed.

The accuracy of the calculated specific attenuation is heavily dependent on the chosen DSD as shown in Section 3.4. In most calculations the Laws and Parsons DSDs is typically assumed. In this study several DSD shapes have been evaluated from the conventional exponential distributions to the gamma, lognormal and Weibull distributions. The more sophisticated DSDs overcome the shortfalls of the exponential distributions which tend to over-estimate the number of small and large raindrops.

In section 3.5 the difference between the extinction cross section evaluated for spherical raindrops and for the more realistic Prupacher and Pitter (1971) is shown. Vertical polarizations will have a slightly smaller specific attenuation and horizontal polarizations a slightly larger specific attenuation than that calculated using Mie theory for spheres. Hence future work should entail the evaluation of the extinction cross sections for realistically-shaped raindrops and include the effect of drop shape in this model.

Once the specific attenuation has been evaluated for necessary frequency and rain-rate range, path averaging is performed to predict the rain attenuation over the communication link. In the next chapter path attenuation models and the cumulative time statistics of surface-point rain rates are discussed.

Chapter 4

Rain-Rate statistics

4.1 Introduction

Knowledge of the surface-point rain rate is a prerequisite for a variety of engineering applications. Today, rain rates are recorded throughout the world and in many of these cases over long periods of time. However, most long-term rainfall records are available only at relatively large durations (integration times) typically 1 hour and more or as extreme rainfall depths over these periods. These rainfall statistics may satisfy the traditional requirements for agriculture and hydrology but for the evaluation of rain attenuation, rain-rate distributions for much shorter durations are needed.

Measurements of rain rates for 5-minute integration time are becoming more frequent but even this duration may prove inadequate to model the substantial temporal and spatial variability of rain. For example, assuming the average fall velocity of a raindrop is 8 ms^{-1}, a 5-minute surface-point rain rate will correspond to the spatial averaging of approximately 2.4 km of vertically varying rain rates.

Fortunately, truly instantaneous rain rates are not necessary since rapid fluctuations in the rain rate will not necessarily translate into equivalent fluctuations in attenuation due to the spatial averaging over the propagation path. For the evaluation of rain attenuation 1-minute rain rates have hence been found to be the most desirable, to remove variations due to rain gauge limitations, such as small sampling area and contamination due to atmospheric turbulences (Crane 1996). Subsequently the International Telecommunications Union (ITU) has adopted 1-minute rates as the standard for the evaluation of rain attenuation. However, 1-minute rain rates are not readily available throughout the world. Even when available, records need to span several years (typically 10 years or more) before "stable" annual statistics can be obtained.

To overcome the unavailability of 1-minute rainfall data, several investigators (e.g. Rice and Holmberg 1973; Dutton and Dougherty 1979, 1984; Tattelman and Scharr 1983; Tattelman et al. 1994) have devised models to estimate the 1-minute rain-rate distributions from the available climatologically data.

Rice and Holmberg (1973) examined rainfall data in USA and proposed a model for the 1-minute rain-rate cumulative time distribution requiring only two input parameters, the mean annual precipitation M and the thunderstorm ratio β. The Rice-Holmberg model (R-H) is based upon two rainfall types, "Mode 1" for thunderstorm (convective) rain and "Mode 2" for uniform (stratiform) rain. The total rainfall per year is thus the sum of the total rain for each mode. i.e. $M = M_1 + M_2$ and hence the thunderstorm ratio may be defined as $\beta = M_1/M$. Although M is readily available throughout South Africa, β is more difficult to obtain. Rice and Holmberg (1973) provided global maps for β but the resolution over South Africa is inadequate to account for the variability in the South African climate.

Dutton and Dougherty (1973, 1979, 1984) extended the R-H model to facilitate error analysis and account for year-to-year variability. The Dutton-Dougherty model (D-D) also requires M and β as inputs. A method for calculating β, based on the monthly rainfall maxima for 30 consecutive years was also presented and the regional maps for Europe and USA were refined. However for South Africa, the difficulty in obtaining β

with sufficient resolution still remains making both the D-D and R-H model undesirable.

Tattelman and Scharr (1983) presented a monthly model for 1-minute rain rates. The input parameters include the precipitation index I, the monthly mean temperature $\overline{T}$ and a latitude-temperature term $f\left(L,T\right)$. The precipitation index is defined as the ratio of the mean monthly precipitation and the number of rainy days per month. The definition of a rainy day depends on the countries adopted threshold, most commonly 0.1 inch, 1 inch or 1 mm. Tattelman and Scharr (1983) provided the coefficients for each of these thresholds and for exceedance levels ranging from 0.01% to 2% of the month. Monthly models are practical because in many locations the occurrences of heavy rainfall are limited to only a few months of the year. During these months the annual predictions are often exceeded. The Tattelman-Scharr model however does have drawbacks and is generally invalid for very dry and cold climates. Since a large proportion of South Africa is arid, this model as also not desirable. Also exceedance levels below 0.01% are also necessary.

Lin (1975, 1978) applied extreme-value statistical theory to the annual maxima rain rates and showed that together with the mean annual precipitation M, the rain-rate distribution for all rain rates can be approximated by a lognormal distribution. Lin (1978) successfully obtained a 5-minute rain-rate distribution for USA and proceeded to predict the rain attenuation for both terrestrial and satellite communication links (Lin 1977; Lin 1979).

Seeber (1985) adapted this technique for South Africa using the depth-duration-frequency curve developed by Midgley and Pitman (1978). The only input parameters needed are M and the climate designation, defined as either "inland" or "coastal". Although this technique has a course climatic designation, its simplicity makes it desirable for use in South Africa. Furthermore, available rainfall data may be easily integrated into the model to yield more accurate results. Consequently, Lin's extreme-value model has been chosen for this study. Although this model does not provide 1-minute rain-rate distributions, it does take us one step closer because several techniques have been derived to convert the cumulative rain-rate distributions of an available integration time to that for the required 1-minute durations (e.g. Ajayi and Ofoche 1984, Segal 1986, Moupfouma 1995).

In the subsequent sections 5-minute rain-rates will be obtained using Lin (1976, 1978), Seeber (1985) and Midgley and Pitman (1978). Ajayi and Ofoche (1983) provided an empirical relationship for converting 5-minute rain-rate distributions to 1-minute distribution from the measurements in Ife-Ife, Nigeria. Their results are also comparable to that of Flavin (1981), who used rain data from several climatic regions. The Ajayi and Ofoche (1983) relation may accordingly be applied to South Africa to estimate the 1-minute distributions. An alternative approach suggested in Moupfouma et al. (1995) is also examined at these locations.

Although it is always preferable to use local rainfall statistics to obtain rain-rate distributions, reliable long term rainfall data is not always available. In such cases generalised estimates are required. Several global rain-rate models have been developed (Crane 1980, ITU-R P.837) based on the geographically location and climate. These global models provide empirical relations and their coefficients for each of the various climatic regions. Unfortunately, climate-based models are more suited for application over wide areas and often cannot adequately represent the small-scale spatial variations that occur within each rain climate. Thus if possible the global climate-based models should be used as a starting point and together with available rain data a more accurate rain-rate distribution can then be obtained.

In this chapter the term "τ − minute rain rate" is commonly used and refers to the average value of the rain rate over a τ − minute interval. This may be calculated by

$$R^{\tau-\min} = H^{\tau-\min} \cdot \frac{60}{\tau} = \frac{H^{\tau-\min}}{D}, \qquad (4.1)$$

where $H^{\tau-\min}$ is the accumulated rainfall depth over the $\tau-$minute interval and τ is the rain-gauge integration time in minutes. Alternatively, the integration time can be given in hours by D. Hence a 1-minute rate, $(\tau = 1$ and $D \simeq 0.01667)$ as defined in (4.1), is the average rain rate over a 1-minute interval.

4.1.1 Outline of chapter

In Section 4.2 global rain-rate climate models are discussed. These models are based upon the climatic classification of the region, thus a description of the various climatic zones in South Africa is also useful and is provided in the Appendix. Crane's global rain-rate climate model and the ITU-R P.837 global rain-rate model are discussed and simulated.

Section 4.3 involves a discussion of extreme value theory and the procedure for obtaining 5-minute rain-rate distributions for any location in South Africa, using the depth-duration-frequency curve. More accurate 5-minute distributions can be provided by using actual rainfall data from annual maxima series when available. Consequently 5-minute distributions are obtained for 8 locations in South Africa. Thereafter these distributions are converted to 1-minute rain-rate distributions using the Ajayi and Ofoche (1983) relation. The results are compared to the global rain-rate climate models.

In Section 4.4 and Section 4.5, the models of Moupfouma (1987) and Moupfouma and Martin (1995) are discussed and simulated for South Africa. The Moupfouma and Martin (1995) models for temperate regions and tropical/subtropical regions are particularly useful for the 0.001 % and lower probabilities. A comparison of all the models with 1-minute rain-rate measurements in Durban is given in Section 4.6.

This estimate of the surface-point 1-minute rain-rate is only the first step. Rain exhibits significant spatial and temporal variation. Hence the rain-rate profile along the propagation path is also required. In Section 4.7, the Crane (1980) attenuation model and the ITU recommendation (ITU-R P530-9) are discussed and the chapter is concluded in Section 4.8.

4.2 Global rain-rate climate models

It is always preferable to use local rainfall statistics to obtain rain-rate distributions. Unfortunately reliable long term rainfall data is not always available. In such cases generalised estimates are required. Several global rain-rate models have been developed for 1-minute rain-rate durations (Crane 1980, ITU-R P.837) based on the geographic location, altitude, topography and other climatic factors.

For each of these models, the empirical relations and their coefficients are available for the various climatic regions. Unfortunately, climate-based models are more suited for application over wide areas and often cannot adequately represent the small-scale spatial variations that often occur within each rain climate. Thus if possible the global climate-based models should be used as a starting point and together with available rain data a more accurate rain-rate distribution can then be obtained.

The earth's climate can be classified into six distinct classes or biomes. Each class is distinguished by the mean monthly temperature T, mean annual precipitation M and the vegetation in the region. The Köppen climate classification system is the most widely used for determining the climatic designation. Accordingly a description of the Köppen system is provided in the Appendix. Using this system South Africa can be divided into 12 different climatic zones (Seeber 1985) as described in the Appendix C.

4.2.1 Crane's global rain-rate climate model

Using the Köppen system as a basis, Crane (1980) divided the world into 8 major rainfall climates designated **A – H**. Region **A** and **B** correspond to the driest regions (polar) and **G** and **H** are for the wettest climates (tropical). Sub-tropical regions are designated by **E** and **F** and temperate location by **C** and **D**. Region **D** was further sub-divided into **D_1**, **D_2** and **D_3**, where **D_1** is the driest and **D_3** the wettest. Region **B** has also been divided into two subdivisions. Figure 4-1 shows the various climatic regions and boundaries.

From Figure 4-1, South Africa is divided in 5 climatic regions **F** (Karoo and Northern Cape), **C** (southern coastal region and Eastern Cape), **D_1** (Free State and North West), **D_2** (KwaZulu-Natal, Gauteng and Mpumalanga) and **D_3** (Northern Province).

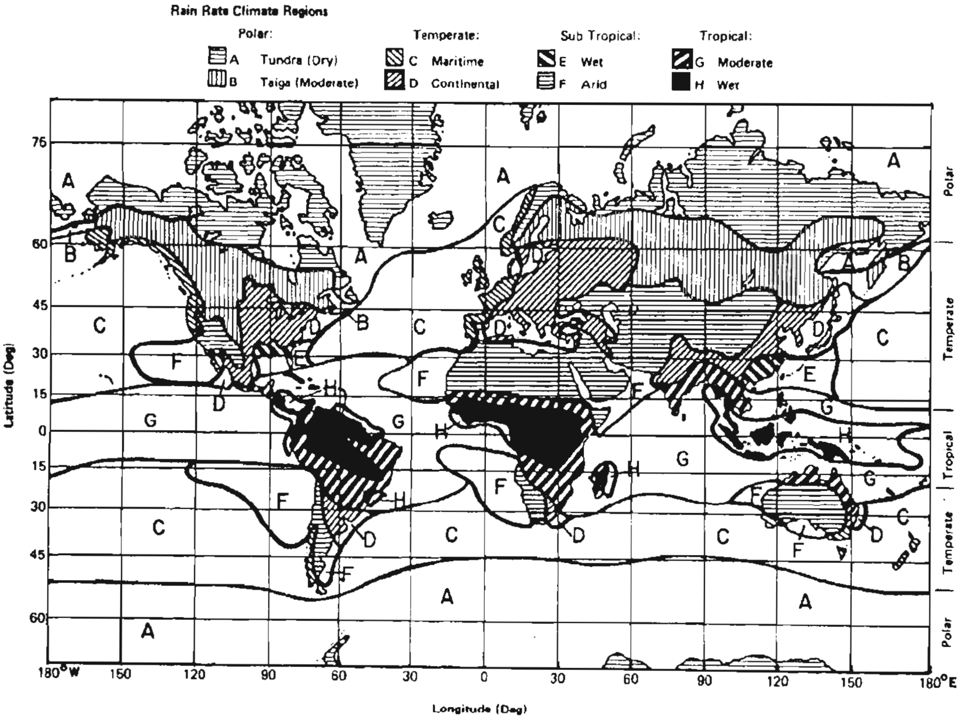

Figure 4-1 : Climate region boundaries from Crane (1980, Figure 3).

The rain-rate distributions for each of these regions are given in Table 4-1. These values correspond to the rain-rate intensity that is exceeded for P% of the year. The distribution functions are plotted in Figure 4-2

Table 4-1 : Rain-rate distributions for the global rain-rate climate model from Crane (1996, Table 3.1)

Percent of year	**Rain Climate Regions**										
	A	**B_1**	**B_2**	**C**	**D_1**	**D_2**	**D_3**	**E**	**F**	**G**	**H**
0.001	0.0	0.1	0.2	0.3	0.2	0.3	0.0	0.2	0.1	1.8	1.1
0.002	0.0	0.2	0.4	0.6	0.6	0.9	0.8	1.8	0.1	3.4	3.3
0.003	0.1	0.4	0.7	1.1	1.2	1.5	2.0	3.3	0.2	5.0	5.8
0.005	0.2	0.8	1.4	1.8	2.2	3	4.6	7.0	0.6	8.4	12.4
0.01	0.5	1.5	2.4	2.9	3.8	5.3	8.2	12.6	1.4	13.2	22.6
0.02	1.1	2.2	3.4	4.1	5.3	7.6	11.8	18.4	2.2	17.7	33.1
0.03	1.5	2.9	4.4	5.2	6.8	9.9	15.2	24.1	3.1	22.0	43.5
0.05	2.5	4.5	6.8	7.7	10.3	15.1	22.4	36.2	5.3	31.3	66.5
0.1	4.0	6.8	10.3	11.5	15.3	22.2	31.6	50.4	8.5	43.8	97.2
0.2	5.5	9.0	13.9	15.6	20.3	28.6	39.9	62.4	11.8	55.8	125.9
0.3	6.9	11.3	17.6	19.9	25.4	34.7	47.0	72.2	15.0	66.8	152.4
0.5	9.9	16.1	25.8	29.5	36.2	46.8	61.6	91.5	22.2	90.2	209.3
1	13.8	22.3	35.7	41.4	49.2	62.1	78.7	112	31.9	118	283.4
2	17.5	27.8	43.8	50.6	60.4	75.6	93.5	130	41.4	140.8	350.3
3	20.9	32.7	50.9	58.9	69.0	88.3	106.6	145.4	50.4	159.6	413.9
5	28.1	42.6	63.8	71.6	86.6	114.1	133.2	176.0	70.7	197.0	542.6

4.2.2 ITU-R P.837 global rain-rate model

Another useful global rain-rate model has been provided by the ITU (ITU-R P. 837) The ITU has split the earth into 14 climatic zones, **A** (light rains) to **Q** (heavy rains). The climate boundaries for Africa are depicted in Figure 4-3.

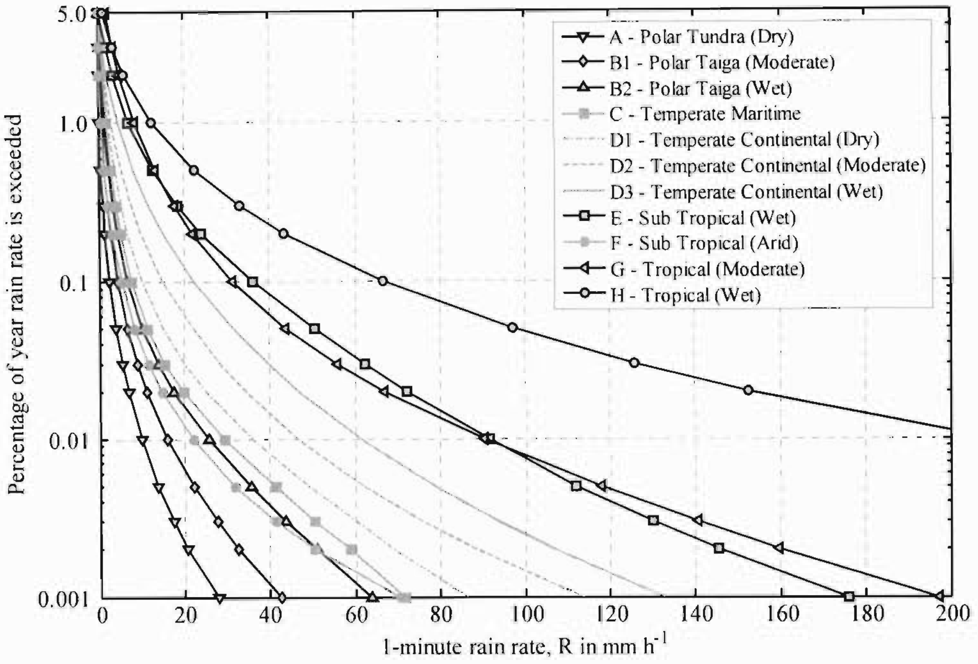

Figure 4-2 : Rain-rate distributions for Crane's global rain-rate climate model.

As shown, the South African rain-rate is described by 4 zones, **C**, **D**, **E** and **K**. The rain-rate distributions for the regions applicable to Africa are given in Table 4-2 for exceedance probabilities ranging from 0.001% to 5% of the year.

Table 4-2 : : Rain-rate distributions for the ITU rain-rate model from ITU-R P.837.1 (Table 1)

Percent of year	**Rain Climate Regions**									
	A	**C**	**D**	**E**	**J**	**K**	**M**	**N**	**P**	**Q**
1	0.1	0.7	2.1	0.6	8	1.5	4	5	12	24
0.3	0.8	2.8	4.5	2.4	13	4.2	11	15	34	49
0.1	2	5	8	6	20	12	22	35	65	72
0.03	5	9	13	12	28	23	40	65	105	96
0.01	8	15	19	22	35	42	63	95	145	115
0.003	14	26	29	41	45	70	95	140	200	142
0.001	22	42	42	70	55	100	120	180	250	170

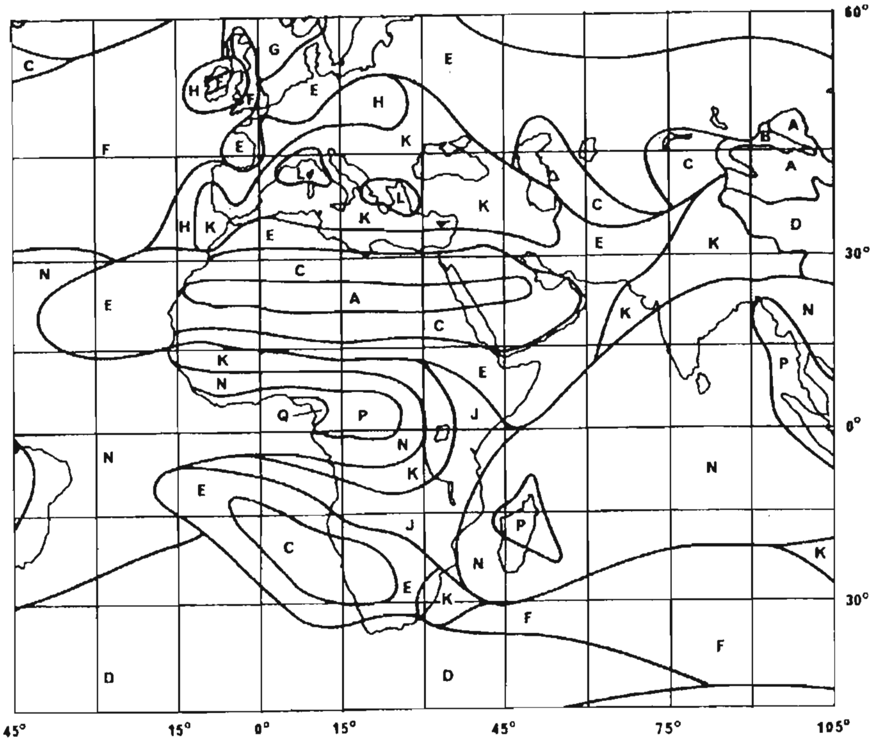

Figure 4-3 : Climate region boundaries for Africa from ITU-R P.873 (Figure 3).

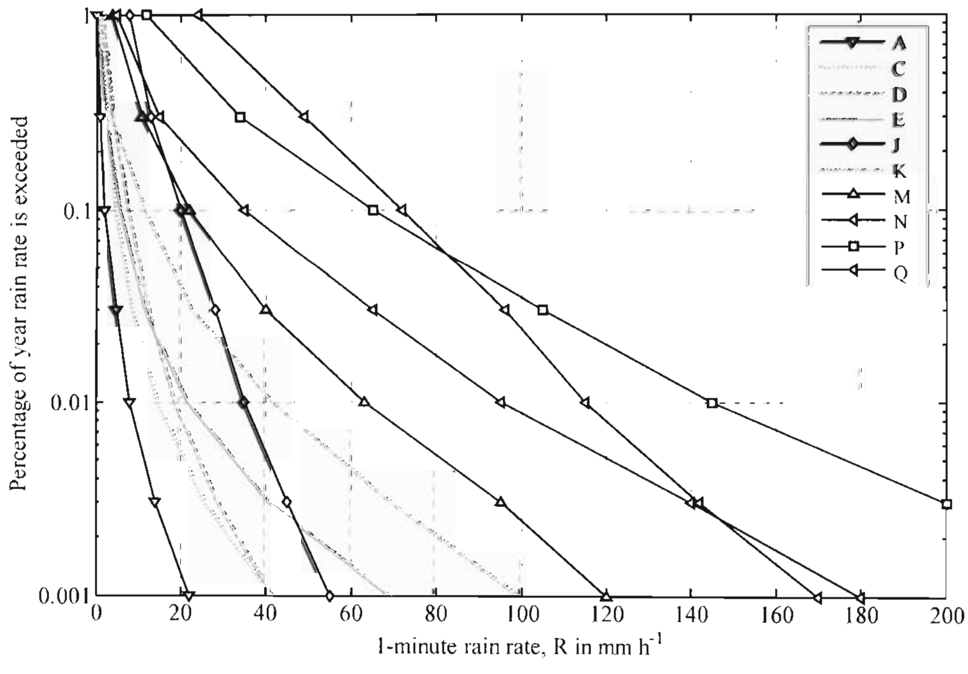

Figure 4-4 : Rain-rate distributions for the ITU rain-rate climate model.

Although the above-mentioned climate-based models are easy to use, they are often not detailed enough to account for variations within each climatic zone. This is more so the case in South Africa since it comprises of 12 varying climatic zones according to the Köppen system. Furthermore, the ITU boundaries for the South African climate are different from those in Crane's global model. The difference between the climatic designations in these models is illustrated in Figure 4-5. According to the ITU boundaries, the South African climate is noticeably dryer than predicted by the Crane boundaries. With this disparity it is difficult to choose an appropriate estimate for South Africa.

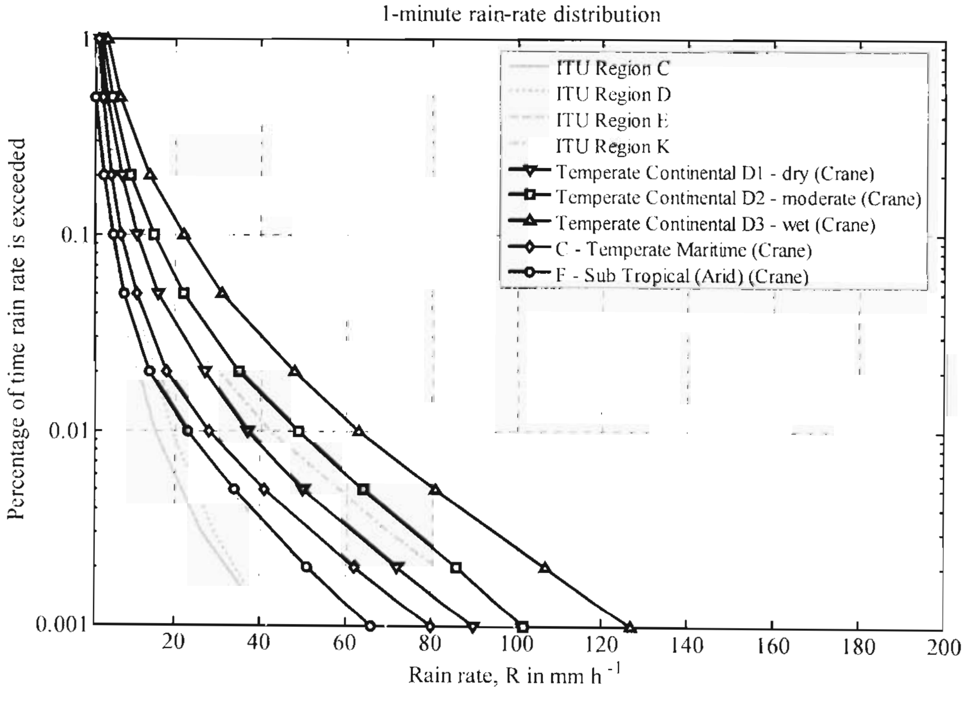

Figure 4-5 : Comparison of the ITU climate zones and Crane's climatic zones for South Africa.

Fortunately, the original ITU model has been updated periodically as new data becomes available. The latest recommendation is ITU-R P.837-4 is more accurate and provides global maps of the 0.01% exceedance probabilities. Bilinear interpolation of the contours in the global map is used to predict the rain-rate distribution at any location given the latitude and longitude coordinates. The ITU has also released a program to perform these calculations and it has been used in the next section for comparison purposes. However, since the interpolation is still based on the climatic designation, the problem of climatic resolution is still not resolved. Locations that exhibit a combination of two or more climates will not be estimated accurately. Thus whenever possible, one should take advantage of the available rainfall records that are reliable and comprehensive to augment these global maps. In the next section the technique of using the extreme-value rainfall records is discussed.

4.3 Rain-rate distributions from extreme-value statistics

Traditionally, the South African Weather Bureau (SAWB) performed rainfall measurements for only relatively larger durations (typically 1 hour or more). Rainfall measurements for 15 minutes were rare and available only at selected locations. Today the measurements of rain rates are far more extensive and available for durations down to 5 minutes. However, long term statistics, such as the annual extreme-values, are still not readily available for these smaller durations.

The most extensive report of the annual extremes was presented for several locations in WB36 (Department of Transport 1974). This publication contains the annual maxima for 15-, 30-, 45-, 60 and 1440-minute durations. Using these annual maxima series, Midgley and Pitman (1978) developed a depth-duration-frequency (DDF) diagram for South Africa. The DDF relationships are particularly useful for agriculture and flood estimation, where they are used to predict rainfall exceedance probabilities. To further improve accuracy, Smithers and Schulze (2002) applied the theory of L-moments to the South Africa rainfall data. From their studies accurate estimates of rainfall depths and durations along with the associated exceedance probabilities are now available for durations as little as 5 minutes.

Lin (1976) showed that the theory of extreme-value statistics can be applied to a series of annual maximum rain rates for a specified location to obtain the rain-rate distribution for higher rain rates ($R > 50$ mm h^{-1}) at that location. The extreme value method was extended to all rain rates in Lin (1978) by also considering the mean average rainfall (MAR) at the location. Using this extreme-value method, Lin successfully obtained the rain-rate distribution for 5-minute durations in USA. The 5-minute rain-rates were then used for the prediction of the rain attenuation for both terrestrial and satellite communications (Lin 1977; Lin 1979).

Seeber (1985) examined the feasibility of Lin's extreme value theory to the data available in WB36 (Department of Transport 1974) and it was shown to be applicable for the evaluation of 5-minute rain rate in South Africa. Together, with the depth-duration-frequency curves in Midgley and Pitman (1978), 5-minute rain-rate distributions for any location in South Africa can be obtained by providing the mean annual rainfall M and the climatic classification. Unfortunately this technique cannot be extended to obtain 1-minute rainfall, until more rain data becomes available. However, the SAWB has expressed their intention to update their publication of annual extremes and include the 5-minute annual extremes within the next few years. With this new data it may be possible to make adjustments to the short-duration rain relationships and further extend the model to 1-minute integrations as well.

For now the 5-minute rain-rate distributions will be estimated using the technique of Lin (1976, 1978) and Seeber (1985). The 8 stations with the longest records (± 40 years) provided in WB36 (Department of Transport 1974), will be examined. These stations include Cape Town (D.F. Malan), East London, Durban (Louis Botha), Bloemfontein, Kimberly, Johannesberg (Jan Smuts), Pretoria and Pietersberg.

Using the annual maxima series for each of these locations along with the predictions from Smithers and Schulzer (2002), using their GPS locations, the 5-minute annual extremes will be estimated. Thereafter 5-minute rain-rate distributions are obtained and converted to 1-minute distributions using the relationship in Ajayi and Ofoche (1983) and as suggested in Moupfouma et al. (1995).

4.3.1 Extreme-value theory

Extreme value theory plays an important role in many engineering applications. In the context of this study, namely the attenuation due to rain, the communications engineer is primarily interested in the occurrence of extreme events of rainfall, rather than their mean values. Basically if, at the required location, the probability that a particular rain rate is exceeded is known then the corresponding attenuation probabilities for that location can also be determined.

Gumbel (1958) made a significant impact in the area of extreme value theory and initiated several advances in this field. The Gumbel and log-Gumbel distributions have been found to be particularly useful for extreme value analysis of rainfall (e.g. Lin 1976; Midgley and Pitman 1978). Lin (1976) showed that moderate to low rain rates can be closely approximated by the lognormal distribution. However instability did occur at extreme values of rain rates. Lin (1976) proceeded to show that assuming a lognormal distribution of parent rain rate, the extreme rain rates can be accurately modelled using the log-Gumbel distribution.

4.3.2 The Gumbel and Log-Gumbel Distributions

Let X be an arbitrary random variable and X_1 will represent the largest value in a given year. The values of annual maxima X_1 vary randomly from year to year. The cumulative probability distribution of X_1, denoted by $F_{X_1}(x)$, can be approximated using the statistics of extremes as follows

$$F_{X_1}(x) = P(X_1 \geq x) = 1 - e^{-e^{-y}}, \tag{4.2}$$

where y is called the reduced variate given by

$$y = \alpha(x - U). \tag{4.3}$$

$P(X_1 \geq x)$ is the probability (expressed as a fraction of years) that the variate x is exceeded by X_1. The frequency of this occurrence (or return period) is denoted by $Q(x)$ (expressed in years) and is given by

$$Q(x) = Q(X_1 \geq x) = \frac{1}{F_{X_1}(x)} = \frac{1}{1 - e^{-e^{-y}}}. \tag{4.4}$$

The random variable X can denote the $n-$minute rain rate $R^{n\text{-min}}$ or the $n-$minute rainfall depth $H^{n\text{-min}}$. The distribution given in (4.2) is then a type 1 extreme distribution and is often called the Gumbel distribution.

If X denotes the logarithmic form of $R^{n\text{-min}}$ or $H^{n\text{-min}}$, i.e. $\ln\left(R^{n\text{-min}}\right)$ or $\ln\left(H^{n\text{-min}}\right)$, then (4.2) is a type 2 extreme distribution commonly referred to as the log-Gumbel distribution. The reduced variate x is then also lognormal defined and (4.3) becomes

$$y = \alpha\left[\ln(x) - U\right]. \tag{4.5}$$

Both $F_{X_1}(x)$ and $Q(x)$ are completely determined by the scale and location parameters denoted in (4.3) and (4.5) by α and U, respectively. These parameters are related to the mean and standard deviation of X_1.

Consider the series of measured annual maxima $X_1(j)$, where $j = 1, 2, 3, \cdots, M$ denotes the year. Hence $X_1(3)$ is the maximum value of X measured in the third year of the M observed years.

The mean and standard deviation of $X_1(j)$ are given by

$$\overline{X}_1 = \frac{1}{M}\sum_{j=1}^{M} X_1(j) \text{ and } \sigma_X = \sqrt{\overline{X_1^2} - \overline{X}_1^{\,2}}, \tag{4.6}$$

respectively, where

$$\overline{X_1^2} = \frac{1}{M}\sum_{j=1}^{M}\left[X_1(j)\right]^2. \tag{4.7}$$

Using (4.6) and (4.7) the mean and standard deviation of $Z(j)$ can be similarly obtained, where $Z(j)$ is given by

$$Z(j) = -\ln\left[-\ln\left(\frac{j}{M+1}\right)\right]. \tag{4.8}$$

The scale parameter α and location parameter U are then given by

$$\alpha = \frac{\sigma_Z}{\sigma_X} \text{ and } U = \overline{X}_1 - \frac{\overline{Z}}{\alpha} \tag{4.9}$$

The asymptotic values for α and U (when $M \to \infty$) can be obtained by using the method of moments as follows

$$\alpha_{MOM} = \frac{\pi}{\sqrt{6}\cdot\sigma_X} \text{ and } U_{MOM} = \overline{X}_1 - \frac{\gamma}{\alpha}, \tag{4.10}$$

where $\gamma = 0.57721$ is Euler's constant.

4.3.3 Depth-duration-frequency diagram for South Africa

WB36 (Department of Transport 1974) contains the annual maximum rainfall depths H_1 for 15-, 30-, 45-, 60- and 1440-minute durations. Using $(4.2)-(4.10)$ Midgley and Pitman (1978) fitted Gumbel and log-Gumbel distributions to the stations with longest recorded data (± 40 years). For the Gumbel distribution $X_1 = H_1$ and $x = h$ while for the log-Gumbel distribution $X_1 = \ln(H_1)$ and $x = \ln(h)$. A chi-square goodness of fit test revealed the overall acceptability of the log-Gumbel distribution for the South African data. Log-Gumbel distributions for the annual maximum rainfall depths H_1 are given as follows

$$F_{X_1}(h) = P(H_1 \geq h) = 1 - e^{-e^{-y'}} = \frac{1}{Q(h)}, \tag{4.11}$$

where

$$y' = \alpha'\left[\ln(h) - U'\right]. \tag{4.12}$$

Analysis of the log-Gumbel means reveal that μ increases with the mean annual precipitation, M and a clear distinction was noted between the "coastal" and "inland" stations especially at lower integration times. Midgley and Pitman (1978) attributed this to the higher incidence of convective thunderstorm activity in the interior regions. This resulted in high intensity rainfall depths over small durations. However since such thunderstorm activity generally does not last for long durations the rainfall depth over the large integration times (1440-minute) is not much different than that observed during a prolonged maritime stratiform rain. Thus for the 1440-minute duration there was no clear distinction between the log-Gumbel means for "coastal" and "inland" stations. Midgley and Pitman (1978) fitted the following relations between the log-Gumbel means μ and M, the mean annual precipitation in mm as given in Table 4-3.

Analysis of the log-Gumbel standard deviations σ showed no trend as observed for the log-Gumbel means. There was no increase with integration time or in M. Furthermore, the standard deviations showed no distinction between the two climatic regions. Midgley and Pitman (1978) thus chose a constant value for the standard deviation equal to the average of the standard deviations observed for the stations with longest recorded data (± 40 years) given by $\sigma_{\text{all}} = 0.359$. The asymptotic scale and location parameters are given by (4.10) as follows

$$\begin{aligned} \alpha' &= \frac{\pi}{\sqrt{6}\cdot 0.359} = 3.5726, \text{ and} \\ U' &= \mu - \frac{\gamma}{\alpha'} = \mu - \frac{0.57721}{3.5726} = \mu - 0.16157. \end{aligned} \tag{4.13}$$

Table 4-3 : The log-Gumbel mean for 15-, 60- and 1440-min for "coastal" and "inland" regions.

Integration time	**Log-Gumbel mean, μ**	
	"Coastal" region	**"Inland" region**
15-minute	$\mu^{15\text{min}}_{\text{coastal}} = 0.0742 \cdot M^{0.5} + 0.4902$	$\mu^{15\text{min}}_{\text{inland}} = 0.0570 \cdot M^{0.5} + 1.3995$
60-minute	$\mu^{60\text{min}}_{\text{coastal}} = 0.0786 \cdot M^{0.5} + 1.0647$	$\mu^{60\text{min}}_{\text{inland}} = 0.0598 \cdot M^{0.5} + 1.9020$
1440-minute	$\mu^{1440\text{min}}_{\text{both}} = 0.0640 \cdot M^{0.5} + 2.3559$	

The scale parameter α' is thus invariant with integration time. Using the rainfall measurements taken in Europe, Watson (1981, cited in Seeber 1985) also found the scale parameter to be invariant, though for a specific location. This supports the hypothesis that the constant value for the scale parameter as given in (4.13) can also be applied for the evaluation of 5-minute distributions.

The location parameter U' is dependent on the integration time. U' can be determined at any location using the appropriate value for μ as given in Table 4-3. However this is applicable only for 15-, 60-, and 1440-minute integration time. For other integration times, a method of interpolating and extrapolating is required. This can be achieved by the following relation as shown in Midgley and Pitman (1978)

$$R = \frac{R_0}{(1+BD)^n}, \tag{4.14}$$

where R is the average rain rate in mm h^{-1} for the duration D in hours. The rain rate R is related to the rainfall depth H as given in (4.1). The parameters B, R_0, and n are constants dependent on the mean annual precipitation, the return period and the climatic classification.

Using (4.1), (4.14) can be modified to yield the following equivalent relation for rainfall depth

$$H = \frac{R_0 D}{(1+BD)^n}. \tag{4.15}$$

The relation (4.14) has also been established empirically outside of South Africa by Watson (1981, cited in Seeber 1985) for the annual maxima in the United Kingdom.

The rainfall depth h can then be solved for any return period by making the variate y' in (4.11) the subject of the formula and substituting in (4.12) as shown below

$$h = \exp\left(-\frac{1}{\alpha'} \cdot \ln\left\{\ln\left[\frac{Q(h)}{Q(h)-1}\right]\right\} + U'\right). \tag{4.16}$$

For a 20-year return period, $Q(h)$ = 20 years and using (4.13) and (4.16), the rainfall depth h becomes,

$$h_{20-\text{year}} = \exp\left(\frac{2.9702}{3.5726} + \mu - 0.16157\right). \tag{4.17}$$

The log-Gumbel mean μ can be obtained for 15-, 60- and 1440 minute intervals using the values in Table 4-3. The rainfall depths for these three durations can be used along with the relation (4.1) and (4.15) to solve simultaneously for B, R_0, and n for the given M, return period and the climatic classification. Using the above technique, these parameters were obtained for a 20 year return period and $M = 500$ mm. The values are given in Table 4-4.

Table 4-4 : The parameters B, R_0 and n for $Q(y)$ = 20 years and MAR =500 for "coastal" and "inland" regions.

Integration time	**"Coastal" region**	**"Inland" region**
B	4.779	4.164
R_0	122.8	217.8
n	0.7372	0.8832

Using the Table 4-4, Midgley and Pitman (1978) presented a depth-duration-frequency diagram (DDF) for Southern Africa. The DDF diagram contained 3 quadrants and provided the probability (or return period) of exceeding a particular rainfall depth for various durations (or integration times) ranging from 6 minutes to 100 hours. Following their example, the DDF diagram was constructed and shown in Figure 4-6.

Quadrant A contains the relationship between the integration time D and the annual maximum rainfall depth $h_a = h_{20-year}$ exceeded for a return period of 20 years and a MAR of 500 mm.

Quadrant B relates rainfall depth h_a to that for any $b-$year return period. Using (4.16) the return period for $b-$years is given as follows

$$h_b = \exp\left(-\frac{1}{\alpha'}\cdot\ln\left\{\ln\left[\frac{Q(h_b)}{Q(h_b)-1}\right]\right\}+U'\right). \tag{4.18}$$

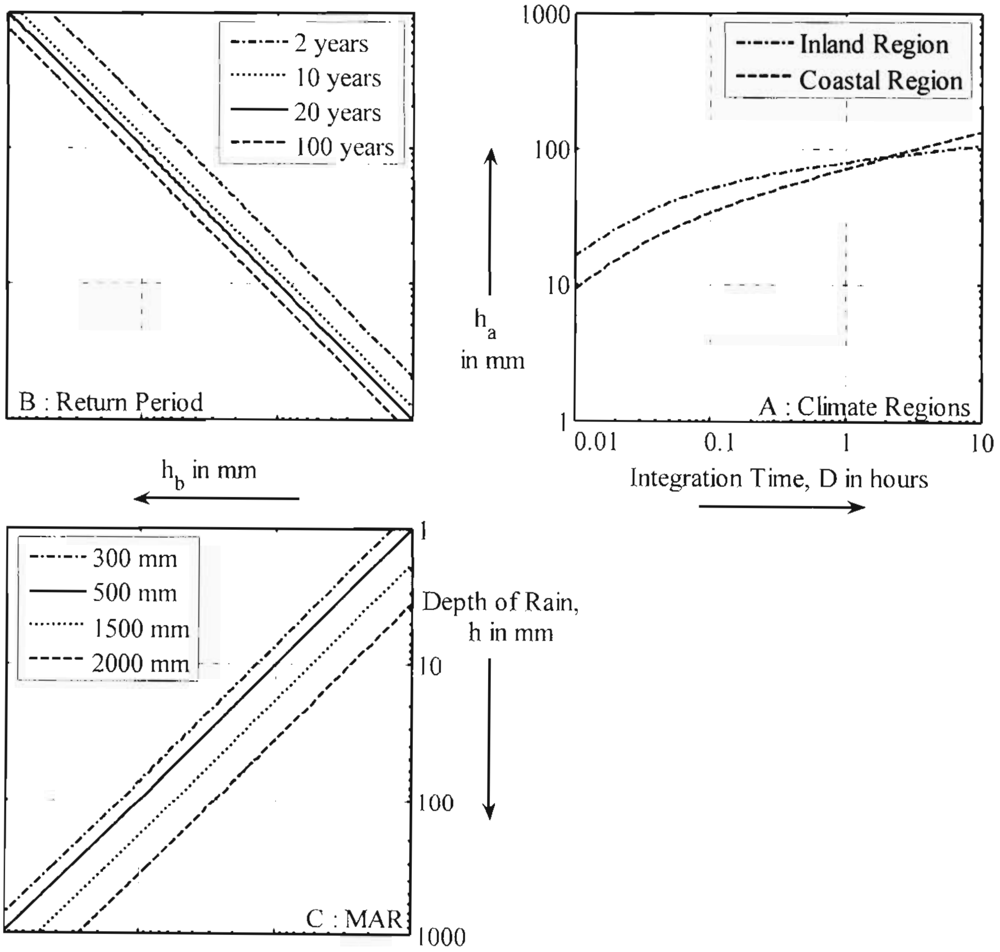

Figure 4-6 : The depth-duration-frequency diagram for point rainfall in South Africa (Midgley and Pitman 1978).

The ratio between h_a and h_b is given by

$$\frac{h_b}{h_a} = \frac{\exp\left(\frac{y_b}{\alpha'}+U'\right)}{\exp\left(\frac{2.9702}{\alpha'}+U'\right)} = \exp\left(\frac{y_b-2.9702}{3.5726}\right) \tag{4.19}$$

Quadrant C transforms rainfall depth h_b for mean annual precipitation M = 500 mm to any other value for M by the ratio

$$h = h_b F = h_a F \cdot \exp\left(\frac{y_b-2.9702}{3.5726}\right). \tag{4.20}$$

F is empirically related to M the mean annual precipitation in mm as follows

$$F = 0.25 + 1.61\times 10^{-3} M . \tag{4.21}$$

The DDF in Figure 4-6 thus only requires two input parameters, the mean annual precipitation M ranging from 50 mm to 2000 mm and climatic classification, i.e. two regions "inland" and "coastal". The "inland" region is characterised by convective thunderstorm rain while in the "coastal" region widespread frontal (maritime stratiform) rain predominates. As a rule of thumb the "coastal" region may be considered as any region within 100 km from the coastline and "inland" regions are areas more than 100 km away. Although this definition is fairly coarse it can be applied without much difficulty for the South African region.

For many locations long term rain data may not be readily available. Since several techniques do exist to obtain the mean annual precipitation for these regions the DDF can still be applied to such locations. The simple designation of climatic regions may be at the expense of accuracy especially for regions where the behaviour is a combination of these two climates. Nevertheless, the ease at which this model can be applied warrants its usage. Furthermore if a greater degree of accuracy is required the generalised mean and standard deviations given in Table 4-3, can be replaced with those obtained from long term measurements.

4.3.4 5-minute rain-rate distributions

Seeber (1985) used the above mentioned analytical relationships (4.11)−(4.21) to obtain 5-minute rainfall depths and obtained 5-minute rain-rate distributions for South Africa. The relationship between the rain rate, R and the rainfall depth, H in (4.1) may be applied to the annual maxima rainfall depth, H_1 and variate rainfall depth, h, thus

$$R_1 = \frac{H_1}{D} \text{ and } r = \frac{h}{D}. \tag{4.22}$$

Thus log-Gumbel distributions for the annual maximum rainfall R_1 are given as follows

$$F_X(r) = P(R_1 \geq r) = 1 - e^{-e^{-y}} = \frac{1}{Q(r)} \tag{4.23}$$

where

$$y = \alpha\left[\ln(r) - U\right] \tag{4.24}$$

It follows that

$$P(R_1 \geq r) = P\left(\frac{H_1}{D} \geq \frac{h}{D}\right) = P(H_1 \geq h), \tag{4.25}$$

hence

$$P(R_1 \geq r) = P(H_1 \geq h), \text{ and } 1 - e^{-e^{-y}} = 1 - e^{-e^{-y'}}, \tag{4.26}$$

which implies $y = y'$.

Substituting (4.22) in (4.24) yields

$$y = \alpha\left[\ln\left(\frac{h}{D}\right) - U\right] = \alpha\left[\ln(h) - \{U + \ln(D)\}\right] = \alpha'\left[\ln(h) - U'\right]. \quad (4.27)$$

Consequently

$$\begin{aligned} \alpha &= \alpha' = 3.5726, \text{ and} \\ U &= U' + \ln(D). \end{aligned} \quad (4.28)$$

Using (4.22), (4.20) becomes

$$r = \frac{h_a}{D} F \cdot \exp\left(\frac{y_b - 2.9702}{3.5726}\right), \quad (4.29)$$

and substituting in (4.27) gives

$$y = \alpha\left[\ln(r) - U\right] = 3.5736 \cdot \left(\ln\left[\frac{h_a F}{D} \cdot \exp\left(\frac{y_b - 2.9702}{3.5726}\right)\right] - U\right). \quad (4.30)$$

Solving for U yields

$$U = \ln\left(\frac{h_a F}{D}\right) + \left(\frac{y_b - y - 2.9702}{3.5726}\right). \quad (4.31)$$

Since h and h_b are related via a constant in (4.20), their returns periods are thus equal which implies $y_b = y$. Subsequently (4.31) simplifies to

$$U = \ln\left(\frac{h_a F}{D}\right) - \left(\frac{2.9702}{3.5726}\right). \tag{4.32}$$

Substituting (4.15) in (4.32) gives

$$U = \ln\left(\frac{R_0 \cdot F}{(1+BD)^n}\right) - (0.8314), \tag{4.33}$$

where B, R_0, and n are given for the "inland" and "coastal" climate regions as given in Table 4-4. Thus using (4.21), (4.28), (4.33) and Table 4-4, generalised values for the extreme-value parameters α and U can be obtained for any location in South Africa if the mean annual precipitation and the climatic designation are given. However if long term measurements are available these parameters can be obtained directly from the actual mean and standard deviations calculated using $(4.6)-(4.9)$ and then solving for B, R_0, and n simultaneously via (4.15). The scale parameter is invariant with integration time and thus the average value from the measurements can be used for α and U can be extrapolated for $5-$minute durations using (4.33).

Lin (1978) showed that the rain-rate distribution for all rain rates can be approximated by the following lognormal distribution

$$P(R \geq r) \approx \frac{1}{2} P_0 \cdot \operatorname{erfc}\left[\frac{\ln r - \ln R_m}{\sqrt{2} \cdot S_R}\right] \tag{4.34}$$

where, S_R is the standard deviation of $\ln(R)$ during the rain event, R_m is the median value of R during the rain event and P_0 is the probability that it will rain. R is the rain rate and $\operatorname{erfc}(\sim)$ and $\ln(\sim)$ are the complementary error function and natural logarithm respectively. The parameters S_R, R_m and P_0 can be solved simultaneously if α, U (for the relevant integration time) and M are known. The transcendental equations are given as follows

$$S_R = \frac{P_0 \cdot N}{\alpha} \cdot \phi\left[\Phi^{-1}\left(1 - \frac{1}{P_0 \cdot N}\right)\right], \tag{4.35}$$

$$R_m = \exp\left[U - S_R \cdot \Phi^{-1}\left(1 - \frac{1}{P_0 \cdot N}\right)\right], \text{ and} \tag{4.36}$$

$$M = 8760 \cdot e^{\frac{S_R^2}{2}} \cdot R_m \cdot P_0, \tag{4.37}$$

where $\phi(\sim)$ denotes the normal probability density function and $\Phi^{-1}(\sim)$ is the inverse of the standard unit normal probability density function. $N = 8760/D$ is the number of rain-gauge integration time intervals per year and D is the integration time in hours.

4.3.5 Obtaining 1-minute rain-rate distributions

When the SAWB releases the updated version of the annual extremes a generalised model can be attempted. For now the annual maxima provided in WB36 (Department of Transport 1974) has been used and the 8 stations with the longest records (± 40 years) have been considered to illustrate the technique. For each integration time, the mean and standard deviation have been calculated and used to obtain the Log-Gumbel parameters.

Table 4-6 contains the asymptotic values, calculated using (4.10), and henceforth denoted by α_{MOM} and U_{MOM}, as well as those obtained from the annual maxima series, calculated using (4.9), and henceforth denoted by α_S and U_S, for 15-, 60- and 1440-minute integration time.

Table 4-5 : The mean and standard deviations for eight locations provided in WB36 (Department of Transport 1974)

Location		**Integration Time**					
		15- minute		**60-minute**		**1440-minute**	
		Series	**Moment**	**Series**	**Moment**	**Series**	**Moment**
Cape Town (D.F Malan)	α	3.8212	4.3030	3.3316	3.7516	4.3815	4.9339
	U	2.0863	2.0943	2.6326	2.6418	3.4463	3.4532
East London	α	2.3418	2.6487	2.3504	2.6584	2.3441	2.6513
	U	2.5159	2.5294	3.2467	3.2600	4.2411	4.2545
Durban (Louis Botha)	α	2.7723	3.1218	2.6020	2.9300	2.7538	3.1010
	U	2.7713	2.7822	3.5103	3.5220	4.2401	4.2511
Bloemfontein	α	3.0830	3.4716	3.1900	3.5922	3.5384	3.9845
	U	2.5684	2.5783	3.2136	3.2231	3.7082	3.7168
Kimberly	α	3.1132	3.5057	2.5587	2.8813	4.0700	4.5831
	U	2.5169	2.5267	3.0580	3.0699	3.7085	3.7160
Johannesburg (Jan Smuts)	α	3.3806	3.8068	2.7809	3.1316	3.1060	3.4976
	U	2.6884	2.6974	3.2612	3.2721	3.8825	3.8923
Pretoria	α	4.0263	4.5339	3.5886	4.0411	3.8394	4.3235
	U	2.7197	2.7273	3.3344	3.3429	3.9826	3.9905
Pietersberg	α	2.9690	3.3433	2.9996	3.3778	2.6545	2.9891
	U	2.6565	2.6667	3.2110	3.2212	3.6069	3.6184

In Seeber (1985), a constant scale parameter $\alpha = 3.5726$ was used. This was adopted to reduce complexity and provide an estimate for regions with insufficient or no rainfall records. Since the stations considered in this study have records for ± 40 years, to improve accuracy the scale parameter should be calculated for each station rather than using the constant scale parameter. As discussed, for any location, the scale parameter is invariant with integration time. Thus for 5-minute durations, the scale parameter was assumed to be the mean value of the other durations, i.e. $\alpha^{5\text{-min}} = \text{mean}\left(\alpha^{r\text{-min}}\right)$.

The location parameter can then be calculated by modifying (4.33) as follows

$$U^{5\text{-min}} = \ln\left(\frac{R_0}{(1+BD)^n}\right) - \left(\frac{2.9702}{\alpha^{5\text{-min}}}\right). \tag{4.38}$$

The parameters B, R_0, and n as defined in (4.15) were calculated for each location for a return period of 20-years, using the values in Table 4-3. The parameters S_R, R_m and P_0 can hence obtained using (4.35) - (4.37). In the above-mentioned procedure either the series values or the asymptotic values given in Table 4-3 can be used. Table 4-6 contains the values for α, U, W, S_R, R_m and P_0 calculated for 5-minute integration time using α_{MOM} and U_{MOM}.

Table 4-6 : Log-Gumbel and lognormal parameters for 5-minute integration time

Location	α	U	S_R	R_m	P_0
Cape Town	3.644	3.725	0.998	1.424	0.026
East London	2.336	4.184	1.891	0.023	0.717
Durban	3.016	4.574	1.247	1.218	0.043
Bloemfontein	3.653	4.414	0.898	5.587	0.007
Kimberly	3.423	4.117	0.980	3.009	0.009
Johannesburg	3.383	4.403	1.041	2.763	0.017
Pretoria	4.317	4.413	0.771	7.883	0.008
Pietersberg	3.346	4.258	1.014	2.988	0.011

From the values in Table 4-6 the 5-minute cumulative rain-rate distributions can be obtained using (4.34) for each location. Ajayi and Ofoche (1983) provided an empirical relationship for converting 5-minute rain-rate distributions to 1-minute distribution. The relationship is as follows

$$R^{1\text{-min}} = 0.991 \cdot \left(R^{5\text{-min}}\right)^{1.098}, \tag{4.39}$$

where $R^{1\text{-min}}$ is the 1-minute rain rate and $R^{5-\text{min}}$ is the equiprobable 5-minute rain rate. The rain rates are expressed in mm h^{-1}

Although this result is based on measurements in Ife-Ife, Nigeria, the relation is also comparable to that of Flavin (1981), who used rain data from several climatic regions from Australia, Europe, USA and Canada. The Flavin (1981) relation is given as follows

$$R^{1\text{-min}} = 0.990 \cdot \left(R^{6-\text{min}}\right)^{1.054}, \qquad (4.40)$$

where $R^{1\text{-min}}$ is the 1-minute rain rate and $R^{6-\text{min}}$ is the equiprobable 6-minute rain rate and the rain rates are expressed in mm h^{-1}

The Ajayi and Ofoche (1983) relation may accordingly be applied to South Africa to estimate the 1-minute distributions. Once reliable long-term 1-minute rain data is available this relationship should be further examined to improve accuracy. For now it will suffice based upon agreement in both temperate and tropical climates.

Using the relation in (4.39), the 5-minute cumulative rain-rate distributions were converted to 1-minute distributions for each location. The distributions are shown in Figure 4-7.

As expected Cape Town (sub-tropical arid) and East London (temperate maritime), followed by Kimberly (dry continental) have the lowest exceedence probabilities for a given rain rate. The inland locations, i.e. Pietersberg, Johannesburg, Pretoria and Bloemfontein fall under a continental climate (moderate and wet) thus a high degree of convectivity can be expected at the 5 minute and lower durations, as reflected by the higher exceedance probabilities for a given rain rate. Durban has the wettest climate from all the stations, with an annual rainfall around 1000 mm.

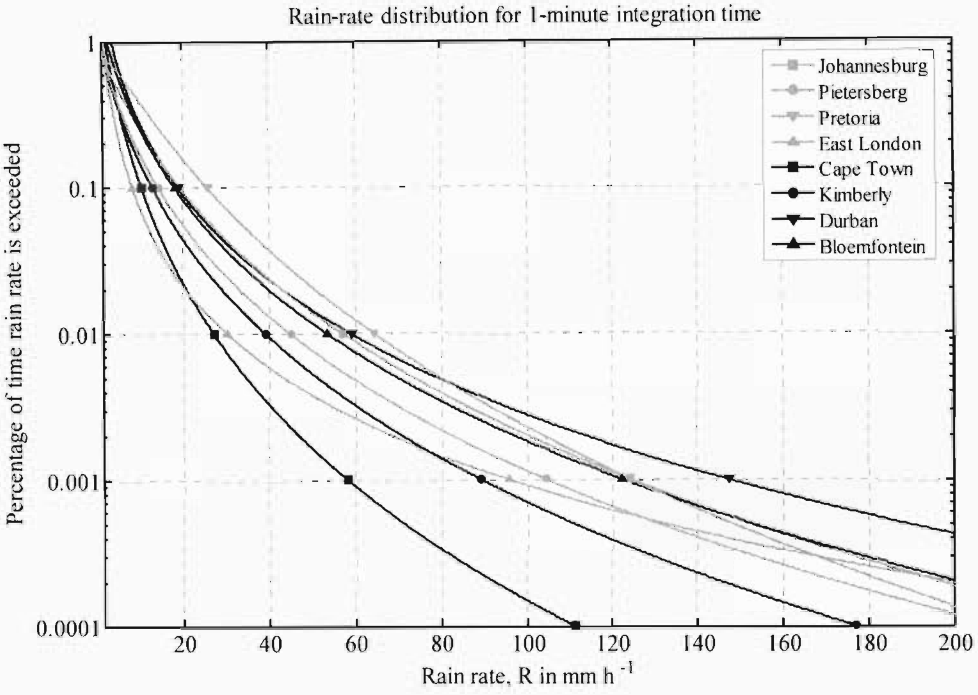

Figure 4-7 : 1-minute cumulative rain-rate distributions for 8 locations in South Africa from annual maxima series.

In the model, suggested by Seeber (1985), only 2 climatic regions are defined. As discussed generalised values for the extreme-value parameters α and U can be obtained for any location in South Africa from mean annual precipitation and the climatic designation, by using (4.21), (4.28), (4.33) and Table 4-3. Using this method, the 1-minute cumulative rain-rate distributions can also be obtained. However, because of the course climatic description (only 2 climate types) accuracy will reduced especially for location displaying a combination of a "coastal" and "inland" climate. The 1-minute cumulative rain-rate distributions using the above-mentioned procedure are shown in Figure 4-8.

As it can be seen in Figure 4-8 the rain-rate distribution for Durban is under-estimated. This is expected because although Durban is on the coast, the rainfall for this region does exhibit strong convectivity and hence it is classified as part of the wettest sub-region of the temperate continental climates. Furthermore, the model is inadequate to provide better resolution for areas with similar mean annual precipitation in the same climate ("inland" or "coastal"). This is illustrated by the similarity between the distributions for Pietersberg and Pretoria. Based upon the annual maxima, Pretoria should have a higher exceedance probabilities for a given rain rate as shown in the proposed model.

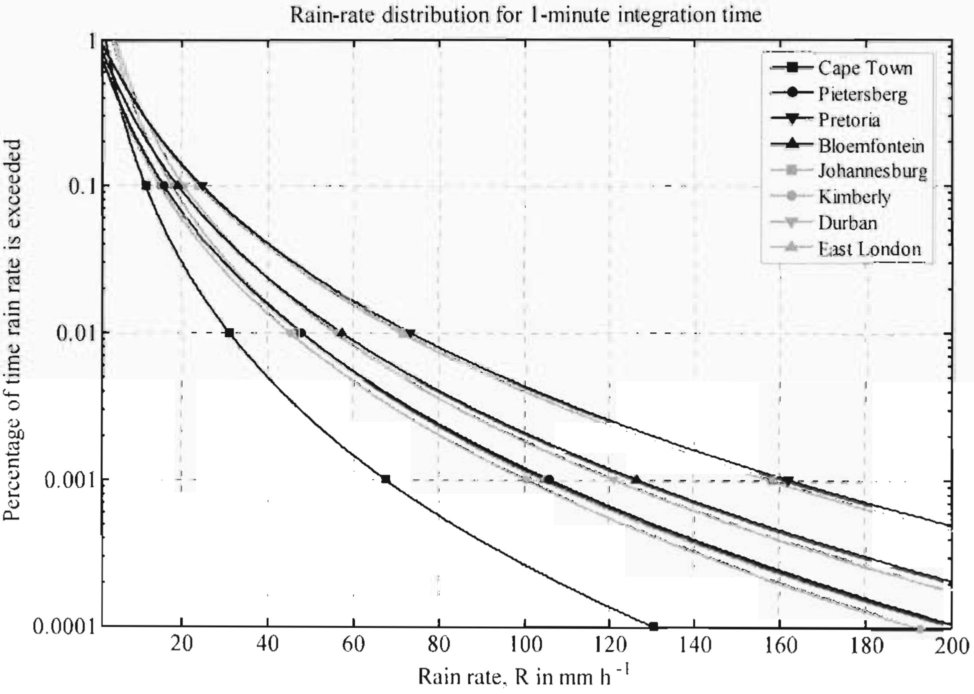

Figure 4-8 : 1-minute cumulative rain-rate distributions for 8 locations in South Africa using Seeber (1985).

The latest ITU recommendation, ITU-R P.837-4 does provide a more accurate prediction for the Durban and Pretoria climates. Using the software program released by the ITU, the 1-minute cumulative rain-rate distributions can be obtained for each location and are shown in Figure 4-9.

Although the ITU global model does better account for the increased convectivity in certain locations the lack of resolution is still evident and some locations have nearly the same exceedance probabilities (e.g. Johannesburg and Pretoria) although the annual maxima series might indicate otherwise.

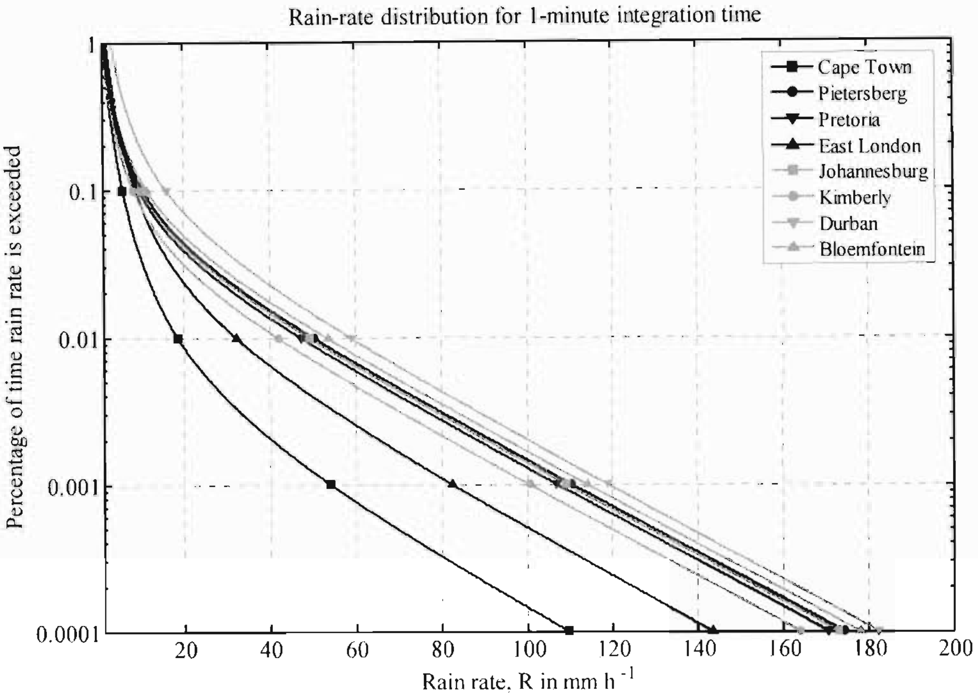

Figure 4-9 : 1-minute cumulative rain-rate distributions for 8 locations in South Africa using ITU-R P.837-4.

The 1-minute rain-rate distribution for each location has been shown along with the ITU prediction for the location in Figure 4-10 to Figure 4-17. The predicted 1-minute distribution is shown as a solid dark line and the ITU prediction is displayed as the dark dotted line. In addition Crane's climatic zones for South Africa have also been included for comparison. These include **F** (Karoo and Northern Cape), **C** (southern coastal region and Eastern Cape), **D_1** (Free State and North West), **D_2** (KwaZulu-Natal, Gauteng and Mpumalanga) and **D_3** (Northern Province).

As indicated in Figure 4-10, the proposed model predicts a greater exceedance probability for Cape Town than the ITU model as opposed to East London in Figure 4-11, where there is a much closer agreement with the ITU model.

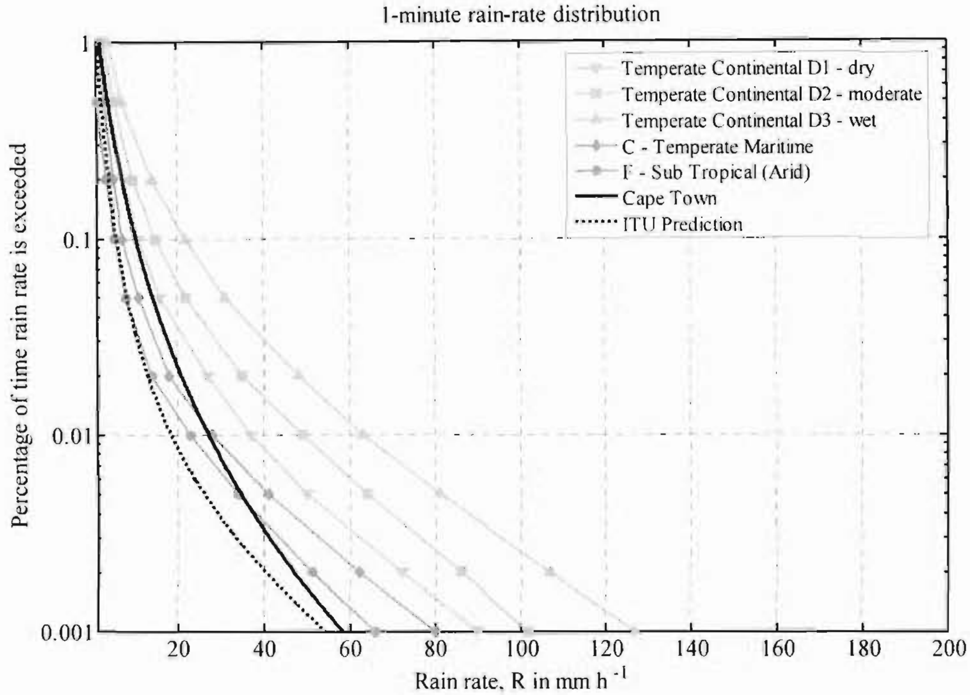

Figure 4-10 : 1-minute cumulative rain-rate distributions for Cape Town.

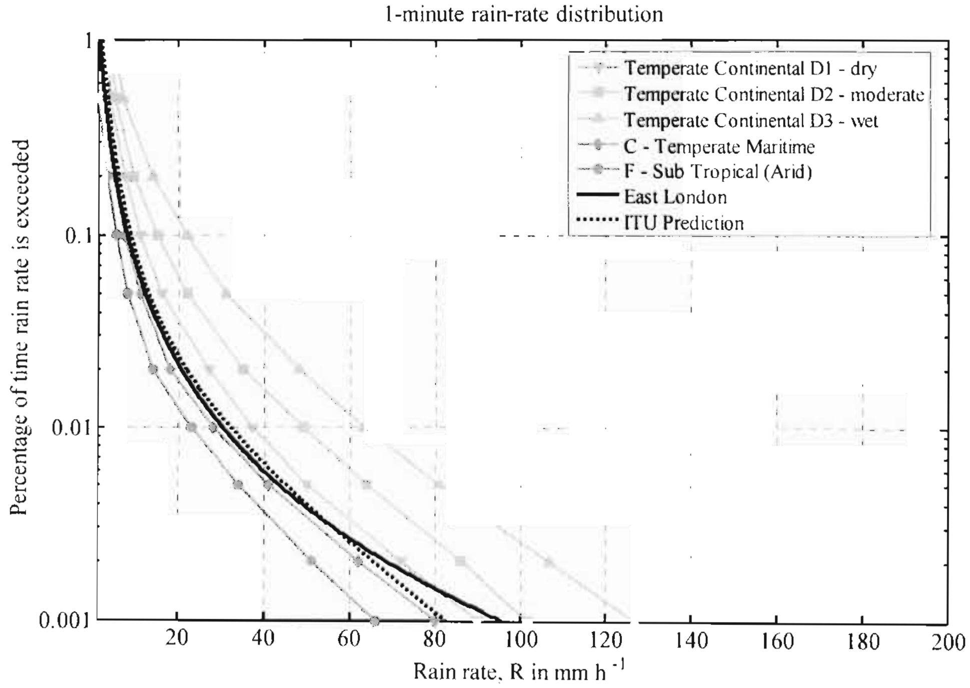

Figure 4-11 : 1-minute cumulative rain-rate distributions for East London.

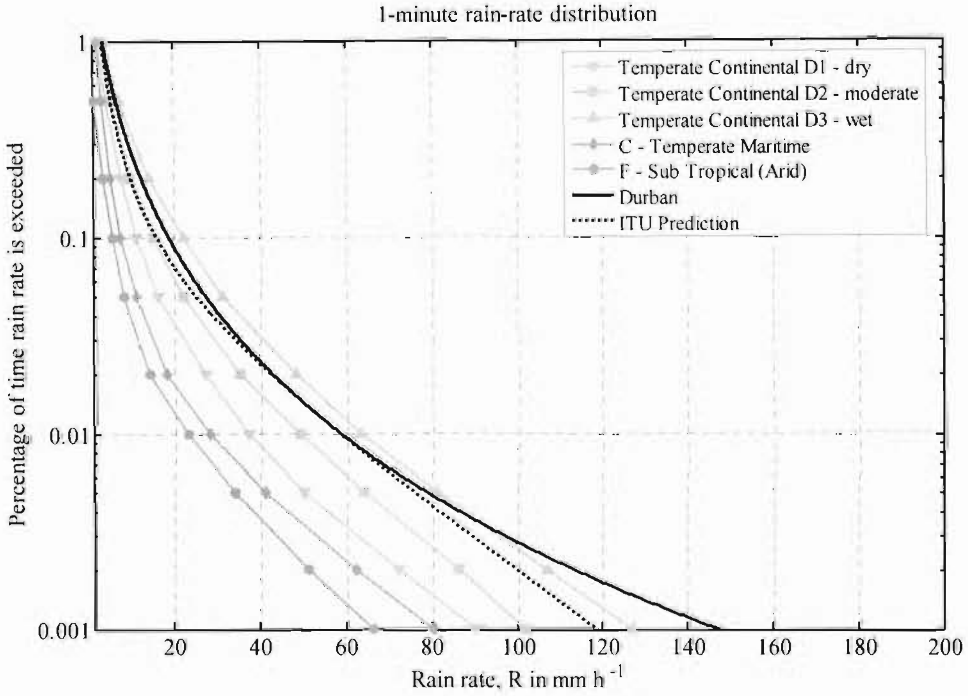

Figure 4-12 : 1-minute cumulative rain-rate distributions for Durban.

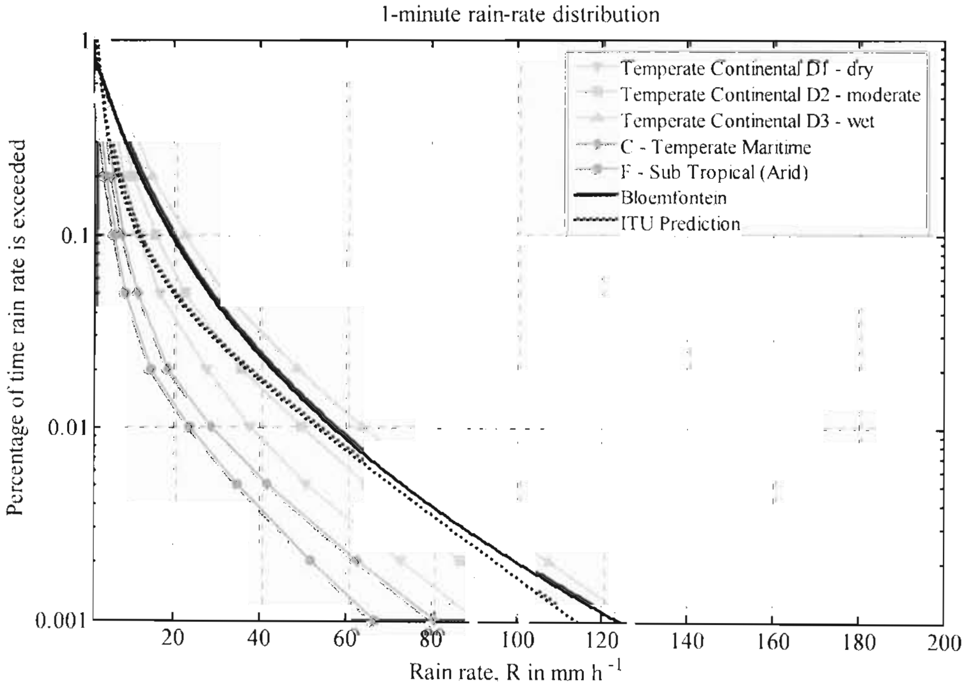

Figure 4-13 : 1-minute cumulative rain-rate distributions for Bloemfontein.

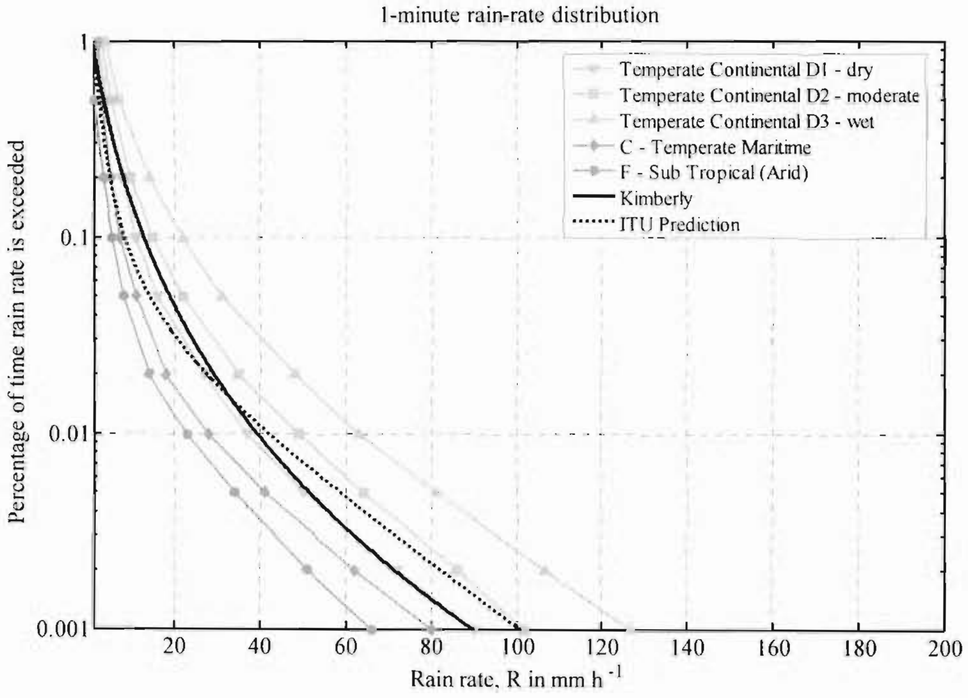

Figure 4-14 : 1-minute cumulative rain-rate distributions for Kimberly.

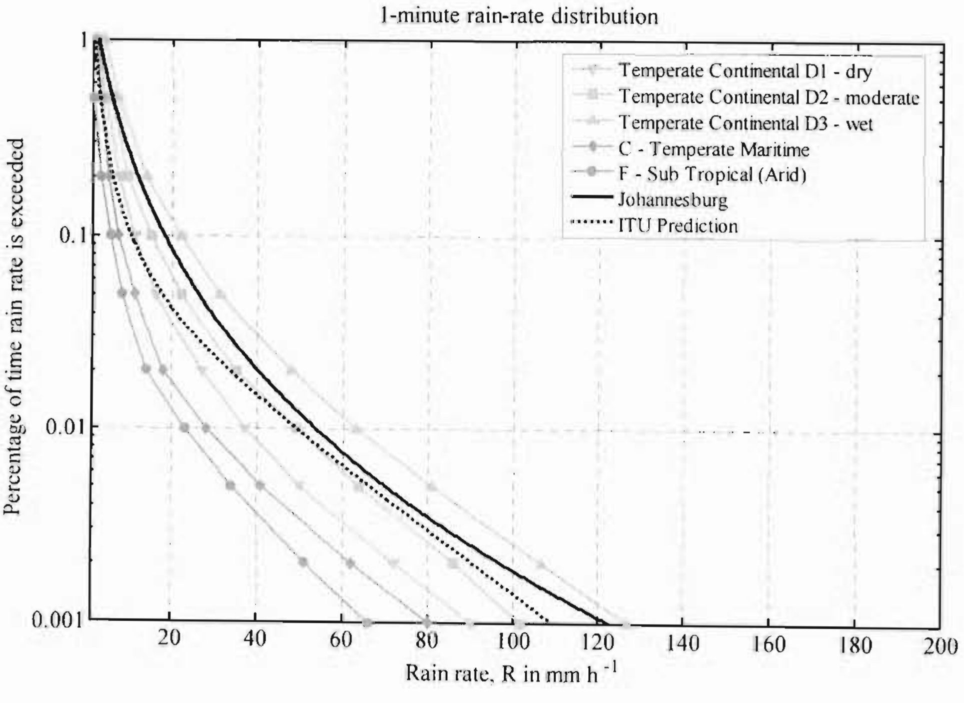

Figure 4-15 : 1-minute cumulative rain-rate distributions for Johannesburg.

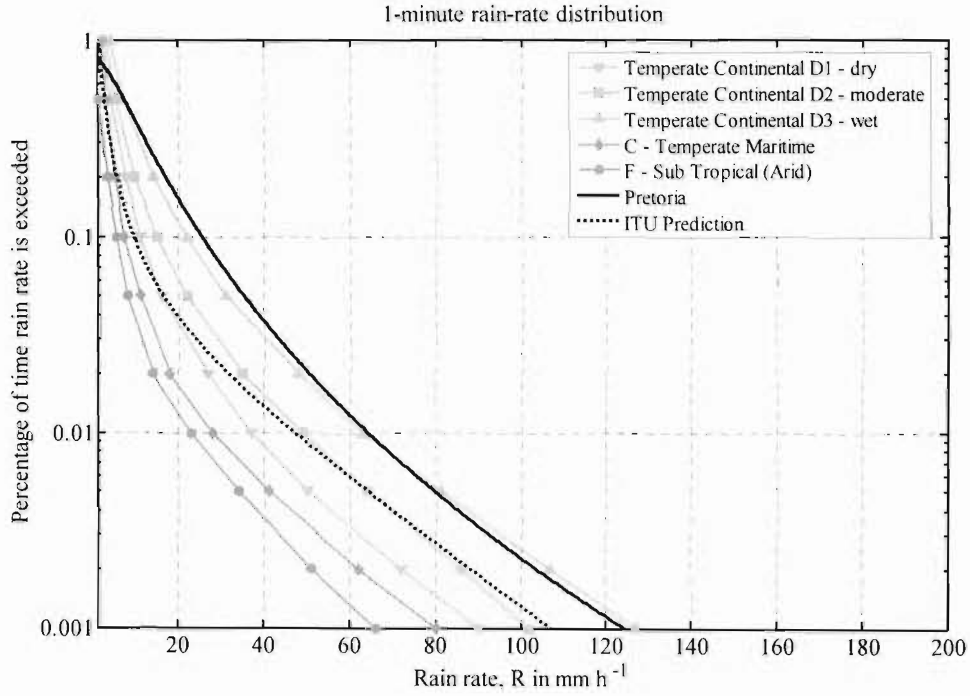

Figure 4-16 : 1-minute cumulative rain-rate distributions for Pretoria.

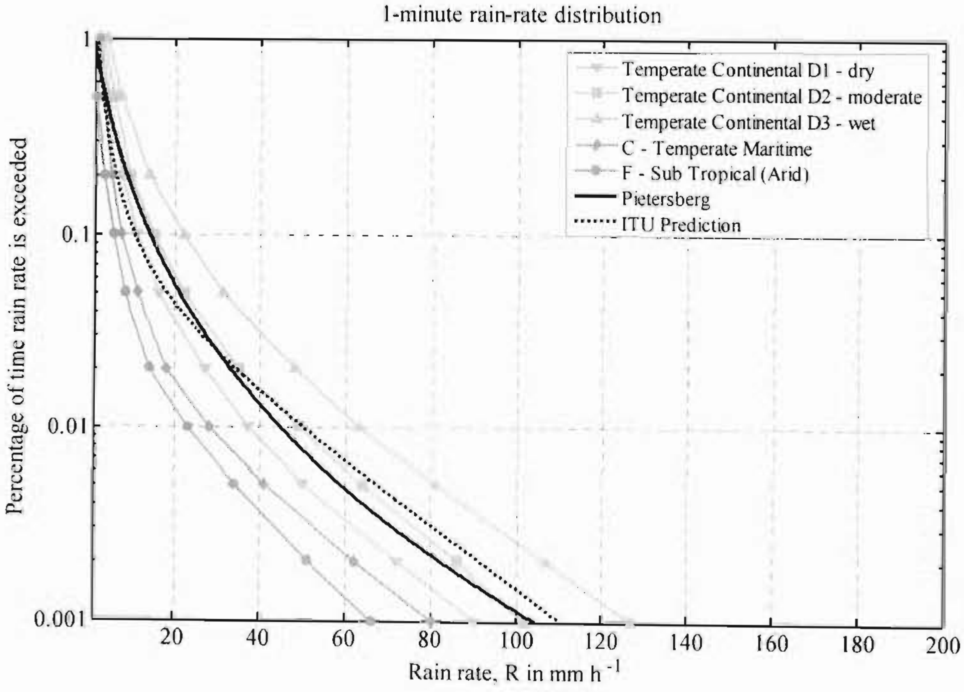

Figure 4-17 : 1-minute cumulative rain-rate distributions for Pietersburg.

For Pretoria, there is a marked difference with the ITU model predicting a far lower exceedance probability. The ITU prediction between Johannesburg and Pretoria are very similar, since it is climate-based and because of the interpolation technique. However analysis of the annual extreme series would indicate that Pretoria is prone to a more convective activity as compared to Johannesburg. Such variations will be reflected in the proposed model since it uses the actual available rainfall data

4.4 Moupfouma (1987) model

As mentioned, the ITU provides two global maps. One is a map of the ITU climatic zones and their boundaries, shown for Africa in Figure 4-3. The other provides the contours of the 1-minute rain rate exceeded for 0.01% of the year. This rain rate will be denoted by $R_{0.01}$. The rain rate exceeded for other percentages of time are also useful. Moupfouma (1987) suggest the following relationship

$$P(R \geq r) = a\frac{e^{-ur}}{r^{b}}, \tag{4.41}$$

where the parameters a, b and u depend on the climate and integration time. This relation is valid for rain rates $r > 2$ mm h^{-1}. The parameters a and b can be related to u and $R_{0.01}$ as follows

$$\begin{aligned} a &= 10^{-4}\left(R_{0.01}\right)^{b} e^{\left(u \cdot R_{0.01}\right)} \\ b &= 8.22\left(R_{0.01}\right)^{-0.584}. \end{aligned} \tag{4.42}$$

$R_{0.01}$ is the 1-minute rain rate in mm h^{-1} exceeded for 0.01% of the year and accounts for the shape of the distribution and u determines the slope.

Moupfouma (1987) found u to be dependent on the climate zone and the rain rate.

$$u = \lambda r^{-s}. \tag{4.43}$$

The parameters λ and s are given in Moupfouma (1987) for ITU climate zones **D – P.**

Table 4-7 : Values for the parameters λ and *s* according to the climatic zone from Moupfouma (1987, Table 4)

Climate Zone	D	E	J	K	M	N	P
λ	0.18	0.05	0.07	0.05	0.05	0.033	0.035
s	0.33	0.29	0.18	0.17	0.09	0.06	0.10

Using the ITU predictions of $R_{0.01}$ for the eight chosen locations, the cumulative distributions can be calculated using (4.41)–(4.43) and Table 4-7. The results are shown in Figure 4-18.

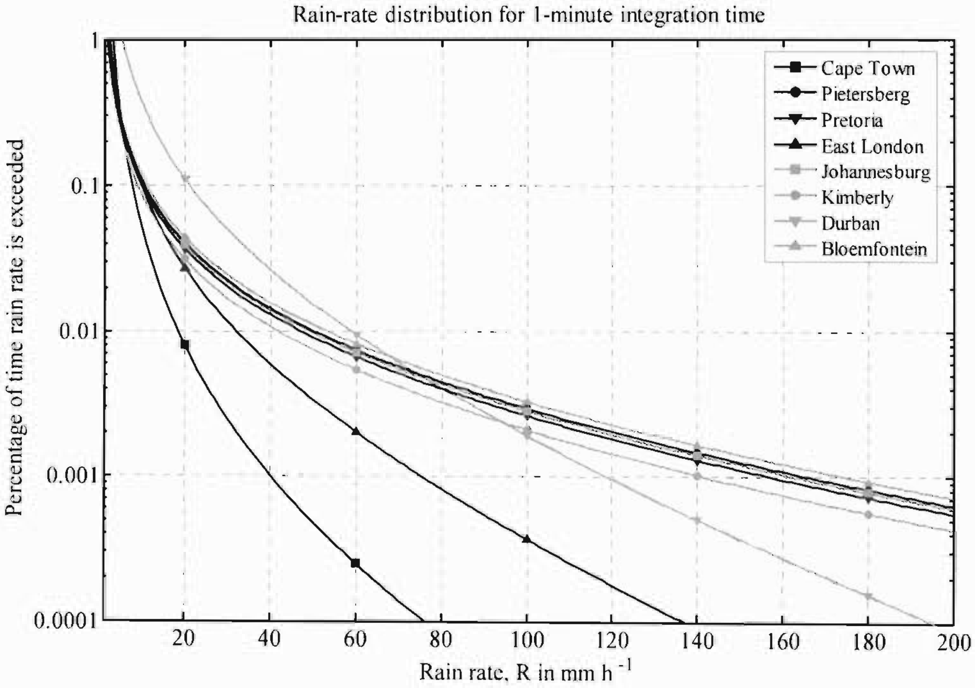

Figure 4-18 : 1-minute cumulative rain-rate distributions for 8 locations in South Africa using Moupfouma (1987).

As expected, since the parameters λ and s are climate-based there is little difference between Pretoria, Johannesburg, Bloemfontein and Pietersburg. This once again points out the inability for climate-based models to resolve small-scale variations with a climate zone. The difference between the Moupfouma (1987) model and the ITU model is shown in Figure 4-19. The predictions using Moupfouma (1987) are indicated as dashed lines.

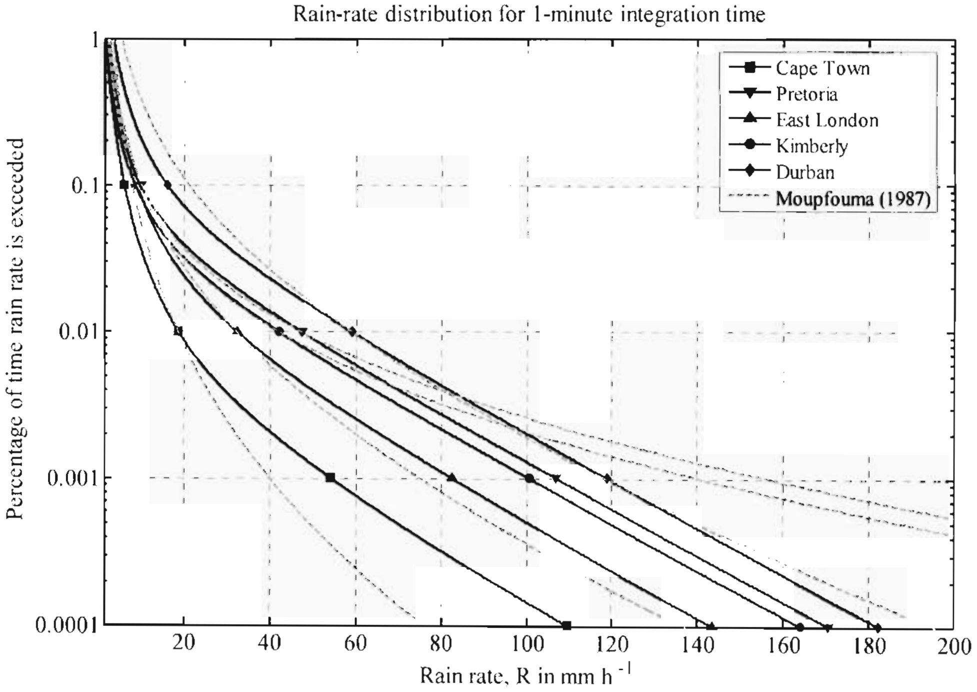

Figure 4-19 : Comparison of Moupfouma (1987) model and the ITU-R P.837-4 predictions.

4.5 Moupfouma and Martin (1995) models

Moupfouma and Martin (1987) improved upon the previous Moupfouma (1987) model. The climate parameter was now defined for either temperate locations or tropical and sub-tropical locations. The cumulative distribution is given by

$$P(R \geq r) = \left(\frac{R_p + 1}{r + 1}\right)^b e^{u \cdot (R_p - r) + \ln[P(R_p)]}, \tag{4.44}$$

where

$$b = \left(\frac{r}{R_p} - 1\right) \cdot \ln\left(1 + \frac{r}{R_p}\right), \tag{4.45}$$

and R_p is the rain rate exceed p % of the year.

The climate parameter u determines the slope and is defined for temperate zones as

$$u = \frac{-\ln[P(R_p)]}{R_p \cdot \left[1 + \eta\left(\frac{r}{R_p}\right)^{\beta}\right]}. \tag{4.46}$$

For tropical and sub-tropical zones u is given by

$$u = \frac{-\ln[P(R_p)]}{R_p} \cdot e^{-\lambda\left(\frac{r}{R_p}\right)^{\gamma}}. \tag{4.47}$$

If the 0.01% exceedance for 1-minute integration time is used

$$R_p = R_{0.01} \text{ and } P(R_p) = 0.01\ \%. \tag{4.48}$$

Consequently (4.44) becomes

$$P(R \geq r) = 100\left(\frac{R_{0.01} + 1}{r + 1}\right)^b e^{u \cdot (R_{0.01} - r) + \ln[10^4]}, \tag{4.49}$$

where the factor 100 accounts for the time to be expressed as percentages.

The parameter b becomes

$$b = \left(\frac{r}{R_{0.01}} - 1 \right) \cdot \ln \left(1 + \frac{r}{R_{0.01}} \right). \tag{4.50}$$

For the 0.01% exceedance probability, Moupfouma and Martin (1995) have determined the climate parameter for a temperate locations as follows

$$u = \frac{-\ln\left[10^4\right]}{R_p \cdot \left[1 + 4.56 \left(\frac{r}{R_{0.01}} \right)^{1.03} \right]}. \tag{4.51}$$

For a tropical and subtropical regions the climate parameter is given by

$$u = \frac{-\ln\left[10^4\right]}{R_{0.01}} \cdot e^{-1.066 \cdot \left(\frac{r}{R_{0.01}} \right)^{0.214}}. \tag{4.52}$$

Once again the ITU predictions of $R_{0.01}$ have been used for each location. The cumulative distributions have been calculated for both temperate and tropical locations and compared to the Moupfouma (1987). Once again there, was little difference between Pretoria, Johannesburg, Bloemfontein and Pietersburg. The difference between the Moupfouma (1987) model and the Moupfouma and Martin (1995) model for temperate and tropical locations are shown in Figure 4-20 – Figure 4-23 for Cape Town, East London, Durban and Kimberly, respectively.

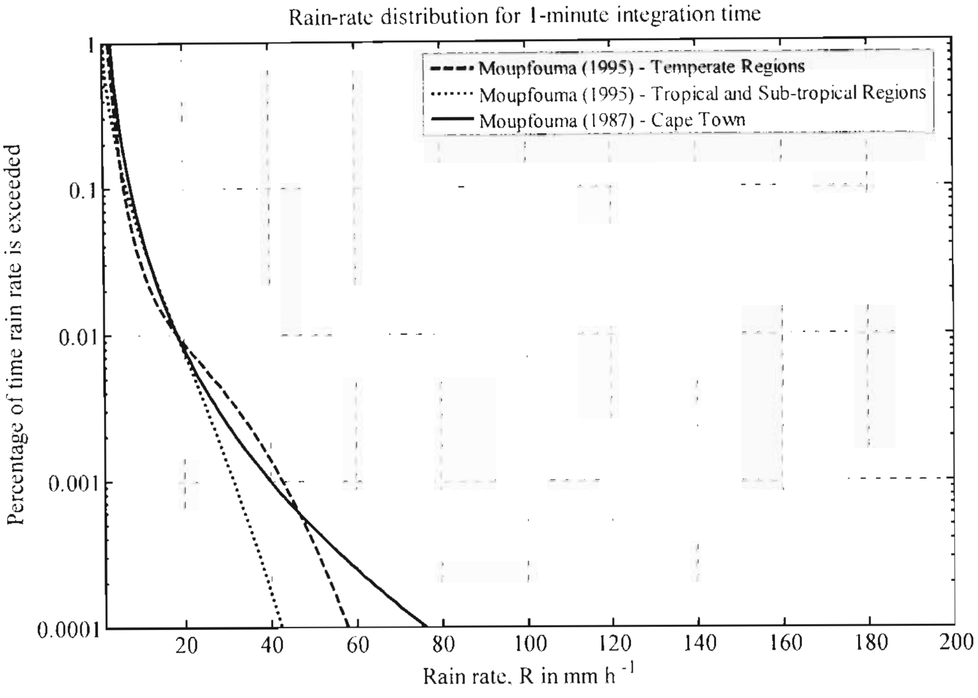

Figure 4-20 : Comparison of Moupfouma (1987) model and Moupfouma and Martin (1995) model for Cape Town.

In this section several different techniques of obtaining 1-minute rain-rate distributions have been discussed. It has been shown that climate-based models are often not adequate to account for small-scale variations within each climate zone. The exceedance probabilities for locations within any climate zone tend to be very similar. This is not necessarily the case, especially when certain sub-regions within a given climate zone exhibit behaviour of two or more climates. South Africa has 12 climate zones according to the Köppen System and hence the resolution of climate-based rain-rate models should be fine-tuned and improved upon to improve accuracy.

Apart from the scale, the shape of the rain-rate distribution also varies significantly across the different climates as indicated by Moufouma and Martin (1995) and shown in Figure 4-20 – Figure 4-23.

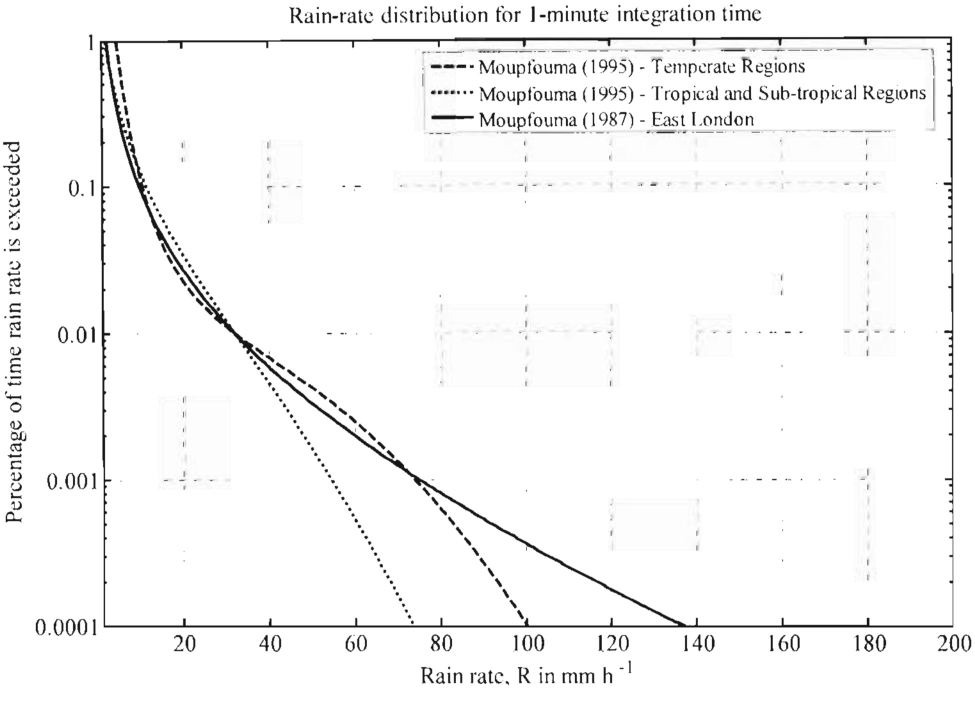

Figure 4-21 : Comparison of Moupfouma (1987) model and Moupfouma and Martin (1995) model for East London.

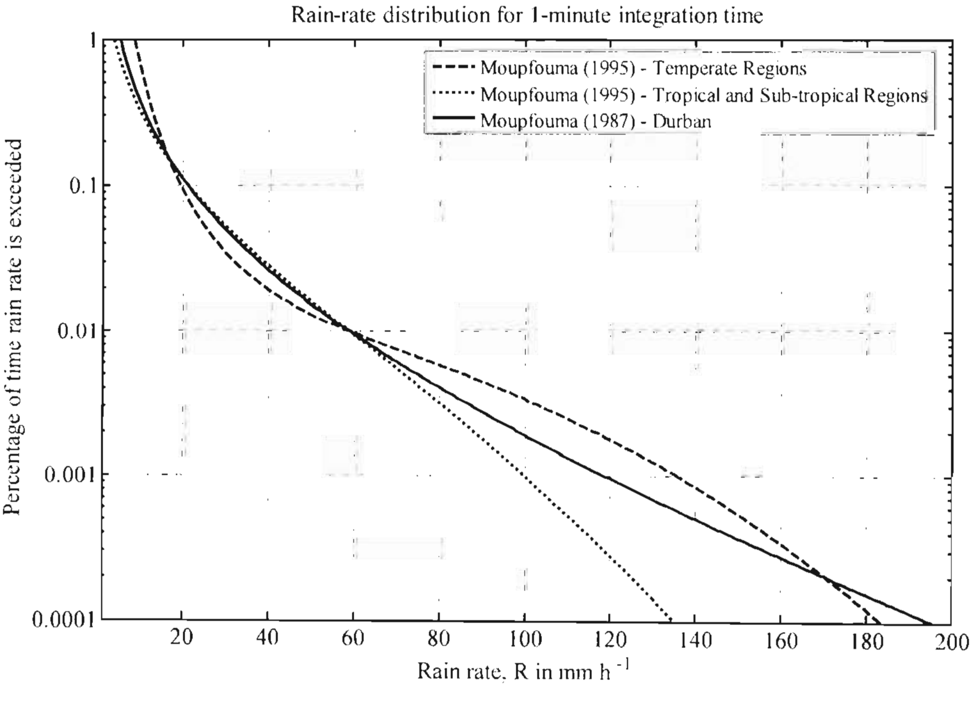

Figure 4-22 : Comparison of Moupfouma (1987) model and Moupfouma and Martin (1995) model for Durban.

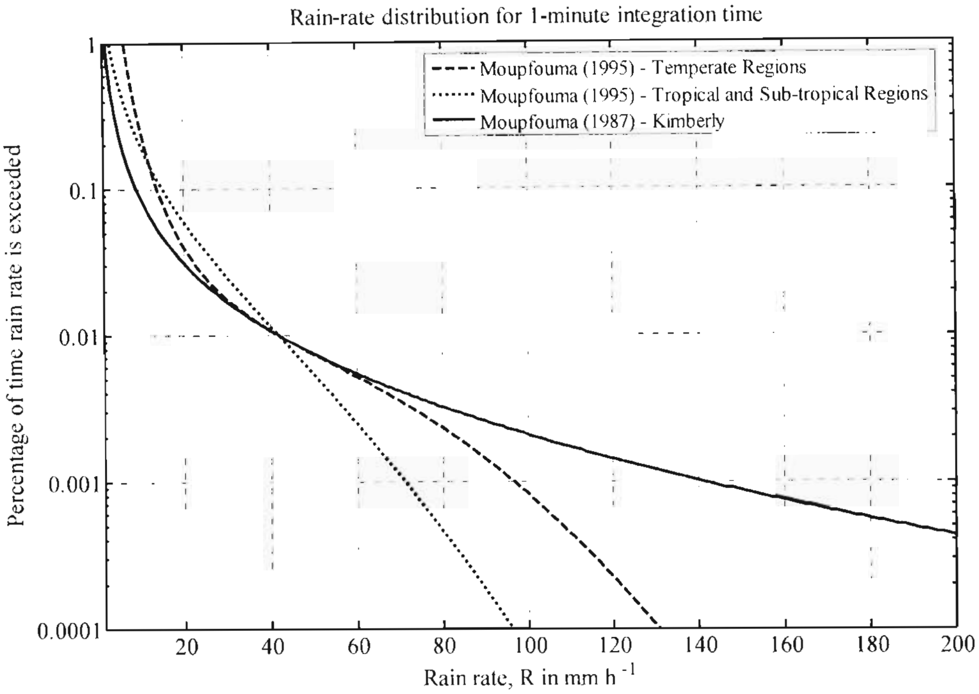

Figure 4-23 : Comparison of Moupfouma (1987) model and Moupfouma and Martin (1995) model for Kimberly.

4.6 Comparison with 1-minute rain-rate measurements

Rainfall was measured at the Durban, UKZN – Howard College Campus, from December 2003 – November 2005. The rain-rate was recorded once every minute. These measurements were run concurrently with rain attenuation measurements. But this companion campaign was only run from February 2004 – September 2005. The cumulative distribution of the measured 1-minute rain-rate distribution is shown, along with the different rain-rate models in Figure 4-24.

The Seeber (1985) model provides 5-minute distribution for Durban using the coastal climate. The Ajayi and Ofoche (1983) relation given in (4.39) was used to convert this distribution to a 1-minute rain-rate distribution. The proposed model extreme-value uses the techniques in Seeber (1985), Lin (1976, 1978) and Ajayi and Ofoche (1983) on the actual extreme rain data recorded in WB36 (Department of Transport 1974). The ITU model, and the Moupfouma (1987) and Moupfouma (1995) models for providing 1-minute rain-rate distributions, are also shown for comparison.

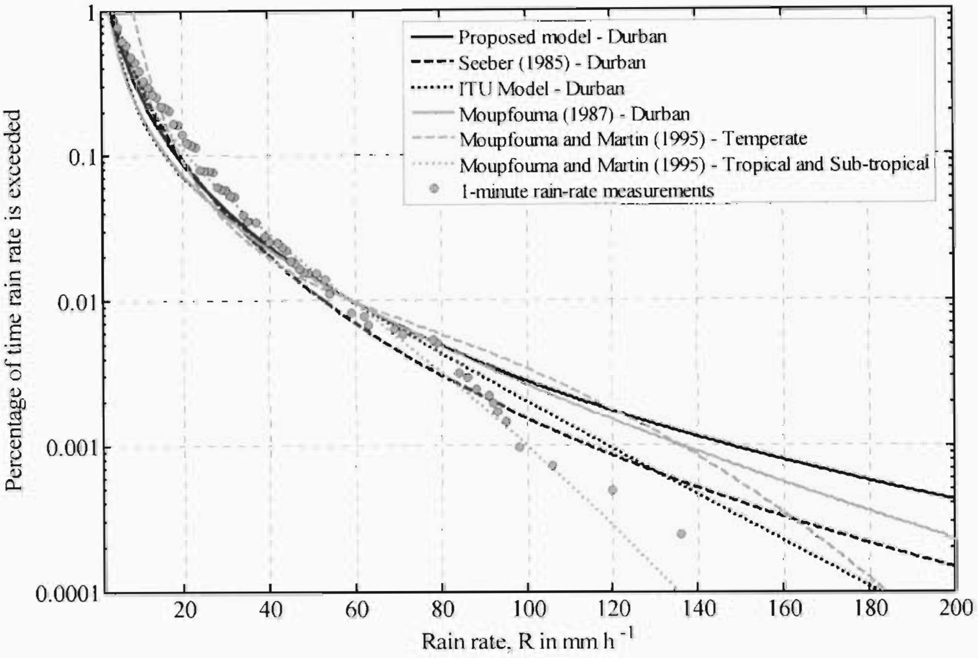

Figure 4-24 : Comparison of models with 1-minute rain-rate data for Durban over 2003.

As shown in Figure 4-24, the proposed extreme-value model provides the good estimate for Durban, especially over the rain-rates $R \leq 80$ mm h^{-1}, which are particularly important for the evaluation of the rain exceeded for 0.01 % of the year. For the lower probabilities, the Moupfouma and Martin (1995) model for tropical and sub-tropical regions seems to be better suited. One should not read too much from such short-term rainfall data and Crane (1996) warns against the use of any rainfall data spanning less than 10 years, especially when analysing the lower probabilities. However, the measurements do show good correlation with the models for the higher probabilities.

In the absence of reliable, long-tem rainfall data, the ITU-R P.837 global rain-rate models can be used to provide a valuable estimate of the 1-minute rain-rate distribution. For South Africa, the Seeber (1985) model together with the Ajayi and Ofoche (1983) relation can also be used to obtain a 1-minute rain-rate distribution. This was examined along with the Lin (1976, 1978) model, resulting in the proposed extreme-value model.

The above-mentioned lognormal distribution provide a good fit for 0.01% of the time and higher probabilities. At the low-percentages (i.e. < 0.01%) lognormal models may tend to over-estimate the attenuation and produce pessimistic results. Some authors (e.g. Watson 1976 and Moupfouma and Martin 1995) have questioned the use of lognormal distributions for this probability range and suggested the use of the gamma distribution and other hybrid models. The Moupfouma and Martin (1995) models for tropical/sub-tropical regions and temperate regions can be used to overcome this problem. The Moupfouma and Martin (1995) models for tropical/sub-tropical regions have shown good comparative results with the rain-rate measurements

This estimate of the surface-point 1-minute rain rate is only the first step. Rain exhibits significant spatial and temporal variation. Hence the rain-rate profile along the propagation path is also required. Crane (1980) developed an attenuation model to convert the point rain-rate to a path-averaged rain rate. The only required inputs are the power-law parameters for the specific attenuation and the surface-point rain rate. This simple and versatile model and will be the subject of discussion in the next section.

4.7 Obtaining path attenuation from surface-point rain-rate

The surface-point 1-minute rain rate can be obtained for any probability of interest by using the proposed rain-rate cumulative distribution. To obtain the rain attenuation along the propagation path, the rain-rate profile and the specific attenuation is needed.

The specific attenuation is expressed in dB km^{-1} as follows

$$\lambda_R = \kappa R_p^{\alpha}, \tag{4.53}$$

where the parameters κ and α are frequency and polarization dependent and R_p is the 1-minute rain rate exceeded for p % of the year. The parameters κ and α are obtained by fitting a power law expression to the specific attenuation for the frequency of interest and R_p can be obtained from the 1-minute rain-rate distribution for the location.

If the rainfall can be considered uniform across the propagation path then the total attenuation A_p for a given rain rate R_p across a path of length L in km is linearly related with distance and hence given by

$$A_p\left(L, R_p\right) = \lambda_R L = \kappa R_p^{\alpha} L \tag{4.54}$$

However, rain rates are generally not uniform over the entire propagation path. Thus the path attenuation will increase non-linearly as the propagation path L increases. To account for the variation of the rain rate along the propagation path L can be replaced by an effective path length L_{eff}.

The effective path length L_{eff} is the hypothetical path length of uniform rain rate R_p, which will produce the same total path attenuation as that of the actual spatially varying rain rate. According to Crane (1996) effective path length L_{eff} can be obtained by using piece-wise exponential functions.

Adequate results have been obtained if two exponential functions are used, one to for distances 0 to $l\left(R_p\right)$ km and another from $l\left(R_p\right)$ km to 22.5 km, each of which are given as follows

$$\begin{aligned} L_{eff} &= \frac{e^{yl(R_p)}-1}{y} + e^{\alpha B} \cdot \frac{e^{zL}-e^{zl(R_p)}}{z} && \text{for} \quad l \le L \le 22.5 \text{ km} \\ L_{eff} &= \frac{e^{yl(R_p)}-1}{y} && \text{for} \quad 0 < L < l \end{aligned} \tag{4.55}$$

where

$$\begin{aligned} B &= 0.83 - 1.7 \cdot \ln\left(R_p\right), \\ c &= 0.026 - 0.03 \cdot \ln R_p, \\ l\left(R_p\right) &= 3.8 - 0.6 \cdot \ln R_p, \\ u &= \frac{B}{l\left(R_p\right)} + c, \\ y &= \alpha u, \text{ and } z = \alpha c. \end{aligned} \tag{4.56}$$

The total attenuation across the path is then given by

$$A_p = \kappa R_p{}^{\alpha} L_{eff}\,. \tag{4.57}$$

The ITU also recommends the used of an effective path length for the evaluation of path attenuation. According to ITU-R P-530-11, the effective path length for a rain rate $R_{0.01}$ exceeded for 0.01% of the year is given by

$$L_{eff} = \frac{L}{1 + L/L_0}, \tag{4.58}$$

where

$$L_0 = 35 \cdot e^{-0.015 R_{0.01}} \tag{4.59}$$

Thus the path attenuation for 0.01% of the year is given by

$$A_{0.01} = \kappa R_{0.01}{}^{\alpha} L_{eff} , \tag{4.60}$$

and to convert to other percentages the following power law may be used

$$\frac{A_p}{A_{0.01}} = 0.12 \cdot p^{-(0.546+0.043 \cdot \log_{10} p)} \tag{4.61}$$

where p can range from 0.001% to 0.1% of the year.

4.8 Conclusion

In the previous chapter the specific attenuation was determined for several DSDs models, using Mie theory for spheres. With the specific attenuation model it is possible to determine the path attenuation at any rain rate for any given radio-link path and frequency of interest. Knowledge of the cumulative distributions of the fade depth and durations due to rain are now necessary and this chapter was devoted to this subject.

Depending on the link availability requirements, communication system designers may need the fade depth exceeded for 0.1, 0.01 or 0.001% of the year.

To perform this task knowledge of the surface-point rain rate is a prerequisite. Rain exhibits considerable temporal and spatial variability and even an integration time of 5 minutes is often too large and inadequate to account for these fluctuations. Thus the rain-rate distributions 1-minute integration time is needed.

However, measurements of 1-minute rain rates are not readily available throughout the world. Several models have been discussed in literature (e.g. Rice and Holmberg 1973;

Lin 1976, 1978; Dutton and Dougherty 1979, 1984; Tattelman and Scharr 1983; and Tattelman et al. 1994).

Some of these models are based upon the climatic designation (e.g. Crane 1980; ITU-R P.837). These climate-based rain-rate models provide a useful estimate of the rain-rate distribution, when there is a lack of meteorological data and are discussed in Section 4.2. These models are however coarse and based on the climatic designation. Thus whenever possible, one should take advantage of the available rainfall records to augment these global maps.

Seeber (1985) examined the extreme-value model of Lin (1976) and it was found to be particularly suitable for application in the South African climate. The extreme-value model (Lin 1976; Seeber 1985) was thus considered in this study. 1-minute rain-rate distributions have subsequently been obtained using measurements of the rainfall extremes, together with the conversion ratio of Ajayi and Ofoche (1983). The formula and analysis using extreme-value statistics are provided in Section 4.3. In Section 4.3 the procedure for obtaining 5-minute rain-rate distributions for any location in South Africa, using the depth-duration-frequency curve. More accurate 5-minute distributions can be provided by using actual rainfall data from annual maxima series when available. Consequently 5-minute distributions are obtained for 8 locations in South Africa. Thereafter these distributions are converted to 1-minute rain-rate distributions. The results are compared to the global rain-rate climate models.

The latest ITU recommendation (ITU-R P.837-4) uses 15 years of data from the European centre of medium-range weather forecast to generate global maps of the rain rate exceeded for 0.01% of the year. The rain rate exceeded for other percentages of the year are also useful, thus a model for evaluating these percentages using 0.01% of the year rain rate is also provided. Some investigators (e.g. Moupfouma 1987 and

Moupfouma and Martin 1995) have suggested alternative rain-rate models. These models are discussed in Section 4.4 and Section 4.5.

The lognormal distribution provides a good fit for 0.01% of the time and higher probabilities. At the low-percentages (i.e. < 0.01%) lognormal models may tend to over-estimate the attenuation and produce pessimistic results. Some authors (e.g. Watson 1976 and Moupfouma and Martin 1995) have questioned the use of lognormal distributions for this probability range and suggested the use of the gamma distribution and other hybrid models. A comparison of all the above-mentioned models, along with 1-minute rain-rate measurements in Durban over a period of approximately 2 years is given in Section 4.6.

This estimate of the surface-point 1-minute rain rate is only the first step. Rain exhibits significant spatial and temporal variation. Hence the rain-rate profile along the propagation path is also required. Crane (1980) developed an attenuation model to convert the point rain-rate to a path-averaged rain rate. This simple and versatile model has been adopted in this study and is discussed in Section 4.7.

A 19.5 GHz terrestrial link was setup between Howard College and Westville campuses of the UKZN. The communication link is 6.3 km long and employs vertical polarization. In the next chapter measurements taken over a two year period (February 2004 – September 2005) will be discussed.

Chapter 5

Path Attenuation

5.1 Introduction

In today's industrialised and technology-driven world, the radio-frequency spectrum has become one of the most valuable resources. In the past, the frequency bands below 10 GHz had been extremely sought after. At these frequencies atmospheric absorption and cosmic noise are negligible, thus long-distance communication systems can be established with reasonable fade margins. However, with the rapid growth of the telecommunications industry, the speed and capacity of existing communication systems have been pushed to the limits. This demand for higher data rates and greater bandwidth, coupled with the rapid congestion of the frequency bands below 10 GHz, has led to the re-evaluation of the usage of the millimetre-wave frequency bands for terrestrial communication links.

System designers of millimetre-wave communication links must account not only for the free-space loss but also the excess attenuation due to gaseous absorption and the presence of rain, fog, mist and clouds in the link budget. Gaseous absorption is dominated by water vapour and oxygen, with peak absorption attenuations near 22 GHz and 60 GHz respectively. The resulting attenuation depends on the operating frequency, temperature, pressure and the concentration of the respective gases in the atmosphere.

Algorithms for this calculation are available in the ITU recommendation ITU-R P.676-6. Since the concentration of oxygen is approximately constant, the resulting specific attenuation is also approximately constant for any given location and operating frequency. Water vapour on the other hand exhibits considerable spatial and temporal variations. Surface maps of water vapour densities are available in the ITU recommendation ITU-R P.836-3.

Using the data provided in ITU-R P.676-6 and ITU-R P.836-3 programs were written in Matlab® to evaluate the absorption attenuation for various atmospheric conditions. Figure 5-1 shows the specific attenuation for dry air and water vapour for an atmospheric pressure of 1013 mbar, a temperature of 25 °C and water vapour density of 10 g m^{-3}. The solid line gives the total specific attenuation.

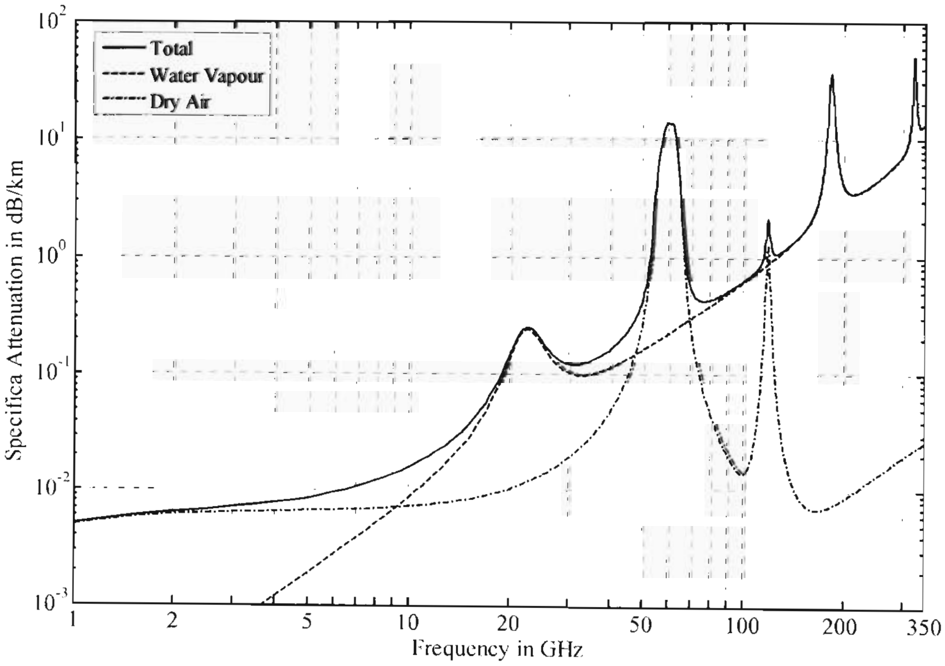

Figure 5-1 : Specific attenuation due to atmospheric gases for frequencies 1 to 350 GHz.

The total specific attenuation has several peaks arising from the absorption spectra of oxygen and water vapour. These peaks are located at approximately 22, 60, 119, 183 and 325 GHz, along with several bands of lesser attenuation around 32, 75, 128 and 215 GHz. Although the total specific attenuation for the bands around 75, 128 and 215 GHz are comparatively lesser, the attenuation at these bands still exceed that of the peak absorption due to water vapour at 22 GHz. This makes the bands above 50 GHz less suitable for terrestrial communication systems, since the propagation path, namely the atmosphere will severely attenuate the signal as the path length increases. These frequencies can be used for very short length communication systems such as intra-building communications and short-range point-to-point links, e.g. LOS links between buildings.

For operating frequencies below 50 GHz, a small fixed fade margin (approximately 1 – 2 dB per 10 km path length) in the link budget can compensate for the atmospheric absorption and still maintain the required performance. Although the losses due to atmospheric absorption are acceptable, the reliability of the communication system is still not guaranteed. Precipitation is a major cause of unwanted attenuation on such links and still needs to be accounted for. Of these, rain is the most severe and the resulting attenuation can exceed all others. For millimetre-wave communication systems, the attenuation due to rain is critical to determining the path length for which system performance can still be maintained. With system reliability diminishing as the path length increases, long distance communication systems are often too unreliable. However over short-haul links, reliability can still be maintained. The millimetre-wave frequencies will thus be most suitable for short and medium distance communications, such as terrestrial point-to-point links and repeater stations.

Knowledge of the specific attenuation will thus be invaluable to determine the path lengths, operating frequency and fade margins required for communication systems.

During rain events, a large fade margin may often be required. It would be uneconomical to implement such margins since they are only needed for a fraction of the time. A model for the effect of rain attenuation would thus be a valuable tool for a systems designer. With such models the system designer can then determine the appropriate fade margin and resulting outage period for the link.

In this study, a theoretical model for the attenuation due to rain is provided. Propagation models and experimental measurements complement one another and whenever possible, the two should be implemented in parallel. A measurement campaign to monitor the attenuation effects of rain was thus also implemented from February 2004 – September 2005. From the above discussion, the frequency band from 18 GHz to 20 GHz is highly suitable for short-haul LOS links. Consequently, a 6.73 km terrestrial LOS link with operating frequency 19.5 GHz was setup between the Howard College and Westville campuses of the UKZN. The primary objective is to investigate the effect of rain attenuation over the link.

5.1.1 Outline of chapter

In this chapter the path attenuation is evaluated for a LOS link which was established between the two campuses of the UKZN. Firstly, in Section 5.2 the various LOS link details are discussed. These include the equipment setup, link parameters, path profile and link budget. Sample link measurements are also given. In Section 5.3 the specific attenuation is calculated using the various DSDs discussed in Chapter 2. This is followed by the evaluation of the path attenuation in Section 5.4. The Crane (1980, 1996) attenuation model is applied to convert the surface-point rain-rate to a path integrated rain-rate. Next, the various 1-minute rain-rate distributions discussed in Chapter 4 are applied to provide the exceedance probabilities for the path attenuation on the LOS link. The simulated results presented in this chapter focus on the operating frequency of the LOS link (19.5 GHz). The analysis at frequencies f = 4, 12, 15, 40 and 80 GHz are provided in the Appendix D.

5.2 The Line-of-sight Link

During the planning of terrestrial LOS systems, quantitative data relating to the fade depths and durations due to rain are necessary. Propagation measurements and models are thus required. A system for monitoring the attenuation due to rain was installed on a 19.5 GHz LOS link between the Howard College and Westville campuses of UKZN. A block diagram of the system is provided in Figure 5-2.

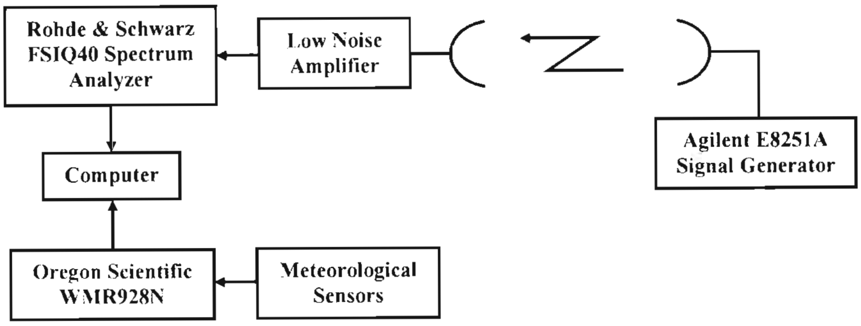

Figure 5-2 : Block diagram of the monitoring system.

The transmitter antenna was installed, 202 m above sea level, on the roof of the Science Building at the Westville campus. The receiver antenna was setup on the roof of the Electrical Engineering Building in the Howard College campus, 165 m above sea level. Valuline® WR42/R220 parabolic antennae with diameter 0.6 m were used at both the receiver and transmitter stations. These antennae provide a gain of 38.6 dBi and have a 3 dB beamwidth of 1.9 degrees at 19.5 GHz. The cabling consisted of FSJ1−50A superflexible coaxial cables of length 6 m at the transmitter and 5.5 m at the receiver.

At the transmitter, an Agilent E8251 signal generator was used to provide a +10 dBm unmodulated continuous-wave (CW) at 19.5 GHz. To date, only the CW signals have been transmitted and the signal strength has been examined.

At the receiver, an Agilent 83018A power amplifier was used to provide additional gain of 27 dB before feeding the signal into the Rohde & Schwarz FSIQ40 Spectrum Analyser. The resolution bandwidth (RBW), video bandwidth (VBW) and frequency span was selected to provide a sweep time of 0.4 seconds. The signal strength could thus be logged every second onto a computer. The weather conditions were also logged using the Oregon Scientific WMR928N Wireless professional weather station. The rain rate was monitored every minute and the rainfall depth over each 1-minute interval, i.e. the amount of rainfall in mm was also logged. The measurements campaign was undertaken from February 2004 to September 2005.

5.2.1 Path Profile

The LOS link is 6.73 km and passes over both hilly (near Westville) and suburban (near Cato Manor) terrain. Due to the highly directive gain of the parabolic antennas used at each of LOS stations, accurate pointing is required. The azimuth required at the Westville transmitter station is 328.34°, and 148.32° is required at the Howard College receiver station. These azimuth details are obtained using the latitude and longitude coordinates and measured clockwise from the reference of the magnetic south. The LOS path is nearly horizontal, with a slight inclination of 0.3° at the receiver. An aerial map of the link is provided in Figure 5-3.

Figure 5-4 shows the path profile for the LOS link. It contains an adjustment to account for the vegetation, buildings and the curvature of the earth. A k-factor or effective radius factor of 0.67 (smaller than unity) is used to examine the clearance for the worst-case of ray bending.

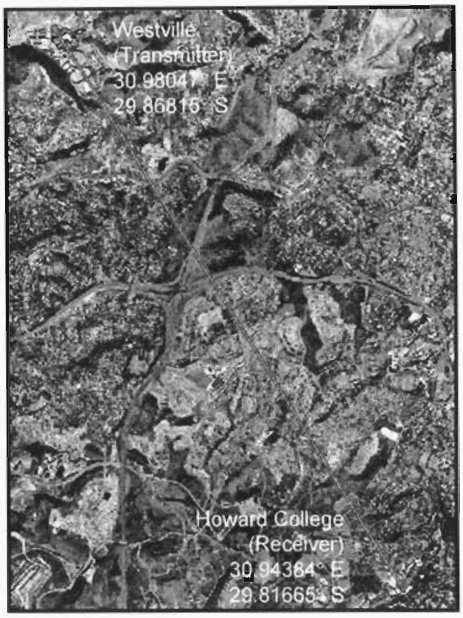

Figure 5-3 : An aerial photograph of the LOS terrestrial link.

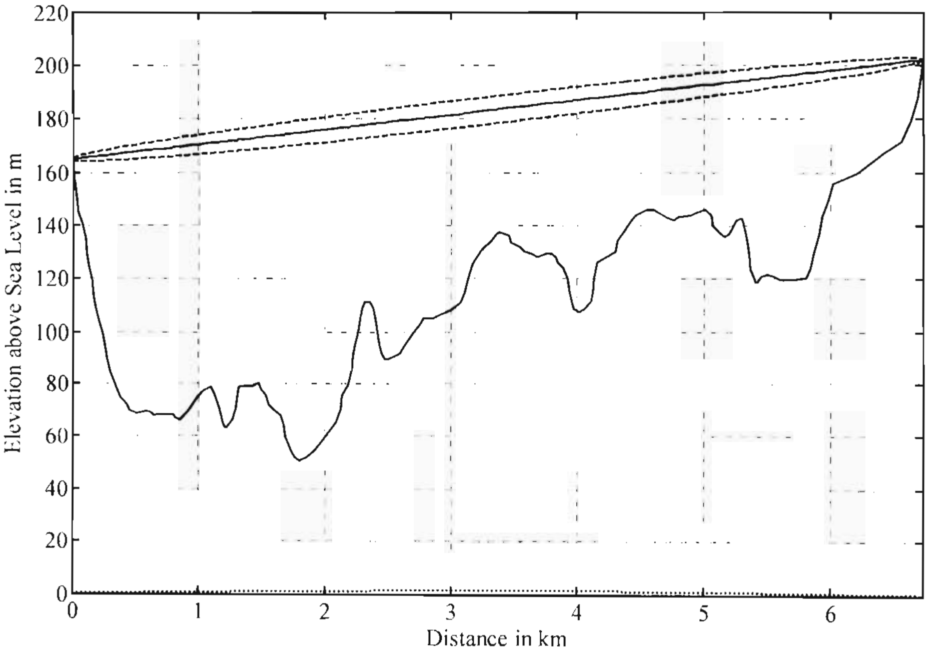

Figure 5-4 : The path profile for the 6.73 km LOS link between the Howard College and Westville campuses.

Figure 5-4 also shows the path clearance from the first Fresnel ellipsoid and the LOS path. Fresnel ellipsoids can be used to estimate the diffraction and reflections along the path. The radius of the first Fresnel ellipsoid is given by,

$$F_1 = 17.3\sqrt{\frac{d_1 d_2}{fd}}, \tag{5.1}$$

where F_1 denotes the radius of the first Fresnel ellipsoid in m, f is the frequency in GHz, d is the total path length in km and d_1 and d_2 are the distances from either station also in km.

According to ITU-R P.830, diffraction fading can be reduced if the antennae heights are sufficiently high so that even in the worst case of refraction, there is still sufficient clearance above any path obstacles. As shown in Figure 5-4 this is the case for the LOS link since there is sufficient path clearance throughout the path length and no obstructions within first Fresnel ellipsoid.

5.2.2 Link Calculations

The various terrestrial link parameters, such as altitude and antenna heights are summarised in Table 5-1. From altitude data in Table 5-1, the transmitting antenna is 178 + 24 = 202 m above sea level. Similarly, the receiver station is 145 + 20 = 165 m above sea level. As suggested in ITU recommendation ITU-R P.530-11, increasing the path inclination should help to reduce multipath propagation. The transmitter antenna was hence installed at the higher altitude, a height approximately 37 m above the receiver antenna.

The link data in Table 5-1 can also be used to estimate the power level of the received signal under typical atmospheric conditions. The link calculations arriving at these values are also given in this section.

Table 5-1 : Terrestrial link parameters

Parameter	Description
Path length	6.73 km
Height of transmitting antenna above the ground	24 m
Altitude of transmitter station above sea level	178 m
Height of receiving antenna above the ground	20 m
Altitude of receiver station above sea level	145 m
Operating frequency	19.5 GHz
Transmitter power	10 mW (10 dBm)
Transmitting/receiver antenna gain	38.6 dBi
Transmitting/receiver antenna beamwidth	1.9 degrees
Free-space loss	135 dB
Total cabling and connector losses	22 dB
Additional Losses (Water Vapour and Oxygen)	1 dB

The signal power level at the receiver P_r may be given as follows

$$\begin{aligned} P_r &= P_t + G_t + G_r + G_a - A_t \\ &= 10\text{ dBm} + 38.6\text{ dB} + 38.6\text{ dB} + 27\text{ dB} - A_t, \\ &= 114.2\text{ dBm} - A_t \end{aligned} \tag{5.2}$$

where P_t is the transmitter output power, G_t and G_r are the antenna gains at the transmitter and receiver, G_a is the amplifier gains and A_t is the total system loss.

The total system loss A_t in the absence of precipitation can be obtained by adding the free-space loss A_0, the atmospheric absorption losses A_a and the cabling losses A_c.

$$\begin{aligned} A_t &= A_0 + A_a + A_c \\ &= 32.4 + 20\log d + 20\log f + 1\text{ dB} + 22\text{ dB} \\ &= 157.8\text{ dB}. \end{aligned} \tag{5.3}$$

In (5.3), the path length $d = 6.73$ km and the operating frequency $f = 19500$ MHz. The atmospheric loss $A_a = (\gamma_o + \gamma_w)d = 1$ dB was obtained for the climate of Durban, where γ_o and γ_w are the specific attenuation for dry air and water vapour respectively. A_a was calculated using the mean annual water vapour density for Durban. Typical values may range from 0.6 dB – 1.6 dB due to seasonal variations. The cabling losses A_c = 22 dB, and includes all connector, branching, radome losses and a safety factor.

From (5.2) and (5.3) a receiver power level of approximately –43.6 dBm can be expected. Measured recordings can be expected to have rapid and slow signal level fluctuations about this value. These fluctuations arise from various propagation phenomena. Slower variations can be attributed to multipath propagation, occurrences of fog or mist along the path and even water vapour density variations while the rapid signal level fluctuations can be caused by scintillation. These signal variations are not due to rain and thus a reference level is determined for each day, by interpolating the periods of no rain. As a result during a rain event, the decrease in signal level from the reference level will be attenuation due to rain.

Figure 5-5 shows the measurements of the receiver power observed on the 29th February 2004. Approximately 60 measurements were taken each minute. These measurements were averaged for each minute. In this way, 1440 1-minute average readings were obtained for each 24-hour period. Thus the 1st reading corresponds to the time 0h01, the 720th reading to 12h00 and the 1440th reading to 24h00.

As illustrated in Figure 5-5, there are rapid fluctuations of small magnitude before 15h00, even though no rainfall was recorded. This is typically due to equipment noise, scintillation and other propagation effects. The solid dashed line is the reference value for the day obtained by averaging the reading over the non-raining periods. Using this reference level, the relative attenuation can be obtained and this is shown in Figure 5-6.

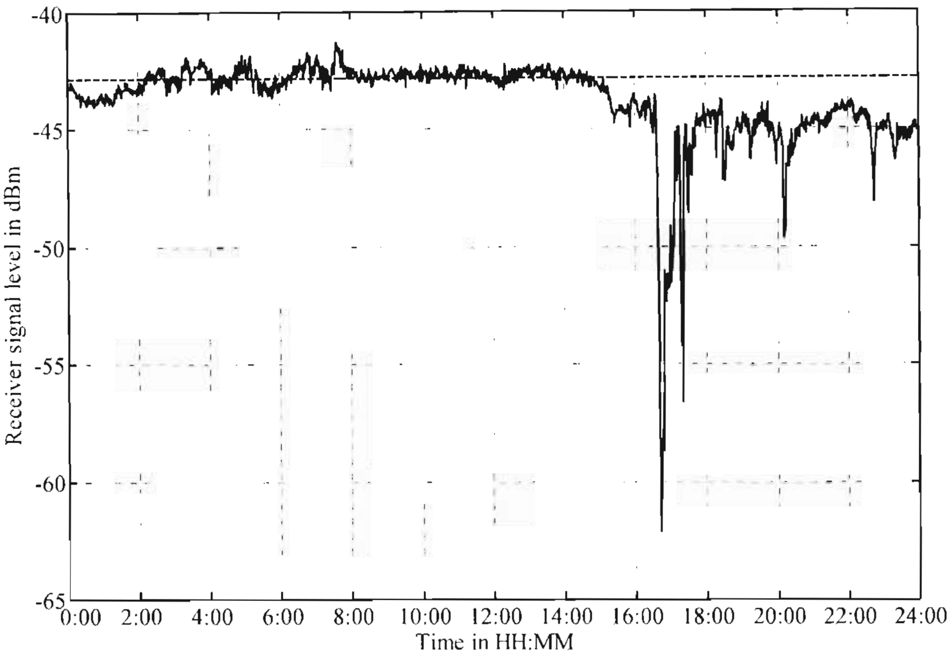

Figure 5-5 : The receiver signal power measurements for the 29th February 2004.

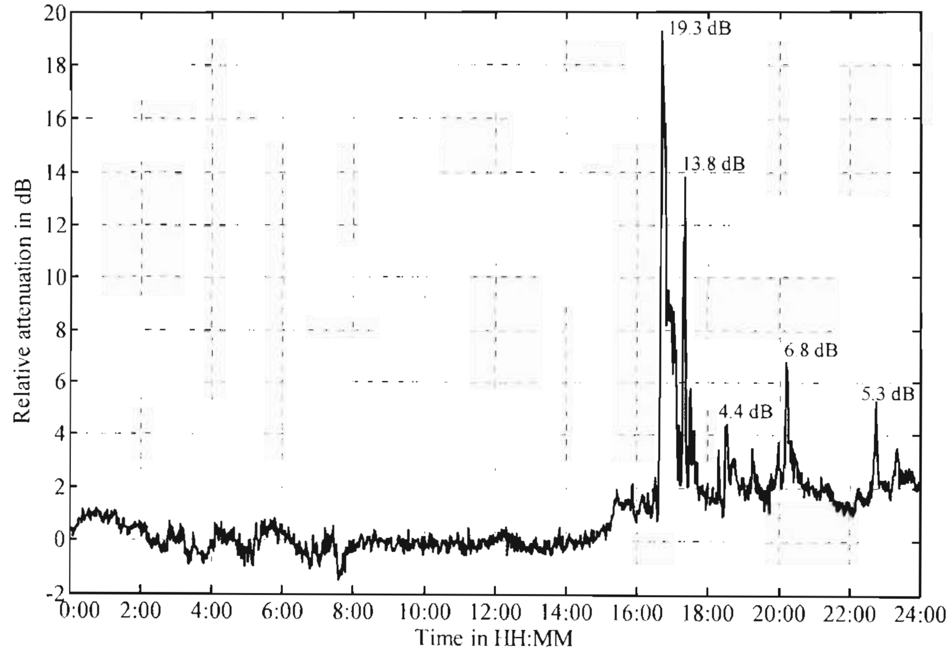

Figure 5-6 : Relative attenuation for the 29th February 2004.

Around 15h27 (927th reading) it began to rain lightly. The rain rate measured at approximately 1 – 2 mm h^{-1}. This corresponded to a measured attenuation of 1.5 – 2.5 dB. More convective rain cells began to pass over the link around 17h39. The measured rain rate increased to approximately 12 mm h^{-1} with a peak value of 37 mm h^{-1} observed at 17h43 (1003rd reading). The corresponding attenuation at this peak was 19.3 dB. The next peak occurred at 17h21 (1041st reading). The attenuation observed was 13.8 dB and corresponded to approximately 27 mm h^{-1}. The rain rate then settled to 2 – 3 mm h^{-1} with slightly heavy rains measured from 5 – 8 mm h^{-1} occurring over brief intervals around 19h33, 20h13 and 23h45.

The observations shown in Figure 5-5 and Figure 5-6 showed good correlation with the rain-rate measurements. Each peak corresponded well with the measured rain rate and rainfall depths. This is not always the case. On some occasions the heavy rainfall cells do not fall directly over the rain gauge. This is the scenario when only a portion of the path length is covered by these rain cells. The rain gauge then measures the lower rain rates (widespread rain) that surround the more convective rain cell. The observed attenuation is then greater than the expected value. This is a common problem, when the rain rate is measured at only a single point on the path. To improve accuracy, a rain gauge network comprising of several rain gauges, each located every 1 – 2 km along the path should be used. In this way a more accurate path-integrated model can be obtained. Due to budgeting constraints this was not possible. To account for the rain rate variation along the path length, the Crane (1980) attenuation model was used to convert the point rain-rate to a path-averaged rain rate as discussed in Chapter 4.

Figure 5-7 shows the relative attenuation observed on the 22nd June 2006. The peaks of 3.0, 5.5 and 7.9 dB correspond to rain-rate measurements of 4, 8 and 15 mm h^{-1} respectively. However the next peak of 7.4 dB was unexpected, since no rainfall was measured based upon the rainfall depths. This was probably due to the 15 mm h^{-1} rain cell having left the propagation path and then re-entering along the LOS path much further away from the receiver and the rain gauge.

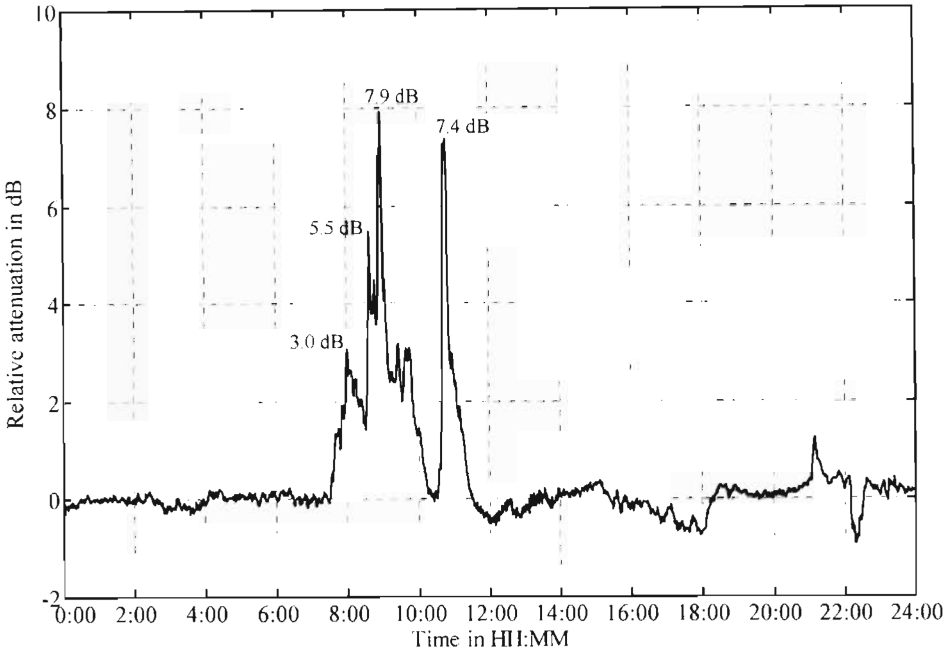

Figure 5-7 : Relative attenuation for the 22nd June 2006.

Figure 5-8 shows a scatter plot of the observed path attenuation against the rain rate measured for the corresponding period. For any given rain rate, the measured path attenuation showed a noticeable variance, especially for rain rates $R < 25$ mm h^{-1}, where most of the readings take place. This was mainly attributed to the fact that the rain rate was measured at only the receiver.

During the measurement campaign the measured rain rate exceeded 35 dB for approximately 0.014 % of the year. This was the noise margin of the receiver and resulted in outages during these intervals.

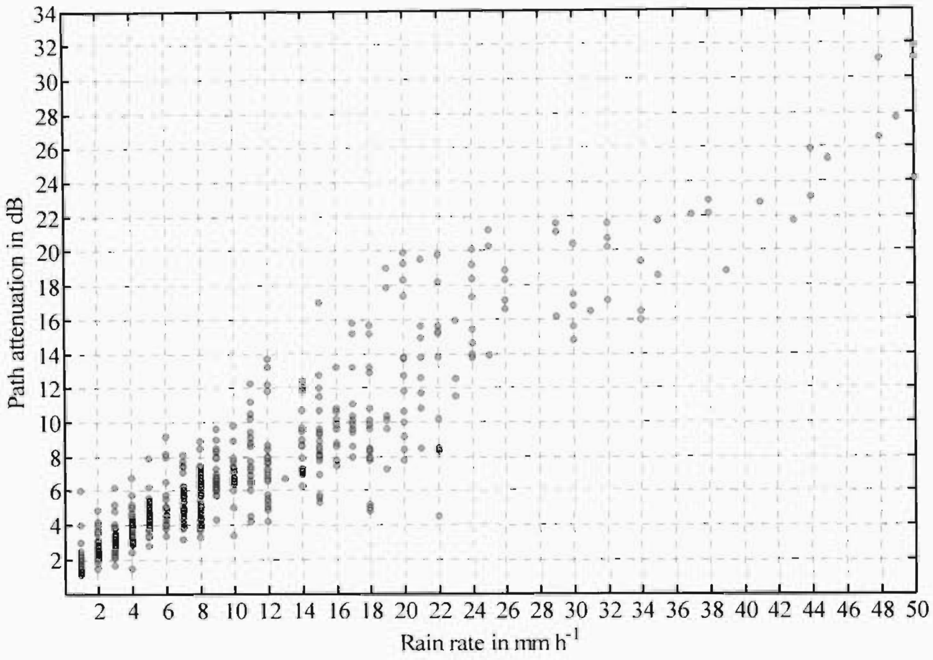

Figure 5-8 : Scatter plot of path attenuation and rain rate.

5.3 Specific Attenuation at 19.5 GHz

In Chapter 4, the specific attenuation was evaluated for spherical raindrops using several theoretical and empirical drop size distributions. These include :

- LP – Laws and Parsons (1943),

three exponential DSDs, namely

- MP – Marshall Palmer (1948),
- JD – Joss-Drizzle (Joss et al. 1968), and
- JT – Joss-Thunderstorm(Joss et al. 1968),

two gamma DSDs, namely

- de Wolf – de Wolf (2001), and
- AU – (Atlas and Ulbrich 1974, cited Jiang et al. 1997),

four lognormal DSDs (Adimula and Olsen 1996), namely

- CS (continental shower),
- TS (tropical shower),
- CT (continental thunderstorm), and
- TT (tropical thunderstorm),

and the Weibull DSD,

- WB – Sekine et al. (1987).

The results shown in Figure 5-9 – Figure 5-19 were simulated in Matlab® as follows. First, the above-mentioned DSDs were normalized via the procedure mentioned in Chapter 2. The extinction cross section for spherical raindrops was then calculated. Thereafter the specific attenuation was evaluated as discussed in Chapter 3. As will be discussed in the following sections, each of the curves were fit to a power-law curve and the Crane (1980, 1996) attenuation model was applied to evaluate the path attenuation. The cumulative rain-rate distributions discussed in Chapter 4 could then be applied to obtain the probability that any particular path attenuation is exceeded.

Figure 5-9 shows the specific attenuation at frequency f = 19.5 GHz using the LP, MP, JT, JD and de Wolf DSDs. As discussed in Chapter 3 the specific attenuation at 19.5 GHz is influenced by the medium-sized raindrops. The effects of the number of larger and smaller raindrops tend to cancel out one another. Thus the specific attenuation for this frequency range (20 GHz – 30 GHz) is relatively inert to variations in the DSD.

The specific attenuation for the LP DSD and the de Wolf DSD are thus slightly greater than the MP DSD, which under-estimates the number of medium-sized drops. The JD DSD has the smallest concentration of medium-sized raindrops and thus the lowest specific attenuation.

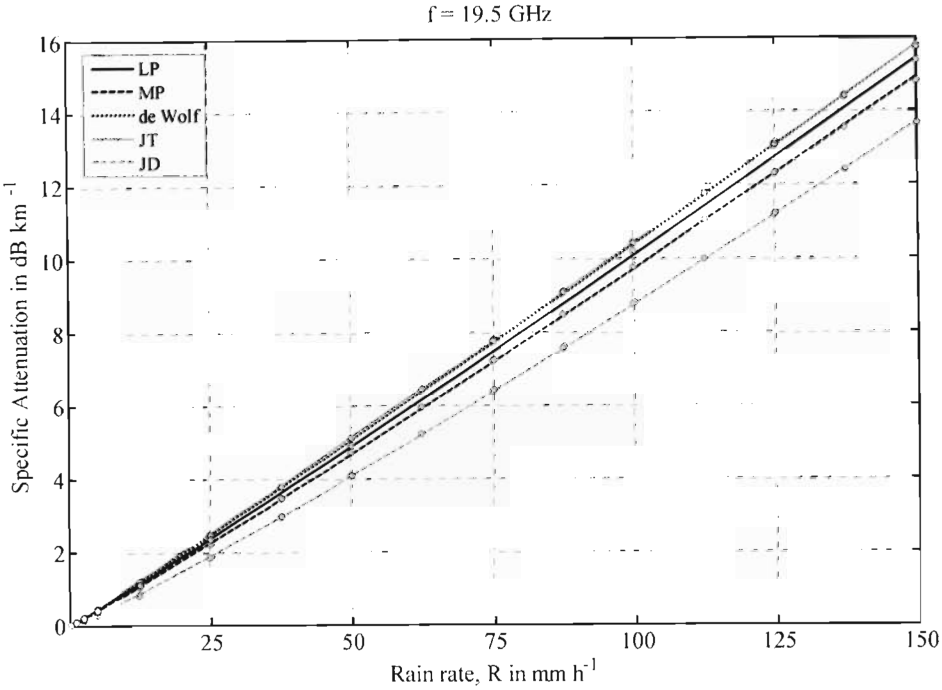

Figure 5-9 : Specific attenuation for f = 19.5 GHz, using the MP, JT and JD exponential DSDs, LP DSD and de Wolf gamma DSD.

At this frequency, the effects of the greater number of large raindrops are offset by the reduced number in small drops, and the JT DSD yields virtually the same as specific attenuation as the de Wolf DSD. This is also the reason why the lognormal DSD yield very similar specific attenuations. The specific attenuation using the four lognormal distributions, CS, TS, CT and TT are shown in Figure 5-10.

Specific attenuation for all the lognormal DSDs lie between that of the MP and JT DSDs. The MP and JT DSDs will thus serve as lower and upper bounds for these DSDs at 19.5 GHz. The specific attenuation for the WB and AU DSDs are shown in Figure 5-11. The results for WB also lie between these two bounds.

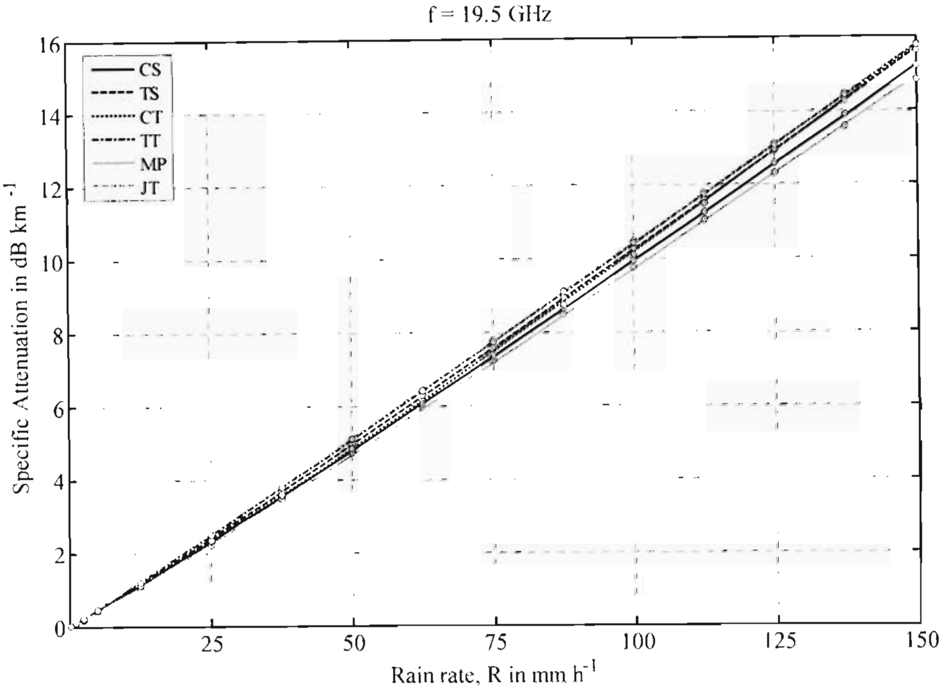

Figure 5-10 : Specific attenuation for f = 19.5 GHz, using the MP and JT exponential DSDs and CS, TS, CT and TT lognormal distributions.

The AU DSD is very similar to the WB DSD but has an increased number of raindrops of diameter D > 4 mm. This explains why for heavy rains R > 65 mm h^{-1} the specific attenuation for AU exceeds that of WB and the other DSDs.

The results presented in Figure 5-9 - Figure 5-11 apply for frequency band around 19.5 GHz. Similar analysis at frequencies f = 4, 12, 15, 40 and 80 GHz are provided in the Appendix D. In general the exponential DSDs provide a useful measure of the effect of DSD on the specific attenuation. The JD DSD shows the influence of the smaller raindrops while the JT indicates the effect of the larger raindrops. For application in rain attenuation, MP and LP are usually more suitable for calculation of the specific attenuation.

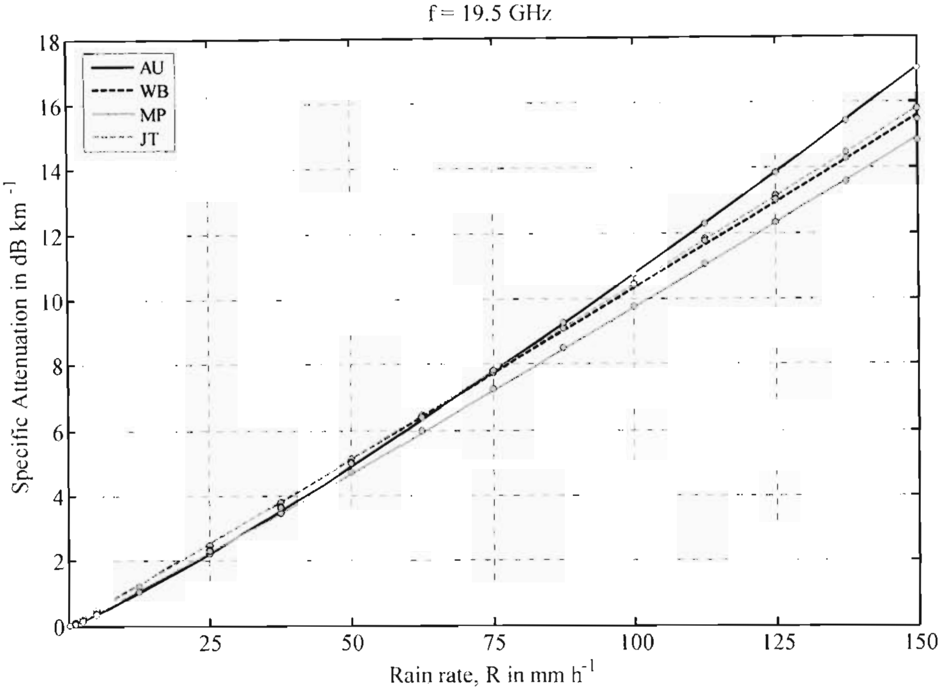

Figure 5-11 : Specific attenuation for *f* = 19.5, using the MP and JT exponential DSDs, AU gamma distribution and the WB Weibull distribution.

Nevertheless, DSDs often vary depending on the climatic and geographical region. This variation can significantly affect the specific attenuation and resulting path attenuation. As a result it may be more suitable to consider a set of DSDs when analysing the attenuation due to rain. Gamma and Weibull DSDs are highly favourable for the high-latitude regions while the lognormal DSDs are well suited for tropical and sub-tropical regions (equatorial and low-latitudes).

5.4 Path Attenuation for LOS link

Each of the specific attenuation curves shown in Figure 5-9 - Figure 5-11 can be related to the rain rate using the following power law

$$\lambda_R = \kappa R^{\alpha}, \tag{5.4}$$

where λ_R is the specific attenuation due to rain with units dB km^{-1}. The power-law parameters κ and α have been obtained for each of the above-mentioned DSDs and are given in Table 5-2. The Crane (1980, 1996) attenuation model can now be applied to evaluate the path attenuation. The procedure has been as described in Chapter 4. The results are shown in Figure 5-12.

Table 5-2 : The power law relationship parameters for the specific attenuation at 19.5 GHz for various DSDs

Drop Size Distribution	κ	α
LP – Laws and Parsons (1943)	0.0812	1.0472
Wolf – Gamma distribution (de Wolf 2001)	0.0873	1.0376
AU – Gamma distribution (Atlas and Ulbrich 1974)	0.0567	1.139
WB – Weibull distribution (Sekine et al. 1987)	0.0962	1.0155
Exponential DSDs		
JD – Joss – Drizzle (Joss et al. 1968)	0.0539	1.1052
JT – Joss – Thunderstorm (Joss et al. 1968)	0.0935	1.0239
MP – Marshall and Palmer (1948)	0.0743	1.0584
Lognormal DSDs (Adimula and Olsen 1996)		
CS – Continental Shower	0.0789	1.0501
CT – Continental Thunderstorm	0.0732	1.0718
TS – Tropical Shower	0.0821	1.0479
TT – Tropical Thunderstorm	0.0901	1.031

From the three exponential DSDs shown in Figure 5-12, JT has the greatest path attenuation followed by MP and then JD. This is expected from the specific attenuation analysis for 19.5 GHz in the previous section. The de Wolf gamma DSD lies very close to the JT DSD. All the lognormal DSDs have path attenuations between the JT and MP DSD.

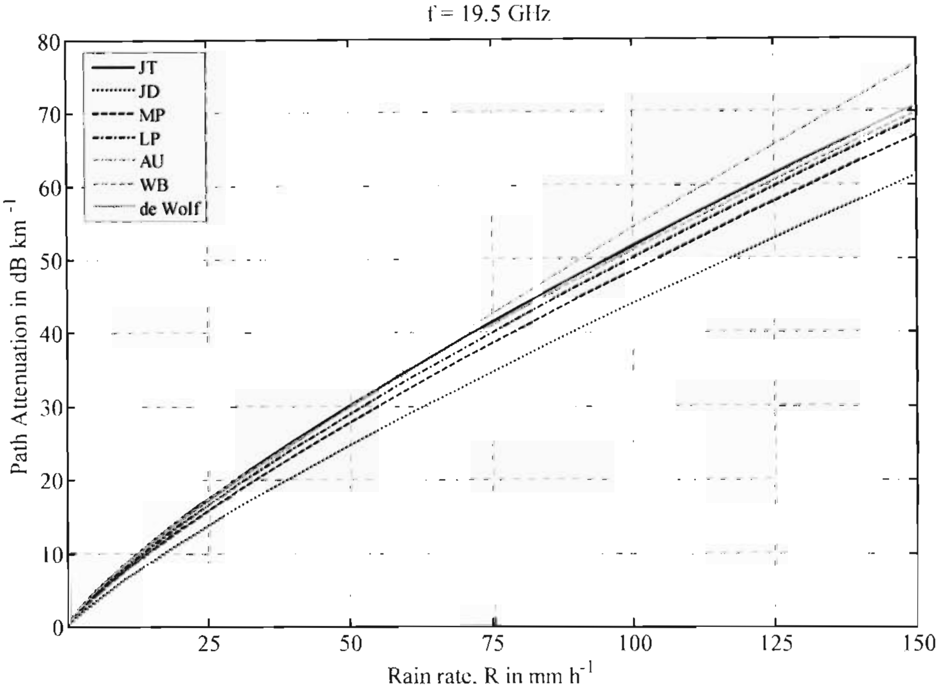

Figure 5-12 : Path attenuation for f = 19.5 GHz LOS link, using the MP, JT and JD exponential DSDs, LP DSD, de Wolf and AU gamma DSDs and the WB Weibull DSD.

At the frequencies around 19.5 GHz, the path attenuation is relatively invariant of the DSD. At others frequencies, the variations due to the DSD are quite considerable and can result in changes up to 50 % in the calculated path attenuation. To illustrate this effect analysis was also performed at frequencies f = 4, 12, 15, 40 and 80 GHz and the results are given in the Appendix D. A comparison of the path attenuation calculated using the above-mentioned DSDs are shown, together with the LOS link measurements in Figure 5-13.

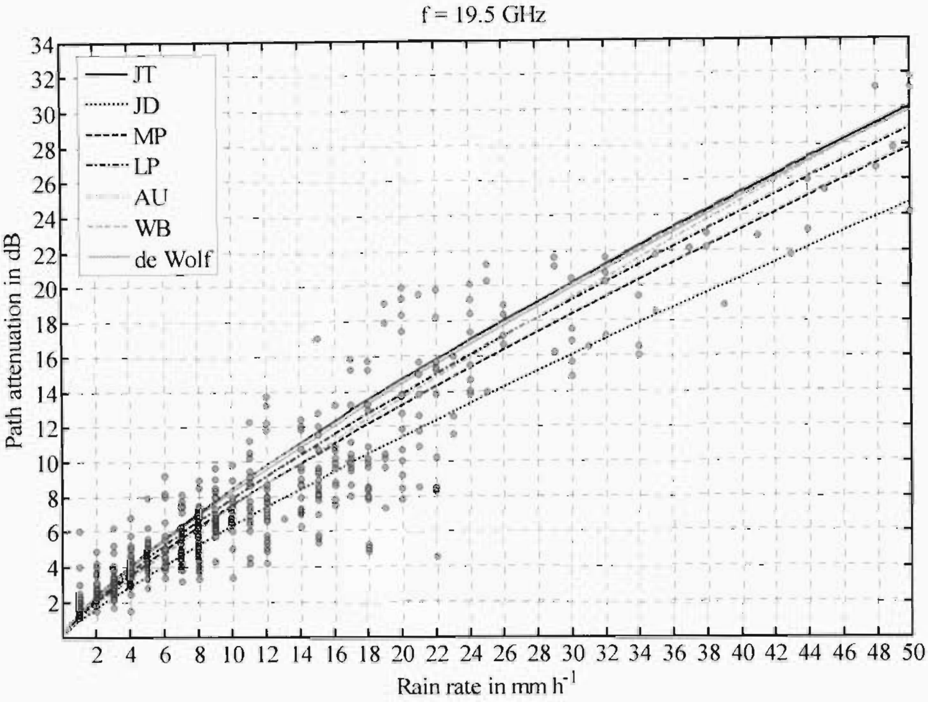

Figure 5-13 : Comparison of the path attenuation using the various DSDs and the LOS link measurements.

5.5 Path Attenuation exceedance probabilities

In Chapter 4, 1-minute rain-rate cumulative distributions were discussed. Using the theory of extremes (Lin 1976; Seeber 1985) and the Ajayi and Ofoche (1983) conversion ratio, 1-minute cumulative distributions where obtained. The ITU-R P.837 global rain-rate climate model, the Moupfouma and Martin (1987) model and the temperate model and tropical/subtropical model Moupfouma (1995) were also examined. These cumulative rain-rate distributions together with the path attenuation can be used to analyse the time any particular path attenuation is exceeded. The results for the proposed extreme-value model for Durban are shown in Figure 5-14.

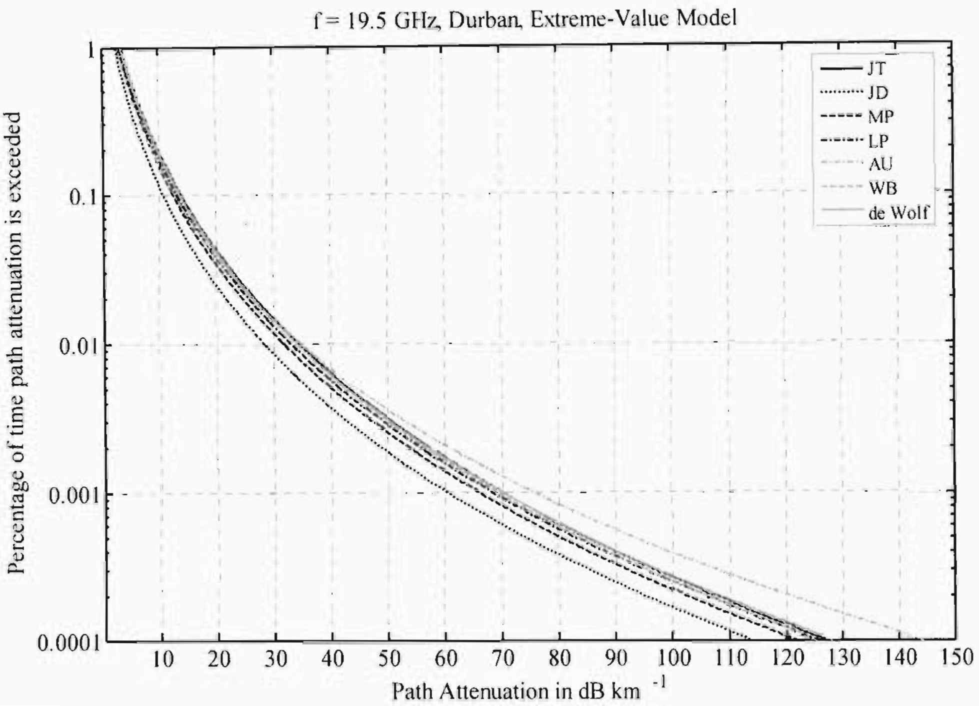

Figure 5-14 : Percentage of time path attenuation is exceeded using the proposed Extreme Value Model.

According to Figure 5-14, the path attenuation exceeded 0.01 % of the year is 28.3.dB for the JD DSD and 35.6 dB for the AU model. This means that for approximately, 53 minutes a year one can expect the path attenuation to exceed 28.3 dB – 35.6 dB. The exceedance for 0.001 % of the year (5.3 minutes) ranges from 60.5 dB for the JD DSD and 75.4 dB for the AU DSD. For frequencies above about 10 GHz the de Wolf gamma DSD (de Wolf 2001), was found to be most suitable for temperate-continental climates, such as that found in Durban, and the western part of South Africa. Using this DSD, the path attenuation exceeded 0.01 % of the year is 34.0 dB and for 0.001 % the attenuation exceeded is 69.9 dB. The results when using the Seeber (1985) extreme-value model are shown in Figure 5-15.

As illustrated in Chapter 4, the Seeber (1985) extreme-value predicts a smaller rain rate at the lower exceedences. Thus for 0.001 % of the year the attenuation exceeded ranges from about 49.2 dB – 60.9 dB. The results using the ITU-R P.837 model are shown in

Figure 5-16. The results for the Moupfouma (1987) model and the Moupfouma and Martin (1995) temperate and tropical/subtropical rain-rate models of are given in Figure 5-17 – Figure 5-19.

The lognormal distribution provides a good fit for 0.01% of the time and higher probabilities. At the low-percentages (i.e. < 0.01%) lognormal models may tend to over-estimate the attenuation and produce pessimistic results. This can be seen from the result in Figure 5-17 – Figure 5-19. The Moupfouma and Martin (1995) temperate and tropical/subtropical rain-rate models may be better suited for the lower probabilities. For 0.001 % of the year the attenuation exceeded ranges from about 56.4 dB – 70.2 dB for the temperate model and 43.7 dB – 54.1 dB for the tropical/subtropical model. Sufficient long-term measurements may prove the latter rain rate distribution model to be more suitable for Durban.

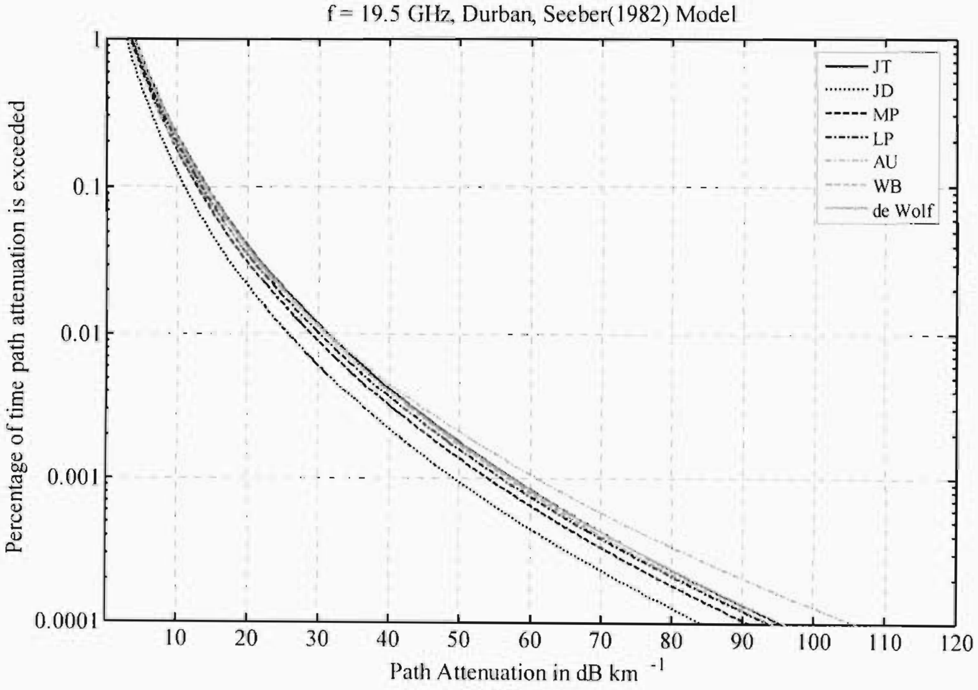

Figure 5-15 : Percentage of time path attenuation is exceeded using the Seeber (1985) extreme-value model.

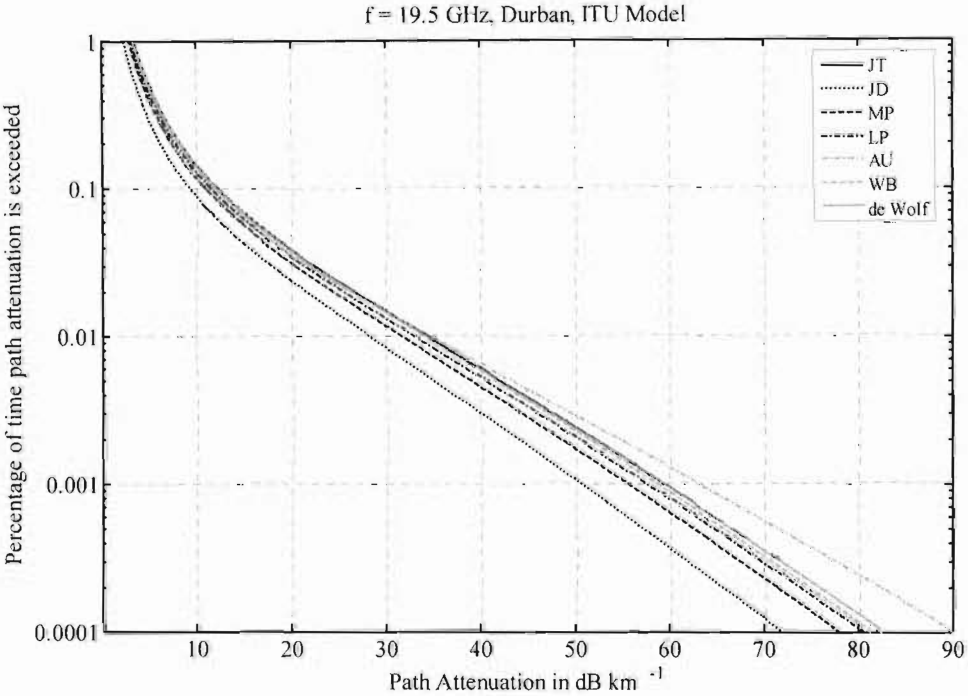

Figure 5-16 : Percentage of time path attenuation is exceeded using the ITU Model.

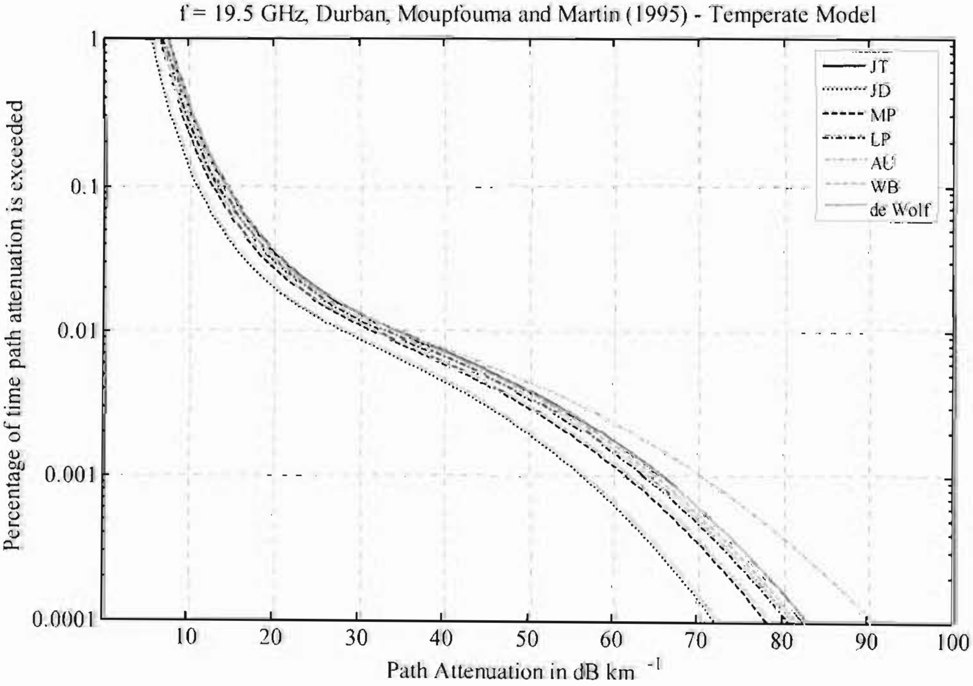

Figure 5-17 : Percentage of time path attenuation is exceeded using the Moupfouma (1995) temperate model.

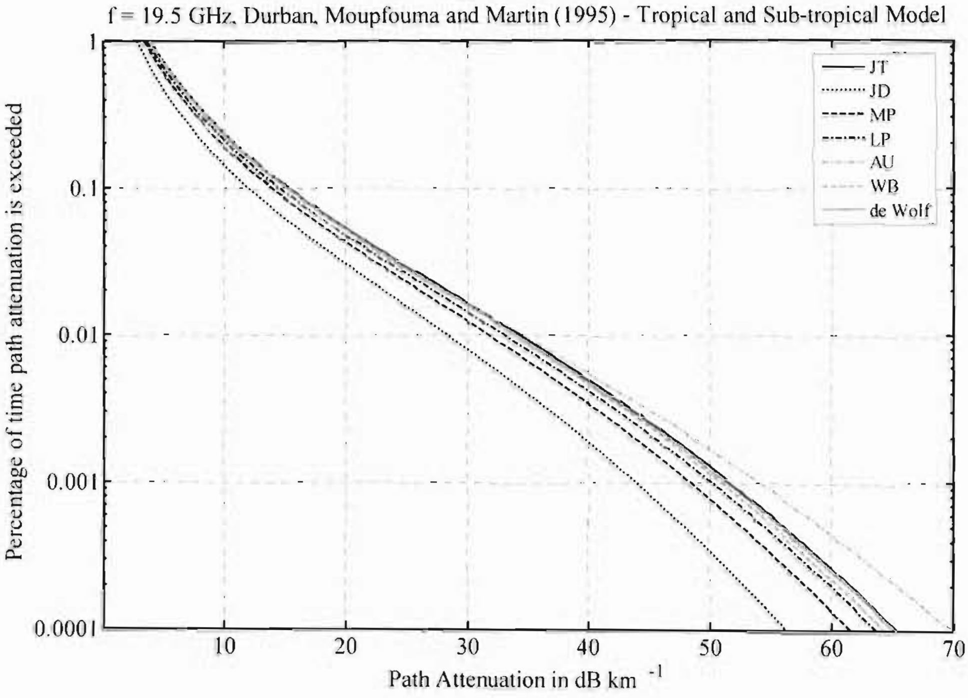

Figure 5-18 : Percentage of time path attenuation is exceeded using the Moupfouma (1995) tropical/subtropical model.

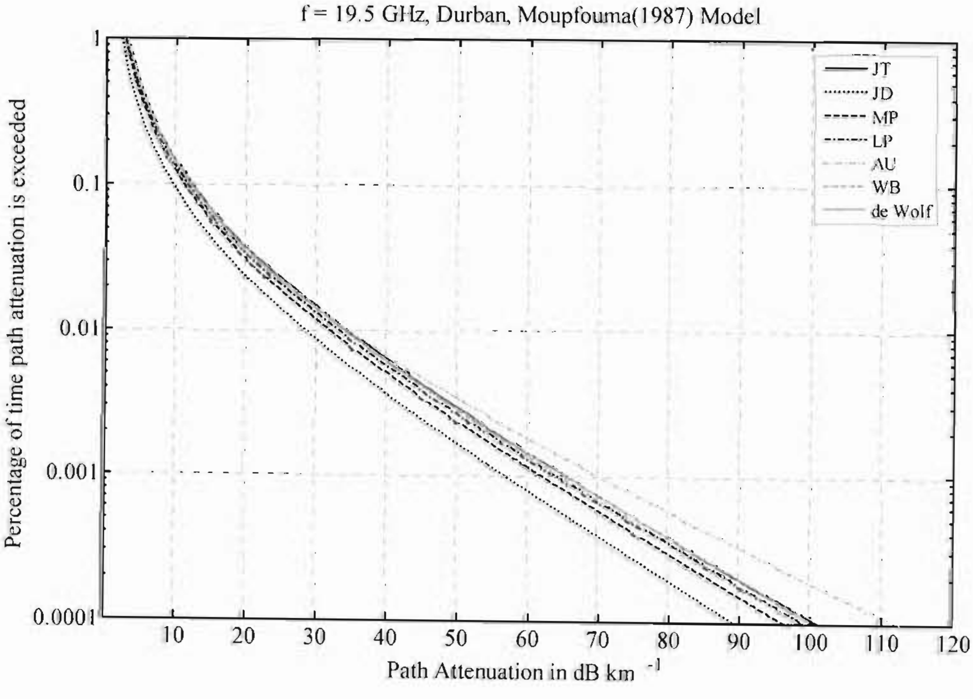

Figure 5-19 : Percentage of time path attenuation is exceeded using the Moupfouma and Martin (1987) model.

5.6 Conclusion

In this chapter the path attenuation and exceedance probabilities were evaluated for the 6.73 km LOS link established between the two campuses of the UKZN. The various LOS link details such as the equipment setup, link parameters, path profile and link budget were provided in Section 5.2. Sample link measurements were also given.

In Section 5.3 the specific attenuation was calculated using the exponential, gamma, lognormal and Weibull DSDs. From the three exponential DSDs, JT DSD had the greatest path attenuation followed by the MP DSD and then the JD DSD. This is as expected from the specific attenuation for 19.5 GHz. The specific attenuation for the de Wolf gamma DSD was very close to the JT DSD. All the lognormal DSDs have path attenuations between the JT and MP DSD and the Weibull DSD exhibited the highest specific attenuation for rain-rates exceeding approximately 65 mm h^{-1}.

The Crane (1980, 1996) attenuation model was then applied to convert the surface-point rain-rate to a path integrated rain-rate. The evaluation of the resulting path attenuation is given in Section 5.4. The results in this chapter focus on 19.5 GHz, the operating frequency of the LOS link. At the frequencies around 19.5 GHz, the specific attenuation and hence the path attenuation is relatively invariant of the DSD. This is because at 19.5 GHz the attenuation is strongly influenced by the medium-sized raindrops. At others frequencies, the variations due to the DSD are quite considerable and can result in changes up to 50 % in the calculated path attenuation. To illustrate this effect analysis was also performed at frequencies f = 4, 12, 15, 40 and 80 GHz and the results are given in Appendix D.

Finally, the various 1-minute rain-rate distributions discussed in Chapter 4 were applied to provide the exceedance probabilities for the path attenuation on the LOS link. The results using the proposed extreme value model for the 1-minute cumulative distributions, along with the Seeber (1985) model, the ITU-R P.837 global rain-rate climate model, the Moupfouma (1987) tropical and subtropical models and the Moupfouma and Martin (1995) model were presented. These cumulative rain-rate distributions together with the path attenuation can be used to analyse the time any particular path attenuation is exceeded.

Knowledge of the specific attenuation is invaluable to determine the path lengths, operating frequency and fade margins required for communication systems. During rain events, a large fade margin may often be required. It would be uneconomical to implement such margins since they are only needed for a fraction of the time. A model for the effect of rain attenuation would thus be a valuable tool for a systems designer. With such models the system designer can then determine the appropriate fade margin and resulting outage period for the link. For example with the proposed link operating at 19.5 GHz, if the de Wolf DSD model is applied, along with the proposed extreme value rain-rate model, the attenuation exceeded for 0.1 % (8.5 hours) will be 14 dB. For 0.01 % (53 minutes) of the year the attenuation is greater than 35 dB and for 0.001 % (5.3 minutes) the attenuation exceeds 70 dB. The designer can then decide what fade margin is necessary and what the resulting outage periods will be.

Chapter 6

Conclusion

For millimetre-wave communication systems, rain is a serious cause of attenuation and is the critical factor hindering system performance. Knowledge of the specific attenuation is invaluable to determine the path lengths, operating frequency and fade margins required for communication systems. Since the specific attenuation is heavily dependent on the DSD, the effect of the various DSDs on link availability needs to be examined and hence is the subject of this research.

During rain events, a large fade margin may often be required. It would be uneconomical to implement such margins since they are only needed for a fraction of the time. A cumulative distribution model of the fade depth and duration due to rain will thus be a valuable tool for a systems designer. With such models the system designer can then determine the appropriate fade margin and resulting outage period for the link.

The conversion of rain rate to specific attenuation is a crucial step in the analysis of the total path attenuation and hence radio-link availability. It is now common practice to relate the specific attenuation and the rain rate using the simple power law relationship. The power-law parameters are then used in the path attenuation model, where the spatial variations of rainfall are estimated by a path-integration of the rain rate. These power law parameters are strongly influenced by the DSD. There exists, fundamentally two forms of DSD. One form corresponds to the distribution of raindrops present in a unit volume of air, while the other corresponds to the distribution arriving at a surface of unit area. For the evaluation of the specific attenuation, we are interested in the former, while ground-based measurement devices often provide the latter. To convert between these two forms the terminal velocity of raindrops in air is required.

Many models for the DSD have been suggested in literature, from the traditional exponential, to the gamma, lognormal and Weibull distributions. The type of DSD varies depending on the geographical location and rainfall type. An important requirement of DSDs is that they are consistent with rain rate. i.e. the DSD must satisfy the rain-rate integral equation. Thus before application in the specific attenuation calculations, normalisation needs to be performed to ensure the consistency.

The specific attenuation was evaluated for spherical raindrops using the following theoretical and empirical drop size distributions

- LP – Laws and Parsons (1943),

three exponential DSDs, namely

- MP – Marshall Palmer (1948),
- JD – Joss-Drizzle (Joss et al. 1968), and
- JT – Joss-Thunderstorm(Joss et al. 1968),

two gamma DSDs, namely

- de Wolf – de Wolf (2001), and
- AU – (Atlas and Ulbrich 1974, cited Jiang et al. 1997),

four lognormal DSDs (Adimula and Olsen 1996), namely

- CS (continental shower),
- TS (tropical shower),
- CT (continental thunderstorm), and
- TT (tropical thunderstorm),

and the Weibull DSD,

- WB – Sekine et al. (1987).

Once the specific attenuation (dB/km) has been evaluated for necessary frequency and rain-rate range, the parameters for the power-law relation are determined. These parameters are then used to determine the path attenuation. Rain exhibits significant spatial and temporal variation. Hence the rain-rate profile along the propagation path is also required. Crane (1980) developed an attenuation model to convert the point rain-rate to a path-averaged rain rate. The only required inputs are the power-law parameters for the specific attenuation and the rain rate.

Using the above model, for a given radio-link path and frequency of interest, it is possible to determine the path attenuation for any given rain rate. Knowledge of the cumulative distributions of the fade depth and durations due to the rain are now needed. Depending on the link availability requirements, communication system designers may need the fade depth exceeded for 0.1, 0.01 or 0.001% of the time.

To perform this task knowledge of the surface-point rain rate is a prerequisite. Long term statistics of rain rates of short integration time are needed. Even an integration time of 5 minutes is insufficient to account for the substantial temporal and spatial variability of rain. Fortunately, truly instantaneous rain rates are not necessary since rapid fluctuations in the rain rate will not necessarily translate into equivalent fluctuations in attenuation due to the spatial averaging over the propagation path. For application in rain attenuation statistics, 1-minute rain rates have been found to be the most desirable, to remove variations due to rain gauge limitations, such as small sampling area and contamination due to atmospheric turbulences (Crane 1996). Hence 1-minute rates have been adopted as the standard for the evaluation of rain attenuation by researchers and the International Telecommunications Union (ITU).

In this study several models for the determining the surface-point 1-minute cumulative rain-rate distributions for South Africa were examined. An extreme-value model (Lin 1976; Seeber 1985) was examined for South Africa. Using the measurements of the rainfall extremes in WB36 (Department of Transport, 1974) and the conversion ratio of Ajayi and Ofoche (1983) it is possible to obtain 1-minute rain-rate distributions, as shown in this study. In the absence of reliable long-term data the global rain-rate climate models (Crane 1980; ITU-R P.837) can be used and were also examined. The ITU global rain-rate model provides superior results over the Crane global model and utilises bilinear interpolation to resolve distributions within each climatic zone. Unfortunately, the ITU model is less reliable in regions that display characteristics of two climatic types. Thus whenever possible, one should make use of available rainfall data to augment the global rainfall models. The models discussed thus far are based on the lognormal distribution. Such models are very reliable for the higher probabilities (0.01% and higher). For the lower probabilities (less than 0.01%), the gamma models are better suited. The Moupfouma (1987) lognormal model and the Moupfouma and Martin (1995) gamma models for temperate and tropical/subtropical regions have also been considered.

Finally, each rain-rate model is then used to evaluate the cumulative distributions of the fade depth and duration due to rain. For each rain-rate model, the effect of the choice of DSDs on link availability can then be examined. For microwave and millimetre-wave communication systems, the fade margin required to maintain system reliability is often too large and uneconomical to implement, since they are only needed for a fraction of the time. The cumulative distribution model of the fade depth and duration due to rain will thus be a valuable tool for a systems designer. With such models the system designer can then determine the appropriate fade margin and resulting outage period for a given radio-link path.

6.1 Summary of Dissertation

The numerical calculation of the scattering and attenuation of electromagnetic waves by rain requires detailed knowledge of the microphysical properties of raindrops such as raindrop size, fall velocity and drop-size distribution (DSD). This is the focus of Chapter 2 of this dissertation.

Firstly the fall velocity of raindrops is examined using the Gunn and Kinzer (1949) measurements of the terminal velocity at sea level and several analytical descriptions thereof are discussed in Section 2.2. It is shown that a polynomial model of order 3 can provide good approximate of the terminal velocity at sea level. Thereafter models for arbitrary atmospheric conditions are examined, concluding with the Best (1950) model for variation with height in the S.T. and I.C.A.N. standard atmospheres. The terminal velocity is essential for evaluating the consistency of DSD with rain rate and in the normalisation procedure.

The size and shape of a raindrop is required for the calculations of the scattering and extinction cross section of a single raindrop. A brief preamble to raindrop scattering is given in Section 2.3. Mie scattering calculations are extremely computationally complex for non-spherical shapes, such as for spheroidal and realistically raindrops (e.g. Pruppacher and Pitter 1971), hence the classical approach of using spherical raindrops has been adopted. Matzler (2003) showed that the specific attenuation although not exactly the same as that calculated using Mie theory for spherical raindrops, requires only a small correction (less than 8 %).

To extend the scattering and extinction model of a single raindrop to that experienced during a rain event, the drop-size distribution of raindrops is required. DSDs exhibit significant spatial and temporal variability. The average DSDs for several rainfall types were thus examined in Section 2.4. Firstly, the Laws and Parson (1943) drop-size distribution measurements are discussed along with gamma function approximations thereof. Thereafter exponential DSDs were examined. The importance of self-consistency with rain rate was discussed. Thereafter gamma, lognormal and Weibull DSD models are examined. To ensure that the DSDs satisfy the rain-rate integral equation, each DSDs is normalised using a second order polynomial of the logarithm of the rain rate.

This chapter is concluded with an investigation of the dielectric properties of water in Section 2.5. The Debye approximations and empirical models of Ray (1972) and Liebe (1991) are examined for frequencies up to 1 THz. The frequency and temperature dependent complex refractive index of water is instrumental in the calculation of the total and scattering cross-section of raindrops.

Typical raindrops have diameters ranging from 0.1 mm to 7 mm. Thus, for the millimetre-wave frequency range the drop-size is comparable to wavelength hence Mie scattering theory is applicable. Evaluation begins with the computation of the extinction and scattering cross sections of a single raindrop in Section 3.3.

In Section 3.4 the specific attenuation is evaluated using the DSD models discussed in Chapter 2. This includes the conventional exponential distributions, along with more sophisticated DSDs such as the gamma, lognormal and Weibull distributions. These

DSD models overcome the shortfalls of the exponential distributions which tend to over-estimate the number of small and large raindrops.

In Chapter 4 the global rain rate models was introduced. These models are based upon the climatic classification of the region. Crane's global rain-rate climate model and the ITU-R P.837 global rain-rate model have been discussed and simulated for the South African climates.

Thereafter, methods of obtaining surface-point cumulative rain-rate distributions have been discussed. Using the theory of extremes (Lin 1976; Seeber 1985), 1-minute cumulative distributions have been obtained and compared to the global rain-rate climate models (Crane 1980; ITU-R P.837). Alternative techniques (Moupfouma 1987; Moupfouma and Martin 1995) have also been examined.

Finally the Crane (1980) attenuation model was discussed to convert the point rain-rate to a path-averaged rain rate.

A 19.5 GHz terrestrial link was setup between Howard College and Westville campuses of the UKZN. The communication link is 6.3 km long and employs vertical polarization. In Chapter 5 sample link measurements taken over link were discussed. The various LOS link details such as the equipment setup, link parameters, and path profile and link budget were provided in Section 5.2.

In Section 5.3 the specific attenuation was calculated using the above mentioned DSDs. From the three exponential DSDs, JT DSD had the greatest path attenuation followed by the MP DSD and then the JD DSD. This is as expected from the specific attenuation for 19.5 GHz. The specific attenuation for the de Wolf gamma DSD was very close to the JT DSD. All the lognormal DSDs have path attenuations between the JT and MP DSD and the Weibull DSD exhibited the highest specific attenuation for rain rates exceeding approximately 65 mm h^{-1}.

At the frequencies around 19.5 GHz, the specific attenuation and hence the path attenuation is relatively invariant of the DSD. This is because at 19.5 GHz the attenuation is strongly influenced by the medium-sized raindrops. At others frequencies, the variations due to the DSD are quite considerable and can result in changes up to 50 % in the calculated path attenuation. To illustrate this effect analysis was also performed at frequencies f = 4, 12, 15, 40 and 80 GHz and the results are given in the Appendix.

From these results it may be seen that in general the exponential DSDs, tend to underestimate the mediums-sized raindrops and overestimate the small and large sized raindrops. The JT DSD has an increased number of large drop-sizes while the JD DSD the concentration is dominated by the smaller raindrops. Their effects on the specific attenuation can be seen by analysis of the lower frequencies, below 12 GHz and larger frequencies, above 19.5 GHz. At the lower frequencies the larger drop sizes dominate and hence the JT DSD will provide the highest specific attenuation and thus act as an upper bound. Similarly, the JD DSD will result in smallest specific attenuation and behave as a lower bound. There use will thus result in a pessimistic and optimistic model, respectively. For a better reflection of the average DSD for moderate and higher rain rates, the MP DSD should be used. The LP DSD is also used frequently and adopted as a standard by the ITU. It is valid for many climates.

As the frequency increases, the medium-sized and smaller raindrops begin to dominate. Thus to overcome the shortfall of the exponential distributions (i.e. the tendency to over-estimate the number of small and large raindrops), more sophisticated DSDs are needed. The gamma and Weibull DSDs are found to be highly suitable for millimetre wave application in the mid- and higher latitudes. For the Durban climate (temperate-continental) the de Wolf DSD should serve as a good reflection of the DSD shape. For subtropical and tropical regions, especially in the equatorial regions, the lognormal DSD is often better suited. In these regions the DSDs exhibit greatest concentration in the mediums-sized raindrops and the choice of an exponential DSD as been found to be generally inadequate.

In Section 5.4, the Crane (1980, 1996) attenuation model was then applied to convert the surface-point rain-rate to a path integrated rain-rate. The evaluation of the resulting path attenuation is given for the 19.5 GHz LOS link. The results for the other frequencies are shown in the Appendix D.

Finally, the various 1-minute rain-rate distributions discussed in Chapter 4 were applied to provide the exceedance probabilities for the path attenuation on the LOS link. The results using the proposed extreme value model for the 1-minute cumulative distributions, along with the Seeber (1985) model, the ITU-R P.837 global rain-rate climate model, the Moupfouma (1987) tropical and subtropical models and the Moupfouma and Martin (1995) model were presented. These cumulative rain-rate distributions together with the path attenuation can be used to analyse the time any particular path attenuation is exceeded.

The climate-based rain-rate models provide a useful estimate of the rain-rate distribution, when there is a lack of meteorological data. The models are however coarse and based on the climatic designation. Crane's global rain-rate climate model and the ITU-R P.837 global rain-rate model have been considered and simulated for the South African climates. The ITU model does provide superior results over the Crane's global model since it relies on bilinear interpolation to provide a superior resolution within each climatic zone. However this interpolation is still based on the climatic maps, hence the problem of climatic resolution is still not resolved. Locations that exhibit a combination of two or more climates will not be estimated accurately. Thus whenever possible, one should take advantage of the available rainfall records that are reliable and comprehensive to augment these global maps.

The extreme-value model is one such model that can provide good results, especially for probabilities exceeding 0.01%. An alternative model is suggested in Moupfouma (1987). For the low probabilities (less than 0.01%), a gamma model might be better suited. A reliable model is provided in Moupfouma and Martin (1995) for temperate climates, and tropical/subtropical climates.

Knowledge of the specific and path attenuation is invaluable to determine the path lengths, operating frequency and fade margins required for communication systems. During rain events, a large fade margin may often be required. It would be uneconomical to implement such margins since they are only needed for a fraction of the time. A model for the effect of rain attenuation would thus be a valuable tool for a systems designer. With such models the system designer can then determine the appropriate fade margin and resulting outage period for the link. For example with the proposed link operating at 19.5 GHz, if the de Wolf DSD model is applied, along with the proposed extreme value rain-rate model, the attenuation exceeded for 0.1 % (8.5 hours) will be 13.6 dB. For 0.01 % (53 minutes) of the year the attenuation is greater than 34 dB and for 0.001 % (5.3 minutes) the attenuation exceeds 69.9 dB. The designer can then decide what fade margin is necessary and what the resulting outage periods will be.

6.2 Future Work

The size and shape of a raindrop is also required in scattering and extinction cross sections calculations. In this study, to reduce computation time, spherical raindrops have been assumed. This introduces a polarization error, where the attenuation calculated by the model will be slightly greater than that observed for vertical polarisations and smaller than that observed for horizontal polarizations. Preliminary studies on the raindrop shape have been undertaken and are provided in Appendix A. Future work should incorporate these drop shape models into the evaluation of rain attenuation.

Appendix A

A.1 Raindrop Shape

The size of raindrops can vary from the tiniest drops with diameters as little as 0.1 mm, which is comparable to droplets found in clouds, to relatively large drops with diameters of 7.0 mm. Raindrops will rarely get larger than diameters of 7 mm since they become hydrodynamically unstable and break up very quickly during their fall. This large variation in drop size is met with an equal variation in drop shape. Preliminary studies on the shape of raindrops has been performed and presented in this appendix.

Knowledge of drop shape and their variation with drop size is essential for the calculation of the scattering and extinction cross sections. Mie scattering calculations are computationally intense for non-spherical shapes, such as those discussed in this appendix, thus to reduce computation time, the classical approach of using spherical raindrops was adopted in this study. Furthermore, in this study the focus is primarily on the influence of the DSD on rain attenuation. The presented models for the drop shape can be used in the future studies to evaluate the scattering and extinction cross sections for realistically shaped raindrops and hence include the effects of drop shape to this study.

The shape of raindrops has been examined photographically by many investigators (e.g. Jones 1959; Pruppacher and Beard 1970; Ugai et al. 1977 and Andsager et al. 1999). These studies have shown that the common approach of assuming a spherical raindrop is misleading. From their extensive wind-tunnel measurements, Pruppacher and Beard (1970) demonstrated that at terminal velocity only drops with diameter $D \leq 0.3$ mm have no measurable deformation and can be considered spherical.

Using these measurements, Pruppacher and Pitter (1971) and Beard and Chuang (1987, 1990) have developed semi-empirical expressions to describe the equilibrium shape of raindrops falling at terminal velocity. It was shown that for 0.3 mm $< D <$ 1.0 mm, raindrops are slightly deformed and may be approximated by oblate spheroids. This deformation increases progressively and in the diameter range 1.0 mm $< D <$ 4.0 mm raindrops are deformed into asymmetric oblate spheroids with a flat base. This flattening of the base becomes increasingly pronounced for the larger drop sizes.

Using first-order perturbation theory, Pruppacher and Pitter (1971) further showed that $D >$ 4.0 mm a concave depression begins to form at the centre of the flattened base, once again becoming more pronounced as the drop size increases. However this is where Pruppacher and Pitter (1971) and Beard and Chuang (1987, 1990) differ. Beard and Chuang (1987) showed that such depressions will rarely occur at equilibrium and may be observed primarily in oscillating drops, as collaborated by photographic measurements, which indicated only a pronounced flat base.

Because of the non-uniformity in the shape, raindrops cannot be unambiguously described by a single length. Throughout this study and all calculations the equivolumetric or effective diameter, simply referred to as the drop diameter D, is used. This is the diameter of a sphere with the same volume as that of the deformed raindrop. In some cases it may be more convenient to use the equivolumetric or effective radius a_0, where $a_0 = 0.5D$.

A.2 Raindrop Axial Ratios

One of the simplest measures of drop distortion is given by the axial ratio a/b. This is the ratio of the height $2a$, which is the distance from the top to the silhouette base of the drop, and $2b$, the maximum width of the drop.

A cross-sectional view of a deformed raindrop is shown in Figure A-1. The cross-section is given as a polar plot of the meridional plane passing through the centre of the drop. The surface of the raindrop can thus be described by the polar coordinates r and θ shown below. Note that r is equal to the effective radius a_0 only when the raindrop is spherical in shape.

To reduce the computational complexity several authors (e.g. Oguchi 1973, 1983) have approximated the deformation of raindrops as oblate spheroids. In their studies a linear relationship between the axial ratio and drop diameter was assumed.

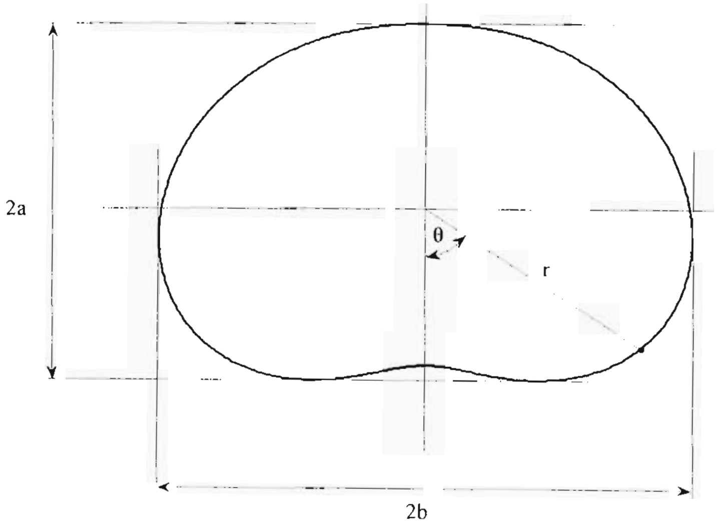

Figure A-1 : Cross-section view of a raindrop.

Two such linear fits are A and B are given by

$$A = \frac{a}{b} = 1 - 0.05D \quad \text{and} \quad B = \frac{a}{b} = 1 - \left(\frac{0.41}{9}\right) \cdot D. \tag{A.1}$$

From their wind-tunnel measurements Pruppacher and Beard (1970) also suggested a linear relationship. Their empirical formula is given by

$$\frac{a}{b} = 1.030 - 0.062D \tag{A.2}$$

However, these linear fits tend to overestimate the deformation of small raindrops and underestimate the larger drop sizes. Pruppacher and Pitter (1971) provided a more accurate perturbation model to the experimental measurements. Their results have been used by numerous subsequent authors. A revised numerical model was developed by Beard and Chuang (1987) and is written as

$$\frac{a}{b} = 1.0048 + 0.0057 \cdot \left(\frac{D}{10}\right) - 2.628 \cdot \left(\frac{D}{10}\right)^2 + 3.682 \cdot \left(\frac{D}{10}\right)^3 - 1.677 \cdot \left(\frac{D}{10}\right)^4 \tag{A.3}$$

The above-mentioned axial ratios along with the Pruppacher and Pitter (1971) and Beard and Chuang (1987) measurements are illustrated in Figure A-2. The two linear approximations A and B have been shown as light dashed lines.

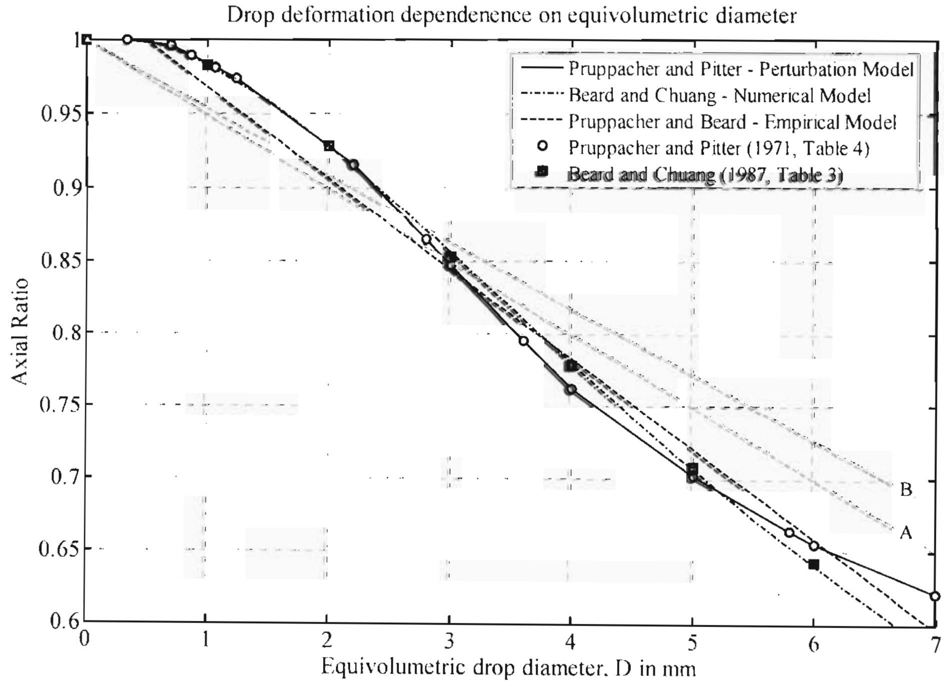

Figure A-2 : Raindrop axial ratios as a function on drop diameter.

A.3 Oblate Spheroidal Raindrops

Oguchi (1973) used the axial ratio B, given in (A.1) and approximated the deformation of raindrops as oblate spheroids. For oblate spheroidal raindrops, the shape is defined by the minor and major semiaxes, which in return can be related to the effective drop diameter via the axial ratios. Using the axial ratio B, given in (A.1), the minor and major semiaxes for effective drop diameters within the range 0.5 mm < D < 7.0 mm have been calculated and are specified in Table A-1.

Table A-1 : Effective diameter and minor and major semiaxes for oblate spheroidal raindrops

Effective Radius, *D* (mm)	Minor semiaxis, *a* (mm)	Major semiaxis, *b* (mm)
0.25	0.24619	0.25193
0.50	0.48470	0.50783
0.75	0.71543	0.76791
1.00	0.93830	1.03236
1.25	1.15319	1.30141
1.50	1.36001	1.57531
1.75	1.55865	1.85431
2.00	1.74899	2.13871
2.25	1.93090	2.42881
2.50	2.10427	2.72495
2.75	2.26895	3.02751
3.00	2.42481	3.3369
3.25	2.57169	3.65355
3.50	2.70944	3.97798

A cross-sectional view of the shape of 6 selected drops, namely D = 0.5, 2.5, 4.0, 5.0, 6.0 and 7.0 mm, from Table A-1 is illustrated in Figure A-3. Each cross section is a polar plot of the meridional plane passing through the centre of the oblate spheroid. All plots have been normalised relative to the effective radius a_0, where $a_0 = 0.5D$ to better illustrate their deformation relative to that of an equivolumetric sphere.

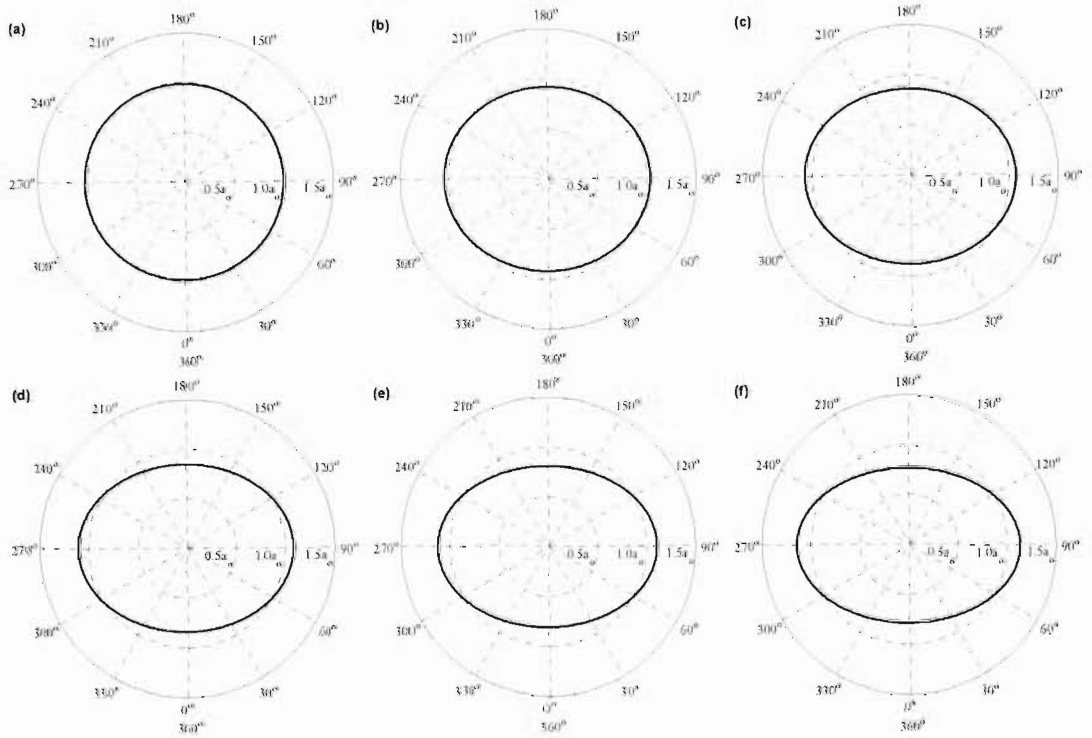

Figure A-3 : Shape of oblate spheroidal raindrops with D = 0.5, 2.5, 4.0, 5.0, 6.0 and 7.0 mm, (a) - (f) respectively.

A.4 Pruppacher and Pitter Raindrop Shape

For a more realistic representation of drop shape the semi-empirical model of Pruppacher and Pitter (1971) can be used. Pruppacher and Pitter (1971) numerically solved the pressure balance equation for raindrops falling at terminal velocity and this resulted in a good agreement between theory and the experimental measurements. The drop surface is represented by a cosine series fit as follows

$$r = a_0\left(1 + \sum_{n=0}^{\infty} c_n \cos n\theta\right) \tag{A.4}$$

where a_0 is the equivolumetric radius, c_n are the deformation coefficients and r and θ are the polar coordinates as shown in Figure A-1. Normalisation relative to a_0 yields

$$r' = \frac{r}{a_0} = \left(1 + \sum_{n=0}^{\infty} c_n \cos n\theta\right) \tag{A.5}$$

Pruppacher and Pitter (1971) showed that truncation of the cosine series at c_9 is possible without any noticeable error. The values of the deformation coefficients are provided in Table A-2.

Table A-2 : Deformation coefficients for selected effective radii, from Pruppacher and Pitter (1971, Table 4)

Effective Radius, a_0 (mm)	**Deformation coefficients, $\times 10^5$**								
	c_0	c_2	c_3	c_4	c_5	c_6	c_7	c_8	c_9
0.1711	−12	−36	−3	0	0	0	0	0	0
0.3505	−69	−208	−27	0	1	0	0	0	0
0.433	−181	−543	−97	−3	5	−2	0	0	0
0.532	−314	−939	−189	−12	10	−1	0	−1	0
0.62	−447	−1334	−300	−27	17	−2	1	−1	1
1.10	−1431	−4259	−1105	−173	632	25	3	−12	−4
1.40	−2344	−6977	−1843	−288	101	42	5	−19	−7
1.50	−2670	−7948	−2214	−330	115	48	5	−22	−8
1.80	−3659	−10889	−2963	−462	156	65	8	−30	−11
2.00	−4296	−12783	−3539	−551	182	77	9	−35	−13
2.50	−5734	−17053	−4959	−775	237	102	12	−47	−18
2.90	−6822	−20280	−6166	−971	274	122	14	−55	−21
3.00	−7089	−21070	−6482	−1023	283	127	15	−57	−22
3.50	−8380	−24888	−8151	−1310	318	149	18	−67	−25
4.00	−9763	−28966	−10143	−1677	346	173	21	−76	−29

A cross-sectional view of the shape of 9 selected drops, namely a_0 = 0.35, 0.62, 1.1, 1.5, 2.0, 2.5, 3.0, 3.5 and 4.0 mm, from Table A-2 is illustrated in Figure A-4. Once again each cross section is a polar plot of the meridional plane passing through the centre of the drop and all plots have been normalised relative to the equivolumetric radius a_0.

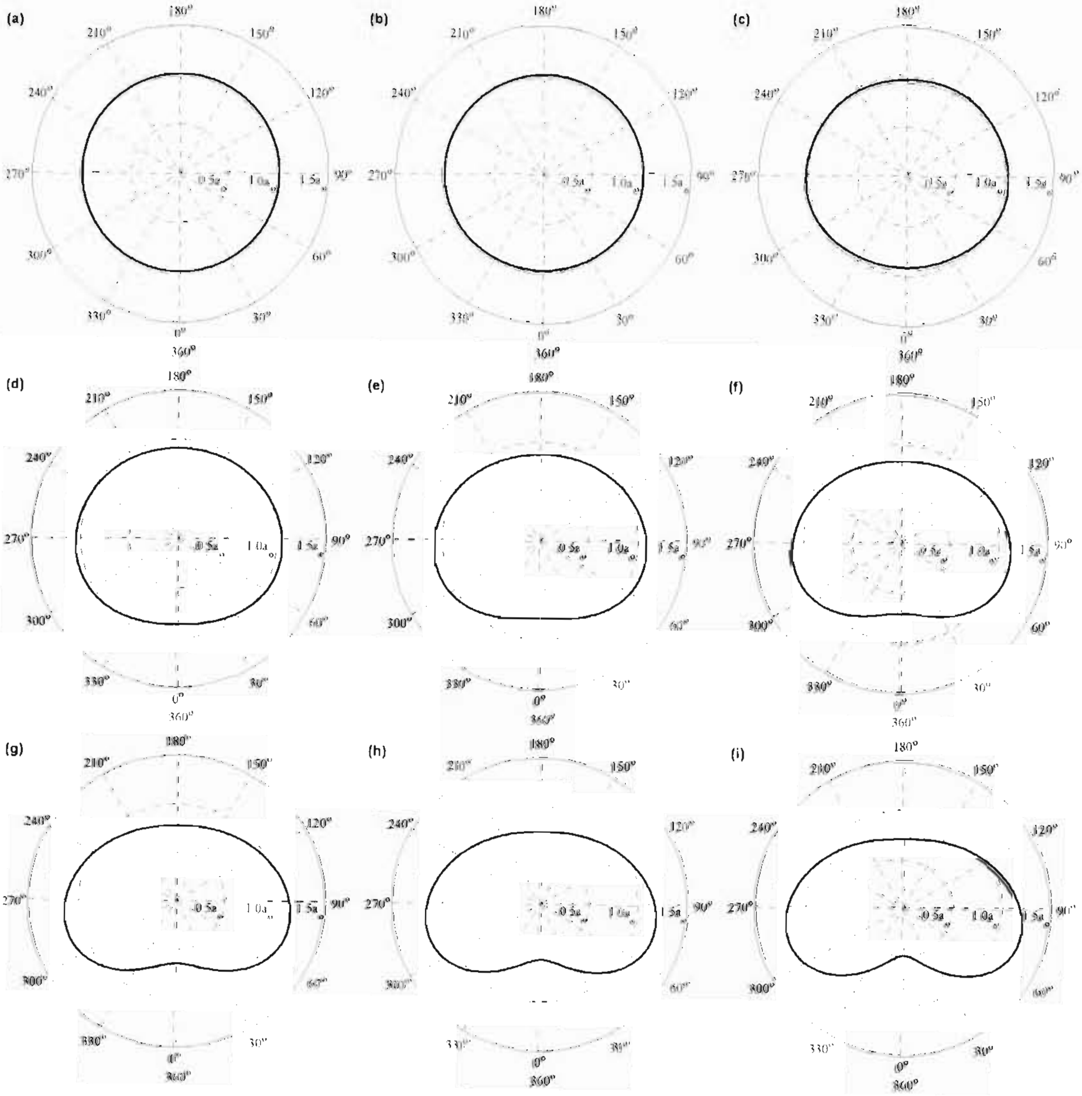

Figure A-4 : Shape of Pruppacher and Pitter (1971) raindrops with effective radius a_0 = 0.35, 0.62, 1.1, 1.5, 2.0, 2.5, 3.0, 3.5 and 4.0 mm, shown in (a) - (i), respectively.

As shown in Figure A-4, raindrops are only slightly deformed for $D < 1.0$ mm. The deformation increases dramatically thereafter with a concave depression emerging for $D < 4.0$ mm. This deformation is clearly non-linear with respect to drop size. This considerable non-linearity can be seen in the corresponding axial ratio for Pruppacher and Pitter (1971) perturbation model as shown in Figure A-2.

The Pruppacher and Pitter (1971) raindrop shape has been subsequently used by several authors in the evaluation of rain attenuation and cross-polarization. An excellent example is provided Oguchi (1977), where the deformation coefficients were re-evaluated for the 13 radii appearing in the Laws and Parson (1949) drop-size distribution.

A.5 Beard and Chaung Raindrop Shape

In Beard and Chuang (1987), a revised model for equilibrium drop shape was developed. It was shown that the concave depression in Pruppacher and Pitter (1971) will rarely occur at equilibrium since a very high base pressure is necessary. For $D < 2$ mm, the new model deviates little from the perturbation model of Pruppacher and Pitter (1971). However, as the drop diameter increases the difference between these two models becomes more noticeable, with the revised model predicting a more flattened base than Pruppacher and Pitter (1971) model.

The revised model provided a better fit to the photographic measurements of Pruppacher and Beard (1970) for 2 mm $< D <$ 6 mm. For $D > 6$ mm, the model underestimates the flattening of the base. This was corrected in Beard and Chuang (1990). The adjusted model of Beard and Chuang (1990) is valid for 1 mm $< D <$ 9 mm.

The deformation of the drop surface is again modelled by the cosine series in (A.4). The coefficients are provided in Table A-3.

Table A-3 : Coefficients for effective diameter 2.0 mm < D < 6.0 mm, from Beard and Chuang (1987, Table 4)

Effective Radius, a_0 (mm)	**Deformation coefficients, $\times 10^4$**										
	c_0	c_1	c_2	c_3	c_4	c_5	c_6	c_7	c_8	c_9	c_{10}
0.50	-28	-30	-83	-22	-3	2	1	0	0	0	0
0.75	-72	-70	-210	-57	-6	7	3	0	-1	0	1
1.00	-134	-118	-385	-100	-5	17	6	-1	-3	-1	1
1.25	-211	-180	-592	-147	4	32	10	-3	-5	-1	2
1.50	-397	-247	-816	-188	24	52	13	-8	-8	-1	4
1.75	-388	-309	-1042	-221	53	75	15	-15	-12	0	7
2.00	-481	-359	-1263	-244	91	99	15	-25	-16	2	10
2.25	-573	-401	-1474	-255	137	121	11	-36	-19	6	13
2.50	-665	-435	-1674	-258	187	141	4	-48	-21	11	17
2.75	-755	-465	-1863	-255	242	157	-7	-61	-21	17	21
3.00	-843	-472	-2040	-240	299	168	-21	-73	-20	25	24
3.25	-930	-487	-2207	-222	358	175	-37	-84	-16	34	27
3.50	-1014	-492	-2364	-199	419	178	-56	-93	-12	43	30

Beard and Chuang (1990) provides one of the most accurate drop shape models to date and if required it can also consider the influence electric stress caused by external electric fields and surface charges on the behaviour of drop shape. The results shown here have ignored such effects since the equilibrium drop shape is sufficient for this study.

A cross-sectional view of the shape of 6 selected drops, namely a_0 = 1.0, 1.5, 2.0, 2.5, 3.0 and 3.5 mm, from Table A-3 is illustrated in Figure A-5. Each cross section is normalised relative to the equivolumetric radius a_0.

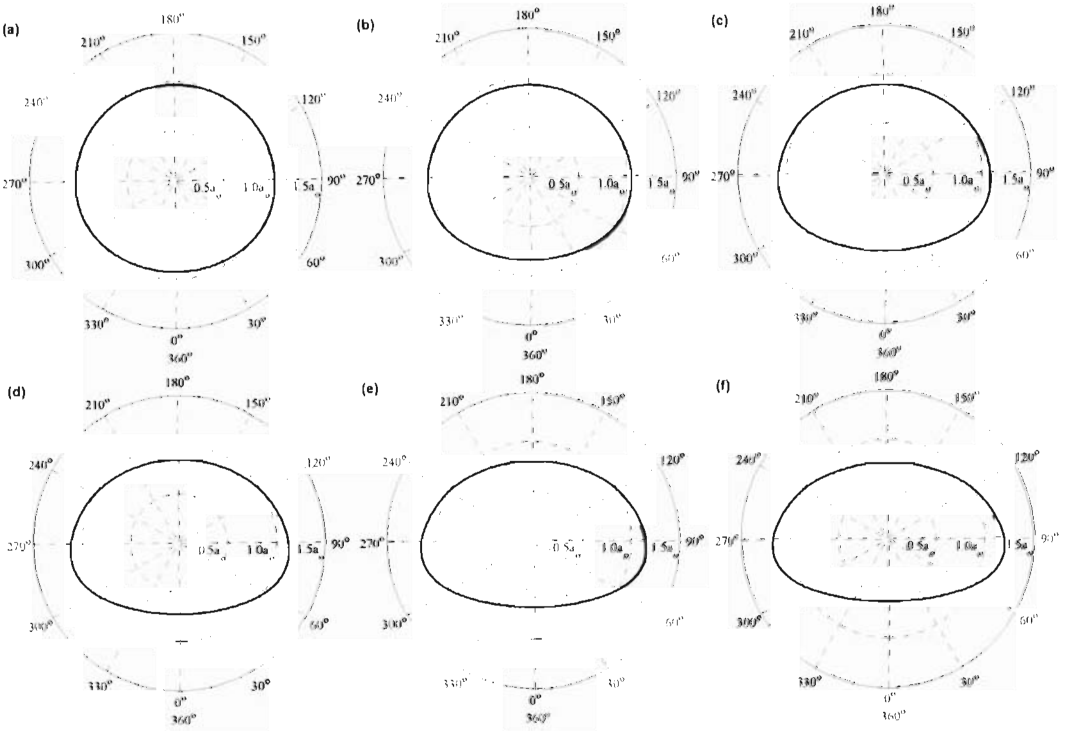

Figure A-5 : Shape of Beard and Chaung (1990) raindrops with a_0 = 1.0, 1.5, 2.0, 2.5, 3.0 and 3.5 mm, (a) - (f) respectively.

A.6 Comparison of Raindrop Shape Models

In this appendix oblate spheroidal, Pruppacher and Pitter (1971) and Beard and Chuang (1990) shapes have been examined. A comparison of these drop shape models is given in Figure A-6. The oblate spheroidal raindrops are shown on the top, Pruppacher and Pitter (1971) raindrops in the middle and the Beard and Chuang (1990) model at the bottom. For each of these models, raindrops of size a_0 = 0.5, 1.0, 1.5, 2.0, 2.5, 3.0 and 3.5 mm have been shown. As previously, each cross section is a polar plot of the meridional plane passing through the centre of the raindrop. However, this time, all cross section shapes have been drawn to the same scale (i.e they are not normalized). Spheres with effective radius a_0 = 1.0, 2.0, 3.0, 4.0 and 5.0 mm have also been shown for comparison as dashed circles divided into 30° sectors.

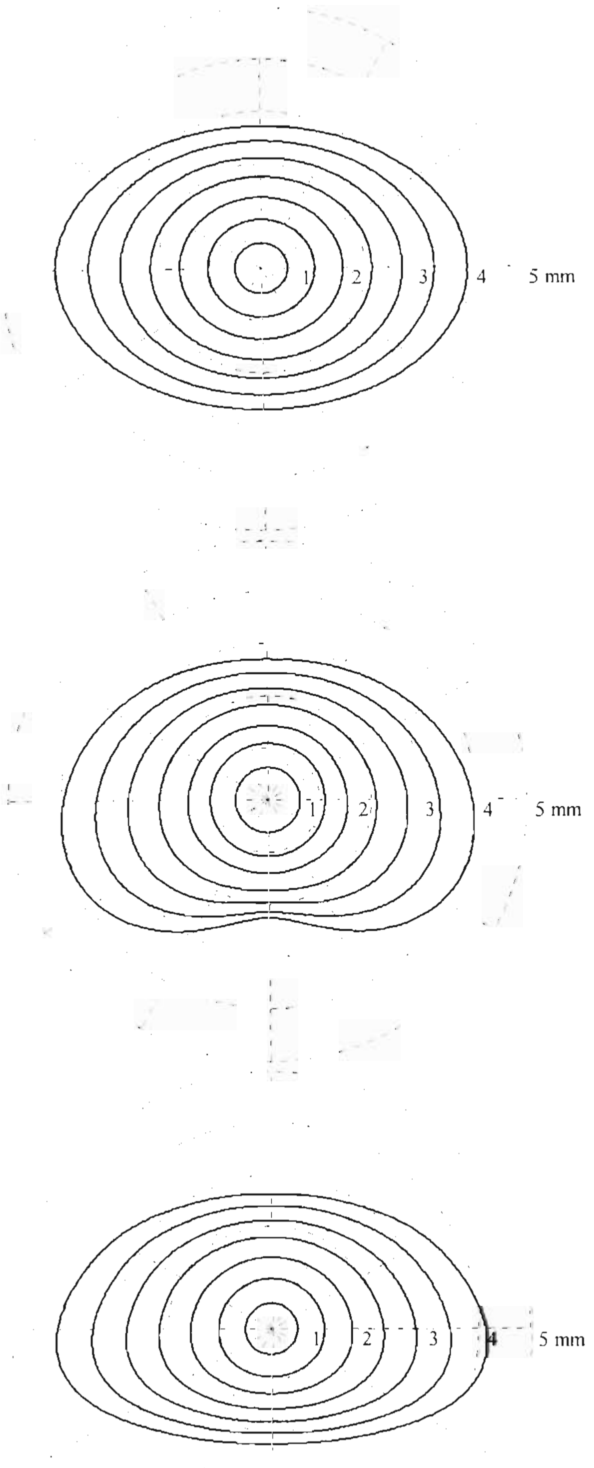

Figure A-6 : Comparison of the oblate spheroidal (top), Pruppacher and Pitter (1971) (middle) and Beard and Chuang (1990) (bottom) raindrops shapes.

The evaluation of Mie scattering for these nonspherical shapes is very complicated and several numerical and analytical techniques are required. To reduce the complexity some authors (e.g. Oguchi 1973; Morrison and Cross 1974; de Wolf 2001) have approximated the deformation of raindrops as oblate spheroids.

For a more realistic description, many authors (e.g. Li et al. 1994, 1995, 1998 and Der-Phone and Chen 2001) have used the Pruppacher and Pitter (1971) raindrop shape. Future work should also evaluate the Beard and Chuang (1990) which has been shown to be more accurate for larger the drops sizes.

Appendix B

B.1 Canting Angle of Raindrops

The fall velocity and shape of raindrops were examined under idealised equilibrium conditions in Section 2.2 and Appendix A, respectively. In this section the validity and consequences of these assumptions will be examined. Thereafter raindrop canting will be investigated. Raindrop shape and canting angle are important for the evaluation of the differential attenuation and cross polarization.

Raindrop canting is one of the major consequences of the nonspherical shape of raindrops. The axes of typical raindrops will not necessarily align with the vertical direction but instead cant due to vertical winds gradients and turbulences. Although the raindrops canting angle is more critical for analysis of depolarization than attenuation, it is nevertheless an important microphysical property of raindrops and will be discussed.

B.2 Approximations and Assumptions

The first major assumption made in this chapter was that the vertical fall velocity of raindrops is equal to the terminal fall velocity. This is valid only in the absence of vertical components of wind. Updrafts and downdrafts will cause the actual fall velocity to deviate about this value. For this study, namely terrestrial communication links employing millimetre-waves, we are specifically interested in the lower parts of the atmosphere, approximately 300 m above the ground. Hence the turbulent nature of the upper portions of the atmosphere can be ignored and in the absence of obstacles, such as mountains and buildings, it is valid to assume zero vertical wind velocities. Also raindrops only need to fall between 12 and 17 m before reaching terminal velocity (Wang and Pruppacher 1977).

For a terrestrial link the propagation path is some distance below the cloud base, hence the encountered raindrops would have fallen a sufficient distance to reach their terminal velocity. Consequently during a typical rain event the propagation path can be assumed to be dispersed with an assortment of raindrops each falling at its terminal velocity.

In Appendix A, it was assumed that the equilibrium shape is an adequate description of typical raindrops in nature. The reality is that turbulence due to the wake of other falling raindrops and wind can cause raindrops to have large asymmetric distortions and oscillating vibrations (e.g. Jones 1959; Ugai et al. 1977; Oguchi 1983). However, such considerations are beyond the scope of this study.

To reduce computation time, the classical approach of using spherical raindrops was adopted in this study. This is acceptable for attenuation calculations, however, the results will slightly over-estimate for vertical polarizations and under-estimate for horizontal polarizations. Matzler (2003) showed that the specific attenuation, although not exactly the same as that calculated using Mie theory for spherical raindrops, requires only a small correction (less than 8 %). Also the shape of the raindrop is more instrumental in evaluating the depolarization and cross-polarization effects as oppose to the attenuation. In this appendix the preliminary research into canting angle and cross-polarization is provided.

B.3 Cross Polarization and Differential Attenuation

Apart from the signal attenuation, which is the focus of this study, cross polarization is yet another major problem experienced during a rain event. Today, typical terrestrial communication systems may employ both horizontal and vertical linear polarizations to increase system capacity. To ensure reliability in such communication systems adequate cross-polarization isolation (XPI) is required. However raindrops are nonspherical in shape and rain attenuation is hence polarization dependent. Rain-induced cross polarization can significantly deteriorate the XPI and result in outages and undesirable system performance.

For oblate spheroidal raindrops the dipole moment for horizontal polarization exceeds that for vertical polarization. Consequently horizontal fields are attenuated more than vertical fields. The difference between these two signal attenuations is called the differential attenuation and poses a significant problem in dual-polarization communication systems.

Semplak (1970) performed extensive measurements of the difference and sum attenuations experienced during rain storms occurring over a 1 year period. There were no instances of the vertical field exceeding the horizontal field. This indicates that although the raindrop shape may have great variability (Jones 1959; Ugai et al. 1977), the average drop shape is indeed oblate.

Differential attenuation is influenced by the canting angle of the raindrops. For example, if raindrops were oblate spheroids and aligned 45° to the horizontal, the resulting differential attenuation would be zero. The canting angle θ can be measured either with respect to the horizontal or vertical axis as shown in Figure B-1.

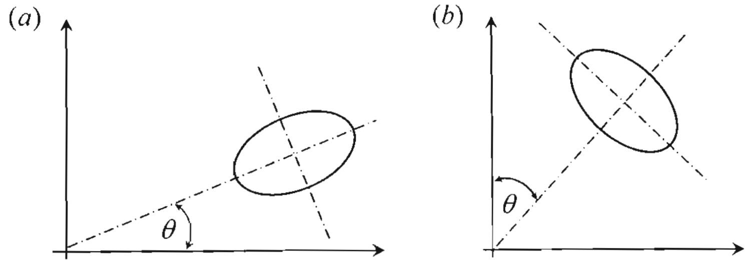

Figure B-1 : Canting angle of raindrop with respect to the horizontal axis (a) and vertical axis (b).

B.4 Historical Review

Since raindrops have a non-spherical shape, the canting angle becomes important for the evaluation of differential attenuation and cross polarization. All raindrops do not experience the same canting angle but rather form an angle distribution with the mean typically close to the axis. Knowledge of the mean, variance and shape of the canting angle distribution can be indispensable for modelling purposes.

The earliest measurements of raindrop canting date back to Saunders (1971). These measurements were derived from the angle between the horizontal axis and the major axis of the 2-D drop images as shown in Figure B-1 (a). Although this may not be equal to the 3-D canting angle, theory has shown that only the component of the angles in a plane perpendicular to the direction of propagation are required for calculations. Saunders (1971) confirmed that the measured canting angles do differ for different raindrops and showed that they exhibit a normal distribution with a mean of about +7°. Similar reports by Ugai et al. (1977) have showed that the canting angle does indeed follow a normal distribution with the mean and variance dependent on the nature of the storm.

Initial propagation models (e.g. Oguchi 1973; Watson 1976; Wolf 1996) considered an equiorientated rain medium, where all raindrops were assumed to have the same orientation throughout the propagation path. These constant canting angle models are based on the hypothesis that if the angle distribution is fairly even, the effects of the raindrops with negatively canted angles will tend to cancel out the effects of the positively canted ones and thus yield and average canting angle. Watson (1976) proposed that only a single parameter, namely the equivalent mean canting angle is necessary for the evaluation of cross polarization. The equivalent mean canting angle is defined as that value of canting angle in a constant canting angle model that is required to produce the same cross polarization as that occurring during the rain event. If the standard deviation of canting angles during the rain event is sufficiently small, the equivalent mean canting angle would then be approximately equal to the actual mean canting angle.

Watson (1976) performed measurements at 11 GHz over a 3 year period. An equivalent mean canting angle between 2° and 3° was found to be typical and provide good agreement with the measurements. The typical value for heavy rain during thunderstorms was about 4° and this value could be used by system designers for a 0.01% fade depth. Observation at 16.5 GHz by McCormick et al. (1976) also yielded small mean canting angles in the order of 5°. It was observed that although the direction of canting is strongly influenced by the horizontal wind direction there is no dependence of the horizontal wind speed. These observations are agreeable with the physical model suggested by Bruusaard (1976) explained later in this section.

Observations by radar measurements reveal very small mean canting angles typically below 2°. The higher canting angles observed in terrestrial links was believed to be due to the closer proximity to the ground. Furthermore it was observed that the mean canting angle is greater at the onset of a thunderstorm and generally becomes smaller as the storm progresses. This may be accounted by the greater contribution of large raindrops initially during a thunderstorm and hence the dependence of canting angle on drop size. These observations ultimately led to the development of more complicated models incorporating a distribution of canting angles (Brussaard 1976; Oguchi 1977; Kaya 1980; Howard 1982).

B.5 Brussaard Model for Mean Canting Angle Distribution

Brussaard (1976) proposed a physical model for evaluating the mean canting angle dependence on drop size and height above ground. This model was later modified by Beard and Jameson (1983) for higher altitudes and Howard (1982) to evaluate the statistical variance.

Brussaard (1976) postulated that the canting of raindrops is not due to the horizontal wind speed U but rather the vertical wind gradient U'. If the horizontal wind speed was constant the raindrop would merely align with the vertical and only the trajectory would be inclined which explains observations. The mean canting angle θ is given by

$$\tan\theta = \frac{v \cdot U'}{g} F(m,x) \tag{B.1}$$

where g is the gravitation constant, v is the terminal velocity, $U' = (dU/dh)$ is the vertical wind gradient, m is the a terrain roughness factor, and

$$x = \frac{gh}{v^2}, \tag{B.2}$$

$$F(m,x) = x^{1-m} e^x \cdot \Gamma(m,x) \tag{B.3}$$

and $\Gamma(m,x)$ is the incomplete gamma function as follows

$$\Gamma(m,x) = \int_x^{\infty} e^{-p} p^{(m-1)} dp \tag{B.4}$$

In order to evaluate the vertical wind gradient U', the dependence of wind speed U on height h is required.

Brussaard (1976) suggested the following power law dependence

$$\left(\frac{U}{U_r}\right) = \left(\frac{h}{h_r}\right)^m \tag{B.5}$$

where U_r is the wind speed at a reference height h_r and m is the terrain roughness factor. Typical values for m include 0.1 for sea, 0.2 for moderate terrain roughness and 0.3 - 0.4 for urban areas. The mean canting angles for 4 selected heights, h= 10, 20, 40 and 80 m is given in Figure B-2. The reference wind speed U_r=15 ms^{-1} at h_r = 10 m and a moderate terrain (m = 0.2) was assumed.

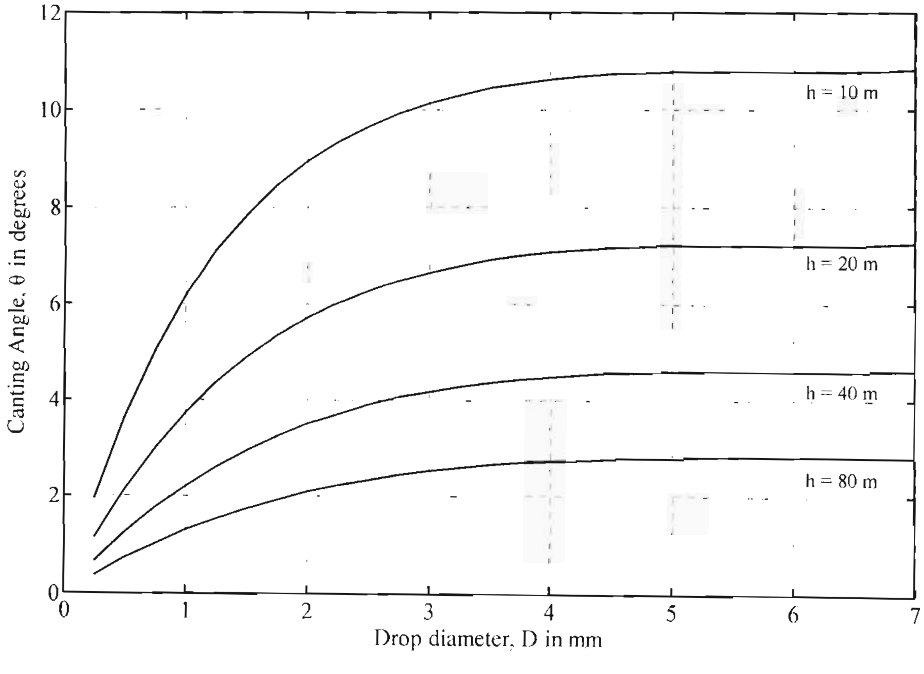

Figure B-2 : Raindrop canting angle as a function of drop diameter and height above ground.

Figure B-2 shows that the canting angle becomes independent of the drop size for approximately $D > 3.0$ mm. The canting angle decreases with increasing height. Thus rain depolarization can be reduced by merely increasing tower height on terrestrial links. Another approach which is strongly favoured by several investigators is the Gaussian form suggested by Oguchi (1977). In this model the raindrop canting angle is independent of the drop size. Instead the canting angle is given in terms of two angles, a transverse canting angle and a longitudinal angle, where both are independent and have Gaussian distributions. These models can be used in future studies to evaluate cross-polarization.

Appendix C

C.1 Köppen Climate Classification System

In 1900, Wladimir Köppen introduced as system to classify the earth's climate into five distinct classes. Each class or biome is distinguished by the mean monthly temperature T, mean annual precipitation M and the vegetation in the region. Figure C-1 (from Microsoft® Encarta® Encyclopedia 2003) illustrates the climatic boundaries of the different biomes.

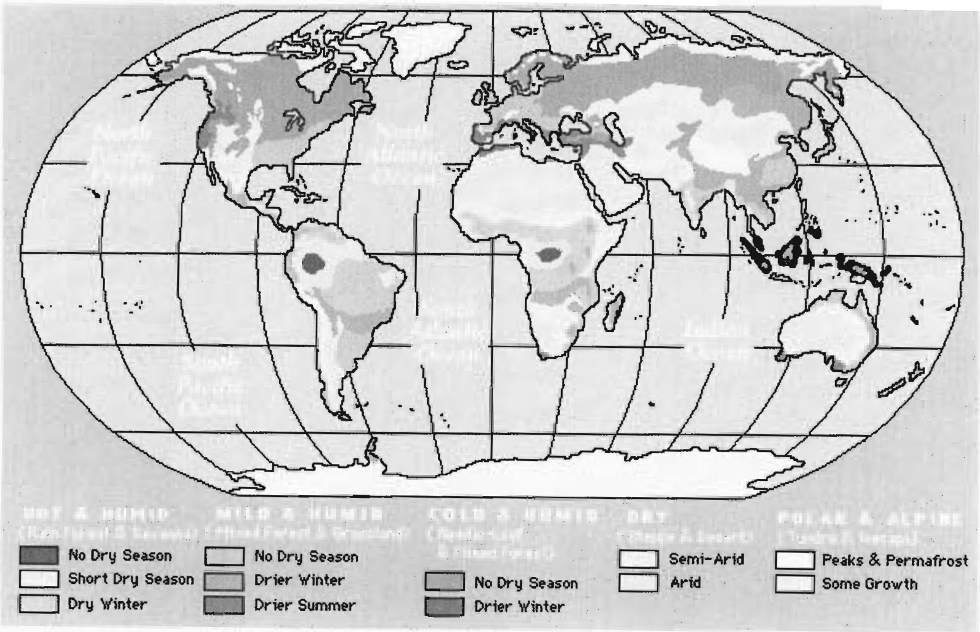

Figure C-1 : The different climate and terrestrial biomes from Microsoft® Encarta® Encyclopedia 2003.

Today the Köppen climate classification system is the most widely used for classifying the world's climates and an additional sixth zone, as well as 4 sub-zones have been introduced. According to the Köppen system, each climate zone is designated by a capital letter. Sub-divisions within each zone are denoted by small letters. A description of the different climate zones is given in Table C-1 and the sub-divisions are given in Table C-2.

Table C-1 : Köppen climate zone classification

Climate Zone	
A: Moist Tropical	Extends 15° – 25° north and south of the equator. High temperatures throughout the year $T \geq 18$ °C and $M \geq 1500$ mm.
B : Dry	Extends from 20° – 35° north and south of the equator and in large continental regions of the mid-latitudes, surrounded by mountains. Little rain throughout the year $M \leq 860$ mm and great daily temperature ranges. Dry climates are further subdivided into **S** – semi-arid (steppe) and **W** – arid (desert).
C : Moist Subtropical Mid-Latitude	Extends from 30 – 50° north and south of the equator. Mild Winters. $T \geq 10$ °C for the warmest months and 0 °C $\leq T \leq 18$ °C for the coldest months.
D : Moist Continental Mid-Latitude	Extend pole ward from the **C** climates. Seasonal temperatures vary widely. Cold Winters. $T \geq 10$ °C for the warmest months and $T \leq 0$ °C for the coldest months. Very little annual precipitation.
E : Polar	Very cold Winters and Summer with ice and tundra. $T \leq 10$ °C throughout the year. Polar climates are further subdivided into **T** – tundra and **F** – ice caps.
H : Highlands	Exceptional high altitude regions. Climate vary depending on surrounding zones.

Table C-2 : Köppen climate sub-type classification

Sub-types based on temperature and precipitation	
f	Consistent rainfall throughout the year. Subtype of **A**, **C**, **D**.
m	Monsoon rain. Short dry season. Majority of rain falls during the hottest months. Subtype of **A**.
s	Dry season is summer. ≥ 70 % of M falls during winter. Subtype of **C**.
w	Dry season is winter. ≥ 70 % of M falls during summer. Subtype of **A**, **C**, **D**.
a	$T \geq 22$ °C for the warmest month. Subtype of **C**, **D**.
b	$T < 22$ °C for the warmest month. Subtype of **C**, **D**.
c	Cool short summers. $T \geq 10$ °C for less than four months. Subtype of **C**, **D**.
d	Very cold winters. $T < -37$ °C for the coldest month. Subtype of **D**.
h	Hot and dry. $T \geq 0$ °C throughout the year. Subtype of **B**.
k	Hot and cold. $T < 0$ °C for at least one month. Subtype of **B**.

C.2 South African climate regions and boundaries

Using the Köppen system, South Africa can be divided into 12 climatic regions as shown Figure C-2 according to Seeber (1985, Figure 30). A description of each zone is given in Table C-3 from Seeber (1985, Table 8).

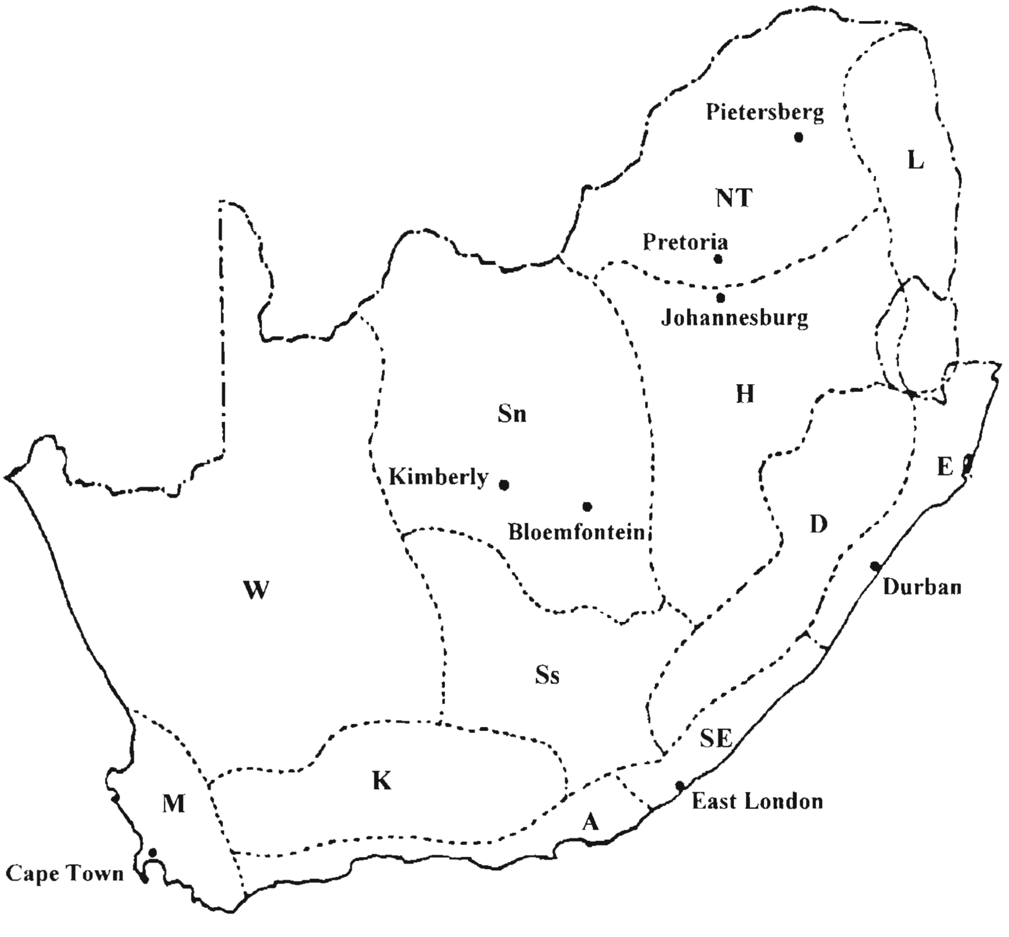

Figure C-2 : Map of South African climate regions and boundaries from Seeber (1985, Figure 30).

As it can be seen from the Figure C-2, the South African climate is fairly complicated, especially with and the presence of the Drakensberg escarpment and large masses of arid and semi-arid regions. The majority of South Africa has more rain during the summer months except for the south-western regions of Western Cape which have winter rain and dry summers.

Although South Africa has 12 different climatic zones, according to ITU-R P.837 it has been divided into only 4 different regions for rainfall climates, the climatic maps are given in Chapter 4. Crane (1980) divided South Africa into 5 regions.

Table C-3 : African climatic regions from Seeber (1985, Table 8)

Climatic classification for South African (Köppen System)	
W	*Northern Cape* : Dessert climate. **(BW)**
M	*South-Western Cape* : Mediterranean climate with winter rain. **(Cs)**
K	*Karoo* : Desert climate. **(BW and BSk)**
A	*Southern coastal belt* : Rain during all seasons. **(Cf)**
SE	*South-eastern coastal belt* : Warm temperate with summer rain. **(Cfw)**
E	*Eastern coast and Zuland* : Sub-tropical with summer rain. **(Cfw and Cfa)**
D	*Drakensberg and interior KwaZulu-Natal* : Warm temperate with summer rain. **(Cwb)**
L	*Lowveld (Northern province)* : Hot steppe with summer rain. **(BShw)**
NT	*Northern Province* : Hot steppe with summer rain. **(BShw)**
H	*Highveld (Mpumalanga, Gauteng and Free State)* : Warm temperate with summer rain. **(Cwb)**
Sn	*Northern Steppe (Free State and North-West)* : Steppe summer and autumn rain. **(BSw)**
Ss	*Southern Steppe (Eastern Cape and Free State)* : Cold Steppe with autumn rain. **(BSkw)**

Appendix D

D.1 Path Attenuation Graphs

The conversion of rain rate to specific attenuation is a crucial step in the analysis of the total path attenuation and hence radio-link availability. It is now common practice to relate the specific attenuation and the rain rate using the simple power law relationship. The power-law parameters for the specific attenuation have been evaluated for each frequency f = 4, 12, 15, 19.5, 40 and 80 GHz and each DSD. The results are given in Table D-1 - Table D-6.

Table D-1 : The power law relationship parameters for the specific attenuation at 4 GHz for various DSDs

Drop Size Distribution	κ	α
LP – Laws and Parsons (1943)	0.000651	1.104
Wolf – Gamma distribution (de Wolf 2001)	0.000437	1.208
AU – Gamma distribution (Atlas and Ulbrich 1974)	0.000208	1.382
WB – Weibull distribution (Sekine et al. 1987)	0.000331	1.244
Exponential DSDs		
JD – Joss – Drizzle (Joss et al. 1968)	0.000836	0.978
JT – Joss – Thunderstorm (Joss et al. 1968)	0.000537	1.256
MP – Marshall and Palmer (1948)	0.000503	1.161
Lognormal DSDs (Adimula and Olsen 1996)		
CS – Continental Shower	0.000748	0.975
CT – Continental Thunderstorm	0.000843	0.935
TS – Tropical Shower	0.000758	0.988
TT – Tropical Thunderstorm	0.000743	1.009

Table D-2 : The power law relationship parameters for the specific attenuation at 12 GHz for various DSDs

Drop Size Distribution	κ	α
LP – Laws and Parsons (1943)	0.0249	1.129
Wolf - Gamma distribution (de Wolf 2001)	0.0284	1.114
AU – Gamma distribution (Atlas and Ulbrich 1974)	0.0167	1.233
WB – Weibull distribution (Sekine et al. 1987)	0.0293	1.105
Exponential DSDs		
JD – Joss – Drizzle (Joss et al. 1968)	0.0125	1.205
JT – Joss – Thunderstorm (Joss et al. 1968)	0.0325	1.092
MP – Marshall and Palmer (1948)	0.0217	1.142
Lognormal DSDs (Adimula and Olsen 1996)		
CS – Continental Shower	0.0237	1.099
CT – Continental Thunderstorm	0.0390	0.975
TS – Tropical Shower	0.0206	1.163
TT – Tropical Thunderstorm	0.0269	1.120

Table D-3 : The power law relationship parameters for the specific attenuation at 15 GHz for various DSDs

Drop Size Distribution	κ	α
LP – Laws and Parsons (1943)	0.0468	1.073
Wolf – Gamma distribution (de Wolf 2001)	0.0490	1.073
AU – Gamma distribution (Atlas and Ulbrich 1974)	0.0303	1.185
WB – Weibull distribution (Sekine et al. 1987)	0.0541	1.049
Exponential DSDs		
JD – Joss – Drizzle (Joss et al. 1968)	0.0262	1.151
JT – Joss – Thunderstorm (Joss et al. 1968)	0.0529	1.065
MP Marshall and Palmer (1948)	0.0395	1.100
Lognormal DSDs (Adimula and Olsen 1996)		
CS – Continental Shower	0.0412	1.090
CT – Continental Thunderstorm	0.0439	1.082
TS – Tropical Shower	0.0422	1.101
TT - Tropical Thunderstorm	0.0508	1.067

Table D-4 : The power law relationship parameters for the specific attenuation at 19.5 GHz for various DSDs

Drop Size Distribution	κ	α
LP – Laws and Parsons (1943)	0.0812	1.047
Wolf – Gamma distribution (de Wolf 2001)	0.0873	1.038
AU – Gamma distribution (Atlas and Ulbrich 1974)	0.0567	1.139
WB – Weibull distribution (Sekine et al. 1987)	0.0962	1.016
Exponential DSDs		
JD – Joss – Drizzle (Joss et al. 1968)	0.0539	1.105
JT – Joss – Thunderstorm (Joss et al. 1968)	0.0935	1.024
MP – Marshall and Palmer (1948)	0.0743	1.058
Lognormal DSDs (Adimula and Olsen 1996)		
CS – Continental Shower	0.0789	1.050
CT – Continental Thunderstorm	0.0732	1.072
TS – Tropical Shower	0.0821	1.048
TT – Tropical Thunderstorm	0.0901	1.031

Table D-5 : The power law relationship parameters for the specific attenuation at 40 GHz for various DSDs

Drop Size Distribution	κ	α
LP – Laws and Parsons (1943)	0.437	0.869
Wolf – Gamma distribution (de Wolf 2001)	0.465	0.843
AU – Gamma distribution (Atlas and Ulbrich 1974)	0.421	0.880
WB – Weibull distribution (Sekine et al. 1987)	0.721	0.747
Exponential DSDs		
JD – Joss – Drizzle (Joss et al. 1968)	0.346	0.963
JT – Joss – Thunderstorm (Joss et al. 1968)	0.387	0.863
MP – Marshall and Palmer (1948)	0.415	0.888
Lognormal DSDs (Adimula and Olsen 1996)		
CS – Continental Shower	0.304	1.005
CT – Continental Thunderstorm	0.224	1.085
TS – Tropical Shower	0.372	0.945
TT – Tropical Thunderstorm	0.358	0.938

Table D-6 : The power law relationship parameters for the specific attenuation at 80 GHz for various DSDs

Drop Size Distribution	κ	α
LP – Laws and Parsons (1943)	0.892	0.782
Wolf – Gamma distribution (de Wolf 2001)	0.927	0.724
AU – Gamma distribution (Atlas and Ulbrich 1974)	1.286	0.681
WB – Weibull distribution (Sekine et al. 1987)	1.839	0.574
Exponential DSDs		
JD - Joss – Drizzle (Joss et al. 1968)	1.510	0.778
JT – Joss – Thunderstorm (Joss et al. 1968)	0.777	0.757
MP – Marshall and Palmer (1948)	1.202	0.738
Lognormal DSDs (Adimula and Olsen 1996)		
CS – Continental Shower	0.809	0.839
CT – Continental Thunderstorm	0.542	0.921
TS – Tropical Shower	0.910	0.775
TT – Tropical Thunderstorm	0.672	0.818

D.2 Path Attenuation Graphs

In Chapter 5 the experimental LOS link between the two campuses of the UKZN was discussed. The terrestrial LOS link was operated at a frequency of 19.5 GHz thus the results presents in Chapter 5 focussed on this frequency. Figure D-1 – Figure D-11 show the path attenuation using the various DSDs, for the frequencies f = 4, 12, 15, 19.5, 40 and 80 GHz. As shown the variation in the calculated path attenuation can be up to 50%. This illustrates the significance of the DSD on the attenuation experienced due to rain and the resulting link unavailability.

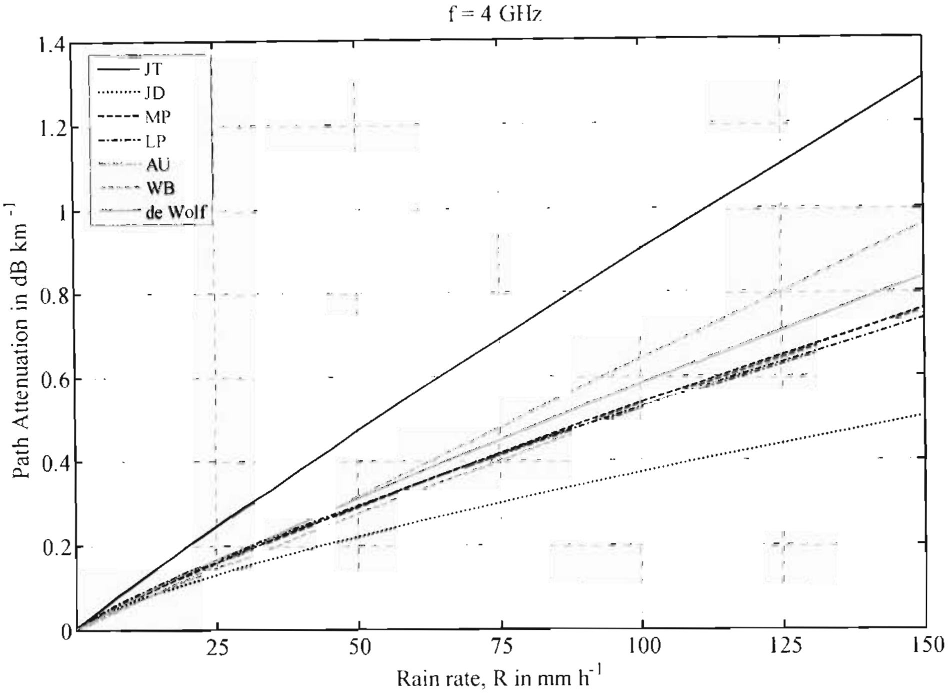

Figure D-1 : Path attenuation for *f* = 4 GHz LOS link, using the MP, JT and JD exponential DSDs, LP DSD, de Wolf and AU gamma DSDs and the WB Weibull DSD.

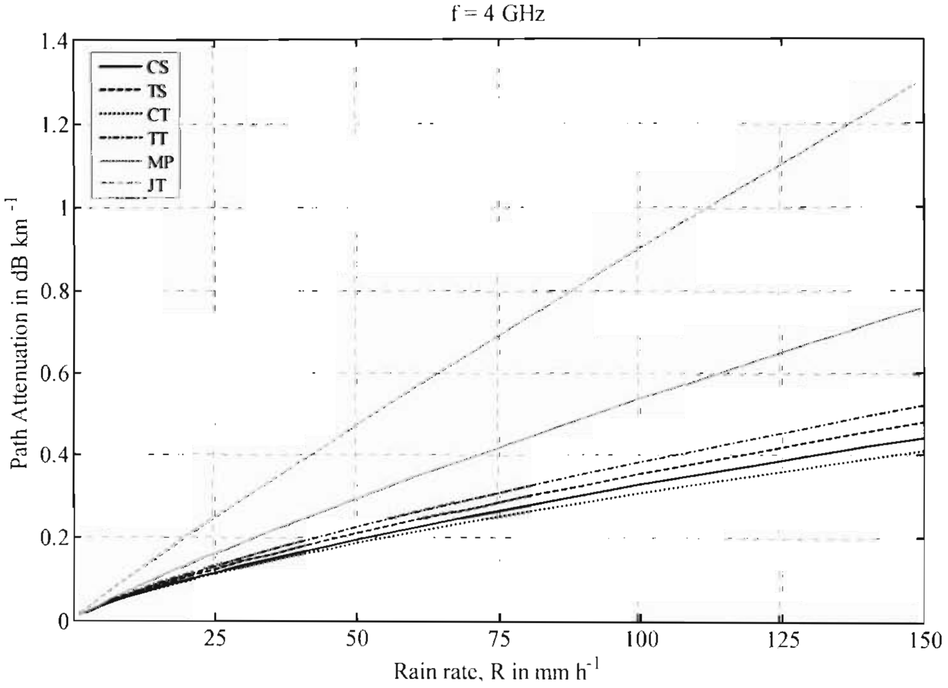

Figure D-2 : Path attenuation for *f* = 4 GHz, using the MP and JT exponential DSDs and CS, TS, CT and TT lognormal distributions.

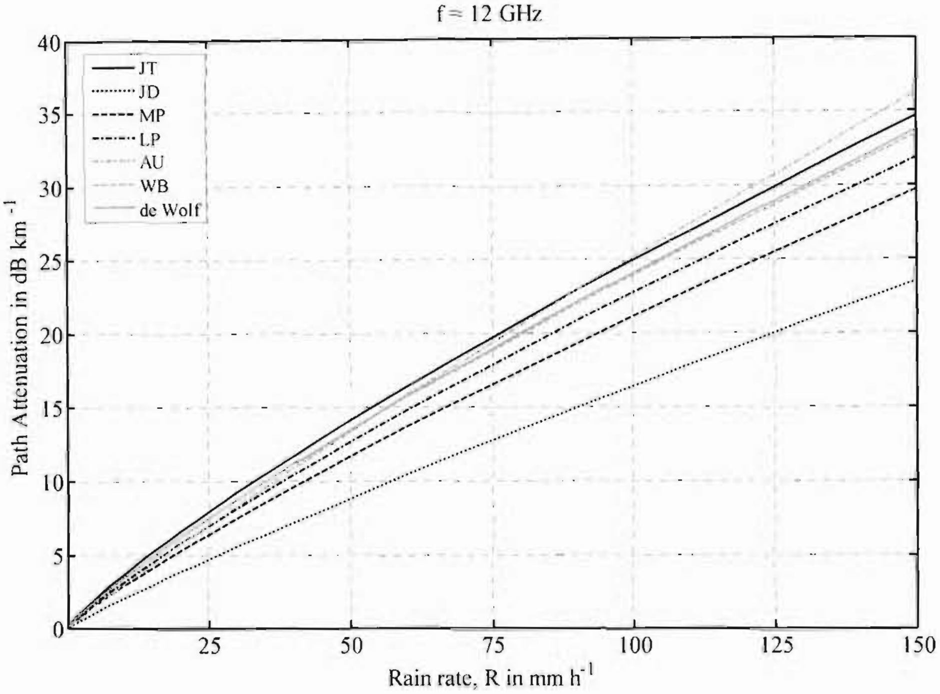

Figure D-3 : Path attenuation for f = 12 GHz LOS link, using the MP, JT and JD exponential DSDs, LP DSD, de Wolf and AU gamma DSDs and the WB Weibull DSD.

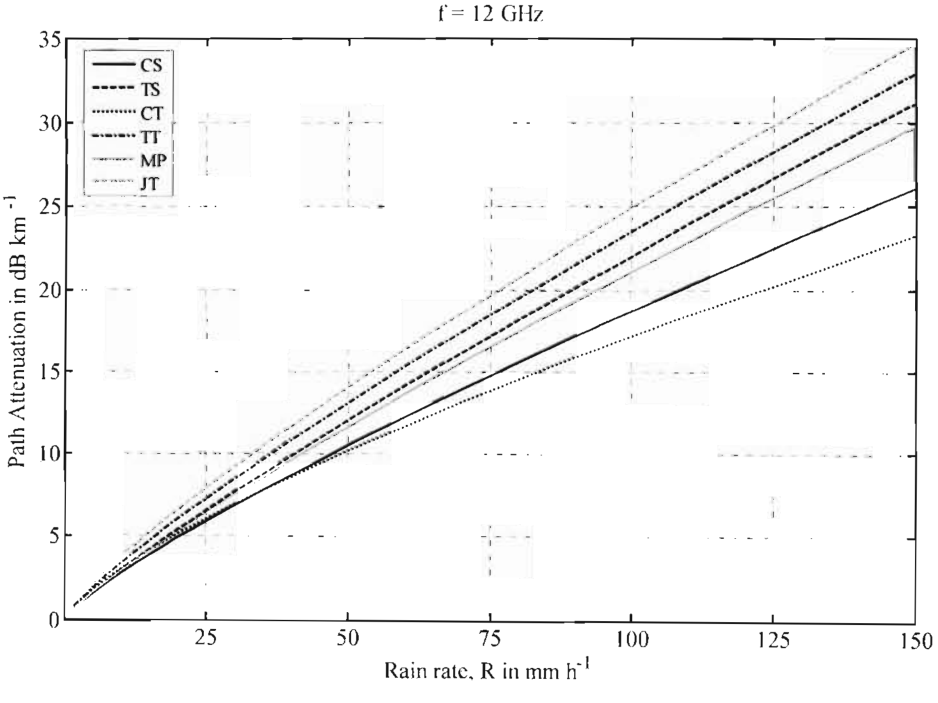

Figure D-4 : Path attenuation for f = 12 GHz, using the MP and JT exponential DSDs and CS, TS, CT and TT lognormal distributions.

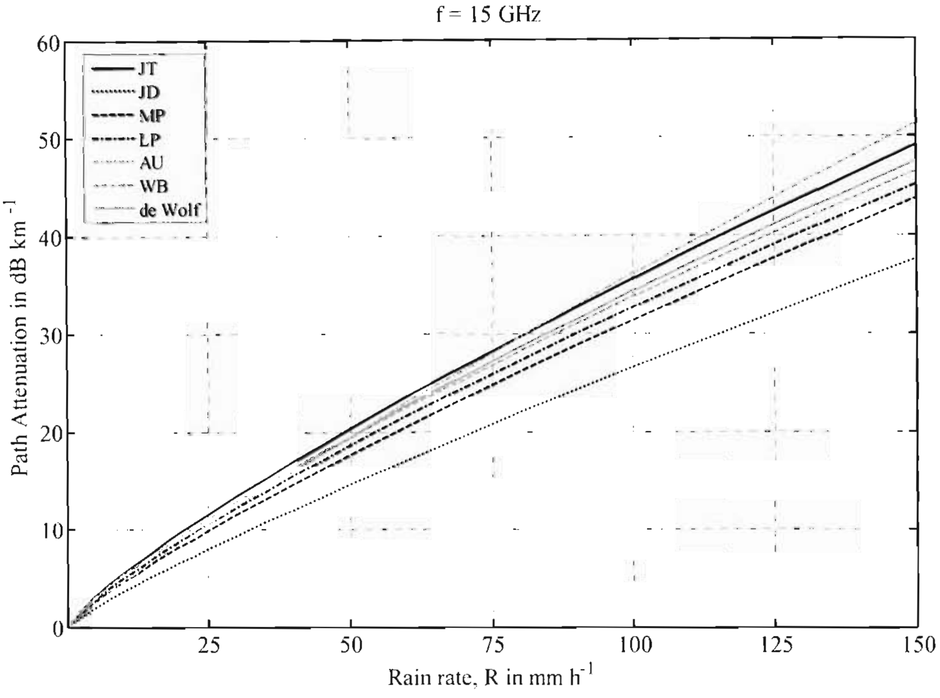

Figure D-5 : Path attenuation for *f* = 12 GHz LOS link, using the MP, JT and JD exponential DSDs, LP DSD, de Wolf and AU gamma DSDs and the WB Weibull DSD.

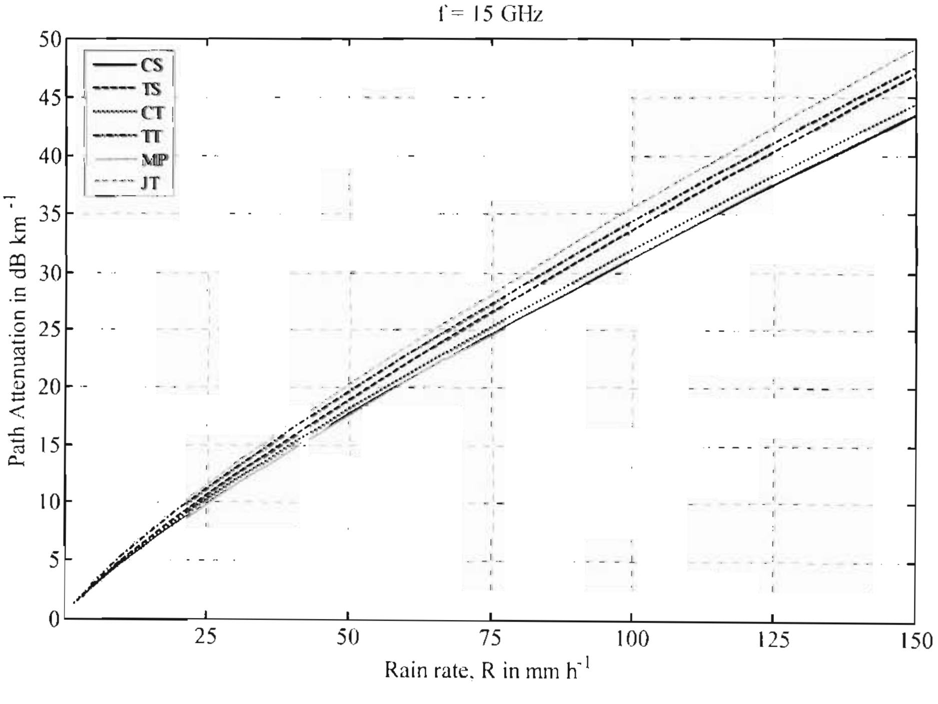

Figure D-6 : Path attenuation for *f* = 15 GHz, using the MP and JT exponential DSDs and CS, TS, CT and TT lognormal distributions.

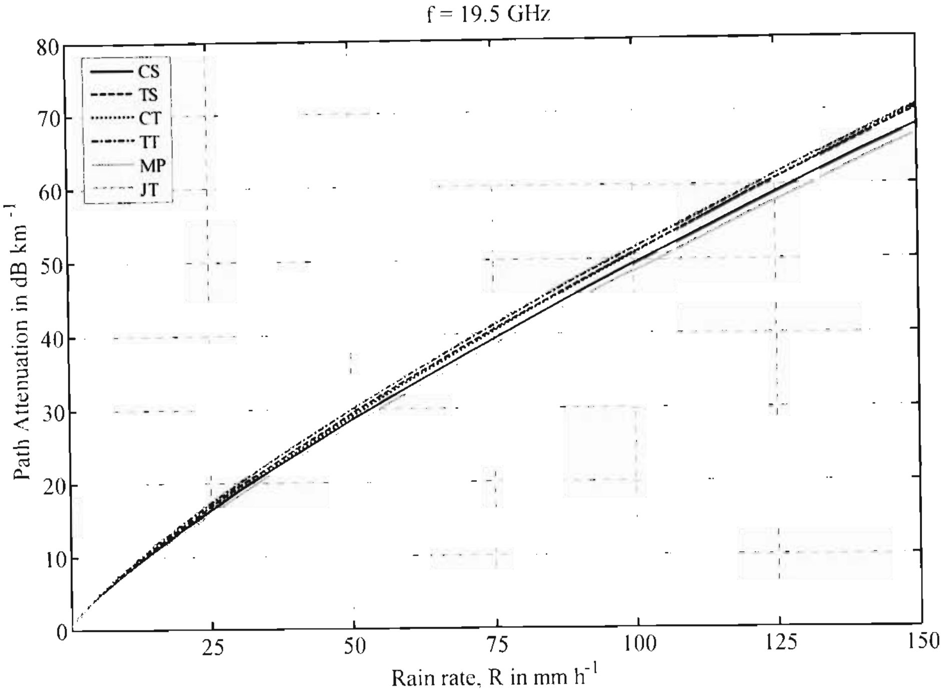

Figure D-7 : Path attenuation for f = 19.5 GHz, using the MP and JT exponential DSDs and CS, TS, CT and TT lognormal distributions.

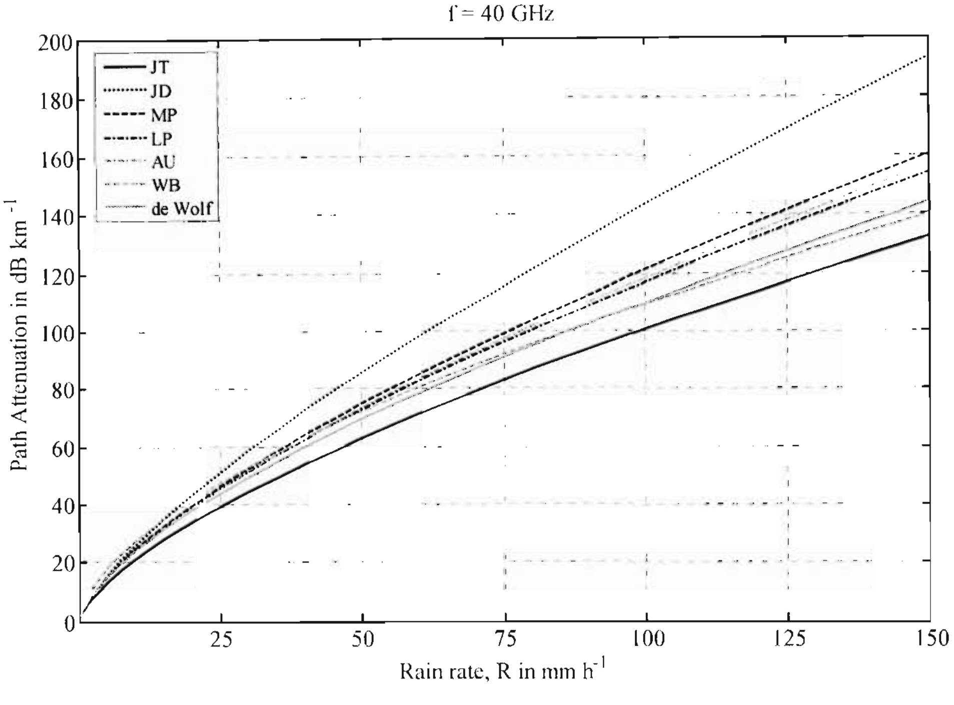

Figure D-8 : Path attenuation for f = 12 GHz LOS link, using the MP, JT and JD exponential DSDs, LP DSD, de Wolf and AU gamma DSDs and the WB Weibull DSD.

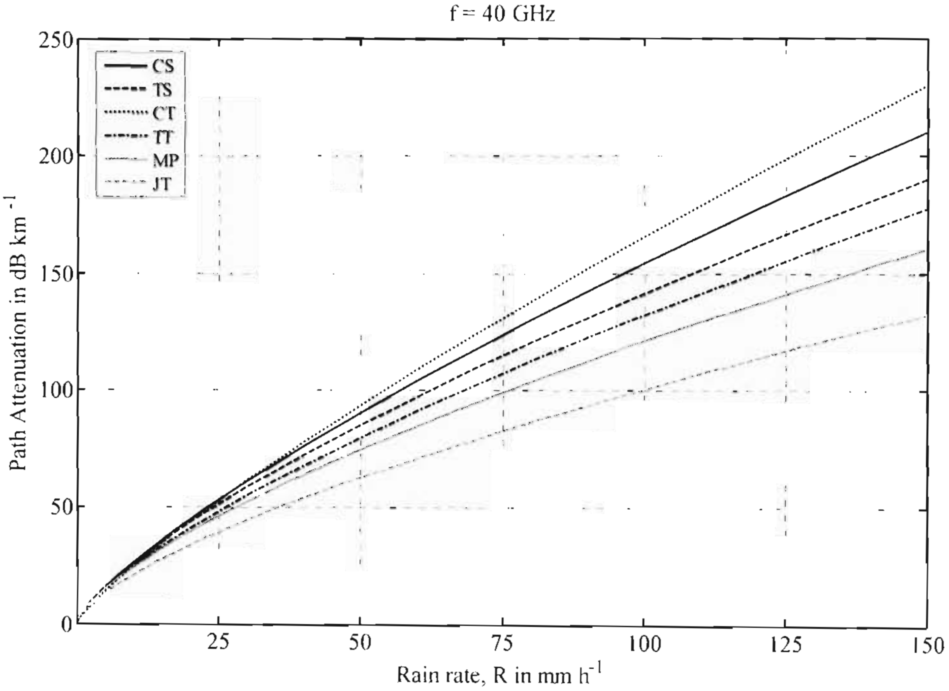

Figure D-9 : Path attenuation for *f* = 40 GHz, using the MP and JT exponential DSDs and CS, TS, CT and TT lognormal distributions.

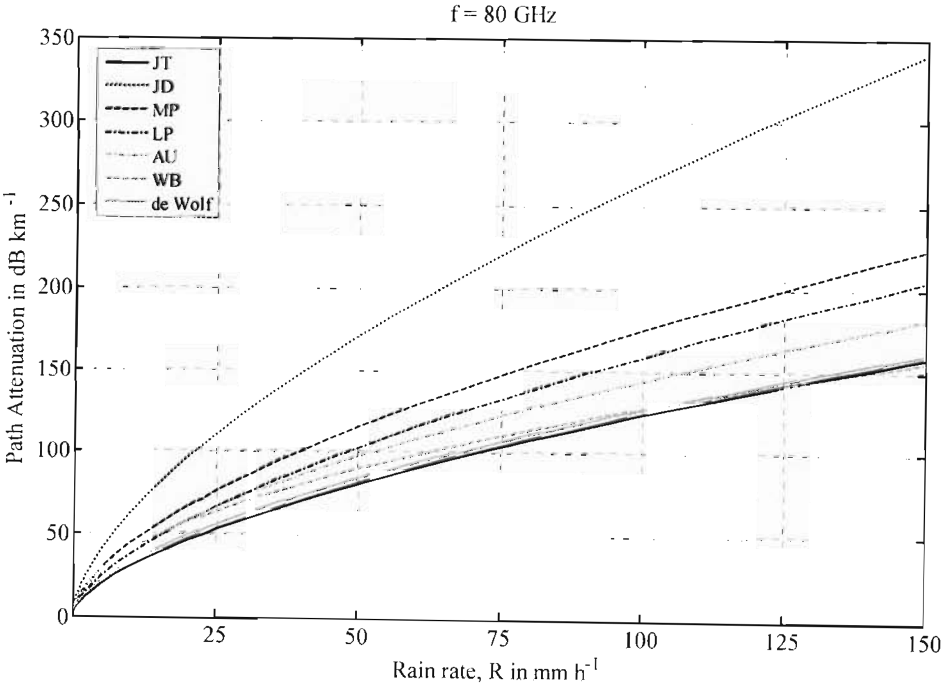

Figure D-10 : Path attenuation for *f* = 12 GHz LOS link, using the MP, JT and JD exponential DSDs, LP DSD, de Wolf and AU gamma DSDs and the WB Weibull DSD.

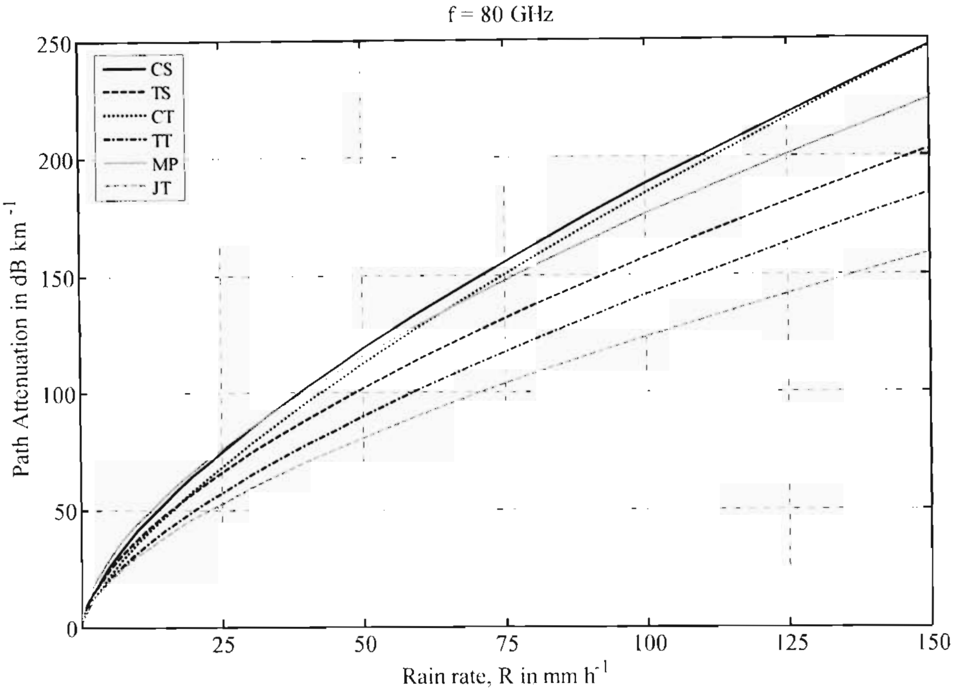

Figure D-11 : Path attenuation for *f* = 80 GHz, using the MP and JT exponential DSDs and CS, TS, CT and TT lognormal distributions.

D.3 Path Attenuation Exceedance Probabilities

Knowledge of the cumulative distributions of the fade depth and durations due to rain are necessary for link design. Depending on the link availability requirements, communication system designers may need the fade depth exceeded for 0.1, 0.01 or 0.001% of the year. Table D-7 – Table D-24 contains the path attenuation exceeded for these percentages of the year, using the various DSDs and rain-rate models, for the frequencies *f* = 4, 12, 15, 19.5, 40 and 80 GHz.

Table D-7 : Path attenuation exceeded for 0. 1% of the year for 4 GHz

Rain-Rate Model / Drop-Size Distribution	Extreme-value model	Seeber (1985)	ITU model	Moupfouma (1987)	Moupfouma and Martin (1995)	
					Temperate	Tropical/Subtropical
LP – Laws and Parsons	0.13	0.13	0.11	0.12	0.13	0.15
de Wolf – Gamma	0.13	0.13	0.11	0.11	0.13	0.15
AU – Gamma	0.11	0.12	0.10	0.10	0.12	0.13
WB – Weibull	0.11	0.11	0.09	0.10	0.11	0.13
JD – Exponential	0.10	0.11	0.09	0.10	0.11	0.12
JT – Exponential	0.19	0.19	0.16	0.17	0.19	0.21
MP – Exponential	0.12	0.13	0.11	0.11	0.13	0.14
CS – Lognormal	0.09	0.10	0.08	0.08	0.10	0.10
CT – Lognormal	0.09	0.09	0.08	0.08	0.09	0.10
TS – Lognormal	0.10	0.10	0.09	0.09	0.10	0.11
TT – Lognormal	0.10	0.11	0.09	0.09	0.11	0.12

Table D-8 : Path attenuation exceeded for 0.01% of the year for 4 GHz

Rain-Rate Model / Drop-Size Distribution	Extreme-value model	Seeber (1985)	ITU model	Moupfouma (1987)	Moupfouma and Martin (1995)	
					Temperate	Tropical/Subtropical
LP – Laws and Parsons	0.34	0.31	0.34	0.34	0.34	0.34
de Wolf – Gamma	0.36	0.33	0.36	0.36	0.36	0.36
AU – Gamma	0.38	0.33	0.38	0.37	0.37	0.37
WB – Weibull	0.32	0.29	0.32	0.32	0.32	0.32
JD – Exponential	0.25	0.23	0.25	0.25	0.25	0.25
JT – Exponential	0.55	0.49	0.55	0.55	0.55	0.55
MP – Exponential	0.34	0.31	0.34	0.34	0.34	0.34
CS – Lognormal	0.22	0.20	0.22	0.22	0.22	0.22
CT – Lognormal	0.21	0.19	0.21	0.21	0.21	0.21
TS – Lognormal	0.24	0.22	0.24	0.24	0.24	0.24
TT – Lognormal	0.26	0.23	0.25	0.25	0.25	0.25

Table D-9 : Path attenuation exceeded for 0.001% of the year for 4 GHz

Rain-Rate Model / Drop-Size Distribution	Extreme-value model	Seeber (1985)	ITU model	Moupfouma (1987)	Moupfouma and Martin (1995)	
					Temperate	Tropical/Subtropical
LP – Laws and Parsons	0.73	0.59	0.61	0.68	0.68	0.53
de Wolf – Gamma	0.82	0.66	0.68	0.76	0.76	0.58
AU – Gamma	0.95	0.74	0.76	0.87	0.87	0.64
WB – Weibull	0.75	0.59	0.61	0.69	0.69	0.52
JD – Exponential	0.50	0.41	0.42	0.47	0.47	0.37
JT – Exponential	1.29	1.02	1.06	1.19	1.19	0.90
MP – Exponential	0.75	0.60	0.62	0.70	0.70	0.53
CS – Lognormal	0.44	0.36	0.37	0.41	0.41	0.33
CT – Lognormal	0.41	0.34	0.35	0.38	0.38	0.31
TS – Lognormal	0.48	0.39	0.40	0.45	0.45	0.35
TT – Lognormal	0.52	0.43	0.44	0.48	0.48	0.38

Table D-10 : Path attenuation exceeded for 0.1% of the year for 12 GHz

Rain-Rate Model / Drop-Size Distribution	Extreme-value model	Seeber (1985)	ITU model	Moupfouma (1987)	Moupfouma and Martin (1995)	
					Temperate	Tropical/Subtropical
LP – Laws and Parsons	5.4	5.6	4.7	4.9	5.6	6.1
de Wolf – Gamma	5.8	6.0	5.1	5.3	6.1	6.6
AU – Gamma	5.3	5.5	4.6	4.8	5.6	6.1
WB – Weibull	5.8	6.0	5.1	5.3	6.1	6.6
JD – Exponential	3.6	3.7	3.1	3.2	3.7	4.1
JT – Exponential	6.2	6.4	5.4	5.6	6.4	7.0
MP – Exponential	4.9	5.1	4.3	4.5	5.2	5.6
CS – Lognormal	4.6	4.8	4.0	4.2	4.8	5.2
CT – Lognormal	4.8	5.0	4.3	4.4	5.0	5.4
TS – Lognormal	5.1	5.2	4.4	4.5	5.3	5.7
TT – Lognormal	5.7	5.8	4.9	5.1	5.9	6.4

Table D-11 : Path attenuation exceeded for 0. 01% of the year for 12 GHz

Rain-Rate Model / Drop-Size Distribution	Extreme-value model	Seeber (1985)	ITU model	Moupfouma (1987)	Moupfouma and Martin (1995)	
					Temperate	Tropical/Subtropical
LP – Laws and Parsons	14.5	13.2	14.5	14.4	14.4	14.4
de Wolf – Gamma	15.5	14.0	15.5	15.4	15.4	15.4
AU – Gamma	15.5	14.0	15.5	15.4	15.4	15.4
WB – Weibull	15.4	14.0	15.4	15.3	15.3	15.3
JD – Exponential	10.2	9.2	10.2	10.2	10.2	10.2
JT – Exponential	16.1	14.7	16.1	16.0	16.0	16.0
MP – Exponential	13.4	12.2	13.4	13.3	13.3	13.3
CS – Lognormal	12.1	11.0	12.1	12.0	12.0	12.0
CT – Lognormal	11.6	10.6	11.5	11.5	11.5	11.5
TS – Lognormal	13.9	12.6	13.9	13.8	13.8	13.8
TT – Lognormal	15.1	13.7	15.1	15.0	15.0	15.0

Table D-12 : Path attenuation exceeded for 0.001% of the year for 12 GHz

Rain-Rate Model / Drop-Size Distribution	Extreme-value model	Seeber (1985)	ITU model	Moupfouma (1987)	Moupfouma and Martin (1995)	
					Temperate	Tropical/Subtropical
LP – Laws and Parsons	31.5	25.5	26.3	29.3	29.3	22.6
de Wolf – Gamma	33.2	27.0	27.8	31.0	31.0	24.0
AU – Gamma	35.7	28.5	29.4	33.1	33.1	25.0
WB – Weibull	33.0	26.8	27.6	30.7	30.7	23.8
JD – Exponential	23.2	18.5	19.2	21.5	21.5	16.3
JT – Exponential	34.2	27.9	28.7	31.9	31.9	24.8
MP – Exponential	29.3	23.7	24.5	27.3	27.3	21.0
CS – Lognormal	25.8	20.9	21.6	24.0	24.0	18.6
CT – Lognormal	23.0	19.0	19.6	21.5	21.5	17.1
TS – Lognormal	30.8	24.8	25.6	28.6	28.6	21.9
TT – Lognormal	32.5	26.3	27.2	30.3	30.3	23.4

Table D-13 : Path attenuation exceeded for 0.1% of the year for 15 GHz

Rain-Rate Model / Drop-Size Distribution	Extreme-value model	Seeber (1985)	ITU model	Moupfouma (1987)	Moupfouma and Martin (1995)	
					Temperate	Tropical/Subtropical
LP – Laws and Parsons	8.3	8.5	7.3	7.5	8.6	9.3
de Wolf – Gamma	8.7	9.0	7.6	7.9	9.0	9.8
AU – Gamma	8.1	8.4	7.0	7.2	8.4	9.2
WB – Weibull	8.8	9.1	7.7	8.0	9.1	9.9
JD – Exponential	6.2	6.4	5.4	5.6	6.4	7.0
JT – Exponential	9.1	9.4	8.0	8.2	9.4	10.2
MP – Exponential	7.7	8.0	6.7	7.0	8.0	8.7
CS – Lognormal	7.8	8.0	6.8	7.0	8.1	8.8
CT – Lognormal	8.0	8.3	7.0	7.3	8.3	9.0
TS – Lognormal	8.3	8.6	7.2	7.5	8.6	9.3
TT – Lognormal	8.8	9.1	7.7	8.0	9.1	9.9

Table D-14 : Path attenuation exceeded for 0.01% of the year for 15 GHz

Rain-Rate Model / Drop-Size Distribution	Extreme-value model	Seeber (1985)	ITU model	Moupfouma (1987)	Moupfouma and Martin (1995)	
					Temperate	Tropical/Subtropical
LP – Laws and Parsons	21.2	19.3	21.2	21.1	21.1	21.1
de Wolf – Gamma	22.3	20.3	22.3	22.2	22.2	22.2
AU – Gamma	22.6	20.4	22.6	22.5	22.5	22.5
WB – Weibull	22.2	20.2	22.1	22.0	22.0	22.0
JD – Exponential	16.9	15.3	16.8	16.7	16.7	16.7
JT – Exponential	23.2	21.2	23.2	23.1	23.1	23.1
MP – Exponential	20.2	18.4	20.2	20.1	20.1	20.1
CS – Lognormal	20.2	18.4	20.2	20.1	20.1	20.1
CT – Lognormal	20.8	18.9	20.8	20.7	20.7	20.7
TS – Lognormal	21.7	19.8	21.7	21.6	21.6	21.6
TT – Lognormal	22.5	20.5	22.4	22.3	22.3	22.3

Table D-15 : Path attenuation exceeded for 0.001% of the year for 15 GHz

Rain-Rate Model / Drop-Size Distribution	Extreme-value model	Seeber (1985)	ITU model	Moupfouma (1987)	Moupfouma and Martin (1995)	
					Temperate	Tropical/Subtropical
LP – Laws and Parsons	44.6	36.4	37.5	41.6	41.6	32.5
de Wolf – Gamma	46.9	38.3	39.4	43.8	43.8	34.1
AU – Gamma	50.7	40.6	42.0	47.0	47.0	35.9
WB – Weibull	45.9	37.6	38.7	42.9	42.9	33.6
JD – Exponential	37.0	29.8	30.8	34.4	34.4	26.4
JT – Exponential	48.5	39.7	40.9	45.3	45.3	35.4
MP – Exponential	43.2	35.1	36.2	40.2	40.2	31.2
CS – Lognormal	42.9	35.0	36.0	40.0	40.0	31.1
CT – Lognormal	43.8	35.7	36.8	40.9	40.9	31.9
TS – Lognormal	46.4	37.7	38.9	43.2	43.2	33.5
TT – Lognormal	47.0	38.4	39.6	43.9	43.9	34.3

Table D-16 : Path attenuation exceeded for 0.1% of the year for 19.5 GHz

Rain-Rate Model / Drop-Size Distribution	Extreme-value model	Seeber (1985)	ITU model	Moupfouma (1987)	Moupfouma and Martin (1995)	
					Temperate	Tropical/Subtropical
LP – Laws and Parsons	13.1	13.5	11.5	11.9	13.6	14.7
de Wolf – Gamma	13.6	14.0	12.0	12.3	14.1	15.2
AU – Gamma	12.8	13.2	11.1	11.5	13.3	14.5
WB – Weibull	13.8	14.2	12.2	12.6	14.3	15.5
JD – Exponential	10.7	11.1	9.4	9.7	11.2	12.1
JT – Exponential	13.8	14.3	12.2	12.6	14.4	15.5
MP – Exponential	12.5	12.9	11.0	11.3	13.0	14.0
CS – Lognormal	12.8	13.3	11.3	11.7	13.3	14.4
CT – Lognormal	12.9	13.3	11.3	11.7	13.4	14.5
TS – Lognormal	13.3	13.7	11.7	12.0	13.8	14.9
TT – Lognormal	13.7	14.1	12.1	12.4	14.2	15.3

Table D-17 : Path attenuation exceeded for 0.01% of the year for 19.5 GHz

Rain-Rate Model / Drop-Size Distribution	Extreme-value model	Seeber (1985)	ITU model	Moupfouma (1987)	Moupfouma and Martin (1995)	
					Temperate	Tropical/Subtropical
LP – Laws and Parsons	33.0	30.1	33.0	32.8	32.8	32.8
de Wolf – Gamma	34.0	31.0	33.9	33.8	33.8	33.8
AU – Gamma	34.6	31.3	34.5	34.4	34.4	34.4
WB – Weibull	34.0	31.1	33.9	33.8	33.8	33.8
JD – Exponential	28.3	25.7	28.3	28.1	28.1	28.1
JT – Exponential	34.3	31.3	34.2	34.1	34.1	34.1
MP – Exponential	31.7	28.9	31.7	31.5	31.5	31.5
CS – Lognormal	32.4	29.6	32.4	32.2	32.2	32.2
CT – Lognormal	33.1	30.2	33.1	32.9	32.9	32.9
TS – Lognormal	33.4	30.5	33.4	33.2	33.2	33.2
TT – Lognormal	34.1	31.1	34.0	33.9	33.9	33.9

Table D-18 : Path attenuation exceeded for 0.001% of the year for 19.5 GHz

Rain-Rate Model / Drop-Size Distribution	Extreme-value model	Seeber (1985)	ITU model	Moupfouma (1987)	Moupfouma and Martin (1995)	
					Temperate	Tropical/Subtropical
LP – Laws and Parsons	68.2	55.9	57.6	63.8	63.8	50.0
de Wolf – Gamma	69.9	57.4	59.1	65.4	65.4	51.3
AU – Gamma	75.4	60.9	62.9	70.2	70.2	54.1
WB – Weibull	69.0	56.8	58.5	64.6	64.6	50.9
JD – Exponential	60.5	49.2	50.7	56.4	56.4	43.7
JT – Exponential	70.0	57.5	59.2	65.5	65.5	51.5
MP – Exponential	66.0	54.0	55.6	61.7	61.7	48.2
CS – Lognormal	67.2	55.0	56.7	62.8	62.8	49.2
CT – Lognormal	69.5	56.7	58.5	64.9	64.9	50.6
TS – Lognormal	69.2	56.7	58.4	64.7	64.7	50.7
TT – Lognormal	69.8	57.3	59.0	65.3	65.3	51.3

Table D-19 : Path attenuation exceeded for 0. 1% of the year for 40 GHz

Rain-Rate Model / Drop-Size Distribution	Extreme-value model	Seeber (1985)	ITU model	Moupfouma (1987)	Moupfouma and Martin (1995)	
					Temperate	Tropical/Subtropical
LP – Laws and Parsons	37.0	38.0	33.2	34.1	38.2	40.9
de Wolf – Gamma	35.8	36.8	32.2	33.0	36.9	39.4
AU – Gamma	37.1	38.1	33.2	34.1	38.3	41.0
WB – Weibull	39.4	40.4	35.8	36.6	40.6	43.0
JD – Exponential	41.0	42.3	36.4	37.5	42.5	45.7
JT – Exponential	32.1	33.0	28.8	29.5	33.1	35.4
MP – Exponential	37.6	38.6	33.6	34.5	38.8	41.6
CS – Lognormal	42.1	43.5	37.2	38.4	43.7	47.1
CT – Lognormal	41.4	42.8	36.3	37.5	43.0	46.7
TS – Lognormal	41.3	42.6	36.8	37.8	42.8	46.0
TT – Lognormal	38.9	40.0	34.6	35.6	40.2	43.2

Table D-20 : Path attenuation exceeded for 0.01% of the year for 40 GHz

Rain-Rate Model / Drop-Size Distribution	Extreme-value model	Seeber (1985)	ITU model	Moupfouma (1987)	Moupfouma and Martin (1995)	
					Temperate	Tropical/Subtropical
LP – Laws and Parsons	81.6	75.4	81.5	81.2	81.2	81.2
de Wolf – Gamma	77.4	71.7	77.3	77.0	77.0	77.0
AU – Gamma	82.4	76.1	82.3	82.0	82.0	82.0
WB – Weibull	79.4	74.1	79.4	79.1	79.1	79.1
JD – Exponential	96.9	88.9	96.8	96.3	96.3	96.3
JT – Exponential	70.4	65.1	70.3	70.0	70.0	70.0
MP – Exponential	83.9	77.5	83.9	83.5	83.5	83.5
CS – Lognormal	102.8	94.1	102.7	102.2	102.2	102.2
CT – Lognormal	107.4	97.7	107.3	106.8	106.8	106.8
TS – Lognormal	96.3	88.6	96.2	95.8	95.8	95.8
TT – Lognormal	90.1	82.9	90.0	89.7	89.7	89.7

Table D-21 : Path attenuation exceeded for 0.001% of the year for 40 GHz

Rain-Rate Model / Drop-Size Distribution	Extreme-value model	Seeber (1985)	ITU model	Moupfouma (1987)	Moupfouma and Martin (1995)	
					Temperate	Tropical/Subtropical
LP – Laws and Parsons	152.6	128.4	131.8	143.9	143.9	116.6
de Wolf – Gamma	142.6	120.5	123.5	134.7	134.7	109.7
AU – Gamma	155.0	130.3	133.7	146.1	146.1	118.2
WB – Weibull	138.7	118.9	121.7	131.6	131.6	109.1
JD – Exponential	191.0	158.5	163.0	179.3	179.3	142.8
JT – Exponential	131.2	110.5	113.4	123.8	123.8	100.4
MP – Exponential	158.7	133.2	136.7	149.5	149.5	120.8
CS – Lognormal	207.7	171.2	176.2	194.5	194.5	153.7
CT – Lognormal	227.1	185.0	190.8	211.9	211.9	164.9
TS – Lognormal	188.0	156.4	160.8	176.6	176.6	141.1
TT – Lognormal	175.3	146.0	150.0	164.7	164.7	131.8

Table D-22 : Path attenuation exceeded for 0. 1% of the year for 80 GHz

Rain-Rate Model / Drop-Size Distribution	Extreme-value model	Seeber (1985)	ITU model	Moupfouma (1987)	Moupfouma and Martin (1995)	
					Temperate	Tropical/Subtropical
LP – Laws and Parsons	55.2	56.7	50.0	51.2	56.9	60.5
de Wolf – Gamma	46.7	47.8	42.5	43.5	48.0	50.9
AU – Gamma	55.7	57.0	50.9	52.0	57.2	60.5
WB – Weibull	55.0	56.1	50.8	51.7	56.3	59.1
JD – Exponential	92.1	94.4	83.4	85.4	94.8	100.8
JT – Exponential	44.1	45.2	40.0	40.9	45.4	48.2
MP – Exponential	63.8	65.4	58.0	59.3	65.6	69.6
CS – Lognormal	61.5	63.2	55.3	56.7	63.4	67.7
CT – Lognormal	55.2	56.9	49.3	50.6	57.1	61.3
TS – Lognormal	55.0	56.4	49.8	51.0	56.6	60.2
TT – Lognormal	47.3	48.5	42.6	43.7	48.8	52.0

Table D-23 : Path attenuation exceeded for 0.01% of the year for 80 GHz

Rain-Rate Model / Drop-Size Distribution	Extreme-value model	Seeber (1985)	ITU model	Moupfouma (1987)	Moupfouma and Martin (1995)	
					Temperate	Tropical/Subtropical
LP – Laws and Parsons	114.1	106.2	114.0	113.6	113.6	113.6
de Wolf – Gamma	92.5	86.5	92.5	92.1	92.1	92.1
AU – Gamma	107.0	100.3	106.9	106.5	106.5	106.5
WB – Weibull	97.7	92.3	97.6	97.3	97.3	97.3
JD – Exponential	189.7	176.6	189.6	188.8	188.8	188.8
JT – Exponential	89.5	83.4	89.4	89.1	89.1	89.1
MP – Exponential	127.7	119.2	127.6	127.1	127.1	127.1
CS – Lognormal	132.5	122.8	132.4	131.9	131.9	131.9
CT – Lognormal	126.4	116.5	126.3	125.8	125.8	125.8
TS – Lognormal	113.1	105.3	113.0	112.6	112.6	112.6
TT – Lognormal	100.3	93.1	100.2	99.8	99.8	99.8

Table D-24 : Path attenuation exceeded for 0.001% of the year for 80 GHz

Rain-Rate Model / Drop-Size Distribution	Extreme-value model	Seeber (1985)	ITU model	Moupfouma (1987)	Moupfouma and Martin (1995)	
					Temperate	Tropical/Subtropical
LP – Laws and Parsons	203.2	173.3	177.5	192.5	192.5	158.6
de Wolf – Gamma	159.5	137.3	140.3	151.6	151.6	126.2
AU – Gamma	179.9	155.9	159.2	171.3	171.3	143.9
WB – Weibull	154.5	136.1	138.7	148.0	148.0	126.9
JD – Exponential	337.1	287.7	294.5	319.4	319.4	263.3
JT – Exponential	157.2	134.6	137.7	149.1	149.1	123.4
MP – Exponential	221.9	190.5	194.9	210.7	210.7	175.0
CS – Lognormal	243.8	206.2	211.4	230.3	230.3	187.7
CT – Lognormal	243.5	203.4	208.9	229.1	229.1	183.9
TS – Lognormal	200.7	171.3	175.4	190.2	190.2	156.8
TT – Lognormal	182.3	154.6	158.5	172.4	172.4	141.0

References

Journals and Conference Publications

Ajayi, O. G., and Ofoche, E. B. C., 1983. Some tropical rainfall rate characteristics at Ife-Ife for microwave and millimeter wave applications, *J. Climate Appl. Meteorol.*, 23, 562–567.

Ajayi, G. O., and Olsen, R. L., 1985. Modeling of as tropical raindrop size distribution for microwave and millimetre wave applications, *Radio Sci.*, 20 (2), 193–202.

Ajayi, G. O., and Adimula, I. A., 1996. Variations in raindrop size distributions and specific attenuation due to rain in Nigeria, *Ann. Telecommunic.*, 51 (1–2), 87–93.

Atlas, D., and Ulbrich, C. W., 1977. Path- and area-integrated rainfall measurement by microwave attenuation in the 1-3cm band, *J. Appl. Meteorol.*, 16, 1322–1331.

Beard, K. V., and Jameson, A.R., 1982. Raindrop canting, *J. Atmos. Sci.*, 40 (10), 448–454.

Bennett, J. A., Fang, D. J., and Boston, R. C., 1983. The relationship between N_0 and A for Marshall-Palmer type raindrop-size distributions, *J. Climate Appl. Meteorol.*, 23, 768–771.

Best, A. C., 1950. Empirical formulae for the terminal velocity of water drops falling through the atmosphere, *Quart. J. R. Met. Soc.*, 76, 302–311.

Brussaard, G., 1976. A meteorological model for rain-induced cross polarization, *IEEE Trans. Antennas Propagat.*, AP–24 (1), 5–11.

Campos, E. F., 1999. On measurement of drop size distribution, *Top. Meteor. Oceanog.*, 6 (1), 24–30.

Crane, R. K., 1971. Propagation phenomena affecting satellite communication systems operating in the centimetre and millimetre wavelength bands, *IEEE Trans. Antennas Propagat,* 59 (2), 173–188.

Crane, R. K., 1971. Prediction of the effects of rain on satellite communication systems, *IEEE Trans. Antennas Propagat,* 65 (3), 456–474.

Crane, R. K, 1975. Attenuation due to rain – a mini review, *IEEE Trans. Antennas Propagat*, AP–23 (5), 750–752.

Crane, R. K., 1980. Prediction of attenuation by rain, *IEEE Trans. Commun.*, COM–28 (9), 1717–1733.

Crane, R. K., 1985. Comparative evaluation of several rain attenuation prediction models, *Radio Sci,* 20 (4), 843–863.

Crane, R. K., 1985. Evaluation of global and CCIR models for estimation of rain rate statistics, *Radio Sci,* 20 (4), 865–879.

Crane, R. K., 2001 A two-component rain model for the prediction of attenuation statistics, *Radio Sci.*, 17 (6), 1371–1387.

Crane, R. K., 2003. A local model for the prediction of rain-rate statistics for rain-attenuation models, *IEEE Trans. Antennas Propagat.*, 51 (9), 2260–2273.

de Wolf, D. A., Russchenburg, W. J., and Ligthart, L. P., 1992. Simplified analysis of line-of-sight propagation through rain at 5-90 Ghz, *IEEE Trans. Antennas Propagat.*, 40 (8), 912–918.

de Wolf, D. A., and Zweisler, A. J, 1996. Rayleigh-Mie approximation for line-of-sight propagation through rain at 5-90 GHz, *IEEE Trans. Antennas Propagat.*, 44 (3), 273–279.

de Wolf, D. A., 2001 On the Laws-Parsons distribution of raindrop sizes, *Radio Sci.*, 36 (4), 639–642.

Dutton, E. J., and Dougherty, H. T., 1979. Year-to-year variability of rainfall for microwave applications in the U.S.A., *IEEE Trans. Commun.*, COM–27 (5), 829–832.

Dutton, E. J., and Dougherty, H. T., 1984. A second modeling approach to year-to-year rainfall variability in the U.S.A for microwave/millimeter wave applications, *IEEE Trans. Commun.*, COM–32 (10), 1145–1148.

Fang, D. J., and Chen, C. H., 1982. Propagation of centimetre/millimetre waves along a slant path through precipitation, *Radio Sci.*, 35, 989–1005.

Feingold, G., and Levin, Z., 1986. The lognormal fit to raindrop spectra from frontal convective clouds in Israel, *J. Climate Appl. Meteorol.*, 2, 1346–1363.

Gunn, R., and Kinzer, G. D., 1949. The terminal velocity of water droplets in stagnant air, *J. Meteorol.*, 6, 243–248.

Hodson, M. C., 1986. Raindrop size distribution, *J. Climate Appl. Meteorol.*, 25, 1070–1074.

Hogg, D. C., and Chu, T.S., 1975. The role of rain in satellite communications, *Proc. IEEE.*, 63 (9), 1308–1331.

Howard, J., and Gerogiokas, M., 1982. A statistical raindrop canting angle model, *IEEE Trans. Antennas Propagat.*, AP–30 (1), 141–147.

Hogg, D. C., and Chu, T., 1975. The role of rain in satellite communications, *Proc. IEEE,* 63 (9), 1308–1331.

Jiang, H., Sano, M., and Sekine, M., 1997. Weibull raindrop-size distribution and its application to rain attenuation, *IEE Proc. Microw. Antennas Propag.*, 144 (3), 197–200.

Jones, D. A., 1959. The shape of raindrops, *J. Meteorol,* 16, 504–510.

Joss, J., and Gori, E. G., 1978. Shapes of raindrop size distributions, *J. Appl. Meteorol.*, 17, 1054–1061.

Lee, W. C. Y 1979. An approximate method for obtaining rain rate statistics for use in signal attenuation estimating, *IEEE Trans. Antennas Propagat.*, AP–27 (3), 407–413.

Li, L. W., Kooi, P. S., Leong, M. S., Yeo, T. S., and Gao, M., 1995. Microwave attenuation by realistically distorted raindrops: Part 1 – Predictions, *IEEE Trans. Antennas Propagat.*, 43 (8), 811–822.

Li, L. W., Kooi, P. S., Leong, M. S., Yeo, T. S., and Gao, M., 1995. Microwave attenuation by realistically distorted raindrops: Part 2 – Predictions, *IEEE Trans. Antennas Propagat.*, 43 (8), 823–828.

Li, L. W., Kooi, P. S., Leong, M. S., and Yeo, T. S., 1994. On the simplified expression of realistic raindrop shapes, *Micowave and opt. technol.lett.*, 7 (4), 201–205.

Lin, D., and Chen, H., 2002. An empirical formula for the prediction of rain attenuation in frequency range 0.6-100 Ghz, *IEEE Trans. Antennas Propagat.*, 50 (4), 545–551.

Lin, S. H., 1976. Rain-rate distributions and extreme-value statistics, *Bell Syst. Tech. J.*, 55 (8), 1111–1124.

Lin, S. H., 1977. More on rain-rate distributions and extreme-value statistics, *Bell Syst. Tech. J.*, 57 (5), 1545–1568.

Lin, S. H., 1977. Nationwide long-term rain rate statistics and empirical calculation of 11-GHz microwave rain attenuation, *Bell Syst. Tech. J.*, 56 (9), 1581–1604.

Markowitz, A. H., 1976. Raindrop size distribution expressions, *J. Appl. Meteorol.*, 15, 1029–1031.

Marshall, J. S., and Palmer, W. McK., 1948. The distributions of raindrops with size, *J. Meteorol*, 5, 165–166.

McCormick, G. C., and Hendry, A., 1975 Principles for the radar determination of the polarization properties of precipitation, *Radio Sci.*, 10 (4), 421–434.

McCormick, G. C., Hendry, A., and Allan, L.E., 1976. Depolarization over a link due to rain: Measurements of the parameters, *Radio Sci.*, 11 (8–9), 741–749.

McCormick, G. C., and Hendry, A., 1976. Polarization-related parameters fro rain: Measurements obtained by radar, *Radio Sci.*, 11 (8–9), 731–740.

Medhurst, R. G., 1964. Rainfall attenuation of centimetre waves: Comparison of theory and measurement, *IEEE Trans. Antennas Propagat.*, AP–12, 550–566.

Moupfouma, F., 1987. More about rainfall rate and their prediction for radio systems engineering, *Proc. IEE.*, 134 (6), 527–537.

Moupfoma, F., and Martin, L., 1995. Modelling of the rainfall rate cumulative distribution for the design of satellite and terrestrial communication systems, *Int. J. Satellite Comm.*, 13, 105–115.

Moupfoma, F., 1995. Anew theoretical formulation for calculation of the specific attenuation due to precipitation particles on terrestrial and satellite radio links, *Int. J. Satellite Comm.*, 15, 89–99.

Oguchi, T., 1973 Attenuation and phase rotation of radio waves due to rain: Calculations at 19.3 and 34.8 GHz, *Radio Sci.*, 8 (1), 31–38.

Oguchi, T., 1977. Scattering properties of Pruppacher-and-Pitter from raindrops and cross polarization due to rain: Calculations at 11, 13, 19.3 and 34.8 GHz, *Radio Sci.*, 12 (1), 41–51.

Oguchi, T., 1981. Scattering by hydrometeors: A survey , *Radio Sci.*, 16 (5), 691–730.

Oguchi, T., 1983. Electromagnetic wave propagation ands scattering in rain and other hydrometeors, *Proc. IEEE.*, 71 (9), 1029–1078.

Olsen, R. L., and Rogers, D. V., and Hodge, D.B., 1978. The aR^b relation in the calculation of rain attenuation, *IEEE Trans. Antennas Propagat.*, AP-26 (2), 318–329.

Olsen, R. L., 1981. Cross polarization during precipitation on terrestrial links: A review, *Radio Sci.*, 16 (5), 761–779.

Olsen, R. L., 1982. A review of theories of coherent radio wave propagation through precipitation media of randomly oriented scatterers, and the role of multiple scattering, *Radio Sci.*, 17 (5), 913–928.

Pruppacher, H. R., and Beard, K. V., 1970. A wind tunnel investigation of the internal circulation and shape of water drops falling at terminal velocity, *Quart. J. R. Met Soc.*, 96, 247–256.

Pruppacher, H. R., and Pitter, R. L., 1971. A semi-empirical determination of the shape of cloud and rain drops. *J. Atmos. Sci.*, 28, 86–94.

Ray, P. S., 1972. Broadband Complex Refractive Indices of Ice and Water, *Appl. Opt.*, 11 (8), 1836–1844.

Rice, P. L., and Holmberg, N. R., 1973. Cumulative time statistics of surface-point rainfall rates, *IEEE Trans. Commun.*, COM–21 (10), 1131–1136.

Rogers, R. R., 1976. Statistical rainstorm models: Their theoretical and physical foundations, *IEEE Trans. Antennas Propagat.*, 8, 547–565.

Saunders, M. J., 1971. Cross polarization at 18 and 30 GHz due to rain, *IEEE Trans. Antennas Propagat.*, AP–19 (2), 273–277.

Sander, J., 1975. Rain attenuation of millimetre waves at λ = 5.77, 3.3, and 2mm, *IEEE Trans. Antennas Propagat.*, 23 (2), 213–220.

Segal, B., 1986. The influence of rain gauge integration time on measured rainfall-intensity distribution functions, *J. Atmospheric Oceanic Tech.*, 3 (4), 662–671.

Seliga, T. A., and Bringi, V. N., 1978. Potential use of radar differential reflectivity measurements at orthogonal polarization for measuring precipitation, *J. Appl. Meterol.*, 15 (1), 69–76.

Sekhon, R. S., Strivastava, R. C., 1971. Doppler radar observations of drop-size distributions in a thunderstorm , *J. Atmos. Sci.*, 28, 983–994.

Sekine, M., Chen, C., and Musha, T., 1979. Rain attenuation from log-normal and Weibull raindrop-size distributions, *IEEE Trans. Antennas Propagat.*, AP–35 (3), 358–359.

Semplak, R. A., 1970 Effect of oblate raindrops on attenuation at 30.9 GHz, *Radio Sci.*, 5 (3), 559–564.

Shkarapofsky, I. P., 1979. Dependence of rain attenuation and cross-polarization on drop size distribution, *IEEE Trans. Antennas Propagat.*, AP–27 (4), 538–542.

Strivastava, R. C., 1977. Parameterization of raindrop size distributions, *J. Atmos. Sci.*, 35, 108–117.

Tattelman, P., and Scharr, K. G., 1983. A model for estimating one-minute rainfall rates, *J. Climate Appl. Meteorol.*, 22, 1575–1580.

Tattelman, P., and Grantham, D. D., 1985. A review models for estimating 1 min rainfall rates for microwave attenuation calculations, *IEEE Trans. Commun.*, COM–33 (4), 361–372.

Tattelman, P., Larson, K. P., and Andrew, J. M., 1994. A climatological model for 1-min precipitation Rates, *J. Appl. Meteorol.*, 34, 1020–1027.

Thomas, D. T., 1971 Cross-polarisation distortion in microwave radio transmission due to rain, *Radio Sci.*, 6 (10), 833–839.

Torres, D. S., Porra, J. M. and Creutin J. D., 1983. A general formulation for raindrop size distribution, *J. Appl. Meteorol.*, 33, 1494–1502.

Ugai, S., Kato, K., Nishijima, N. Kan, T., and Tazaki, K., 1977. Fine structure of rainfall, *Ann. Telecommunic..*, 32 (1–2), 422–429.

Uijlenhoet, R., 1998. Raindrop size distributions and radar reflectivity-rain rate relationships for radar hydrology, *Hydrol. Earth. Syst. Sci.*, 5 (4), 615–627.

Ulbrich, C. W., 1983. Natural variations in the analytical form of the raindrop size distribution, *J. Appl. Meteorol.*, 22, 1764–1775.

Yeo, T. S., Kooi, P. S., Leong, M. S., 1993, A two-year measurement of rainfall attenuation of CW microwaves in Singapore, *IEEE Trans. Antennas Propagat.*, 41 (6), 709–712.

Watson, P. A., 1976. Cross polarisation measurements at 11 GHz, *Proc. IEE.*, 123 (7), 667–675.

Watson, P. A., 1976. Survey of measurements of attenuations by rain and other hydrometeors, *Proc. IEE.*, 123 (9), 863–871.

Waldvogel, A., 1974. The N_0 jump of raindrop spectra, *J. Atmos. Sci.*, 31, 1067–1078.

Zhou, X. Z., Li, T., S., and Leong, M., S., 2001. Cumulative distributions of rainfall rate and microwave attenuation in Singapore's tropical region, *Radio Sci.*, 35 (3), 751–756.

Reports

Adamson, P. T., 1977. Extreme Values and return periods for rainfall in South Africa, *Rep. No. 78*, Department of Water Affairs, Pretoria.

Cermac, D., Fiser, O., and Schejal, V., 2005. Electromagnetic scattering by raindrops, *COST 280 PM 9-109*, ESTEC, Pardubice, The Czech Republic

Department of Transport, 1974. Extreme values of rainfall temperature and wind for selected return periods – Part 2, *Rep. No. WB36*, Weather Bureau publication, Pretoria.

Ippolito, L. J., 1989. Propagation handbook for satellite systems, *Rep. No. 1082 (04)*, Westinghouse Electric Corporation, Maryland.

Matzler, C., 2000. Radiative transfer models for microwave radiometry, *COST Action 712*, Meteorology, Institute of Applied Physics, University of Bern

Matzler, C., 2002. Drop-size distributions and Mie computations for rain, *IAP RES. Rep. No. 2002-16*, Meteorology, Institute of Applied Physics, University of Bern.

Matzler, C., 2002. Effects of rain on propagation, absorption and scattering of microwave radiation based on the Dielectric model of Liebe, *IAP RES. Rep. No. 2002-10*, Meteorology, Institute of Applied Physics, University of Bern.

Matzler, C., 2002. Matlab functions for Mie scattering and absorption, *IAP RES. Rep. No. 2002-08*, Meteorology, Institute of Applied Physics, University of Bern.

Matzler, C., 2002. Matlab functions for Mie scattering and absorption: Version 2, *IAP RES. Rep. No. 2002-11*, Meteorology, Institute of Applied Physics, University of Bern.

Midgley, D. C, and Pitman, W. V., 1978. A depth-duration frequency diagram for point rainfall in Southern Africa, *Rep. No. 2/78,* Hydrological research unit, University of the Witwatersrand, Johannesburg.

Smithers, J. C., and Schulze, R. E., 2002. Design rainfall and flood estimation in South Africa, *Rep. No. K5/1060*, School of Bioresources engineering and environmental hydrology, University of Natal, South Africa.

Zhang, W., and Moayeri, N., 1999. Power-law parameters of rain specific attenuation, *IEEE 802.16 Rep. No. 24,* National Institute of Standards and Technology.

Zhang, W., and Moayeri, N., 2000. Use of Various Raindrop Size Distributions for different Geographical Locations in Calculating the Rain Specific Attenuation, *IEEE 802.16 Rep. No. 41,* National Institute of Standards and Technology.

ITU Recommendations

ITU-R P.341–5, The concept of transmission loss for radio links, 1999.

ITU-R P.530–11, Propagation data and prediction methods required for the design of terrestrial line-of-sight systems, 2005.

ITU-R P.676–5, Attenuation by atmospheric gases, 2001.

ITU-R P.837–1, Characteristics of precipitation for propagation modelling, 1994.

ITU-R P.837–2, Characteristics of precipitation for propagation modelling, 1999.

ITU-R P.837–3, Characteristics of precipitation for propagation modelling, 2001.

ITU-R P.837–4, Characteristics of precipitation for propagation modelling, 2003.

ITU R. P.383, Specific attenuation model for rain for use in prediction methods, 1992.

ITU R. P.838–1, Specific attenuation model for rain for use in prediction methods, 1999.

ITU R. P.838–2, Specific attenuation model for rain for use in prediction methods, 2003.

ITU R. P.838–3, Specific attenuation model for rain for use in prediction methods, 2005.

ITU R P.525–2, Calculation of free space attenuation, 1994.

ITU R P.526–8, Propagation by diffraction, 2003.

ITU R P.840–3, Attenuation due to clouds and fog 1999.

Thesis

Seeber, R. J., 1985, *An extreme value model of surface-point rain-rate distribution for the prediction of microwave rain attenuation in Southern Africa*, Thesis, University of Pretoria.

Books

Abramowitz, M., and Stegun, I. A., 1968. *Handbook of mathematical functions*, 5th ed. New York: Dover publications, Inc.

Bayvel, L. P., and Jones, A. R., 1981. *Electromagnetic scattering and its applications*. London: Applied science publishers.

Collin, R. E., 1985. *Antennas and radiowave propagation*. U.S.A: McGraw-Hill.

Crane, R. K, 1996. *Electromagnetic wave propagation through rain*. Canada: John Wiley and sons.

Freeman, R. L., 1987. *Radio system design for telecommunications (1-100 GHz).* New York: John Wiley and sons.

Greenstein, L. J., 1988. *Microwave digital radio.* U.S.A: IEEE Press.

Ishimaru, A., 1978. *Wave propagation and scattering on random media: Volume 1.* New York: Academic Press.

Ishimaru, A., 1991. *Electromagnetic wave propagation, radiation, and scattering.* New Jersey: Prentice Hall.

Kyle, T. G., 1991. *Atmospheric transmission, emission and scattering.* London: Pergamon Press.

Pruppacher, H. R., and Klett, J. D., 1978, *Microphysics of clouds and precipitation.* Boston: Reidel.

Sadhiku, M. N. O., *Numerical techniques in electromagnetics.* 2nd ed. Boca Raton: CRC Press.

Shibuya, S., 1987. *A basic atlas of radio-wave propagation.* New York: John Wiley and sons.

Shaw, E. M., 1994. *Hydrology in Practice.* 3rd ed. London: Chapman and Hall.

Stratton, J. A., 1941. *Electromagnetic Theory.* London: McGraw-Hill.

Tai, C. T., 1994. *Dyadic green functions in Electromagnetic theory.* 2nd ed.. New York: IEEE Press.

Townsend, A. A. R., 1987. *Analog line-of-sight radio links.* London: Prentice Hall.

Tsang, L., Kang, J. A, and Ding, K. H., 2000. *Scattering of electromagnetic waves: Theories and applications.* New York: John Wiley and sons.

Van de Hulst, H. C., 1957. Light scattering by small particles. London: Chapman and Hall.